



THE UNIVERSITY
of ADELAIDE

Laser Powder Bed Fusion (L-PBF) 3D printing of
Titanium-based alloys:
Effects of process parameters and post-fabrication
treatments

Alireza Dareh Baghi

School of Mechanical Engineering

Thesis submitted in fulfilment of the requirements
for the degree of Doctor of Philosophy

Submitted: 4th Nov 2022

Abstract

Laser Powder Bed Fusion (LPBF), also known as Selective Laser Melting (SLM), as one of additive manufacturing techniques for fabrication of metallic parts, is being actively developed to manufacture intricate metallic parts for a range of applications. This has resulted in generating great research interests in understanding the principles of the LPBF fabrication and the effects of the process parameters on the as-printed surface topography and microstructure. This is an important step in characterising the capabilities of the manufacturing route due to the correlation between the surface topography-microstructure and mechanical properties of printed metallic parts. Moreover, study of some post treatments and their effects on the microstructure and mechanical properties are as important. Therefore, the main aim of this research project is to study the characteristics of LPBF fabricated titanium based parts and explore the effects of manufacturing parameters and post-process treatments on the microstructure and associated mechanical properties.

Amongst the metallic alloy powders used as the starting material during LPBF process, the fabrication of Ti-6Al-4V (also known as Ti64) components has drawn considerable attention in diverse industrial fields such as aerospace and biomedical. Therefore, the above-mentioned alloy, as one of the most widely researched titanium based alloy, was selected as the material of interest in this project.

In the initial stage of this research, an attempt was made to establish an empirical method for optimisation of process parameters of LPBF by exploring a correlation between the morphology of top surface and the residual porosity of the parts. By categorising the surface morphology into two groups of surfaces with meso roughness and micro roughness, it is proved that top surface morphology is a most reliable measure for

prediction of internal porosity of the Ti64 parts. Moreover, in the optimisation process, a range for the process parameter with their threshold is provided and discussed which can be found in Chapter 3.

Then a fundamental study was conducted to highlight the differences between the powder metallurgy as a traditional near net shape manufacturing route with the layer-wise LPBF technique. It is found that sintered Ti64 parts, have lamellar microstructure of α and β while the microstructure of LPBF fabricated parts has single phase of α' as a result of diffusionless transformation from parent β which had an epitaxial columnar growth. Moreover, it is discovered that the higher strength of LPBF fabricated parts compared to sintered parts is owing to only morphology and refinement of α' because the nano-hardness of bulk α' compared to α is nearly the same. The discussions about these findings are presented in Chapter 4.

For better understanding of the effects of build orientations and surface conditions on mechanical properties of LPBF fabricated parts, a novel design overcame the challenge of fabrication of straight horizontal samples without any post treatment. It is revealed that the vertically deposited samples suffered from premature failure in their truly as-built conditions. The reason behind this problem and the most viable post treatment method is discussed in two journal papers which are represented in Chapters 5 and 6.

The outcome of this research study is five peer-reviewed journal articles and one international conference paper. The thesis is based on four main journal papers presented as four chapters (Chapter 3 to 6) to highlight the main findings and contributions of this study to the field.

While all original published papers (as parts of Chapter 4, 5 and 6) are presented in the Appendix A, the other article which is as a part of this study but not presented in the chapters, along with conference paper are in the Appendix B.

Thesis declaration

I certify that this work contains no material which has been accepted for the award of any other degree or diploma in my name, in any university or other tertiary institution and, to the best of my knowledge and belief, contains no material previously published or written by another person, except where due reference has been made in the text. In addition, I certify that no part of this work will, in the future, be used in a submission in my name, for any other degree or diploma in any university or other tertiary institution without the prior approval of the University of Adelaide and where applicable, any partner institution responsible for the joint award of this degree.

I acknowledge that copyright of published works contained within this thesis resides with the copyright holder(s) of those works.

I also give permission for the digital version of my thesis to be made available on the web, via the University's digital research repository, the Library Search and also through web search engines, unless permission has been granted by the University to restrict access for a period of time.

I acknowledge the support I have received for my research through the provision of an Australian Government Research Training Program Scholarship.

Name: Alireza Dareh Baghi

Signature

Date: 1/11/2022

Acknowledgments

I would like to express my gratitude to many people who helped me fruitify this research study and without their support this work would not be possible.

First and foremost, I would like to thank my supervisors, Dr. Reza Ghomashchi, Dr Shahrooz Nafisi and Prof Heike Ebendorff-Heidepriem for their deep care and support in this project. I thank Dr. Ghomashchi for his patience, support, and guidance; it was a great honour working with him. I should never forget the life-changing advice and support of Dr Shahrooz Nafisi without which, I could never lift my research project to a world class state. I am also thankful to Dr. Reza Hashemi at Flinders University who has graciously arranged my access to the facilities at Flinders for running some experimental tests.

Many thanks to my friends and ex-fellow PhD students at the School of Mechanical Engineering, Dr Sadeq Hooshmand Zaferani and Dr Oveis Pourmehran for their consultation in layout of some sections of the thesis. I would like to thank PhD student, John Daniel Arputharaj for his help and some supplementary experiments he performed. Adelaide Microscopy is gratefully acknowledged for the access provided to electron microscopy facilities. I am also grateful to the Australian Government and Adelaide University for the award of a PhD scholarship.

Thanks to IPAS members, especially Lijesh Thomas and Luis Lima-Marques for access to L-PBF 3D printing machine, ProX200, and sample preparation which was authorized by Prof Heike Ebendorff-Heidepriem. Besides, Alson Kwun Leung Ng is acknowledged for his work on hydrofluoric acid etching. This work was performed in part at the Optofab node of the Australian National Fabrication Facility (ANFF) utilising Commonwealth and South Australian State Government Funding.

I would like to thank Professor Anthony Zander (Head of School) for provision of research facilities at the School, Dr Lei Chen (Postgraduate coordinator) for his guidance on thesis preparation and submission, and Dr. Alison-Jane Hunter (Technical English Editor), for editing research articles, at the School of Mechanical Engineering of the University of Adelaide.

Finally, I need to extend my deepest gratitude and appreciation to my kind wife, Golriz, who was so patient to my hard working, and without her invaluable encouragement it was not possible for me to fulfil this project.

Table of contents

ABSTRACT	I
THESIS DECLARATION	III
ACKNOWLEDGMENTS	IV
TABLE OF CONTENTS	VI
LIST OF PUBLICATIONS INCLUDED IN THIS THESIS	IX
AUTHORS' COMMENTS	XI
LIST OF FIGURES	XII
LIST OF TABLES	XVIII
ABBREVIATIONS AND SYMBOLS	XIX
DEFINITION OF TERMS	XXI
CHAPTER 1 INTRODUCTION	1
1.1 BACKGROUND AND MOTIVATION	1
1.2 LITERATURE REVIEW	3
1.2.1 History of additive manufacturing	3
1.2.2 Methods of additive manufacturing	4
1.2.3 Specific advantages of additive manufacturing	8
1.2.4 Materials for additive manufacturing.....	9
1.2.5 LPFB 3D printing of titanium alloys	11
1.3 RESEARCH GAPS.....	14
1.4 AIMS AND OBJECTIVES.....	15
1.5 STRUCTURE OF THESIS.....	15
1.6 THESIS FORMAT	17
REFERENCES	17
CHAPTER 2 EXPERIMENTAL PROCEDURES	24
2.1 MATERIALS AND FABRICATION ROUTES	24
2.1.1 Material.....	24
2.1.2 Sample preparation	27
2.1.3 Post fabrication processes	32
2.2 MICROSTRUCTURAL CHARACTERISATION	34
2.2.1 Metallographic samples preparation	34
2.2.2 XRD.....	36
2.2.1 Optical microscopy, SEM and EDS analysis.....	37
2.3 SURFACE CHARACTERISATION.....	39
2.4 MECHANICAL PROPERTIES.....	40
2.4.1 Tensile test.....	40
2.4.2 Micro-hardness and nanoindentation.....	42
REFERENCE	44

CHAPTER 3 L-PBF PROCESS OPTIMISATION	45
CHAPTER OVERVIEW	45
3.1 INTRODUCTION	48
3.2 MATERIALS AND EXPERIMENTAL PROCEDURES	50
3.2.1 Materials and L-PBF equipment	50
3.2.2 Design of experiments and L-PBF process parameters	52
3.2.3 Analysis method	55
3.3 RESULTS AND DISCUSSION	57
3.3.1 Surface topography	57
3.3.2 Correlation between surface roughness and porosity	64
3.3.3 Surface quality and process parameters	67
3.3.4 Production rate and Volumetric Energy Density	81
3.4 CONCLUSIONS	82
3.5 ACKNOWLEDGEMENTS	84
REFERENCES:	84
CHAPTER 4 MICROSTRUCTURAL CHARACTERISTICS	88
CHAPTER OVERVIEW	88
4.1 INTRODUCTION	91
4.2 MATERIALS AND EXPERIMENTAL PROCEDURES	92
4.3 RESULTS AND DISCUSSION	98
4.3.1 Microstructural constituents	98
4.3.2 Micro and nano-hardness characteristics	105
4.4 CONCLUSION	114
4.5 ACKNOWLEDGEMENTS	115
REFERENCES:	115
CHAPTER 5 EFFECTS OF BUILD ORIENTATIONS AND SURFACE ON LPBF PARTS	121
CHAPTER OVERVIEW	121
5.1 INTRODUCTION	124
5.2 MATERIALS AND EXPERIMENTAL PROCEDURES	126
5.2.1 Materials	126
5.2.2 Experimental procedures	128
5.3 RESULTS AND DISCUSSION	132
5.3.1 Microstructural characterisation	132
5.3.2 Mechanical properties	136
5.3.3 Fracture analysis	144
5.4 CONCLUSIONS	150
5.5 DECLARATION OF COMPETING INTEREST	151
5.6 ACKNOWLEDGEMENTS	151
REFERENCES	152
CHAPTER 6 SURFACE MACHINING VERSUS THERMAL TREATMENT	156

CHAPTER OVERVIEW	156
6.1 INTRODUCTION	159
6.2 MATERIALS AND EXPERIMENTAL PROCEDURES	162
6.2.1 Materials	162
6.2.2 SLM fabrication equipment and method	163
6.2.3 Tensile samples preparation and heat treatment cycles	164
6.2.4 Analysis methods	168
6.3 RESULTS AND DISCUSSION	168
6.3.1 Microstructural characterisation	168
6.3.2 Mechanical properties	181
6.3.3 Fracture surface analysis	188
6.4 CONCLUSIONS	193
6.5 DECLARATION OF COMPETING INTEREST	194
6.6 ACKNOWLEDGEMENTS	195
REFERENCES	195
CHAPTER 7 CONCLUSION AND FUTURE WORK	199
7.1 SUMMARY AND SIGNIFICANCE	199
7.2 RECOMMENDATIONS FOR FUTURE WORK	203
7.2.1 Process parameters	203
7.2.2 Experiments	204
7.2.3 Post processes	204
APPENDICES: ORIGINAL PUBLISHED PAPERS AS PARTS OF THIS STUDY	205
APPENDIX A: PAPERS PRESENTED IN THE CHAPTERS OF THIS THESIS	205
APPENDIX B: PAPERS NOT PRESENTED IN THIS THESIS	252

List of publications included in this thesis

This thesis by publication, consists of four ‘published’ journal articles, one ‘submitted’ paper and one ‘conference’ paper in accordance with the Academic Program Rules of The University of Adelaide.

According to the policy of Rights and Permissions of “Springer Nature”, authors have the right to reuse their articles, in whole or in part, in their own thesis. Also, in accordance with the policy of “Elsevier”, the author can retain the right to include his/her article in a thesis or dissertation, provided it is not published commercially.

Published Works

1. **A. Dareh Baghi**, S. Nafisi, H. Ebendorff-Heidepriem, and R. Ghomashchi, "Microstructural development of Ti-6Al-4V alloy via Powder Metallurgy and Laser Powder Bed Fusion," *Metals*, 2022 vol. 12, pp. 1462.
2. **A. Dareh Baghi**, S. Nafisi, R. Hashemi, H. Ebendorff-Heidepriem, and R. Ghomashchi, "Experimental realisation of build orientation effects on the mechanical properties of truly as-built Ti-6Al-4V SLM parts," *Journal of Manufacturing Processes*, 2021 vol. 64, pp. 140-152.
3. **A. Dareh Baghi**, S. Nafisi, R. Hashemi, H. Ebendorff-Heidepriem, and R. Ghomashchi, "Effective post processing of SLM fabricated Ti-6Al-4 V alloy: Machining vs thermal treatment," *Journal of Manufacturing Processes*, 2021 vol. 68, pp. 1031-1046.

4. **A. Dareh Baghi**, R. Ghomashchi, R. H. Oskouei, and H. Ebendorff-Heidepriem, "Nano-mechanical characterization of SLM-fabricated Ti6Al4V alloy: etching and precision," *Metallography, Microstructure, and Analysis*, 2019 vol. 8, pp. 749-756.
5. **A. Dareh Baghi**, S. Nafisi, R. Hashemi, H. Ebendorff-Heidepriem, and R. Ghomashchi, " Machining Versus Heat Treatment in Additive Manufacturing of Ti6Al4V Alloy," TMS 2022 151st Annual Meeting & Exhibition Supplemental Proceedings. 2022. Cham: Springer International Publishing.

Submitted manuscript

6. **A. Dareh Baghi**, S. Nafisi, R. Hashemi, H. Ebendorff-Heidepriem, and R. Ghomashchi, " A New Approach to Empirical Process Optimisation of Laser Powder Bed Fusion Process for Ti6Al4V Parts".

Authors' Comments

1. Published articles within this thesis are the last word proofed versions submitted to the journal and are the same as the original published or submitted manuscript, however there are some exceptions listed below.
 - The typesetting has been differed in a way to have a consistent format throughout the whole thesis.
 - The positions of the figures and tables may be different from the final published articles.
 - The numbering of sections, subsections, figures, and tables of each published article has been changed so that it includes the number of the chapter.

Besides, the original published version of all papers in Pdf format are presented in appendices.

2. The 3D printing routine studied in this thesis is Laser Powder Bed Fusion (L-PBF) according to the standard terminology defined in ISO/ASTM 52900:2015(E), however in some published articles as appears in the chapters of this work, the other well-known terminology of Selective Laser Melting (SLM) can be noticed.

List of figures

Figure 1-1: Schematic representation of the working principle of several additive manufacturing categories with main terminology, BJ: Binder jetting (BJ); SL: Sheet lamination (SL), PBF: Powder bed fusion, DED: Direct energy deposition. [32]. Reproduced under license CC-BY-NC-ND.	7
Figure 1-2: Different types of metal-based AM-processes according to methods of accumulation and heat source, reproduced from [33]. Reproduced with permission from Springer Nature [license No. 5303631386287]	8
Figure 1-3: Schematics of a) Laser directed energy deposition (LDED) and b) Laser powder bed fusion (LPBF) [37].....	8
Figure 1-4: Main characteristics of different titanium alloy family groups [40].....	11
Figure 2-1: Image of Malvern Mastersizer 2000 particle size analyser.	26
Figure 2-2: Typical SEM image of Ti6Al4V powder particle in two conditions of a) as-received and b) used, c) particle diameter distribution (PDS) of the new and used powder measured by Malvern analyser [1].	27
Figure 2-3: a) double acting die and punch; b) Ti6Al4V green and sintered samples. ..	28
Figure 2-4: Cubic samples for empirical development of the optimisation of L-PBF process.	30
Figure 2-5: Laser scan strategy used for all L-PBF fabricated samples except cubic samples. [3].....	31
Figure 2-6: Dimensions of dumbbell shape tensile samples [3].	32
Figure 2-7: L-PBF fabricated dumbbell shape tensile and cylindrical bars on the substrate plate, a) horizontal and vertical dumbbell tensile samples and a few vertical cylindrical bars and b) horizontal cylindrical bars.	32
Figure 2-8: Horizontal cylindrical bars before and after being machined by a lathe.	33
Figure 2-9: Image of the tube furnace AY-TF-80-175.	34
Figure 2-10: a) Componentry for etching the samples in accordance with safety in using HF acid, b) six samples are sunk in the etchant with oscillating movement of samples holder.	35
Figure 2-11: a) Rigaku XRD machine used in this project with rotating sample mount, b) glass holder for XRD examination of powder and c) XRD solid sample holder setup.....	37
Figure 2-12: Zeiss Axio Imager2 optical microscope.	38
Figure 2-13: Micro-sectioning by FIB on an as-built L-PBF fabricated sample.....	39
Figure 2-14: Mitutoyo SJ-410 stylus head is measuring the roughness of top surface of an L-PBF fabricated sample.	40
Figure 2-15: a) Initial setup of the specimen inside serrated wedges, b) wedges start releasing and slipping on grip sections of the specimens due to sample short grip sections.	41

Figure 2-16: Developed solid filler for preventing the slippage of serrated wedge grips on tensile specimen.....	42
Figure 2-17: LECO LM700AT machine used for measuring Vickers microhardness by impression of a pyramidal indenter.	43
Figure 2-18: a) Fischer-Cripps IBIS machine for measuring nano-hardness by impression a Berkovich indenter , b) a typical graph of load versus indenter penetration for three phases observed in L-PBF and powder metallurgy samples.	44
Figure 3-1: a) SEM image of Ti64 powder particles, and b) size (diameter) distribution of Ti64 powder particles.	51
Figure 3-2: a) Top view of all cuboid samples on the build plate, b) arrangement of cuboids on the build plate and c) an example of a cuboid sample, A7, fabricated with an embossed letter “A” and series number “7” on its side wall.	55
Figure 3-3: a) paths for stylus travel and halving a sample which are perpendicular to laser path, b) photo of the second halved section of the sample mounted in Bakelite and polished, (sizes on the photos are not to scale).	57
Figure 3-4: a) SEM micrograph of top surface b) optical microscopy of sectioned and c) surface profile of sample A11 ($P=270$ W, $h=50$ μm , $v=1000$ mm/s, $\text{VED}=180$ J/mm ³).	59
Figure 3-5: Waves observed on top surface of C12 ($P=90$ W, $h=75$ μm , $v=333$ mm/s, $\text{VED}=120$ J/mm ³).	59
Figure 3-6: a) SEM micrograph of top surface, b) optical microscopy of transverse section and c) surface profile of sample A10 ($P=270$ W, $h=150$ μm , $v=1800$ mm/s, $\text{VED}=33$ J/mm ³).	60
Figure 3-7: a) SEM micrograph of top surface, b) optical microscopy of transverse section and c) surface profile of sample A13 ($P=270$ W, $h=100$ μm , $v=1000$ mm/s, $\text{VED}=90$ J/mm ³).	62
Figure 3-8: a) SEM micrograph of top surface, b) optical microscopy of transverse section and c) surface profile of sample C2 ($P=90$ W, $h=75$ μm , $v=833$ mm/s, $\text{VED}=48$ J/mm ³).	63
Figure 3-9: Sample A11 with keyhole pores near its surface.	64
Figure 3-10: Porosity versus roughness in samples of a) group A, b) group B and c) group C. The right graphs are the magnified part of left graphs.	67
Figure 3-11: Graph of micro-roughness R_a of all samples.	68
Figure 3-12: SEM images of the top surface of three samples of group C; a) C4, b) C9 and, c) C14.	71
Figure 3-13: Effect of welding speed on the geometry of weld pool due to growth rate, adapted from N. Suutala, [36].	72
Figure 3-14: Top surface morphology of three samples of group A; a) A3, b) A8 and, c) A13.	73
Figure 3-15: Typical surface profiles of samples; a) A3 ($P=270$ W, $h=100$ μm , $v=2500$ mm/s, $\text{VED}=36$ J/mm ³), b) A8 ($P=270$ W, $h=100$ μm , $v=1800$ mm/s, $\text{VED}=50$ J/mm ³) and c) A13 ($P=270$ W, $h=100$ μm , $v=1000$ mm/s, $\text{VED}=90$ J/mm ³). (The distance between the dash lines represents a span of 1mm on the surface).	74

Figure 3-16: Graphs of R_a vs. laser scan speed of, a) group A, b) group B and c) group C (Higher series number of the samples in the legend of the graphs are corresponding to lower scan speed).....	76
Figure 3-17: Graphs of R_a vs hatch spacing of a) group “A” b) group “B” and c) group “C” (In each subgroup, higher series numbers of the sample are related to higher hatch spacing).	78
Figure 3-18: Micro-roughness R_a versus VED. (The graph on the right is the enlarged part of the left graph.)	80
Figure 3-19: Graph of production rate versus VED of all samples fabricated with laser power 270 W, 180 W.....	82
Figure 4-1: Size distribution of Ti64 powder particles.....	93
Figure 4-2: spherical morphology of Ti64 powder with satellite and particles inside particles.....	94
Figure 4-3: a) sectioning plan for hardness measurement of L-PBF fabricated vertical and horizontal samples, b) nano-indentation maps for sectioned discs from vertical and horizontal samples.	98
Figure 4-4: SEM of micrographs of etched a) starting powder particles and b) L-PBF sample.	99
Figure 4-5: SEM images of PM samples sintered at 1100°C: a) compacted at 450 MPa and c)735 MPa and PM samples sintered at 1250°C: b) compacted at pressure 450 MPa and d)735 MPa.	101
Figure 4-6: XRD spectra of Ti64 powder, as-built LPBF and PM sample.	102
Figure 4-7: EDS analysis of a) as-built L-PBF fabricated part, b) PM sample (750 MPa/1250 °C).	104
Figure 4-8: Optical micrographs of transverse sections of LPBF parts after etching a) horizontally built cylinder and b) vertically built cylinder.....	105
Figure 4-9: Hardness of PM and L-PBF samples vs. their porosity contents.....	106
Figure 4-10: Backscatter electron image of polished samples in unetched conditions, a) PM and b) L-PBF sample.	107
Figure 4-11: Backscatter electron images of 120 indents on the PM sample in unetched condition.	108
Figure 4-12: Nano-hardness values of the α phase with different contents of vanadium and aluminium.	111
Figure 4-13: Loading and unloading indentations graphs of a) L-PBF, b) α phase-PM and c) β phase-PM samples.	112
Figure 4-14: A 300nm deep penetrated nano-indentation in L-PBF sample.....	114
Figure 5-1: a) Ti64 particle diameter distribution of new powder and used powder, b) Typical SEM image of used Ti64 powder particles after being sieved.....	128
Figure 5-2: Geometry of first batch of the horizontal samples.	129
Figure 5-3: Typical sample of the first batch of the horizontally-built parts after being removed from the substrate.	129

Figure 5-4: Deflection curve of two typical horizontal samples from the first batch...	130
Figure 5-5: a) Vertical sample and reversed deflected design of a horizontal dumbbell shape sample attached to the substrate, b) Vertical and horizontal cylinder to be machined, and c) Final test specimen dimensions, (all units in mm).....	131
Figure 5-6: a) Transverse cutting of horizontal and vertical tensile samples from the “grip section”. b and c) Optical micrographs of etched transverse sections of horizontal and vertical samples, respectively, and d) Schematic 3D model of microstructure architecture, according to the applied tensile load direction.	135
Figure 5-7: Backscattered Electron micrographs of the etched samples sectioned transversely from; a) a horizontal sample, and b) a vertical sample.	136
Figure 5-8: The XRD spectrum of the SLM sample shows no trace of β phase, (the red dashed lines show the position of the expected peaks of the β phase).	136
Figure 5-9: The stress-strain plots, a) machined and as-built horizontals, b) machined and as-built verticals, c) as-built horizontals and verticals, d) machined horizontals and verticals, e) tensile properties of horizontal and vertical samples in two conditions of as-built and machined.....	141
Figure 5-10: a) Longitudinal cutting direction for outer surface morphology, b) Optical microscopy of an as-built horizontal sample, and c) an as-built vertical sample.	142
Figure 5-11: UTS versus Elongation of SLM fabricated Ti64 parts, a) machined horizontals, and b) machined verticals.	144
Figure 5-12: Typical fracture surfaces of (a) as-built horizontal sample, (b) as-built vertical sample, (c) machined horizontal sample and (d) machined vertical sample.	145
Figure 5-13: Optical micrographs of the longitudinal section of the as-built vertical samples to show a) its flat fracture surface and b) the formation of surface initiated crack as a result of the sharp-rooted surface profile.	146
Figure 5-14: Optical micrograph of a crack path for the fracture surface of the as-built horizontal sample with well-developed shear lips.....	147
Figure 5-15: SEM micrographs of the fracture surfaces of a) machined vertical with microcracks inter-connecting between layers. The broken lines show the borderline of the shear lips regions and bulk fracture surfaces on the machined tensile samples, and b) machined horizontal with a typical inter-track void and microcrack.	148
Figure 5-16: Developed porosity in the gauge section of all samples near the fracture surface (gauge section) vs the porosity in the grip section.....	150
Figure 6-1: a) Typical SEM image of Ti64 powder particles, b) Ti64 particle diameter distribution of powder.....	163
Figure 6-2: Laser scan strategy and build direction.....	164
Figure 6-3: a) horizontal deposited rods, b) vertical deposited rods and c) non-machined vertical samples (NMV). (Arrows show the SLM build direction; and the sketched planes demonstrate sectioning for preparation of the metallographic samples).166	

Figure 6-4: Dimensions of the tensile test samples (in mm) according to ASTM E8 [27].	167
Figure 6-5: Longitudinal sectioning through the fractured surfaces of a) MH and b) MV samples.	167
Figure 6-6: Optical micrographs of the grains architecture in MH and MV samples: a) non-heat treated, b) stress-relieved and c) annealed.....	170
Figure 6-7: 3D Schematic of a columnar microstructure in SLM fabricated samples.	170
Figure 6-8: XRD spectra of three sample sections from differently-treated MH samples.	172
Figure 6-9: Optical micrographs (left) and SEM (right images) of MH samples; a) non-heat treated, b) stress-relieved and c) annealed. (Arrows show the globular α phase).....	175
Figure 6-10: EDS point analysis of a) a stress-relieved sample, b) an annealed sample.	176
Figure 6-11: Optical micrographs of the transverse section of a) MH and b) MV samples.	177
Figure 6-12: a) Optical microscopy of a non-heat treated sample, b) the SEM image of inset in the optical microscopy image.	178
Figure 6-13: a) Platinum deposited layer according to the dash line in Figure 6-12, as a preparation for sectioning with FIB, b) location of the EDS lines and the average results of each line.	179
Figure 6-14: a) Optical micrograph of columnar grains in an annealed sample and b) the magnified inset with coarse and globular α phase. (Arrows show the melt pool boundaries)	180
Figure 6-15: Optical microscopy of the outer surface of an NMV sample.	181
Figure 6-16: The stress-strain graphs of MH and MV samples.....	182
Figure 6-17: Tensile properties histogram of all the machined samples. (MH and MV)	182
Figure 6-18: Measured microhardness of the transverse sections of all samples.	184
Figure 6-19: The stress-strain graphs of non-heat treated, stress-relieved and annealed: a) MV and b) NMV samples.....	187
Figure 6-20: Tensile properties histogram of all vertical samples.....	187
Figure 6-21: SEM micrographs of fractured surfaces of MH samples, to show the formation shear lips and fracture topography a) to c) and the formation of dimples at higher magnification as a measure of ductility d) to f).....	189
Figure 6-22: Optical micrographs of etched fractured surfaces (longitudinally sectioned) of MH samples; a) to c) whole fracture surface with shear lips, d) to f) magnification of corresponding insets in a) to c).	190
Figure 6-23: SEM micrographs of all MV fractured surfaces; a) to c) fracture topography and partial views of shear lips, d) to f) lack of fusions and dimples formation in all samples. (Arrow shows a microcrack in the non-heat treated MV)	191

Figure 6-24: Optical micrographs of etched fracture surfaces (longitudinally sectioned) of MV samples; a) to c) shear lips seen under magnification 50, d) to f) magnification of corresponding insets in a) to c). 192

Figure 6-25: Two sites of a fractured surface of a non-heat treated MV sample. 193

List of tables

Table 2-1:Chemical analyses (wt.%) of Ti6Al4V (grade 5) powder and as-printed test samples [1].	25
Table 2-2: Optimised L-PBF process parameters for fabrication Ti6Al4V tensile samples.	31
Table 3-1: Chemical composition of Ti6Al4V (grade 5) powder (wt. %).	52
Table 3-2: Design of Experiments: Group A, B and C.	53
Table 3-3: Roughness average R_a of all cuboids of groups A, B and C.	61
Table 3-4: All samples in group A and B with micro-roughness $R_a < 10 \mu\text{m}$.	80
Table 4-1: Chemical composition of Ti64 powder (wt.%).	94
Table 4-2: LPBF processing parameters for fabrication of Ti64 samples.	95
Table 4-3: Porosity percentage of PM samples.	102
Table 4-4: Nano-hardness of α' , α and β in L-PBF and PM samples.	113
Table 5-1: Chemical composition (wt. %) of Ti64 (grade5) powder.	127
Table 5-2: SLM process parameters to fabricate Ti64 samples.	129
Table 5-3: Results of 2D image analysis of two different sections of an SLM sample to measure the porosity distribution.	133
Table 6-1: Chemical composition (wt. %) of Ti64 (grade5) powder.	162
Table 6-2: SLM process parameters to fabricate Ti64 samples.	163
Table 6-3: Heat treatments performed on the cylindrical samples prior to machining.	165
Table 6-4: FWHM of the peak of the HCP phase of the samples at 2θ diffraction nearly 40.6° , plane (101).	172
Table 6-5: Porosity content in vertical and horizontal samples.	177

Abbreviations and symbols

Abbreviations

AM	Additive Manufacturing
BCC	“Body Centred Cubic” (crystal structure)
DED	Directed Energy Deposition
DLP	Digital light Processing
DMLS	Direct Metal Laser Sintering
EBM	Electron Beam Melting
EDS	Energy Dispersive Spectroscopy
ELI	Extra Low Interstitial
FDM	Fused Deposition Modelling
FIB	Focused Ion Beam
HCP	“Hexagonal Close-Packed” (crystal structure)
HIP	Hot Isostatic Pressing
ICP-AES	Inductively Coupled Plasma Atomic Emission Spectroscopy
IPAS	Institute for Photonics and Advanced Sensing
LDED	Laser Directed Energy Deposition
LENS	Laser Engineered Net Shaping
LMD	Laser Metal Deposition
LPBF	Laser Powder Bed Fusion
OM	Optical Microscopy
PBF	Powder Bed Fusion
PSD	Particle Size Distribution
PM	Powder Metallurgy
RI	Refractive Index
SEM	Scanning Electron Microscopy
SLA	Stereolithography Apparatus
SLM	Selective Laser Melting
SLS	Selected Laser Sintering
TEM	Transmission Electron Microscopy
UTS	Ultimate Tensile Strength
VED	Volumetric Energy Density
WDS	Wavelength Dispersive Spectroscopy
XRD	X-Ray Diffraction
YS	Yield Strength

Symbols	Term	unit
α	HCP crystal structure as one of the titanium alloys allotropies	N/A
α'	Martensitic phase of titanium with HCP crystal structure	N/A
β	BCC crystal structure as one of the titanium alloys allotropies	N/A
$E_{(\text{volumetric})}$	Volumetric energy density	J/mm ³
P	Laser power	W
h	Scan line spacing, or hatch spacing	mm
λ	Laser beam wavelength	nm
t	Layer thickness	mm
v	Laser scan speed	mm/s
R_a	Roughness average	μm
R_z	The average maximum height of surface profile	μm

Definition of terms

Anisotropy

The directionality of any properties of a material, such as strength or ductility.

β transus temperature

The temperature where the β phase in titanium alloys transforms to α phase in a diffusional transformation.

Built direction or orientation

The direction of the layering in LPBF with regards to the Cartesian planes of the machine.

Hatch spacing

Space between two consecutive laser tracks.

Laser beam spot size

The beam diameter of laser on powder bed.

Layer thickness

The average thickness of each solidified layer in LPBF process.

Martensitic transformation

A diffusionless phase transformation in which the resulting crystal structure may be different or distorted from that resulted from diffusional transformation.

Scan speed

The linear speed of the laser vector or laser track.

Scanning strategy

Length and pattern of laser beam vector on one layer and the other consecutive layers.

Chapter 1

Introduction

1.1 Background and motivation

The emergence of additive manufacturing (AM) as a novel fabrication method toward the production of complex three-dimensional (3D) designs from computer generated (virtual) models has convinced the researcher and manufacturing companies to explore its capabilities. ASTM defines additive AM as “a process of joining materials to make objects from 3D model data, usually layer upon layer, as opposed to subtractive manufacturing methodologies.” [1]. This concept is extensively applied to all categories of materials, for instance metals [2, 3] , ceramics [4], and polymers [5].

Currently AM, known as 3D printing, includes several techniques in which a digital 3D design converts into a physical part. This technology can reduce the need for the spare part supply chain. The produced 3D structures and designed physical parts are widely being used in the manufacturing industries, in particular for the medical [6, 7] and aerospace [8] sectors which raise more demands for accurate fabricated models.

3D printing techniques have evolved over time, when in 1981, Hideo Kodama [9] presented a method to manufacture 3D designs by a photopolymer. Subsequently, in 1986 Charles Hull [10] designed the first 3D printer. He invented the stereolithography apparatus (SLA) to fabricate by combining the interaction of lasers and photopolymer resin. The growth in the development of AM technology has continued by introducing Fused Deposition Modelling (FDM), and Selective Laser Melting, SLM (also known as LPBF) followed by selective laser sintering (SLS) [11-16]. The evolution of these techniques founded the 3D printing technology which is being currently used.

At the first stages of 3D printing development, there was a limited type of materials as the feedstock. Over time, other materials have been explored by researchers to be 3D printed. In addition to polymers, ceramics and metals have been employed as a fundamental material in 3D printing. Titanium alloys, such as Ti6Al4V, are amongst popular metals which are receiving increasing attention by manufacturing industry and researchers for 3D printing due to their specific characteristics, particularly corrosion resistance and high ratio of strength to density, specific density.

The 3D printing of metals is performed by melting a single layer of metal over the previous solidified layer, which can eventually create a complex profile. This final structure of 3D printed metallic parts is usually resulted from frequent repeating phase transformation during solidification (liquid-solid) and at solid-state. The microstructure of the final 3D printed metal part will be affected significantly under the combined impacts of directional cooling, fast solidification, and phase transformations within the repeated thermal cycles [17-19]. This rapid solidification decreases elemental diffusion and enhances solid solubility and leads to the formation of metastable phases like martensite in Ti6Al4V alloy which has high strength but low ductility [20, 21]. Moreover,

the microstructural variation between deposited layers and directional grain growth are generally other features of this process [22].

The above-mentioned observations in the 3D printed metallic parts, especially in Ti6Al4V, have impelled researchers and companies to continue looking for solutions to resolve the drawbacks in mechanical properties correlated to the microstructure of Ti6Al4V.

1.2 Literature review

1.2.1 History of additive manufacturing

Additive manufacturing (AM) is a method to fabricate parts layer by layer. This technique is identified with various names, including additive fabrication, rapid prototyping, and 3D printing. 3D printing is the title that mostly used in the market. In this process, the input is a 3D computer-aided design (CAD) model, where the 3D printers divide the 3D model into several 2D designs and fabricate them layer by layer. Hideo Kodama as the inventor of the 3D printing technique in 1981, designed the functional machine to make prototypes [9]. The plotter, as it was called, was equipped with a movable plate within a receptacle containing a polymerization initiator, a polymer cross-linking agent, and a liquid mixture of unsaturated polyester. In this design, the plotters followed a curtailed programmed route guided by the emitting UV light. In this process, polymerization occurred for each layer on the top of the previous layer. His invention created a significant influence on developing additive manufacturing techniques. This progress was continued by Charles Hull's first patent [10] to lead the current 3D printer designs and devices. Charles Hull as the first person who applied for a U.S. patent for his stereolithography design and associated setup in the year 1984, which was issued in 1986. In next stages, the Stereolithography Apparatus 1 (SLA-1) became the first commercially available

additive manufacturing device in 1987, which was performing by using a UV laser to polymerize the light-sensitive liquid polymer material; the method was used for Kodama's design [9].

The ability to fabricate complex designs has manifested 3D-printing as a promising technique for manufacturing technologies. A broad range of outcomes can highlight the performance of AM techniques in various fields, such as a bone replacement [23], satellite propulsion system [24], micro-batteries [25], driven robots [26], quantum dot light-emitting diodes (LEDs) [27], and strain sensors [28].

1.2.2 Methods of additive manufacturing

3D-printers are generally capable of building complex designs via a motion-controlled stage, to assemble powders, inks, and/or filaments. Different types of printheads are being used, including filament extruder, laser melting emitter, inkjet printhead, and a controlled light source. Each technology works based on a different underlying build process. In this field, the ASTM standard on additive manufacturing [29] has classified a list of additive manufacturing, described in the following sections.

- **Material Extrusion:** Material extrusion uses a nozzle to selectively dispense materials, in which the target design is formed by depositing the feed material as a plastic 2D wire. In this process, a 2D layer is added on the top of the previous 2D layer, when the build platform (stage) is moving downward. The strength of the fabricated parts depends on the build direction; however, the fabricated parts in this method are generally not strong with rough surfaces. The main advantage of this technique is its availability as the most inexpensive printers are working based on this method [30, 31].
- **Material Jetting:** Material jetting works by depositing raw-material droplets (e.g., liquid polymers) on the build platform. UV light rays harden the layers. As an advantage,

two materials can be deposited at each run, such as photopolymer and wax. Also, it is feasible to combine a very stiff material with a very flexible compound to create a product with medium stiffness. The high precision of this method is another advantage. However, the durability of products is very low in the case of using photopolymers [30, 31].

- **Binder Jetting:** Binder jetting works based on spraying a liquid binder over a layer of powder, which can be glass, sand, plastic, or metal (Figure 1-1). In fact, the powder layers are bound together wherever the binder droplet is sprayed. As an advantage, in this inexpensive method, an extended range of materials can be used in full colour. The drawback of this method can be the lack of stiffness and the need for post-processing [30, 31].

- **Sheet lamination:** In sheet lamination, parts are fabricated by bonding the sheet layers over each other (Figure 1-1). These sheets are made of various materials, such as adhesive-coated papers, metals, or plastics. A laser is used to cut the sheet in the desired form. This process cannot fabricate complex shapes and the quality of these built parts is relatively low [30, 31].

- **Vat photopolymerization:** A filled vat with liquid resin is used in the vat photopolymerization technique. A light source is employed to initiate the curing process of liquid photopolymer resin, in which the liquid solidifies where the light source presents. By moving down the stage, the parts are made layer by layer. A smooth surface finish is the advantage of this technique, whilst post-processing is required. However, the parts don't have enough stiffness. Stereolithography apparatus (SLA) and digital light processing (DLP) technologies work based on this process [30, 31].

- **Powder bed fusion (PBF):** In the powder bed fusion technique, the build platform is totally filled with powder (Figure 1-1). An energy source is required to fuse and bond the powder particles together. These particles fuse or bond together where the energy source

is present. Therefore, the desired form is achieved by programming the energy source. Both polymers and metals can be used in this method, whilst the fabricated parts can be fully dense with high quality and stiffness. High cost, need for specialised personnel, and post-processing are the main disadvantages of this technique. Selective Laser Sintering (SLS), Selective Laser Melting (SLM), Direct Metal Laser Sintering (DMLS), and Electron Beam Melting (EBM) employ this method [30, 31].

- **Directed energy deposition (DED):** Directed energy deposition uses focused thermal energy to fuse materials by melting when they are being deposited (Figure 1-1). This method is different from the powder bed fusion process, because, in the directed energy deposition method, the powder or wired metal is delivered from a nozzle on the platform and directly heated to melt and create a solid object. This method is used to repair the parts and fabricate large designs. However, this method has low accuracy and needs post-processing, but it can use two different raw materials in a fast process [30, 31]. DED technique is also known as some trade names like LENS (laser engineered net shape) and LMD (laser metal deposition).

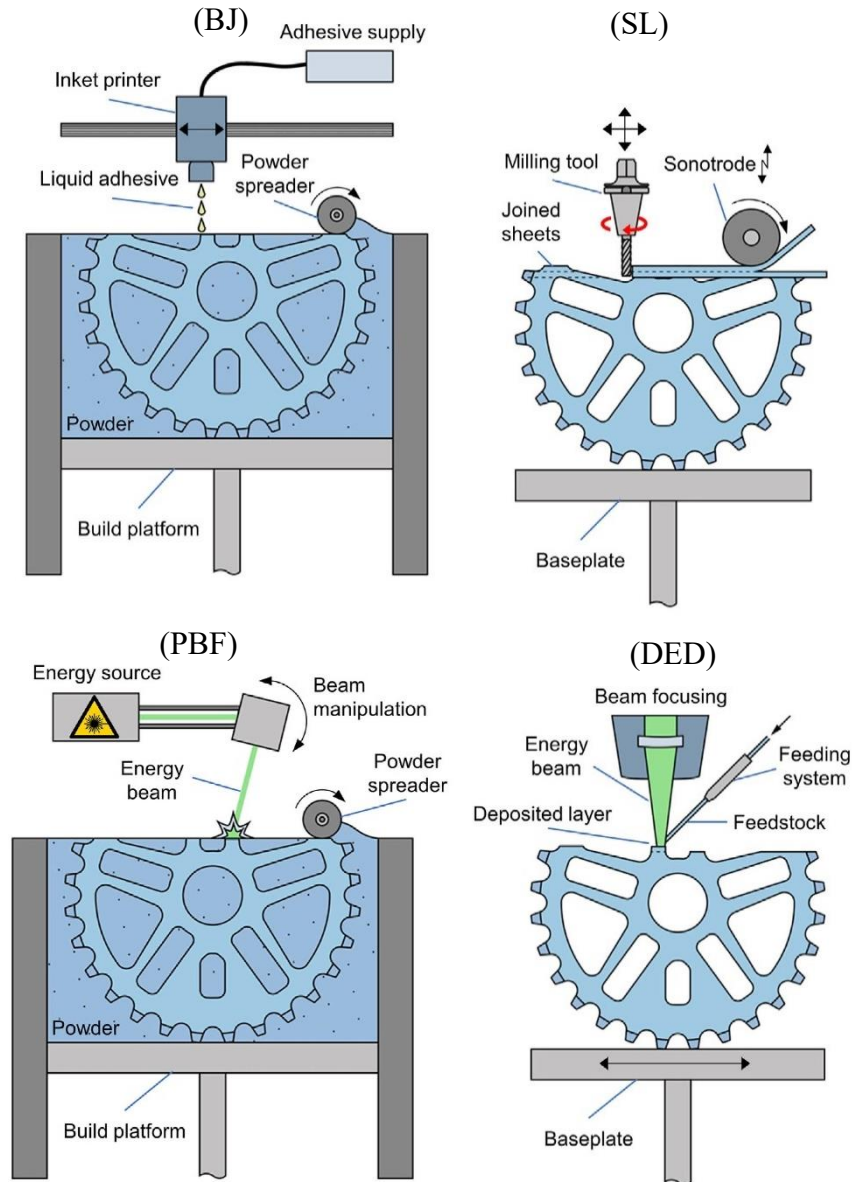


Figure 1-1: Schematic representation of the working principle of several additive manufacturing categories with main terminology, BJ: Binder jetting (BJ); SL: Sheet lamination (SL), PBF: Powder bed fusion, DED: Direct energy deposition. [32].
 Reproduced under license CC-BY-NC-ND.

One of the main growing fields in AM technology is 3D printing of metallic parts. Figure 1-2 exhibits different methods of AM for metal-based parts using different heat sources for binding (either sintering or melting) and the method of accumulation.

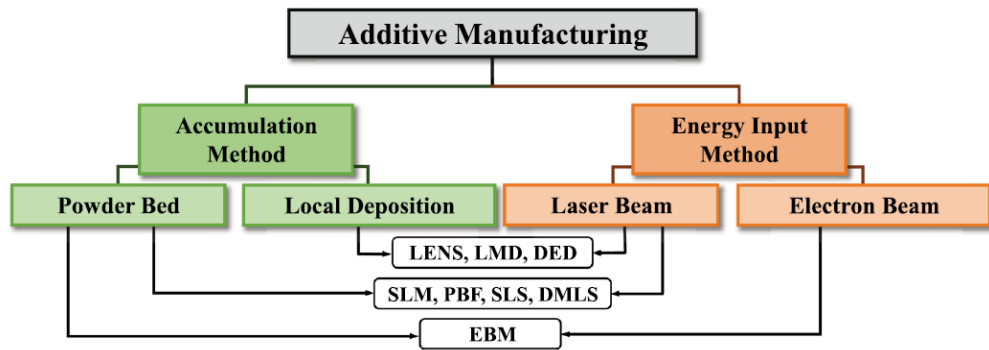


Figure 1-2: Different types of metal-based AM-processes according to methods of accumulation and heat source, reproduced from [33]. Reproduced with permission from Springer Nature [license No. 5303631386287]

Two main laser-based AM processes for production of metallic components are: laser-directed energy deposition, i.e., LDED and laser powder bed fusion, LPBF (which is also known as SLM) , as illustrated in Figure 1-3. The laser-based AM or 3D printing, plays a strategic role for manufacturing industries to meet the increasing demands for innovative designs [34-36].

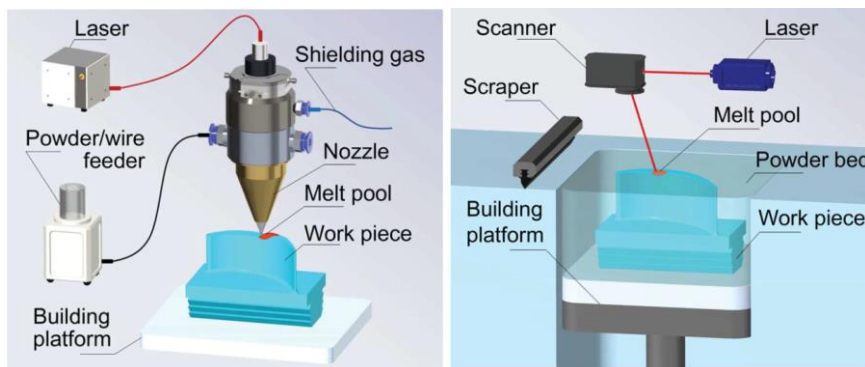


Figure 1-3: Schematics of a) Laser directed energy deposition (LDED) and b) Laser powder bed fusion (LPBF) [37].

1.2.3 Specific advantages of additive manufacturing

Additive manufacturing has various advantages over traditional manufacturing techniques mainly based on the following features.

- Low energy consumption is one of the main beneficial characteristics of AM. This technology needs less energy resources and fewer personnel to create designs and parts. AM lowers the manufacturing cost for any part besides saving time.
- Fabricating very complex shapes, such as lattice structures is not feasible through milling and casting processes. Fabricating components with no need to assemble is another capability of AM.
- One advantage of AM namely as a positive environmental achievement is its capability in reusing the waste materials, such as plastics. For example, the binder jet/powder bed can recycle and reuse excess powder. This feature also highlights the importance of metal 3D printing in the heavy industries (e.g., automotive, and aerospace) where energy and materials saving is essential [38].

1.2.4 Materials for additive manufacturing

Several materials can be used as feedstock in additive manufacturing. The most common materials are mostly either plastic or metal-based compounds. There is a broad range of metals that have been used for AM. Each metal provides specific properties within its applications. Here is a list of metals that are frequently used through 3D printing techniques:

- **Aluminium alloys:** AlSi12 and AlSi10 are two examples of this group used to build engineering components for aerospace and automotive industries. The main properties of these alloys are the high ratio of strength to weight and the thermal characteristics that make them suitable for the realization of parts like heat exchangers [32].
- **Stainless Steel alloys:** These alloys are used to fabricate mechanical parts for an aggressive environment. 316L and 17-4PH grades belong to this group which provide suitable chemical and mechanical properties [32].

- **Chromium based alloys:** CoCrF75 is categorized in this group, which shows very high strength and hardness, specifically with wear resistance and mechanical performances at high temperatures. Another example of this group would be CoCr which is used for the samples that need a high corrosion resistance.
- **Nickel based alloys:** These alloys are mainly used to fabricate parts applicable in aerospace and chemical industries. Depending on the alloys, these materials provide high strength, high corrosion resistance (e.g., Ni625), and fatigue resistance (e.g., Ni718) with excellent cryogenic properties [32].
- **Titanium alloys:** Ti6Al4V (TiGr5) is an example of this group. These materials are used in biomedical applications like surgical implants and orthodontic appliances, which require a good fatigue strength and biocompatibility [39]. This alloy has also an excellent combination of strength and toughness along with excellent corrosion resistance [40]. Having a low density of 4.5 g/cm^3 and ultimate tensile strength (UTS) of around 1400 MPa at room temperature, titanium alloys exhibit a high strength-to-weight ratio [41]. Low contents of interstitial solutes like oxygen, nitrogen in Ti6Al4V as extra low interstitial (ELI) alloy, as known TiGr23, increase the ductility of the part but are accompanied with a slight reduction of the strength [40, 42, 43].

Titanium has two distinct allotropies. Each crystal structure of the titanium is only stable within a particular temperature range. At low temperatures, pure titanium has a hexagonal close-packed (HCP) crystal structure, known as α -phase. At higher temperatures, the body-centred cubic (BCC) crystal structure, β phase, is stable. Pure titanium exhibits an allotropic phase transformation α to β or vice versa at $921 \pm 28 \text{ }^\circ\text{C}$ [44]. The exact transformation temperature is affected by the alloying elements. The alloying elements of titanium can be classified into three categories based on their effects on the α to β transformation temperature (β -transus temperature) [45], i.e. neutral, α -stabilizers, and β -

stabilizers. Figure 1-4 displays the dominant crystal structure of Ti alloys as for instance the Ti-6Al-4V alloy is an α - β Ti alloy.

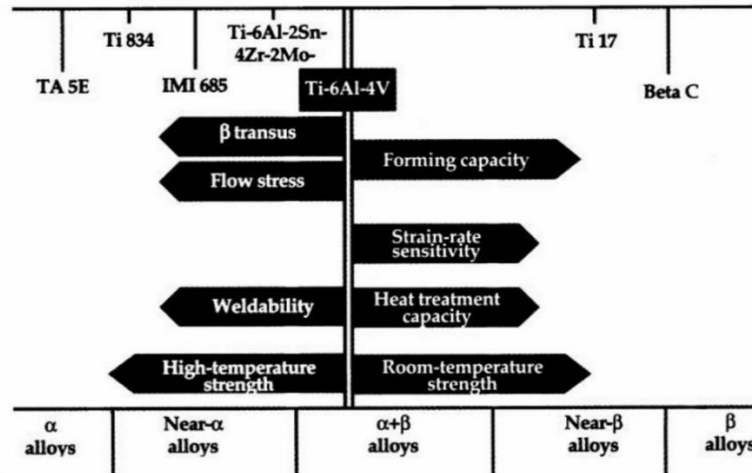


Figure 1-4: Main characteristics of different titanium alloy family groups [40].

For specific characteristics of Ti-6Al-4V (Ti64) alloy, as mentioned above, researchers and industrial companies are interested in fabricating Ti64 parts via 3D printing technique. Investigation on the effect of LPBF process parameters on the microstructure and mechanical properties of Ti64 alloy along with the selection of suitable post processes [20, 46-48] are the main theme of a large body of research activities still continuing [18, 49-53]

1.2.5 LPFB 3D printing of titanium alloys

Due to the chemical reactivity of titanium with other materials at high temperatures, the refining process is costly and consequently, titanium alloys are quite expensive [41]. Moreover, titanium parts are difficult to machine using traditional technologies [54]; and these led titanium alloys to be an ideal target for LPBF.

There are considerable studies on titanium alloys such as commercially pure (CP) titanium and Ti6Al4V produced by LPBF [55-60] . LPBF fabricated titanium parts exhibited higher hardness, ultimate tensile strength (UTS) and, yield strength (YS) with respect to wrought counterparts [45, 61]. However, they still have some shortcomings such as low ductility and anisotropy in mechanical properties that are associated with the process-induced unique microstructure and architecture [58, 62, 63]. Studies performed by Attar et al. [64] and Thijs et al. [56] on LPBF-fabricated Ti-6Al-4V parts indicated the presence of martensitic or diffusionless transformed phase of α' in the microstructure. They have also reported the appearance of columnar grains due to the occurrence of epitaxial growth. The direction of these columnar grains is related to the process parameters [56]. In addition, the process of layer by layer deposition may result in some in-situ microstructural changes as for example reported by Xu et al [65] that an in-situ decomposition of α' to a novel ultrafine lamellar microstructure may occur by selecting a series of LPBF process parameters.

The process parameters which affects the quality of final product are mainly including (but not limited to) laser power and scan speed [66-68], hatch spacing [69], layer thickness [70, 71], scanning strategy [72, 73], building direction and orientation [51, 62, 74-76]. In most of the above research works, quality assessment target for final product was based on the level of porosity in the part, surface roughness and mechanical properties.

Powder particles size and its distribution and morphology, flowability and powder interaction with laser are the other parameters related to powder particles [77]. The research conducted by Attar et al. [78] confirms the effect of particle size on the properties of composite materials fabricated by LPBF.

It has been reported that the energy density, E (J/mm^3) as the average laser energy applied to the system, can be considered as a measure for prediction of the quality and density of LPBF-fabricated parts [21, 56, 67, 79-81]. Equation (1) defined by [82] as a well-known formula for calculating volumetric energy density (VED in J/mm^3), combines four main process parameters of laser power.

$$E_{(volumetric)} = \frac{P}{v \cdot h \cdot t} \quad (1)$$

Where P is the laser power (W), v is the scanning speed (mm/s), h is the hatch spacing (mm) and t is the layer thickness (mm). Thijs et al. [56] reported that the energy density of VED $93 \text{ J}/\text{mm}^3$ is the optimum energy input to reach the highest achievable density, 99.6%, while Attar et al [79] could fabricate their 99.5% dense CP-Ti parts with an energy density of VED $120 \text{ J}/\text{mm}^3$. In some studies like [81, 83] stated that using only VED as a design parameter is not enough however Koutiri [16] found VED as a reliable measure for optimisation of densification but not for surface roughness. So, applicability of energy density in equation (1) and the limitations of each process parameters (1) is not transparent yet.

The anisotropy of strength and ductility in LPBF fabricated titanium parts is another concern which is brought to the attention of researchers [84-87]. Vilaro et al [20] reported that the anisotropy they observed, is attributed to the manufacturing defects and their orientation however it can be diminished by optimisation of process parameters and some post processes like heat treatment [20, 87].

There is still ongoing research on heat treatment of Ti-6Al-4V produced by LPBF [20, 88, 89]. Vrancken et al. [61] stated that heat treatment of LPBF-manufactured Ti-6Al-4V is fairly different compared to conventionally processed Ti-6Al-4V. They have recommended three different heat treatment procedures by which all static mechanical

properties of LPBF-fabricated Ti-6Al-4V will be well above ASTM Standards for forged and cast Ti-6Al-4V.

Apart from heat treatment, some post process of surface treatments like ultrasound surface rolling [90], localised re-melting of surface [91], polishing or chemical etching [89] can sufficiently improve some LPBF-fabricated parts performances like wear or fatigue. Therefore, in most cases, there is a need for post-fabrication treatments to improve mechanical properties or to reduce their anisotropy which adds another process to the manufacturing chain. However, choosing the most viable method for each part according to the complicity of the shape or its application requires further study.

1.3 Research gaps

As mentioned earlier, study of 3D printing is on-going despite of a large body of work already available in open literature. Although the alloy is well-known, there are still some oblivious issues needing further clarification. An empirical optimisation of process parameters and a criterion for inspection of the soundness of LPBF parts, for researcher or production engineers in this field, are difficult to be found in the open literature. A systematic study on build orientation effects on mechanical properties especially in a truly as-built condition is a starting point for further investigation which has been ignored by researchers. This is due to the fact that fabrication of horizontal sample in truly as-built condition is nearly not viable without any post processes. Investigation of some post processes treatments on as-built samples and choosing the most effective post process is the next gap which requires further study.

A comprehensive literature review which introduces the conceptual contents of the journal articles, are presented in different chapters of this thesis.

1.4 Aims and objectives

This project aims to provide further information on the available gaps through experimentation, testing and analysing on small scale LPBF-fabricated Ti-6Al-4V parts.

The aims and objectives of this project are:

- 1) Identifying the most appropriate process parameters by establishing a practical method to produce LPBF-fabricated Ti-6Al-4V parts with the lowest level of porosity.
- 2) Better understanding the effect of LPBF process parameters on the surface morphology and its correlation with bulk porosity to introduce a method for assessing the quality of parts without destructive testing, damaging the parts, or employing costly process like CT tomography.
- 3) Study the effect of built direction on mechanical properties in truly as-built condition and analysing the source of anisotropy.
- 4) Discover the effect of post surface treatment on anisotropy of LPBF fabricated parts in as-built condition.
- 5) Investigating the effect of post process of heat treatment on as-built LPBF fabricated Ti64 parts.
- 6) Comparing different post processes and identifying the most effective and viable post process on mechanical properties.

1.5 Structure of thesis

The thesis is formatted as a collection of manuscripts that have been published in or submitted to high-quality and peer-reviewed journals. This thesis is classified in several chapters to cover various research concepts as follows:

In Chapter 2, details of method of investigation and experimental procedures of the project are presented.

In Chapter 3, the effects of main process parameters of LPBF on the roughness and surface topography of as-printed Ti6Al4V samples are studied. The topography of top surface of LPBF fabricated parts are categorised into two groups of surfaces with meso-roughness and micro-roughness. Then it is discussed how micro-roughness could be used as a criterion for optimisation of process parameters to obtain as-printed Ti6Al4V parts with porosity lower than 0.15%.

Chapter 4 presents the microstructural development of the Ti64 alloy fabricated via two routes of powder metallurgy and LPBF. The starting raw materials for both manufacturing routes are powder particles and both routes have common advantages like environmentally friendly in terms of the lowest waste of material compared to conventional subtractive manufacturing techniques.

In Chapter 5, the effect of two built orientations of vertical and horizontal on mechanical properties is studied. This chapter, which is covered by a published paper, a novel design for fabrication of horizontal tensile samples without any distortion is introduced. Then the effect of built direction in truly as-built condition (as-built surface without any heat treatment) is discussed. Then by surface machining post process the effect of built orientation is compared with those samples in the truly as-built condition.

Chapter 6 of this thesis focuses on the effect of built orientation after the LPBF fabricated parts are heat treated. It is revealed how either stress relieving or annealing thermal treatment can be critical for non-machined surface vertical sample in preventing premature failure. After comparing the most effective post processes in improving the

mechanical properties, annealing/stress relieving vs surface machining, suggestions were made for cases where surface machining of parts may not be viable.

In the final chapter, Chapter 7, the key findings of the project and future works based on the outcomes of the current project, are summarised.

1.6 Thesis format

This thesis is based on the collection of the manuscripts produced during the research and has been submitted according to the format approved by the University of Adelaide. The thesis is provided and available in both hard and soft copy which are identical. The soft copy is available online at the University of Adelaide Library and can be viewed by Adobe Reader. The list of publications included in this thesis has already been appeared after table of contents to comply with “Specifications for thesis” approved in 2022 by Adelaide Graduate Centre (AGC).

References

1. *ASTM F2792-12, Standard Terminology for Additive Manufacturing Technologies*. 2012.
2. Haghdad, N., M. Laleh, M. Moyle, and S. Primig, *Additive manufacturing of steels: a review of achievements and challenges*. *Journal of Materials Science*, 2021. **56**(1): p. 64-107.
3. Wei, H., T. Mukherjee, W. Zhang, J. Zuback, G. Knapp, A. De, and T. DebRoy, *Mechanistic models for additive manufacturing of metallic components*. *Progress in Materials Science*, 2021. **116**: p. 100703.
4. Lakhdar, Y., C. Tuck, J. Binner, A. Terry, and R. Goodridge, *Additive manufacturing of advanced ceramic materials*. *Progress in Materials Science*, 2021. **116**: p. 100736.
5. Ghanem, M.A., A. Basu, R. Behrou, N. Boechler, A.J. Boydston, S.L. Craig, Y. Lin, B.E. Lynde, A. Nelson, and H. Shen, *The role of polymer mechanochemistry in responsive materials and additive manufacturing*. *Nature Reviews Materials*, 2021. **6**(1): p. 84-98.
6. Salmi, M., *Additive manufacturing processes in medical applications*. *Materials*, 2021. **14**(1): p. 191.

7. Ghomi, E.R., F. Khosravi, R.E. Neisiany, S. Singh, and S. Ramakrishna, *Future of additive manufacturing in healthcare*. Current Opinion in Biomedical Engineering, 2021. **17**: p. 100255.
8. Blakey-Milner, B., P. Gradl, G. Snedden, M. Brooks, J. Pitot, E. Lopez, M. Leary, F. Berto, and A. du Plessis, *Metal additive manufacturing in aerospace: A review*. Materials & Design, 2021. **209**: p. 110008.
9. Kodama, H., *Automatic method for fabricating a three-dimensional plastic model with photo-hardening polymer*. Review of scientific instruments, 1981. **52**(11): p. 1770-1773.
10. Hull, C.W., *Apparatus for production of three-dimensional objects by stereolithography*. 1986, Google Patents.
11. Mazzoli, A., *Selective laser sintering in biomedical engineering*. Medical & biological engineering & computing, 2013. **51**(3): p. 245-256.
12. Kruth, J.-P., X. Wang, T. Laoui, and L. Froyen, *Lasers and materials in selective laser sintering*. Assembly Automation, 2003.
13. Mwema, F.M. and E.T. Akinlabi, *Basics of fused deposition modelling (FDM)*, in *fused deposition modeling*. 2020, Springer. p. 1-15.
14. Mohan, N., P. Senthil, S. Vinodh, and N. Jayanth, *A review on composite materials and process parameters optimisation for the fused deposition modelling process*. Virtual and Physical Prototyping, 2017. **12**(1): p. 47-59.
15. Enneti, R.K., R. Morgan, and S.V. Atre, *Effect of process parameters on the Selective Laser Melting (SLM) of tungsten*. International Journal of Refractory Metals and Hard Materials, 2018. **71**: p. 315-319.
16. Koutiri, I., E. Pessard, P. Peyre, O. Amlou, and T. De Terris, *Influence of SLM process parameters on the surface finish, porosity rate and fatigue behavior of as-built Inconel 625 parts*. Journal of Materials Processing Technology, 2018. **255**: p. 536-546.
17. Xue, A., X. Lin, L. Wang, X. Lu, H. Ding, and W. Huang, *Heat-affected coarsening of β grain in titanium alloy during laser directed energy deposition*. Scripta Materialia, 2021. **205**: p. 114180.
18. Sun, J., C. Zhang, X. Wang, and F. Wang, *The Microstructure Transformation and Mechanical Properties in Selective Laser Melting Processed Ti-6Al-4V at Different Heights*. Journal of Materials Engineering and Performance, 2021.
19. Panwisawas, C., Y.T. Tang, and R.C. Reed, *Metal 3D printing as a disruptive technology for superalloys*. Nature communications, 2020. **11**(1): p. 2327-2327.
20. Vilaro, T., C. Colin, and J.D. Bartout, *As-Fabricated and Heat-Treated Microstructures of the Ti-6Al-4V Alloy Processed by Selective Laser Melting*. Metallurgical and Materials Transactions A, 2011. **42**(10): p. 3190-3199.
21. Zhao, R., C. Chen, W. Wang, T. Cao, S. Shuai, S. Xu, T. Hu, H. Liao, J. Wang, and Z. Ren, *On the role of volumetric energy density in the microstructure and mechanical properties of laser powder bed fusion Ti-6Al-4V alloy*. Additive Manufacturing, 2022: p. 102605.
22. Frazier, W.E., *Metal additive manufacturing: a review*. Journal of Materials Engineering and performance, 2014. **23**(6): p. 1917-1928.

23. Jakus, A.E., A.L. Rutz, S.W. Jordan, A. Kannan, S.M. Mitchell, C. Yun, K.D. Koube, S.C. Yoo, H.E. Whiteley, and C.-P. Richter, *Hyperelastic “bone”: A highly versatile, growth factor-free, osteoregenerative, scalable, and surgically friendly biomaterial*. *Science translational medicine*, 2016. **8**(358): p. 358ra127-358ra127.
24. Marshall, W.M., J.D. Stegeman, M. Zemba, E. MacDonald, C. Shemelya, R. Wicker, A. Kwas, and C. Kief. *Using additive manufacturing to print a cubesat propulsion system*. in *51st AIAA/SAE/ASEE Joint Propulsion Conference*. 2015.
25. Sun, K., T.S. Wei, B.Y. Ahn, J.Y. Seo, S.J. Dillon, and J.A. Lewis, *3D printing of interdigitated Li-Ion microbattery architectures*. *Advanced materials*, 2013. **25**(33): p. 4539-4543.
26. MacCurdy, R., R. Katzschmann, Y. Kim, and D. Rus. *Printable hydraulics: A method for fabricating robots by 3D co-printing solids and liquids*. in *2016 IEEE International Conference on Robotics and Automation (ICRA)*. 2016. IEEE.
27. Kong, Y.L., I.A. Tamargo, H. Kim, B.N. Johnson, M.K. Gupta, T.-W. Koh, H.-A. Chin, D.A. Steingart, B.P. Rand, and M.C. McAlpine, *3D printed quantum dot light-emitting diodes*. *Nano letters*, 2014. **14**(12): p. 7017-7023.
28. Muth, J.T., D.M. Vogt, R.L. Truby, Y. Mengüç, D.B. Kolesky, R.J. Wood, and J.A. Lewis, *Embedded 3D printing of strain sensors within highly stretchable elastomers*. *Advanced materials*, 2014. **26**(36): p. 6307-6312.
29. ASTM, *ISO/ASTM 52921: Standard terminology for additive manufacturing — Coordinate systems and test methodologies*. 2013.
30. Kruth, J.-P., M.-C. Leu, and T. Nakagawa, *Progress in additive manufacturing and rapid prototyping*. *Cirp Annals*, 1998. **47**(2): p. 525-540.
31. Altıparmak, S.C., V.A. Yardley, Z. Shi, and J. Lin, *Challenges in additive manufacturing of high-strength aluminium alloys and current developments in hybrid additive manufacturing*. *International Journal of Lightweight Materials and Manufacture*, 2021. **4**(2): p. 246-261.
32. Pragana, J., R. Sampaio, I. Bragança, C. Silva, and P. Martins, *Hybrid metal additive manufacturing: A state-of-the-art review*. *Advances in Industrial and Manufacturing Engineering*, 2021. **2**: p. 100032.
33. Smith, J., W. Xiong, W. Yan, S. Lin, P. Cheng, O.L. Kafka, G.J. Wagner, J. Cao, and W.K. Liu, *Linking process, structure, property, and performance for metal-based additive manufacturing: computational approaches with experimental support*. *Computational Mechanics*, 2016. **57**(4): p. 583-610.
34. DebRoy, T., T. Mukherjee, H. Wei, J. Elmer, and J. Milewski, *Metallurgy, mechanistic models and machine learning in metal printing*. *Nature Reviews Materials*, 2021. **6**(1): p. 48-68.
35. DebRoy, T., T. Mukherjee, J. Milewski, J. Elmer, B. Ribic, J. Blecher, and W. Zhang, *Scientific, technological and economic issues in metal printing and their solutions*. *Nature materials*, 2019. **18**(10): p. 1026-1032.
36. Bourell, D.L., D.W. Rosen, and M.C. Leu, *The roadmap for additive manufacturing and its impact*. *3D Printing and Additive Manufacturing*, 2014. **1**(1): p. 6-9.

37. Gu, D., X. Shi, R. Poprawe, D.L. Bourell, R. Setchi, and J. Zhu, *Material-structure-performance integrated laser-metal additive manufacturing*. Science, 2021. **372**(6545): p. eabg1487.
38. Javaid, M., A. Haleem, R.P. Singh, R. Suman, and S. Rab, *Role of additive manufacturing applications towards environmental sustainability*. Advanced Industrial and Engineering Polymer Research, 2021. **4**(4): p. 312-322.
39. Soboyejo, W.O. and T. Srivatsan, *Advanced structural materials: properties, design optimization, and applications*. 2006: CRC press.
40. Donachie, M.J., *Titanium: a technical guide*. 2000: ASM international.
41. Callister, W.D. and D.G. Rethwisch, *Materials science and engineering: an introduction*. Vol. 7. 2007: Wiley New York.
42. *Titanium Alloys*, in *Handbook of Advanced Materials*. 2004. p. 271-319.
43. Joshi, V.A., *Titanium alloys: an atlas of structures and fracture features*. 2006: Crc Press.
44. *SAE AMS 2801B, Heat Treatment of Titanium Alloy Parts (R2014)*. 2014.
45. Peters, M., J. Hemptenmacher, J. Kumpfert, and C. Leyens, *Structure and Properties of Titanium and Titanium Alloys*, in *Titanium and Titanium Alloys*. 2005, Wiley-VCH Verlag GmbH & Co. KGaA. p. 1-36.
46. Murr, L.E., S.A. Quinones, S.M. Gaytan, M.I. Lopez, A. Rodela, E.Y. Martinez, D.H. Hernandez, E. Martinez, F. Medina, and R.B. Wicker, *Microstructure and mechanical behavior of Ti-6Al-4V produced by rapid-layer manufacturing, for biomedical applications*. J Mech Behav Biomed Mater, 2009. **2**(1): p. 20-32.
47. Gong, H., K. Rafi, H. Gu, T. Starr, and B. Stucker, *Analysis of defect generation in Ti-6Al-4V parts made using powder bed fusion additive manufacturing processes*. Additive Manufacturing, 2014. **1-4**: p. 87-98.
48. Dhansay, N.M., R. Tait, and T. Becker. *Fatigue and fracture toughness of Ti-6Al-4V titanium alloy manufactured by selective laser melting*. in *AMI Light Metals Conference 2014, October 15, 2014 - October 17, 2014*. 2014. North West Province, South africa: Trans Tech Publications Ltd.
49. Nicoletto, G., R. Konečná, L. Kunz, and M. Frkání, *Influence of as-built surface on fatigue strength and notch sensitivity of Ti6Al4V alloy produced by DMLS*. MATEC Web Conf., 2018. **165**: p. 02002.
50. Yang, X., Y. Li, M.-g. Duan, W. Jiang, D. Chen, and B. Li, *An investigation of ductile fracture behavior of Ti6Al4V alloy fabricated by selective laser melting*. Journal of Alloys and Compounds, 2022. **890**: p. 161926.
51. Palmeri, D., G. Buffa, G. Pollara, and L. Fratini, *Sample building orientation effect on porosity and mechanical properties in Selective Laser Melting of Ti6Al4V titanium alloy*. Materials Science and Engineering: A, 2022. **830**: p. 142306.
52. Živčák, J., E. Nováková-Marcinčinová, L. Nováková-Marcinčinová, T. Balint, and M. Puškár, *Increasing Mechanical Properties of 3D Printed Samples by Direct Metal Laser Sintering Using Heat Treatment Process*. Journal of Marine Science and Engineering, 2021. **9**(8): p. 821.

53. Liu, J., J. Liu, Y. Li, R. Zhang, Z. Zeng, Y. Zhu, K. Zhang, and A. Huang, *Effects of Post Heat Treatments on Microstructures and Mechanical Properties of Selective Laser Melted Ti6Al4V Alloy*. Metals, 2021. **11**(10): p. 1593.
54. Peters, M. and C. Leyens, *Fabrication of Titanium Alloys*, in *Titanium and Titanium Alloys*. 2005, Wiley-VCH Verlag GmbH & Co. KGaA. p. 245-261.
55. Sallica-Leva, E., A.L. Jardini, and J.B. Fogagnolo, *Microstructure and mechanical behavior of porous Ti-6Al-4V parts obtained by selective laser melting*. J Mech Behav Biomed Mater, 2013. **26**: p. 98-108.
56. Thijs, L., F. Verhaeghe, T. Craeghs, J.V. Humbeeck, and J.-P. Kruth, *A study of the microstructural evolution during selective laser melting of Ti-6Al-4V*. Acta Materialia, 2010. **58**(9): p. 3303-3312.
57. Liu, Y.J., S.J. Li, H.L. Wang, W.T. Hou, Y.L. Hao, R. Yang, T.B. Sercombe, and L.C. Zhang, *Microstructure, defects and mechanical behavior of beta-type titanium porous structures manufactured by electron beam melting and selective laser melting*. Acta Materialia, 2016. **113**: p. 56-67.
58. Rafi, H.K., N.V. Karthik, H. Gong, T.L. Starr, and B.E. Stucker, *Microstructures and Mechanical Properties of Ti6Al4V Parts Fabricated by Selective Laser Melting and Electron Beam Melting*. Journal of Materials Engineering and Performance, 2013. **22**(12): p. 3872-3883.
59. Mahamood, R.M., E.T. Akinlabi, M. Shukla, and S. Pityana, *Scanning velocity influence on microstructure, microhardness and wear resistance performance of laser deposited Ti6Al4V/TiC composite*. Materials and Design, 2013. **50**: p. 656-666.
60. Alcisto, J., A. Enriquez, H. Garcia, S. Hinkson, T. Steelman, E. Silverman, P. Valdovino, H. Gigerenzer, J. Foyos, and J. Ogren, *Tensile properties and microstructures of laser-formed Ti-6Al-4V*. Journal of materials engineering and performance, 2011. **20**(2): p. 203-212.
61. Vrancken, B., L. Thijs, J.-P. Kruth, and J. Van Humbeeck, *Heat treatment of Ti6Al4V produced by Selective Laser Melting: Microstructure and mechanical properties*. Journal of Alloys and Compounds, 2012. **541**: p. 177-185.
62. Simonelli, M., Y.Y. Tse, and C. Tuck, *Effect of the build orientation on the mechanical properties and fracture modes of SLM Ti-6Al-4V*. Materials Science and Engineering: A, 2014. **616**: p. 1-11.
63. Murr, L., S. Quinones, S. Gaytan, M. Lopez, A. Rodela, E. Martinez, D. Hernandez, E. Martinez, F. Medina, and R. Wicker, *Microstructure and mechanical behavior of Ti-6Al-4V produced by rapid-layer manufacturing, for biomedical applications*. Journal of the mechanical behavior of biomedical materials, 2009. **2**(1): p. 20-32.
64. Zhang, L.-C. and H. Attar, *Selective Laser Melting of Titanium Alloys and Titanium Matrix Composites for Biomedical Applications: A Review* Advanced Engineering Materials, 2016. **18**(4): p. 463-475.
65. Xu, W., S. Sun, J. Elambasseril, Q. Liu, M. Brandt, and M. Qian, *Ti-6Al-4V Additively Manufactured by Selective Laser Melting with Superior Mechanical Properties*. Jom, 2015. **67**(3): p. 668-673.

66. Shipley, H., D. McDonnell, M. Culleton, R. Lupoi, G. O'Donnell, and D. Trimble, *Optimisation of process parameters to address fundamental challenges during selective laser melting of Ti-6Al-4V: A review*. International Journal of Machine Tools and Manufacture, 2018. **128**: p. 1-20.
67. Han, J., J. Yang, H. Yu, J. Yin, M. Gao, Z. Wang, and X. Zeng, *Microstructure and mechanical property of selective laser melted Ti6Al4V dependence on laser energy density*. Rapid Prototyping Journal, 2017.
68. Keshavarzkermani, A., E. Marzbanrad, R. Esmaeilzadeh, Y. Mahmoodkhani, U. Ali, P.D. Enrique, N.Y. Zhou, A. Bonakdar, and E. Toyserkani, *An investigation into the effect of process parameters on melt pool geometry, cell spacing, and grain refinement during laser powder bed fusion*. Optics & Laser Technology, 2019. **116**: p. 83-91.
69. Yakout, M., M.A. Elbestawi, and S.C. Veldhuis, *A study of the relationship between thermal expansion and residual stresses in selective laser melting of Ti-6Al-4V*. Journal of Manufacturing Processes, 2020. **52**: p. 181-192.
70. Qiu, C., C. Panwisawas, M. Ward, H.C. Basoalto, J.W. Brooks, and M.M. Attallah, *On the role of melt flow into the surface structure and porosity development during selective laser melting*. Acta Materialia, 2015. **96**: p. 72-79.
71. Ma, M., Z. Wang, M. Gao, and X. Zeng, *Layer thickness dependence of performance in high-power selective laser melting of 1Cr18Ni9Ti stainless steel*. Journal of Materials Processing Technology, 2015. **215**: p. 142-150.
72. Liu, J., G. Li, Q. Sun, H. Li, J. Sun, and X. Wang, *Understanding the effect of scanning strategies on the microstructure and crystallographic texture of Ti-6Al-4V alloy manufactured by laser powder bed fusion*. Journal of Materials Processing Technology, 2022. **299**: p. 117366.
73. Ali, H., H. Ghadbeigi, and K. Mumtaz, *Effect of scanning strategies on residual stress and mechanical properties of Selective Laser Melted Ti6Al4V*. Materials Science and Engineering: A, 2018. **712**: p. 175-187.
74. Hartunian, P. and M. Eshraghi, *Effect of Build Orientation on the Microstructure and Mechanical Properties of Selective Laser-Melted Ti-6Al-4V Alloy*. Journal of Manufacturing and Materials Processing, 2018. **2**(4): p. 69.
75. Agius, D., K.I. Kourousis, C. Wallbrink, and T. Song, *Cyclic plasticity and microstructure of as-built SLM Ti-6Al-4V: The effect of build orientation*. Materials Science and Engineering: A, 2017. **701**: p. 85-100.
76. Palmeri, D., G. Buffa, G. Pollara, and L. Fratini, *The Effect of Building Direction on Microstructure and Microhardness during Selective Laser Melting of Ti6Al4V Titanium Alloy*. Journal of Materials Engineering and Performance, 2021.
77. Kumar, S., *Selective Laser Sintering/Melting*, in *Comprehensive Materials Processing*. 2014, Elsevier. p. 93-134.
78. Attar, H., K.G. Prashanth, L.-C. Zhang, M. Calin, I.V. Okulov, S. Scudino, C. Yang, and J. Eckert, *Effect of powder particle shape on the properties of in situ Ti-TiB composite materials produced by selective laser melting*. Journal of Materials Science and Technology, 2015. **31**(10): p. 1001-1005.

79. Attar, H., M. Calin, L.C. Zhang, S. Scudino, and J. Eckert, *Manufacture by selective laser melting and mechanical behavior of commercially pure titanium*. Materials Science and Engineering A, 2014. **593**: p. 170-177.
80. Do, D.K. and P. Li, *The effect of laser energy input on the microstructure, physical and mechanical properties of Ti-6Al-4V alloys by selective laser melting*. Virtual and Physical Prototyping, 2016. **11**(1): p. 41-47.
81. Bertoli, U.S., A.J. Wolfer, M.J. Matthews, J.-P.R. Delplanque, and J.M. Schoenung, *On the limitations of volumetric energy density as a design parameter for selective laser melting*. Materials & Design, 2017. **113**: p. 331-340.
82. Kruth, J.-P., S. Kumar, and J. Van Vaerenbergh, *Study of laser-sinterability of ferro-based powders*. Rapid Prototyping Journal, 2005. **11**(5): p. 287-292.
83. Prashanth, K., S. Scudino, T. Maity, J. Das, and J. Eckert, *Is the energy density a reliable parameter for materials synthesis by selective laser melting?* Materials Research Letters, 2017. **5**(6): p. 386-390.
84. Thijs, L., M.L.M. Sistiaga, R. Wauthle, Q. Xie, J.-P. Kruth, and J. Van Humbeeck, *Strong morphological and crystallographic texture and resulting yield strength anisotropy in selective laser melted tantalum*. Acta Materialia, 2013. **61**(12): p. 4657-4668.
85. Carroll, B.E., T.A. Palmer, and A.M. Beese, *Anisotropic tensile behavior of Ti-6Al-4V components fabricated with directed energy deposition additive manufacturing*. Acta Materialia, 2015. **87**: p. 309-320.
86. Yang, J., H. Yu, Z. Wang, and X. Zeng, *Effect of crystallographic orientation on mechanical anisotropy of selective laser melted Ti-6Al-4V alloy*. Materials Characterization, 2017. **127**: p. 137-145.
87. Fang, M., F. Hu, Y. Han, J. Le, J. Xi, J. Song, L. Ke, M. Xiao, and W. Lu, *Controllable mechanical anisotropy of selective laser melted Ti6Al4V: A new perspective into the effect of grain orientations and primary grain structure*. Materials Science and Engineering: A, 2021. **827**: p. 142031.
88. Thöne, M., S. Leuders, A. Riemer, T. Tröster, and H.A. Richard, *Influence of heat-treatment on Selective Laser Melting products-e.g. Ti6Al4V*. 2012.
89. Jamshidi, P., M. Aristizabal, W. Kong, V. Villapun, S.C. Cox, L.M. Grover, and M.M. Attallah, *Selective laser melting of Ti-6Al-4V: the impact of post-processing on the tensile, fatigue and biological properties for medical implant applications*. Materials, 2020. **13**(12): p. 2813.
90. Wang, Z., Z. Xiao, C. Huang, L. Wen, and W. Zhang, *Influence of ultrasonic surface rolling on microstructure and wear behavior of selective laser melted Ti-6Al-4V alloy*. Materials, 2017. **10**(10): p. 1203.
91. Siddique, S., M. Imran, M. Rauer, M. Kaloudis, E. Wycisk, C. Emmelmann, and F. Walther, *Computed tomography for characterization of fatigue performance of selective laser melted parts*. Materials and Design, 2015. **83**: p. 661-669.

Chapter 2

Experimental procedures

In this chapter, the experimental procedures employed to achieve the aims of the proposed research project are summarised. The fabrication routes of powder metallurgy and laser powder bed fusion utilised for preparing test pieces, are thoroughly explained. Following the fabrication of specimens, a range of mechanical testing and microstructural characterization techniques employed to analyse the test results, are demonstrated.

2.1 Materials and fabrication routes

2.1.1 Material

The material used for sample preparation was gas-atomised pre-alloyed Ti6Al4V (grade 5) powder supplied by TLS, Technik GmbH & Co, Germany¹. Although the powder size distribution and its chemical analysis were certified by its manufacturer, each batch of powder was examined for chemical composition, particles morphology, size, and size

¹ TLS, Technik GmbH & Co is a subsidiary of ALTANA's ECKART division (www.eckart.net).

distribution prior to fabrication of test samples. This is because the powder batch may have been used by the research group for fabrication of some parts for other projects. Thus, it was critical to re-characterise the powder in terms of chemical composition, size and size distribution. In addition to powder analysis, the as-printed samples were also examined for chemical composition to monitor possible chemistry changes during the fabrication process. The technique employed for measuring the percentage of iron (Fe), vanadium (V), and aluminium (Al) was ICP-AES. The percentages of oxygen, hydrogen, and nitrogen were measured with a LECO ONH836 analyser. For measuring carbon content, the LECO CS200 instrument was used. Table 2-1 [1] summarises the chemical analysis of as-received and reused powder besides bulk sample fabricated from the reused powder.

Table 2-1: Chemical analyses (wt.%) of Ti6Al4V (grade 5) powder and as-printed test samples [1].

Element	Al	V	Fe	O	C	N	H	Ti
ASTM F2924-14	5.50-6.75	3.50-4.50	Max 0.3	Max 0.2	Max 0.08	Max 0.05	Max 0.015	Bal.
AS-received powder	6.39	3.88	0.2	0.077	0.011	0.005	<0.002	Bal.
Used powder	6.15	3.94	0.18	0.098	0.005	0.010	<0.002	Bal.
3D printed bulk sample	6.14	3.97	0.19	0.114	0.005	0.011	<0.002	Bal.

Some minor differences between the alloy chemistry of as-received and reused powder, and 3D printed bulk samples are noticeable, but they are still within the range provided by ASTM F2924-14 [2].

A Malvern Mastersizer 2000, shown in Figure 2-1, was used for analysing the powder particles. A small amount of powder (around 2g) was dispersed in the distilled water and the particle RI (refractive index) was set on 2.15 on Malvern Mastersizer 2000 according

to the manual of analyser suggested for titanium alloys. The absorption factor was fixed on 0.1 as a non-transparent mixture of water and particles.

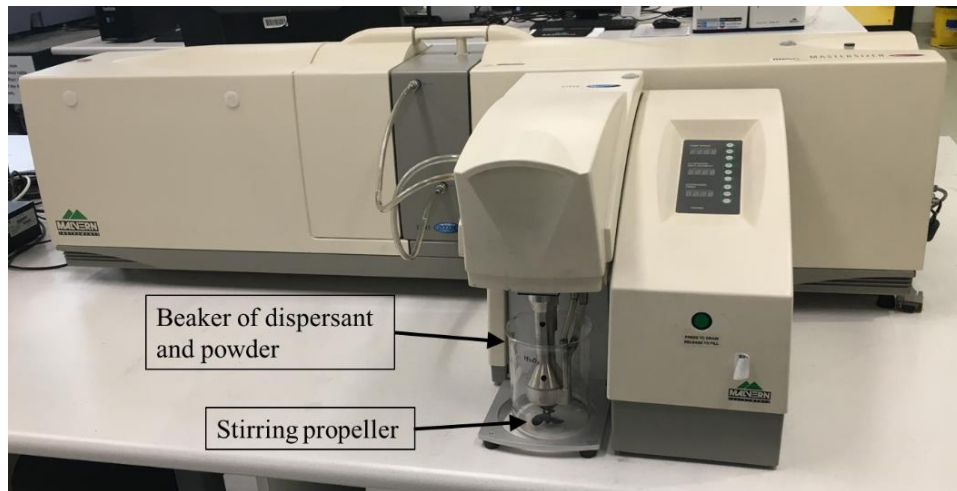


Figure 2-1: Image of Malvern Mastersizer 2000 particle size analyser.

For examination of powder particles morphology, a FEI Quanta 450 FEGSEM was utilised. Figure 2-2a and 2-2b are demonstrating the SEM of the new and used powder respectively while Figure 2-2c [1], illustrates the particle size distribution (PSD) graphs of both as-received and used powders. The median particle size, $d_{0.5} = 22.73\mu\text{m}$ for the as-received powder is slightly smaller than the reused powder, $d_{0.5} = 30.00\mu\text{m}$. The agglomeration and partially sintered small particles in used powder, explains the reason behind the shifting of the peak of the used particles' size to right in Figure 2-2c.

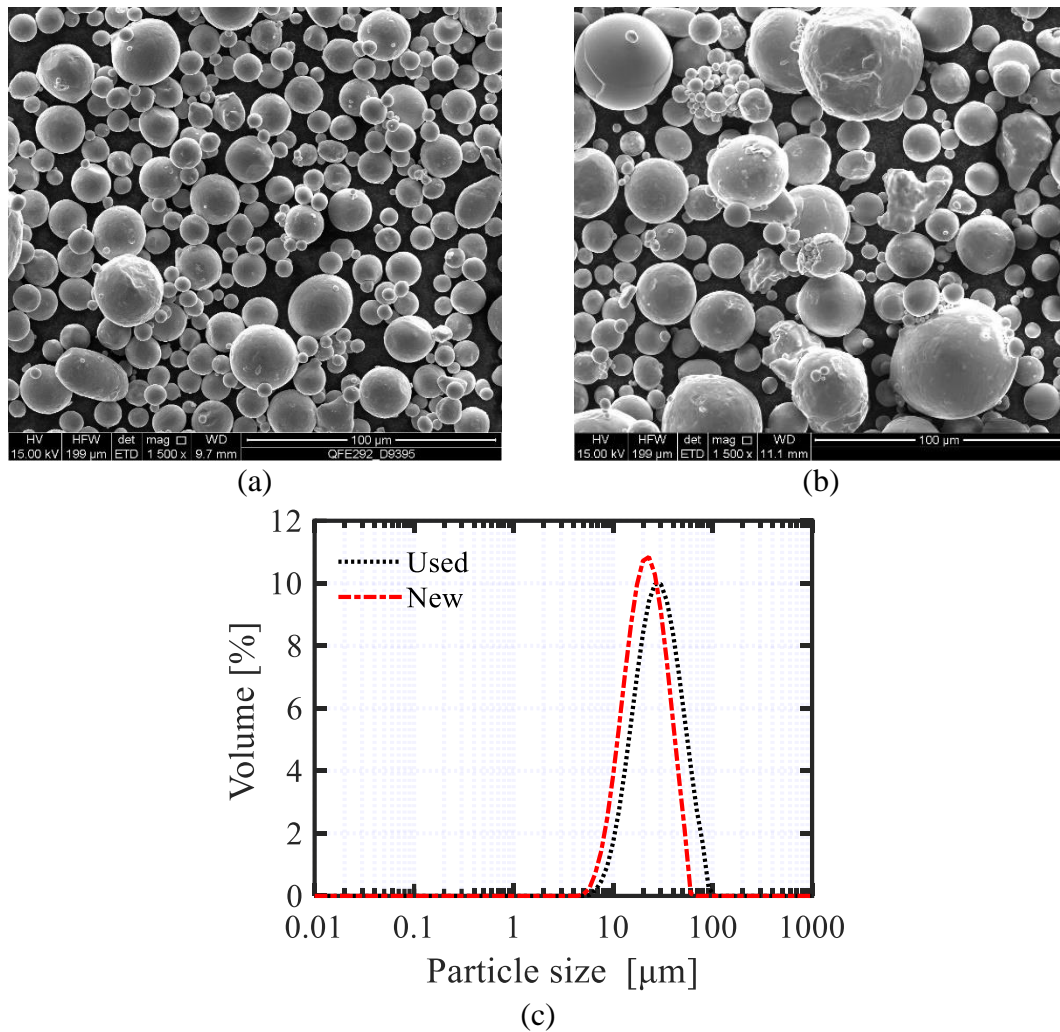


Figure 2-2: Typical SEM image of Ti6Al4V powder particle in two conditions of a) as-received and b) used, c) particle diameter distribution (PDS) of the new and used powder measured by Malvern analyser [1].

2.1.2 Sample preparation

Two main manufacturing routes were employed to fabricate the samples using Ti6Al4V powder material:

- 1- Conventional powder metallurgy (PM).
- 2- Laser powder bed fusion (L-PBF) 3D printing technique, also known as selective laser melting (SLM).

2.1.2.1 Powder metallurgy

For fabrication of PM samples, a uniaxial double acting die with an $\text{Ø}11$ mm punch was employed. The details of powder preparation before being poured into the die for compaction are presented in chapter 4.

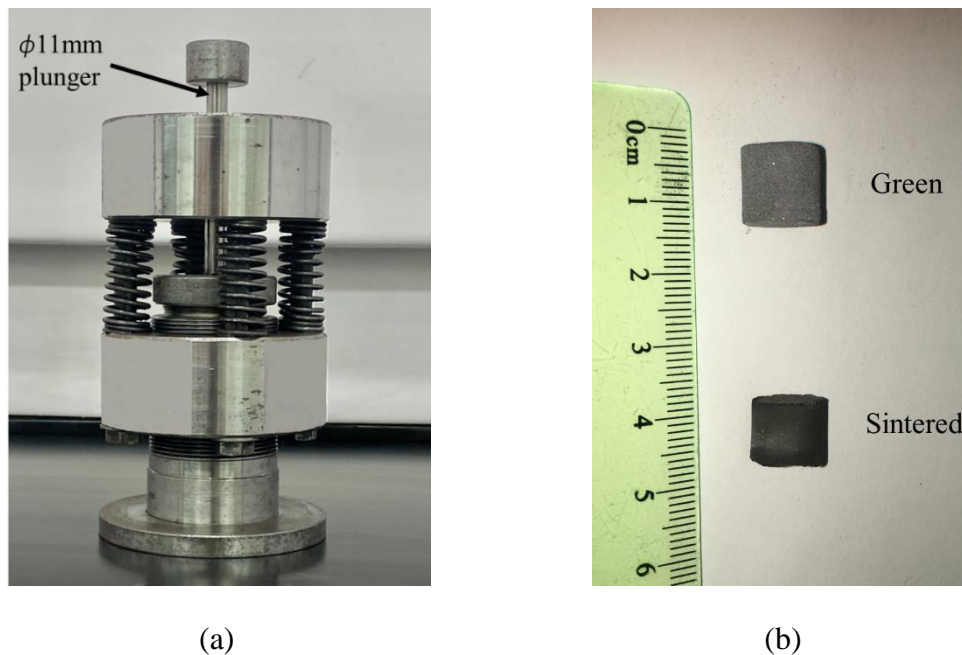


Figure 2-3: a) double acting die and punch; b) Ti6Al4V green and sintered samples.

For compaction of powder in the die, a Mohr & Federhaff AG Mannheim-Germany (M&F 2) 20-tonne hydraulic press was used. Two compaction pressures of 450 and 735 MPa were chosen to fabricate cylindrical PM samples of 11 mm diameter and 8-10 mm long. The green samples were initially heated to 450°C and held for 30 minutes to burn off the lubricant before reaching the sintering temperature. The process of reheating to sintering temperature was carried out in an argon filled tube furnace at two temperatures of 1100°C and 1250°C. The PM samples were held for 1 hour at sintering temperatures before cooling to room temperature at 3°C/min cooling rate. Figure 2-3a shows the image

of the double acting die while Figure 2-3b illustrates a green sample compacted at 735 MPa and a sintered sample (sintered at temperature 1250 °C).

2.1.2.2 L-PBF route

The L-PBF machine used in this project was ProX DMP 200 introduced by 3D SYSTEMS². The laser power source was in continuous mode and can reach maximum of 300W. The laser beam diameter, also known as laser spot size, is 70µm (at +2 mm defocussing of the beam) with wavelength (λ) of 1070nm. The chamber of the ProX-200 L-PBF machine is purged with high purity argon at pressure of 101KPa, and the level of oxygen is regulated at 500 ppm. The samples fabricated via L-PBF route were different in size and shape as explained below:

- **Cubes**

A comprehensive study was conducted to identify the optimised process parameters of the L-PBF route, also see chapter 3. The samples used for optimisation of process parameters were rectangular cubes with 10mm [L] x 10mm [W] x 3.8mm [H]. Figure 2-4 shows all cubic samples attached to the L-PBF substrate plate through their support structure. Three main process parameters of laser power, hatch spacing, and scan speed were variable but scan strategy and layer thickness of 30 µm were fixed. For the cubic samples a uni-directional laser scan strategy along the edge of the samples was specified. For further details about fixed and variable process parameters, please refer to chapter 3.

² www.3dsystems.com

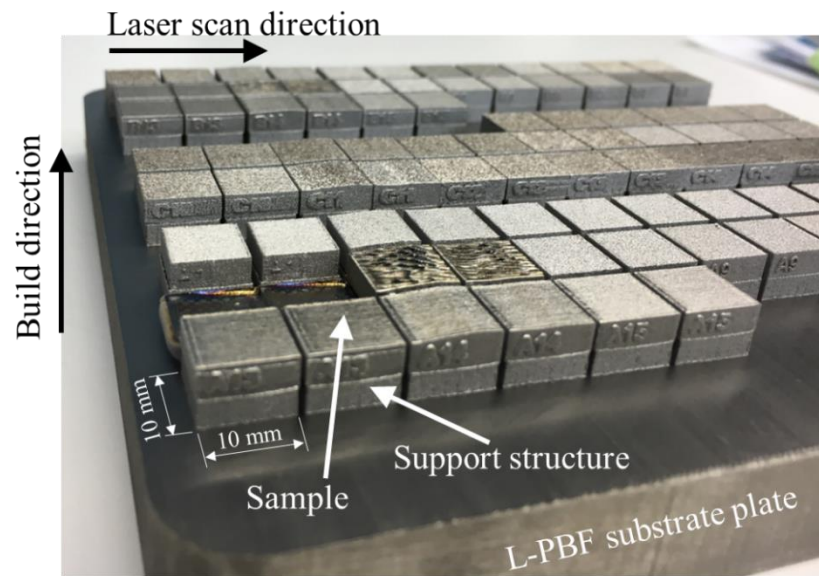


Figure 2-4: Cubic samples for empirical development of the optimisation of L-PBF process.

- **Short Cylinders**

The next series of L-PBF samples were short cylindrical bars with 9mm in diameter and 20mm in length, built vertically and horizontally. These series of L-PBF samples were used for fundamental understanding of the microstructure evolved in parts fabricated via L-PBF routes to compare with powder metallurgy parts.

- **Tensile test samples**

The tensile samples were fabricated with the optimised process parameters, summarised in Table 2-2, rendering a relatively high density Ti6Al4V fabricated parts, i.e., 99.85 %. With respect to laser scan strategy, except the cubic samples which were designed for investigation for optimised parameters, for the other parts in this project, a bi-directional laser vector for each layer was selected. Then the laser pattern was rotating 90° between each consecutive layers ($\pm 45^\circ$ with respect to the X and Y axes) as illustrated in Figure 2-5.

Table 2-2: Optimised L-PBF process parameters for fabrication Ti6Al4V tensile samples.

Laser Power (W)	hatch spacing (μm)	Layer thickness (μm)	Scanning velocity (mm/s)
270	85	30	1800

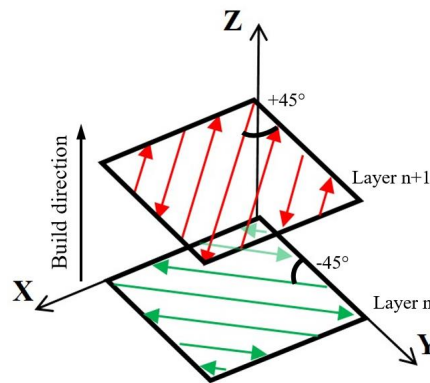


Figure 2-5: Laser scan strategy used for all L-PBF fabricated samples except cubic samples. [3].

Tensile test samples were fabricated in two shapes of as-built dumbbell shape and cylindrical rods. As-built dumbbell samples were ready to be directly tested in tensile testing machine however the rods were required to be machined on a lathe to reach the same shape of as-built dumbbell. Design of dumbbell tensile samples was according to the small size of tensile specimens ASTM E8 [4] standard, in which the gauge length is four times the gauge diameter D , Figure 2-6. The rods were 9.5 mm in diameter and 80 mm in length. The as-built dumbbell and rod samples were fabricated in two orientations of vertical and horizontal. For horizontal dumbbell samples a novel design was implemented for making straight and undistorted horizontal samples without any post treatment. Those samples were named as truly as-built samples since they were not treated

with any kind of post processes. Details about the novel design for horizontal samples are presented in chapter 5. Figure 2-7 displays L-PBF fabricated as-built dumbbell samples and cylindrical rods on the substrate plate.

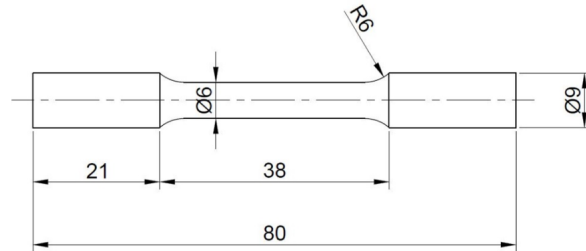


Figure 2-6: Dimensions of dumbbell shape tensile samples [3].

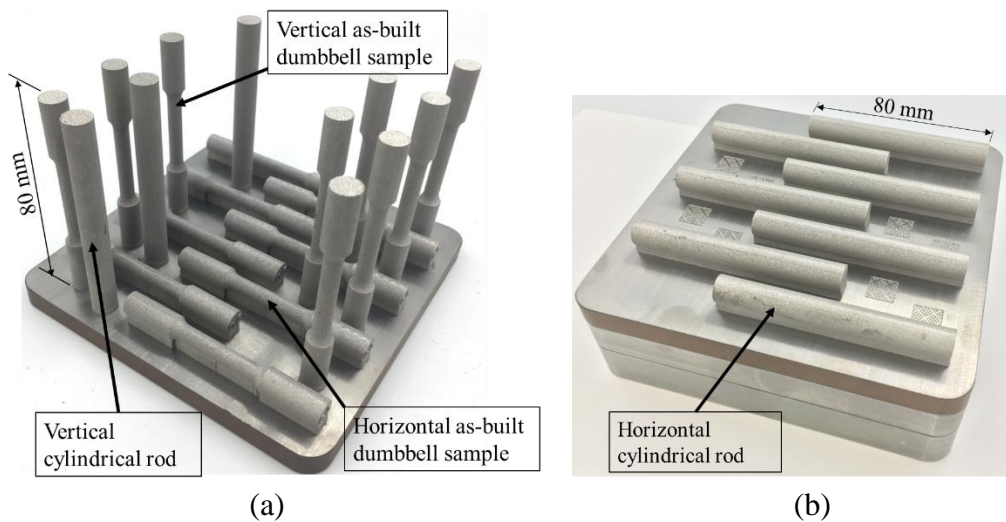


Figure 2-7: L-PBF fabricated dumbbell shape tensile and cylindrical bars on the substrate plate, a) horizontal and vertical dumbbell tensile samples and a few vertical cylindrical bars and b) horizontal cylindrical bars.

2.1.3 Post fabrication processes

Two post fabrication process procedures were employed in this research project: surface machining and thermal treatment.

2.1.3.1 Surface machining

For making the machined dumbbell shape tensile samples out of cylindrical rods, a turning process with an NC lathe machine was employed. After machining the rods on lathe, their final surfaces were polished using a paper backing abrasive with grit size P400. Figure 2-8 shows the dumbbell shape tensile samples machined out of horizontally built rods.

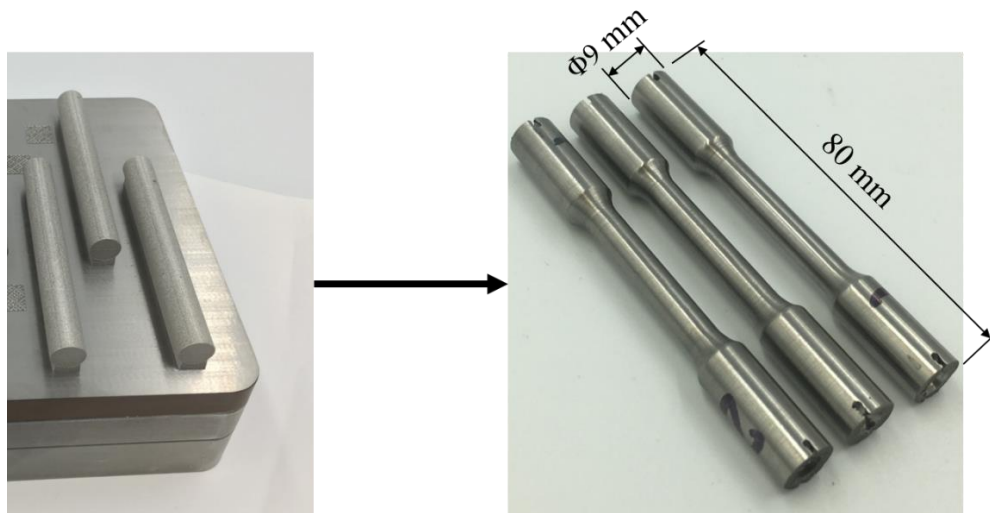


Figure 2-8: Horizontal cylindrical bars before and after being machined by a lathe.

2.1.3.2 Thermal treatment

Figure 2-9 shows a horizontal resistance heating tube furnace model AY-TF-80-175 which was used for conducting the thermal post processes in this study. The tube of furnace was vacuumed with a rotary pump first, then was purged with a very low flow rate of high purity grade argon which maintained during reheating to test temperature set on the tube furnace.

This furnace was also used for sintering the powder metallurgy green samples. It should be noted that before conducting thermal treatments the temperature of the tube furnace within its hot zone (the centre) was measured using a K-type thermocouple to ensure the

furnace set temperature provides the required thermal treatment test temperature. This measurement revealed that the actual temperature in the hot zone of furnace was 35°C to 40°C below the set temperature of furnace. For that reason, a correction factor for a series of temperature ranges was calculated and tabulated. Then for any required heat treatment temperature, its associated correction factor was applied to the set temperature to compensate the drifted values.



Figure 2-9: Image of the tube furnace AY-TF-80-175.

2.2 Microstructural characterisation

2.2.1 Metallographic samples preparation

For preparing metallographic samples from cylindrical test pieces, they were firstly sectioned transversally (i.e., perpendicular to the axis of the sample) and then hot mounted in Bakelite. For non-cylindrical specimens like cubic samples, they were sectioned perpendicular to the laser track followed by Bakelite mounting. For further details of

metallographic samples out of cubes specimens, please see chapter 3. Then all mounted samples were conventionally polished utilising Struers³ Tegramin-25 machine in accordance with application notes for titanium [5]. For final step of polishing, 75% of colloidal silica (grain size $\sim 0.04 \mu\text{m}$) was mixed with 25% of hydrogen peroxide (with concentration 30%). Prior etching procedure, some examinations like measuring the level of porosity, micro-hardness and nano-hardness were carried out on polished samples. Then all metallographic polished samples were etched for 50 seconds using Kroll's reagent (3% HF + 5% HNO₃, and 92% distilled water). Due to the safety issues with HF acid, a sample holder and etchant container were designed and manufactured as shown in Figure 2-10a. In order to obtain a uniform effect of etchant on the surface of the samples, they needed to be fully sunk in petri dish while oscillating movement was applied to the samples holder as shown in Figure 2-10b.

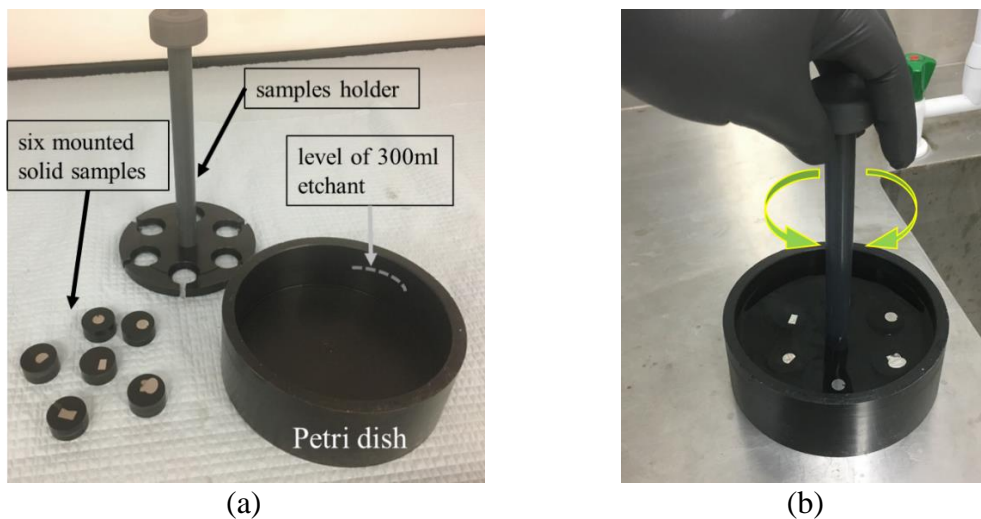


Figure 2-10: a) Componentry for etching the samples in accordance with safety in using HF acid, b) six samples are sunk in the etchant with oscillating movement of samples holder.

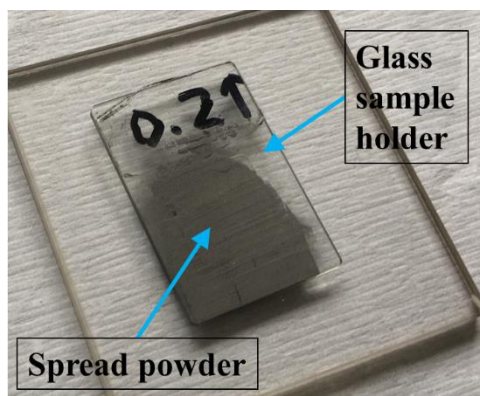
³ www.struers.com

2.2.2 XRD

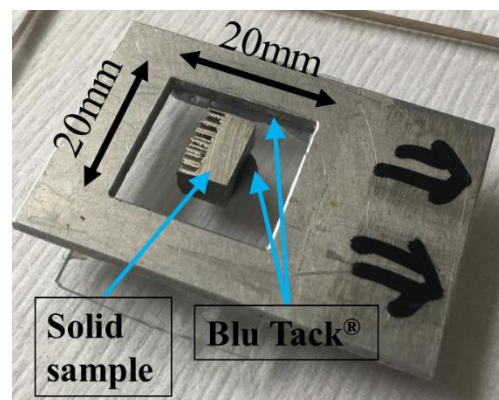
Figure 2-11a shows the Rigaku MiniFlex 600 machine used for XRD examination of the samples. Cu radiation operating at 40kV and 15mA was employed in Rigaku machine, in a continuous scan mode and 2θ angle ranged from 30° to 80° . The divergence slit (DS) size 0.625° was selected for all experiments. For XRD tests of powder particles, around 3g of powder was spread over the glass sample holder, as displayed in Figure 2-11b. However, for solid samples a bracket with a 20mm x 20mm opening with a glass slice at back were used, Figure 2-11c. It was a common practice to attach the solid samples and bracket to the glass slice using a “BOSTIK” Blu Tack[®] as a sticky material. But to ensure that the Blu Tack[®] does not cause any issues with XRD spectrum peaks of solid sample, two cautious measures were established. Firstly, Blu Tack[®] was examined for any XRD spectra due to any impurities or contamination in Blu Tack. In the second step, the sticky material was kept away from the area where the X-ray coincides the sample surface, as shown Figure 2-11c. Finally, the generated report of titanium XRD spectra was compared with that of Blu Tack[®] to make sure there was not any unknown XRD peaks from Blu Tack[®] to interfere with XRD spectra of the sample.



(a)



(b)



(c)

Figure 2-11: a) Rigaku XRD machine used in this project with rotating sample mount, b) glass holder for XRD examination of powder and c) XRD solid sample holder setup.

2.2.1 Optical microscopy, SEM and EDS analysis

Figure 2-12 illustrates the Zeiss Axio Imager2 which was used for optical microscopy. Optical microscopy was performed on all samples before and after etching process. Quantitative metallography was performed on unetched samples to measure porosity content using the image analysis software ImageJ⁴. For the microstructural analysis and

⁴ <http://www.imageJ.net>

elemental composition of materials via Energy Dispersive (X-Ray) Spectroscopy (EDS) method, two scanning electron microscopes of FEI Quanta 450 FEG-SEM, and FIB SEM Helios Nanolab FEI Dual Beam were used. Both SEMs were equipped with SDD detector released by Oxford Instruments and Aztec analysis software.



Figure 2-12: Zeiss Axio Imager2 optical microscope.

For higher magnification with better quality of image Helios Dual Beam is especially the preferred tool which enables in-situ sectioning using the Focused Ion beam (FIB). Figure 2-13, illustrates the application of FIB for micro-sectioning and EDS analysis of specific feature in L-PBF fabricated sample as presented in chapter 6.

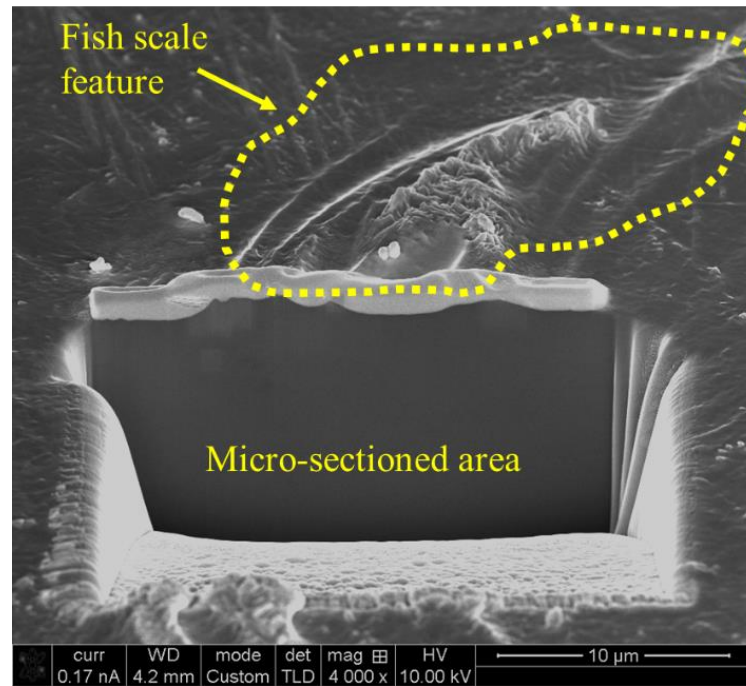


Figure 2-13: Micro-sectioning by FIB on an as-built L-PBF fabricated sample.

2.3 Surface characterisation

A stylus-type surface profilometer and SEM were utilised for characterisation of top surface of L-PBF fabricated parts. SEM was used for examination of surface morphology, and surface profilometer was employed for measuring R_a and the profile of the surface travelled by stylus. Figure 2-14, displays the surface profilometer Mitutoyo SJ-410 which is examining the top surface of an L-PBF fabricated sample. The details of methods of measurement such as the paths and orientations of stylus, are presented in chapter 3.

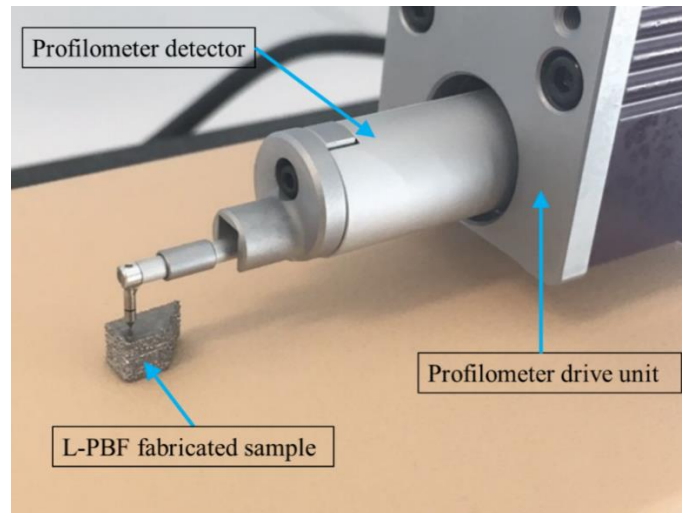


Figure 2-14: Mitutoyo SJ-410 stylus head is measuring the roughness of top surface of an L-PBF fabricated sample.

2.4 Mechanical properties

2.4.1 Tensile test

All tensile tests were carried out at constant crosshead speed of 0.2 mm/min, in open air, at room temperature. The tensile testing machine was an Instron, model 5969 with a 50kN load cell. The strain was measured by an axial clip-on Instron extensometer with gauge length of 25mm. One of the challenges for conducting the tensile tests was the slippage of serrated wedge on the grip sections of specimens. The reason that the slippage happened was related to the short grip length of the tensile test samples causing rotating and releasing the wedge grips, as illustrated in Figure 2-15. It is recommended by ASTM E8 that “if possible, the length of grip section should be long enough to allow the specimen to extend into the (wedge) grips a distance equal to two thirds or more of the length of the (wedge) grips” [4]. However, making tensile samples with long grip sections according to ASTM E8 recommendation was restrained by L-PBF machine limitation where its build platform was 140mm x 140mm with maximum height of build of 100mm.

The author could not find any solutions in open literature to resolve the slippage problem but by developing a mechanical filler stopper, the slip of serrated wedge was completely eliminated. The trial and error showed that the gap between the serrated wedges should not be fully filled with solid filler, but a clearance should be considered to allow the wedges to move when the teeth of wedges penetrate in the grip sections of the specimens. It was found that the optimum thickness of solid filler should be 0.4mm thinner than the gap between serrated wedges, as illustrated in Figure 2-16.

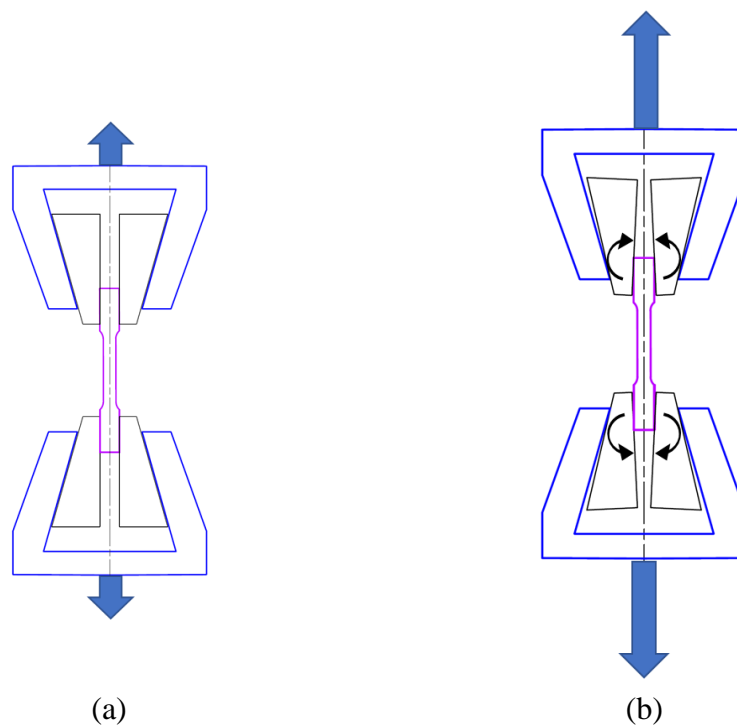


Figure 2-15: a) Initial setup of the specimen inside serrated wedges, b) wedges start releasing and slipping on grip sections of the specimens due to sample short grip sections.

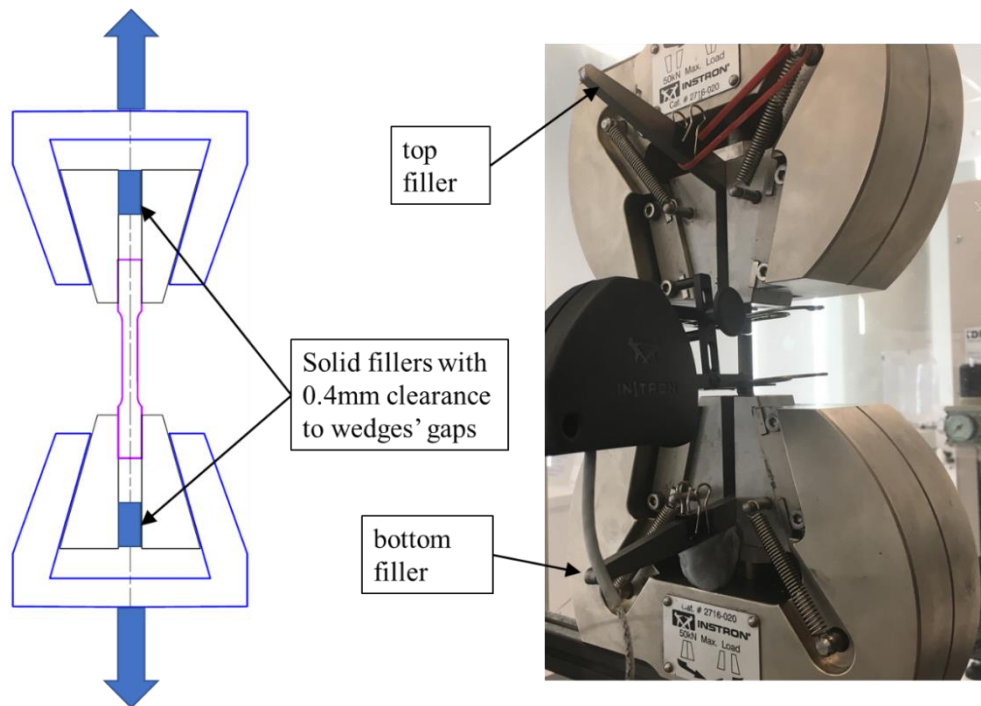


Figure 2-16: Developed solid filler for preventing the slippage of serrated wedge grips on tensile specimen.

2.4.2 Micro-hardness and nanoindentation.

For Vickers' micro-hardness a LECO LM700AT machine was utilised as shown in Figure 2-17. Although it was confirmed by the author [6], as appeared in appendix C, that the etched surface condition does not affect the microhardness results, but most of the tests were performed in unetched (polished) condition at a 300g applied load and dwell time of 10s. After measuring the diagonals of d_1 and d_2 of pyramidal indentations, like the typical indentation shown in Figure 2-17, the integrated software in the micro-hardness machine calculates the HV hardness of the material in the indented point.

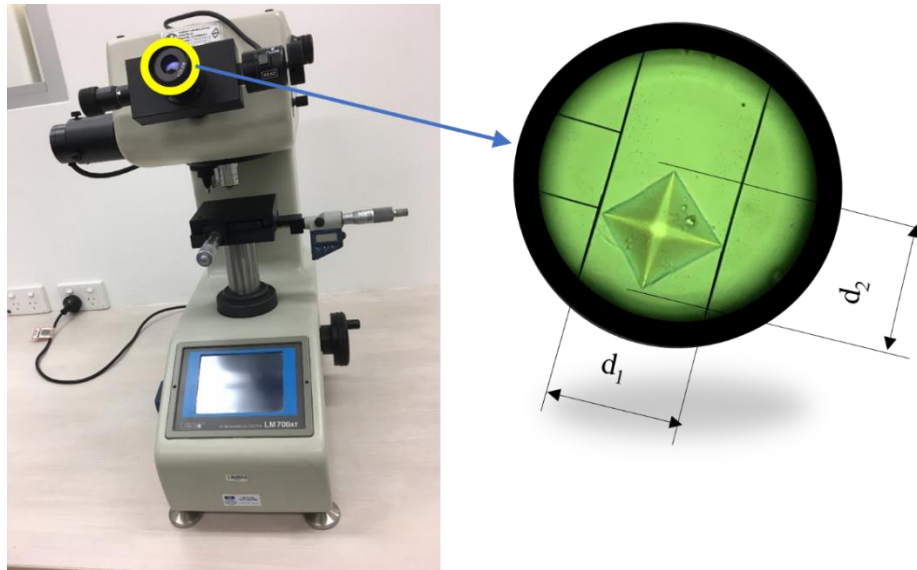


Figure 2-17: LECO LM700AT machine used for measuring Vickers microhardness by impression of a pyramidal indenter.

Figure 2-18a displays the nano-indentation system, Fischer-Cripps IBIS which was employed in this project. Unlike microhardness tests which were not sensitive to the surface condition of metallographic samples, for nanoindentation tests, the surface of all samples must be in polished condition. As presented in chapter 4, all nanoindentation tests were performed with a Berkovich indenter at a constant penetration of 300nm (depth control) and dwell time of 2s. The speed of indenter during loading and unloading was 60nm/s and two data of force (load) and penetration of 20 position were collected during either loading or unloading. The nano-hardness, H , is then calculated by integrated software of IBIS. Figure 2-18b shows a typical graph of load vs penetration depth of indenter of three constituent phases, α , β and martensite α' observed in L-PBF fabricated and powder metallurgy samples.

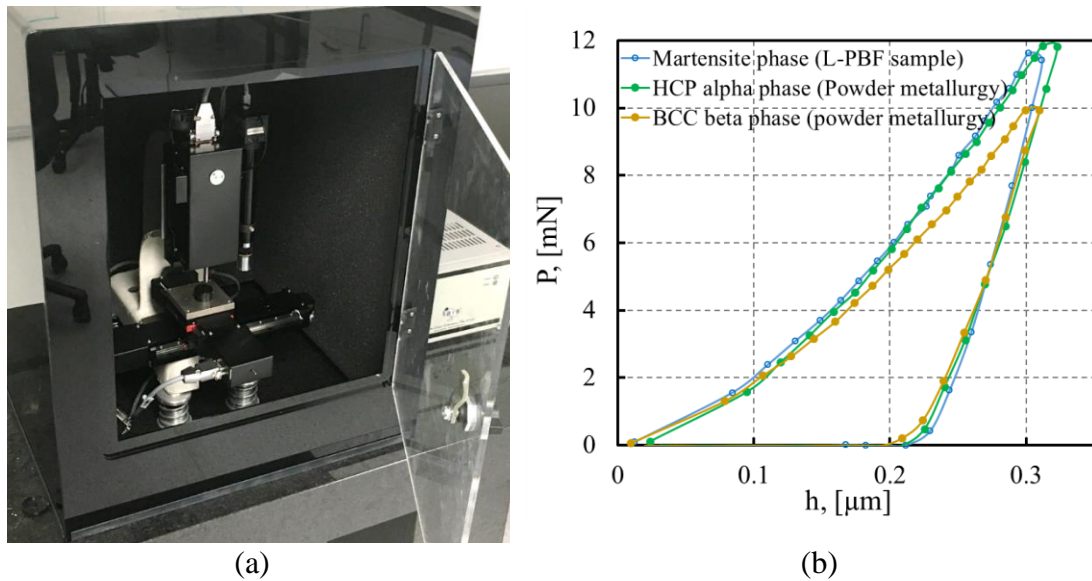


Figure 2-18: a) Fischer-Cripps IBIS machine for measuring nano-hardness by impression with a Berkovich indenter, b) a typical graph of load versus indenter penetration for three phases observed in L-PBF and powder metallurgy samples.

Reference

1. Dareh Baghi, A., S. Nafisi, R. Hashemi, H. Ebendorff-Heidepriem, and R. Ghomashchi, *Experimental realisation of build orientation effects on the mechanical properties of truly as-built Ti-6Al-4V SLM parts*. Journal of Manufacturing Processes, 2021. **64**: p. 140-152.
2. *ASTM F2924-14, Standard Specification for Additive Manufacturing Titanium-6 Aluminum-4 Vanadium with Powder Bed Fusion*. 2014.
3. Dareh Baghi, A., S. Nafisi, R. Hashemi, H. Ebendorff-Heidepriem, and R. Ghomashchi, *Effective post processing of SLM fabricated Ti-6Al-4 V alloy: Machining vs thermal treatment*. Journal of Manufacturing Processes, 2021. **68**: p. 1031-1046.
4. *ASTM E8/E8M -16a Standard Test Methods for Tension Testing of Metallic Materials*. 2016.
5. Struers ApS, C. *Metallographic preparation of titanium*. 2016; Available from: www.struers.com/-/media/Struers.../Application_Note_Titanium_2015_ENG.pdf.
6. Dareh Baghi, A., R. Ghomashchi, R.H. Oskouei, and H. Ebendorff-Heidepriem, *Nano-mechanical characterization of SLM-fabricated Ti6Al4V alloy: etching and precision*. Metallography, Microstructure, and Analysis, 2019. **8**(5): p. 749-756.

Chapter 3

L-PBF process optimisation


Chapter overview

This chapter is based on a paper submitted to “ASM Journal of Materials Engineering and Performance” and highlights the optimum ranges of three main LPBF process parameters for fabricating Ti6Al4V parts and effects of parameters on the final parts. Those main process parameters are laser power, hatch spacing and scan speed and, the main target is obtaining the parts with the lowest porosity and micro-roughness of top surface. The well-known combined parameter of Volumetric Energy Density (VED) is examined for its validity for optimisation of process parameters. The key finding in this research paper, is topography of the top surface of parts which can be categorised in two groups of meso-roughness and micro-roughness. Then by minimising the micro-roughness of the surface through the optimum ranges of parameters the parts with the highest density can be achieved.

Statement of Authorship

Title of Paper	A New Approach to Empirical Optimisation of Laser Powder Bed Fusion Process for Ti6Al4V parts		
Publication status	<input type="checkbox"/> Published <input type="checkbox"/> Accepted for Publication <input checked="" type="checkbox"/> Submitted for Publication <input type="checkbox"/> Unpublished and Unsubmitted work written in manuscript style		
Publication Details	A. Dareh Baghi, S. Nafisi, R. Hashemi, H. Ebendorff-Heidepriem, and R. Ghomashchi, " A New Approach to Empirical Optimisation of Laser Powder Bed Fusion Process for Ti6Al4V parts"; submitted to ASM Journal of Materials Engineering and Performance.		


Principal Author


Name of Principal Author (Candidate)	Alireza Dareh Baghi		
Contribution to the Paper	Developed the ideas and concepts, designed 3D models of the samples, conducted the experiments, acquired the data, interpreted results, and drafted the manuscript		
Overall percentage (%)	85%		
Certification:	This paper reports on original research I conducted during the period of my Higher Degree by Research candidature and is not subject to any obligations or contractual agreements with a third party that would constrain its inclusion in this thesis. I am the primary author of this paper.		
Signature		Date	28/10/2022


Co-Author Contributions


By signing the Statement of Authorship, each author certifies that:

- I. the candidate's stated contribution to the publication is accurate (as detailed above);
- II. permission is granted for the candidate to include the publication in the thesis; and
- III. the sum of all co-author contributions is equal to 100% less the candidate's stated contribution.

Name of Co-Author	Reza Ghomashchi		
Contribution to the Paper	Supervised the work, participated in developing ideas, evaluated the experiments results, and reviewed the discussion and manuscript.		
Signature		Date	28/10/2022

Name of Co-Author	Shahrooz Nafisi		
Contribution to the Paper	Supervised Helped in developing the concept and experimental design and manuscript review.		
Signature		Date	28/10/2022

Name of Co-Author	Reza Hashemi		
Contribution to the Paper	contributed to experimental setup and reviewed the manuscript.		
Signature		Date	24/10/2022

Name of Co-Author	Heike Ebendorff-Heidepriem		
Contribution to the Paper	Provided access to LPBF machine for sample preparation, supervised the work and reviewed the manuscript.		
Signature		Date	24/10/2022

A New Approach to Empirical Optimisation of Laser Powder Bed Fusion Process for Ti6Al4V Parts

Alireza Dareh Baghi, Shahrooz Nafisi, Reza Hashemi, Heike Ebendorff-Heidepriem,
Reza Ghomashchi

Abstract

Optimisation of all the process parameters for laser powder bed fusion (L-PBF), considering the effects of individual parameters on Ti6Al4V fabricated parts, can be complex and challenging. Therefore, for the first time the effects of three main variable process parameters (laser power, scan speed, and hatch spacing) on three outcome parameters (surface roughness, bulk porosity, and production rate of parts) were studied in this work. Then the combination of above-mentioned process parameters in the form of volumetric energy density (VED) was investigated in order to establish a practical method for optimisation of process parameters for making Ti6Al4V parts with the desired quality targets, i.e., the smoothest surface, the lowest bulk porosity and a higher production rate.

It was revealed that although VED is a reliable metric for the optimisation of process parameters, some thresholds and ranges should be considered for all three parameters of laser power, scan speed, and hatch spacing. It was demonstrated that by employing an optimum laser power of 180 W or 270 W and changing the scan speed and hatch spacing to keep VED in the range of 50 J/mm³ to 100 J/mm³, fabrication of samples with micro-roughness $R_a < 10 \mu\text{m}$ and bulk porosity less than 0.15% is achievable.

In addition, the surface of the L-PBF fabricated parts may appear in two categories of surface morphology; wavy surface classified “meso-roughness topography” and non-wavy surface termed “micro-roughness”. Since there was not any correlation between the value of roughness of samples with meso-rough surface and their bulk porosity, and besides, their process parameters were far from optimised parameters, the samples with meso rough surface were not included in the final results. However, it was realised in the samples with micro rough surfaces, the value of their micro-roughness could accurately indicate the porosity content of Ti6Al4V samples.

3.1 Introduction

Laser powder bed fusion (L-PBF) also known as selective laser melting (SLM), is one of the additive manufacturing (AM) techniques that are being progressively developed to fabricate metallic parts for various applications [1, 2]. Ongoing research activities are aiming to optimise the process parameters to improve parts quality through a better understanding of the effect(s) of process parameters on the microstructure, surface finish, and mechanical properties of materials produced by L-PBF [3-5]. A good surface finish is desirable as poor surface conditions could adversely affect the mechanical properties [6, 7]. Although understanding the effect of all the main process parameters, such as laser power, or scan speed, on the quality of final products is necessary; in parametric optimisation procedures, it is hard to involve all the parameters, due to a large number of variables.

To reduce the complexity of optimisation, in previous studies such as [8-10], the aim was to optimise a combined parametric measure termed the energy input or energy density as one of the most important measures. The primary goal of process optimisation in most studies is to fabricate parts with the highest density and smoothest surface [11, 12].

Equation (1) is a well-known formula for calculating volumetric energy density (VED in J/mm^3). It combines the four main process parameters of laser power, P (W); scan speed, v (mm/s); hatch spacing, h (mm), and layer thickness, t (mm). However, in some studies, the researchers have simplified Equation (1) or have changed some of its parameters, according to their research objectives. Carter et al. [13] used two-dimensional energy density (J/mm^2), Equation (2), where the layer thickness was constant, while Wang et al. [14] combined laser power and scan speed to form a linear energy density (LED in J/mm), Equation (3), which is similar to heat input (energy per unit length) in welding [15]. In some other studies [16, 17], the researchers replaced hatch spacing h with laser spot size W_0 in VED, when they attempted to characterize the laser deposition of a single track. Although the equations used for the calculation of energy density may vary in different studies, the concept of energy density is nearly the same and their findings can be used for other research. Bertoli et al. [16] and Prashanth et al [18] stated that using VED as a design parameter still requires caution, while Carter et al [13] found two-dimensional energy density to be a good criterion to check the void area (%). Koutiri [19] reported that VED, as a combined process parameter, is reliable for the optimisation of densification but not for surface roughness. Attar et al [20] and Gong et al [21] reported a non-linear correlation between VED and the density of their titanium fabricated parts.

$$E_{(volumetric)} = \frac{P}{v \cdot h \cdot t} \quad (1)$$

$$E_{(2D)} = \frac{P}{v \cdot h} \quad (2)$$

$$E_{(Linear)} = \frac{P}{v} \quad (3)$$

In Equations (1) to (3), P is laser power while v indicates scan speed, h is hatch spacing, and t represents layer thickness. Although it is still a common practice to use Equation

(1) for calculating VED, by keeping some parameters constant, the applicability of the VED equation in real practice, is not yet clear and this requires a comprehensive investigation. Besides, the acceptable ranges of individual process parameters of laser power, scan speed and hatch spacing are not fully studied.

Since Ti6Al4V (also known as Ti64) alloy, with its applications in industrial fields like the aerospace [22, 23] and biomedical [24, 25], has attracted significant interest for fabricating of parts via L-PBF technique, in this research work Ti64 alloy is the material of interest. So, the main goal of this work was to establish a practical methodology for finding the most suitable L-PBF process parameters (i.e., laser power, hatch spacing, and scan speed) and their effects on the quality of Ti64 samples based on their surface topography, internal or bulk porosity and production rate.

Production rate, as one of the most important outcome parameters, has not been considered in detail in past studies. When a range of optimised process parameters are determined, the production rate can be the deciding factor in finalizing the selected optimised process parameters from the optimisation matrix. The findings and outcome of this study can be applicable to manufacturing industry where commissioning of a newly installed L-PBF machine usually requires optimisation.

3.2 Materials and experimental Procedures

3.2.1 Materials and L-PBF equipment

Pre-alloyed powder Ti-6Al-4V (grade 5) sourced from TLS Technik GmbH & Co. Germany⁵, was used for the preparation of L-PBF samples. Figure 3-1a, which is the SEM image of powder particles, exhibits spherical morphology for the particles. For the SEM metallography, an FEI Quanta 450 FEG-SEM was utilised in its secondary electrons

⁵ TLS, Technik GmbH & Co is a subsidiary of ALTANA's ECKART division (www.eckart.net).

mode, with a beam voltage of 15kV for particle morphology and 20kV for the remaining of micrographs. The working distance (WD) in SEM was set around 10mm. Figure 3-1b shows the size distribution of the powder particles, measured with a Malvern Mastersizer 2000 analyser. For analysis of powder size, a small quantity of Ti64 powder (around 2 grams collected by a laboratory spatula) was dispersed in the distilled water of the beaker of the equipment. The refractive index of the particle (RI) was set on 2.15, according to the manual of analyser suggested for titanium alloys. The absorption factor was fixed on 0.1 as a non-transparent mixture of water and particles.

For the chemical analysis of the powder, ICP-AES technique was used to measure the weight percentage of vanadium, iron, and aluminium. The percentages of all gases were measured using a LECO ONH836 analyser and for carbon a LECO CS200 instrument was employed. The chemical composition of the powder given in Table 3-1 confirms that the powder used for this investigation satisfies the requirement of ASTM F2924-14 [26] for Ti64.

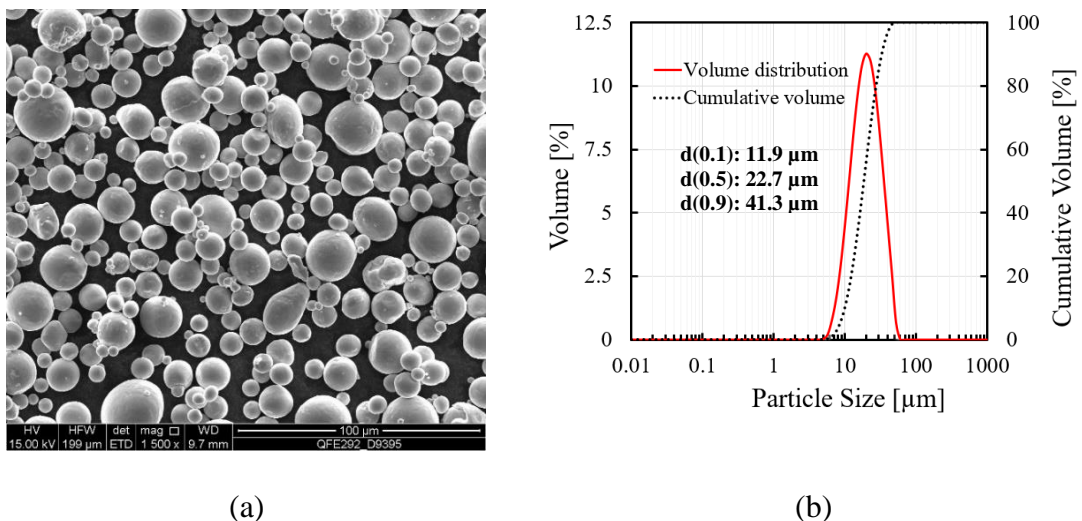


Figure 3-1: a) SEM image of Ti64 powder particles, and b) size (diameter) distribution of Ti64 powder particles.

The L-PBF system, used in this study, was a ProX DMP 200 selective laser melting (SLM) 3D printing machine. This machine employs a fibre laser with a maximum power of $P=300$ W in continuous laser mode. The laser Focal Offset Distance (FOD) was +2 mm rendering a laser beam spot size of $70\ \mu\text{m}$ with a wavelength of $\lambda=1070\text{nm}$. The chamber of the L-PBF was filled with ultra-high purity grade argon and the maximum allowed oxygen content in the chamber was regulated at 500 ppm. The L-PBF process parameters used in this work will be discussed in the next section.

Table 3-1: Chemical composition of Ti6Al4V (grade 5) powder (wt. %).

Element	Al	V	Fe	O	C	N	H	Ti
Ti6Al4V powder	6.15	3.94	0.18	0.098	0.005	0.010	< 0.002	Bal.
ASTM F2924-14	5.50-6.75	3.50-4.50	Max 0.3	Max 0.2	Max 0.08	Max 0.05	Max 0.015	Bal.

3.2.2 Design of experiments and L-PBF process parameters

Design of experiments covers a wide range of VED from $24\ \text{J}/\text{mm}^3$ to $180\ \text{J}/\text{mm}^3$, as given in Table 3-2 (the energy density calculated in Table 3-2 is in accordance with Equation (1) explained in the Introduction). The samples were fabricated as cuboid with dimensions of $10\ \text{mm [L]} \times 10\ \text{mm [W]} \times 3.8\ \text{mm [H]}$ and classified in three groups of A, B, and C. Each group was divided into three subgroups with five samples in each. Therefore, the number of samples in each group (A, B, and C) is fifteen and the total number of samples investigated in this study is forty-five. The series number of each sample follows its group, starting from 1 to 5 for the first subgroup, like B1 to B5 of group B, then 6 to 10 for the second subgroup and, series numbers 11 to 15 for the third subgroup. The L-PBF process parameters of all the samples were designed so that the VED of the samples with the same series number, like A7, B7 and C7, is the same as presented in Table 3-2.

Table 3-2: Design of Experiments: Group A, B and C.

Sample	Laser power, (Watt)	Layer thickness, (μm)	Scan speed, (mm/s)	Hatch spacing, (μm)	VED, (J/mm ³)
Group A	270	30	2500	A1	72
				A2	48
				A3	36
				A4	29
				A5	24
			1800	A6	100
				A7	67
				A8	50
				A9	40
				A10	33
			1000	A11	180
				A12	120
				A13	90
				A14	72
				A15	60
Group B	180	30	1666	B1	72
				B2	48
				B3	36
				B4	29
				B5	24
			1200	B6	100
				B7	67
				B8	50
				B9	40
				B10	33
			666	B11	180
				B12	120
				B13	90
				B14	72
				B15	60
Group C	90	30	833	C1	72
				C2	48
				C3	36
				C4	29
				C5	24
			600	C6	100
				C7	67
				C8	50
				C9	40
				C10	33
			333	C11	180
				C12	120
				C13	90
				C14	72
				C15	60

As seen from Table 3-2, the three process parameters of laser power, scan speed and hatch spacing are the variables. However, the layer thickness for all the samples was the same (30 μm), as recommended by the machine manufacturer. A uni-directional laser scan strategy was chosen for fabricating all cuboids on a 12 mm thick build plate. Figure 3-2a shows all samples on the build plate after removing from L-PBF machine chamber while Figure 3-2b demonstrates the arrangement of the sample on the substrate, corresponding to all samples in Figure 3-2a.

Figure 3-2c illustrates one of the samples, series A7, attached to its support structure as specified on the photograph. The build orientation and laser path direction of sample A7, Figure 3-2c, is identical for all other samples. In order to examine the repeatability of the L-PBF process parameters, each sample had a pair, made with the identical process parameters.

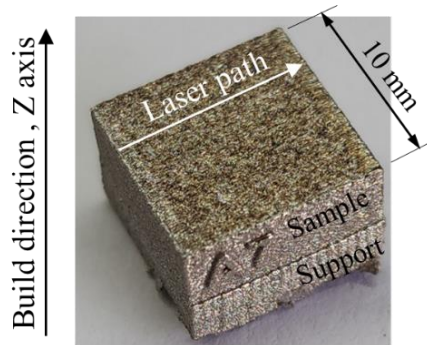
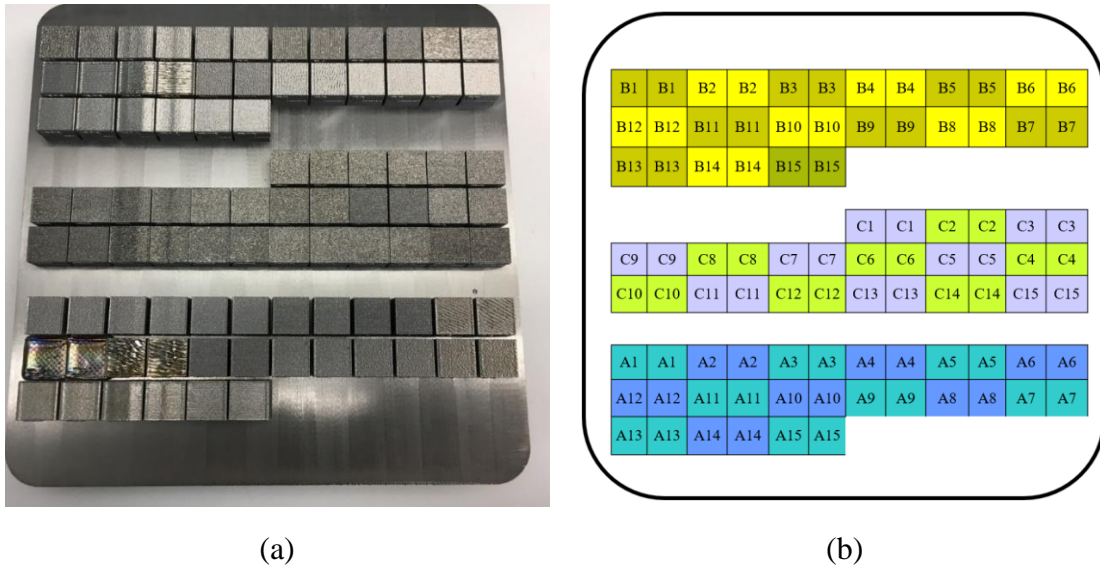


Figure 3-2: a) Top view of all cuboid samples on the build plate, b) arrangement of cuboids on the build plate and c) an example of a cuboid sample, A7, fabricated with an embossed letter “A” and series number “7” on its side wall.

3.2.3 Analysis method

All samples (prepared in duplicate) were inspected visually once removed from the build chamber. Based on the initial examination, all paired samples looked alike, suggesting there is a high degree of repeatability in manufacturing. After removing all samples from the built plate, the R_a (roughness average) and R_z (average maximum height of the profile) [27] of the top surface (the surface viewed in Figure 3-2) of all the samples were measured with a Mitutoyo SJ-410 stylus-type surface profilometer, with tip radius of $2\mu\text{m}$ and angle

of 60°. However, since the R_a and R_z trends were similar (see Figure S1, S2 and S3 in supplementary material), the values of R_a are presented in this report. The roughness measurement was performed on two areas of the surface. All the roughness measurements were performed on the samples' pairs (or twins) as well. The travel path of the stylus was perpendicular to the laser track (see Figure 3-3a), with an evaluation scan length of 3.2 mm. This scan length was more than 20 times the largest hatch spacing, i.e., 150 μm , covering most of the irregularities and periodicities of the surface. Since the R_a value is a guideline of surface roughness [28] and may not be sufficient for characterizing surface quality, it was necessary to examine the surface topography with SEM and analyse the roughness results from a stylus profilometer at the same time.

After measuring the roughness, all the samples were halved using a diamond wheel cutting saw perpendicular to the laser track, as shown in Figure 3-3a, followed by mounting in Bakelite and conventional grinding and polishing down to 1 μm diamond paste. A final polish, a mixture of 75% colloidal silica (0.04 μm) with 25% of hydrogen peroxide (30% concentration) solution, was employed.

Figure 3-3b displays the other halved section of the same sample after being mounted and polished. The support structure is presented in Figure 3-3b. All samples in the polished condition were examined for their porosity content by a Zeiss Axio Imager2 optical microscope and via 2D area fraction image analysis using ImageJ software⁶.

⁶ <http://www.imageJ.net>

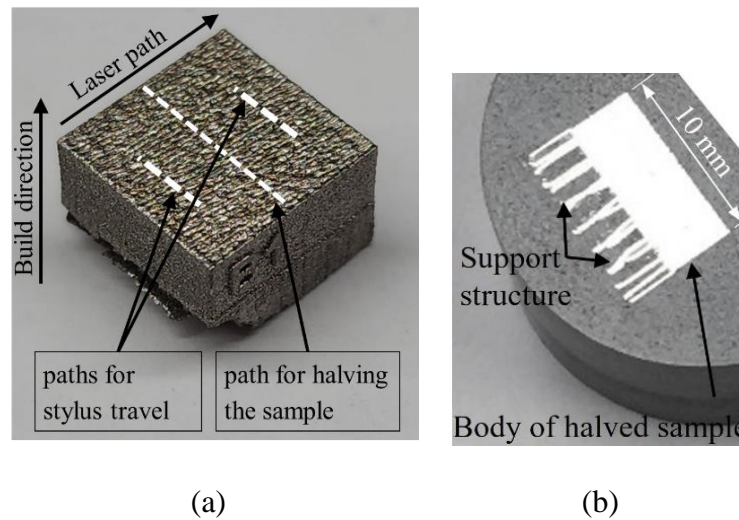


Figure 3-3: a) paths for stylus travel and halving a sample which are perpendicular to laser path, b) photo of the second halved section of the sample mounted in Bakelite and polished, (sizes on the photos are not to scale).

3.3 Results and discussion

3.3.1 Surface topography

Analysis of the surface topography found that the profile of the top surface can fall in two main categories of wavy and non-wavy surfaces. The peak-to-peak distance in wavy surface profile is far greater than the selected hatch spacing. A11 is one example of the samples with a wavy surface profile shown in Figure 3-4. Figure 3-4a displays a SEM image of the A11 top surface, while Figure 3-4b shows optical microscopy of its cross section (transverse to laser path). Figure 3-4c illustrates a typical surface profile of A11 examined with the stylus profilometer. The two dash lines shown in Figure 3-4a, and arrows in Figure 3-4b, demonstrate two typical peaks in A11. Their distances can reach 1mm, i.e., twenty times greater than the hatch spacing of 50 μm for A11. The wavy

surfaces of some samples such as A11 is a result of high energy density (180 J/mm³, Table 3-2). Dai et al [29] reported that when the energy density is relatively high, a combination of a serious fluctuation of melt pool and the material piles up occurs on the top surface. According to the research conducted by Krakhmaleva et al [30]; lowering scan speed (and consequently excessive energy density) causes metal vaporization due to over-heating. This vaporization which is due to selection of improper process parameters can disturb the melt pool.

The roughness of the samples with wavy top surfaces is named meso-roughness while the non-wavy surface is termed micro-roughness. To categorise the samples with the meso-rough and micro-rough surfaces, the distance between the consecutive peaks (wavelength) was firstly measured. If the distance was greater than the hatch spacing, it proved that a few laser tracks were joined together to make a wave. A typical peak to peak distance of 373 μm observed in sample C12 in Figure 3-5, reveals that nearly five laser tracks (with hatch spacing 75 μm) were merged together to make two peaks and a valley between each peak. So, C12 is categorised as a sample with meso-rough surface. The samples with meso-roughness are not included in the optimisation procedures. This is due to the uncertainty in measuring the roughness for wavy surface profile as it comprises two distinct surface topographies, one for the wavy character and the other is the true dimension of the surface asperities classified as roughness.

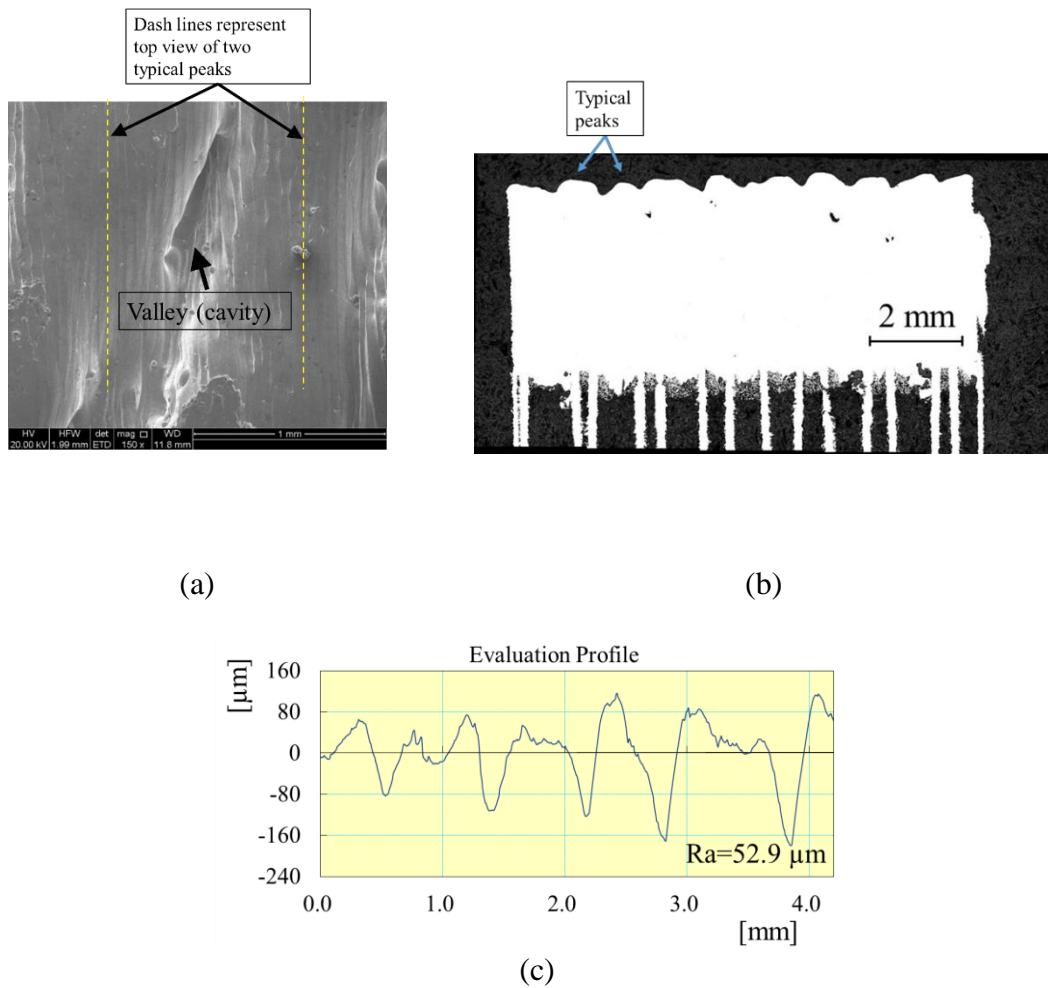


Figure 3-4: a) SEM micrograph of top surface b) optical microscopy of sectioned and c) surface profile of sample A11 ($P=270 \text{ W}$, $h=50 \mu\text{m}$, $v=1000 \text{ mm/s}$, $\text{VED}=180 \text{ J/mm}^3$).

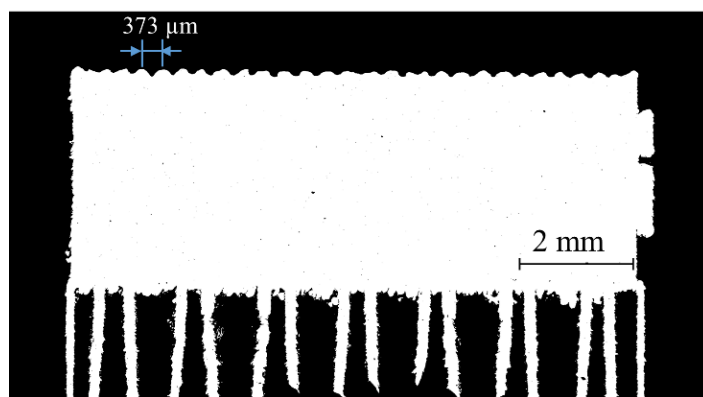


Figure 3-5: Waves observed on top surface of C12 ($P=90 \text{ W}$, $h=75 \mu\text{m}$, $v=333 \text{ mm/s}$, $\text{VED}=120 \text{ J/mm}^3$).

In non-wavy (micro-rough) surfaces, the long distance from peak-to-peak is absent. It should be noted that the periodic pattern of the surface profile in some samples (with non-wavy surfaces) like A10, Figure 3-6c, should not be confused with the wavy surface profile. The peak-to-peak distance in A10 is nearly the same as hatch spacing. This periodic pattern is related to the individual tracks (as seen from Figure 3-6a) and is generally found in samples fabricated with hatch spacing $h \geq 100 \mu\text{m}$. In some cases, like A10, the individual tracks are nearly separated from each other due to an inter-track lack of fusion, leading to the formation of elongated pores, Figure 3-6b.

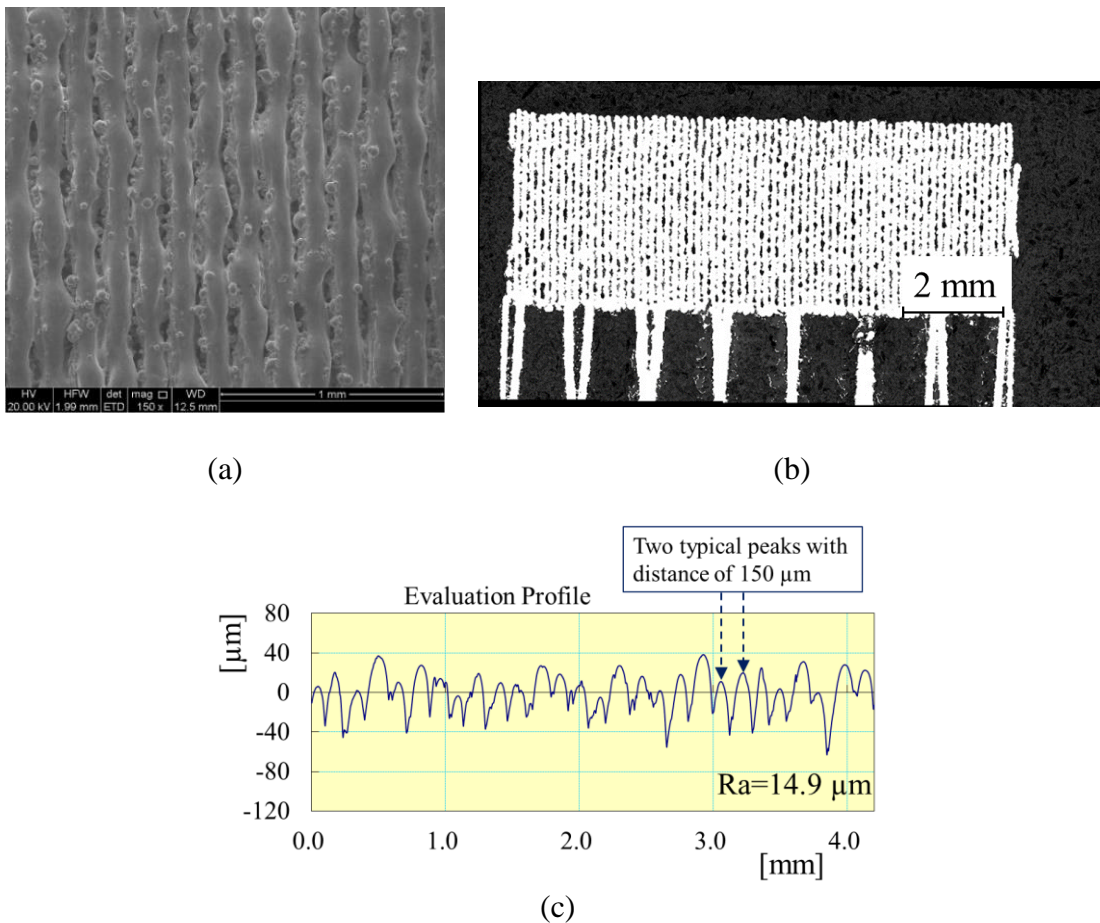


Figure 3-6: a) SEM micrograph of top surface, b) optical microscopy of transverse section and c) surface profile of sample A10 ($P=270 \text{ W}$, $h=150 \mu\text{m}$, $v=1800 \text{ mm/s}$, $\text{VED}=33 \text{ J/mm}^3$).

As seen from Table 3-3, in groups A and B, the wavy surface (meso-roughness) was observed only in the samples with hatch spacing at 50 μm (A6, B6, A11 and B11) where $\text{VED} \geq 100 \text{ J/mm}^3$ (see Table 3-2 for VED). In hatch spacing at 50 μm , the laser beam overlaps with the previous track and, as it starts melting the powder particles, it re-melts a portion of the previous track. However, when $\text{VED} < 100 \text{ J/mm}^3$, meso-roughness (wavy surface profile) does not occur in samples fabricated with hatch space 50 μm , such as A1 and B1. This reveals that the effect of an individual process parameter on the quality of sample is in correlation with the other parameters or their combination.

In group C, the meso-roughness was observed not only in the samples with series numbers 6 and 11 (as observed in groups A and B), but also in C7, C12 and C13, which is attributed to the low laser power in the C group. This will be explained in section 3.3.3.1 when the effect of laser power is discussed.

Table 3-3: Roughness average R_a of all cuboids of groups A, B and C.

Sample	R_a , (μm)	Meso-roughness, (Y)	Sample	R_a , (μm)	Meso-roughness, (Y)	Sample	R_a , (μm)	Meso-roughness, (Y)
A1	9.0		B1	8.3		C1	13.3	
A2	11.8		B2	11.6		C2	12.6	
A3	12.7		B3	11.8		C3	12.6	
A4	15.8		B4	14.3		C4	16.0	
A5	19.9		B5	19.0		C5	20.6	
A6	11.5	Y	B6	18.0	Y	C6	21.0	Y
A7	8.7		B7	4.9		C7	12.4	Y
A8	11.7		B8	7.0		C8	12.2	
A9	12.6		B9	11.0		C9	11.4	
A10	16.3		B10	17.8		C10	16.4	
A11	52.9	Y	B11	11.1	Y	C11	29.8	Y
A12			B12	4.3		C12	28.1	Y
A13	3.6		B13	4.1		C13	17.7	Y
A14	5.5		B14	5.2		C14	11.2	
A15	6.4		B15	6.3		C15	15.4	

Figure 3-7 shows the surface topography and profile of A13, the smoothest surface achieved in this study, with minimal spattered particles on the top surface. Figure 3-8a demonstrates open pores and lumps of semi sintered or partially melted particles on the top surface of C2. Figure 3-8c exhibits the surface profile of C2 with irregularities that are related to the surface features observed in Figure 3-8a. These irregularities are seen in the cross section of sample C2 in Figure 3-8b.

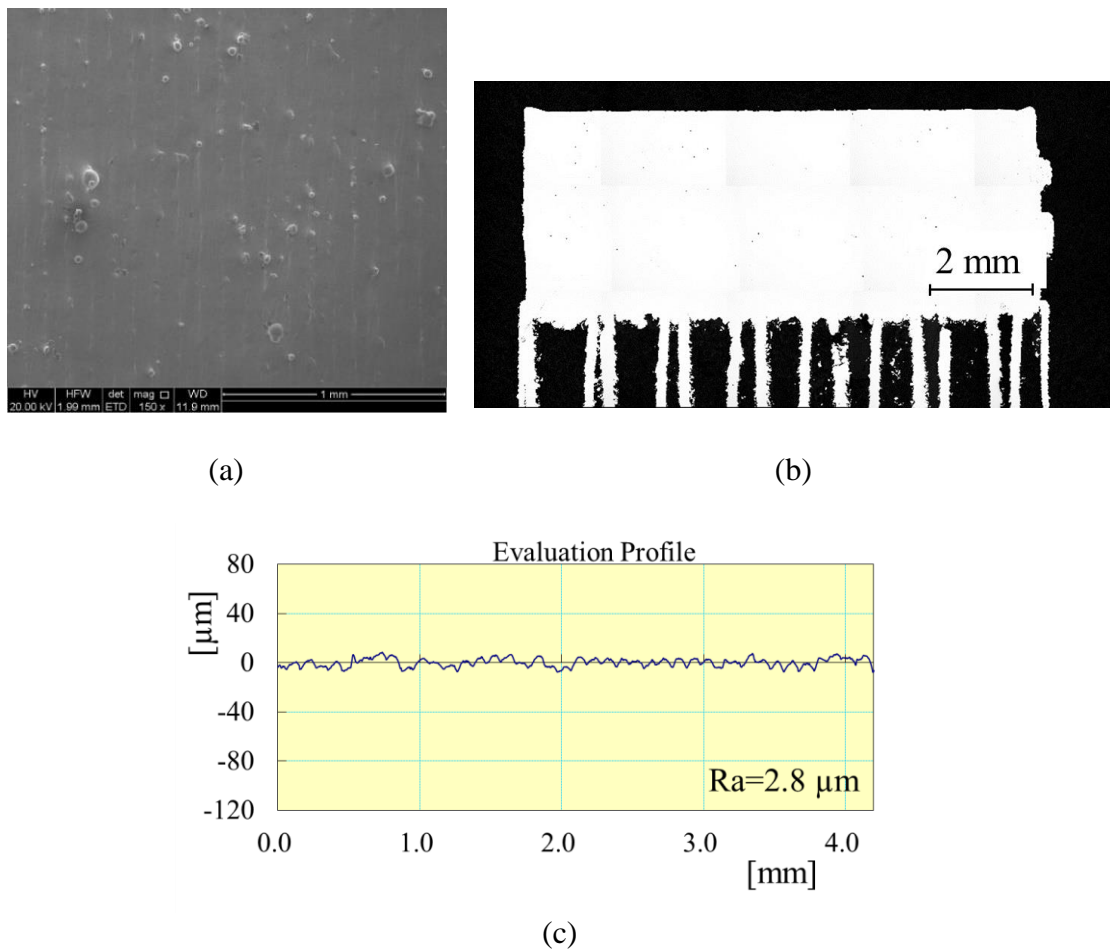


Figure 3-7: a) SEM micrograph of top surface, b) optical microscopy of transverse section and c) surface profile of sample A13 ($P=270$ W, $h=100$ μm, $v=1000$ mm/s, $VED=90$ J/mm³).

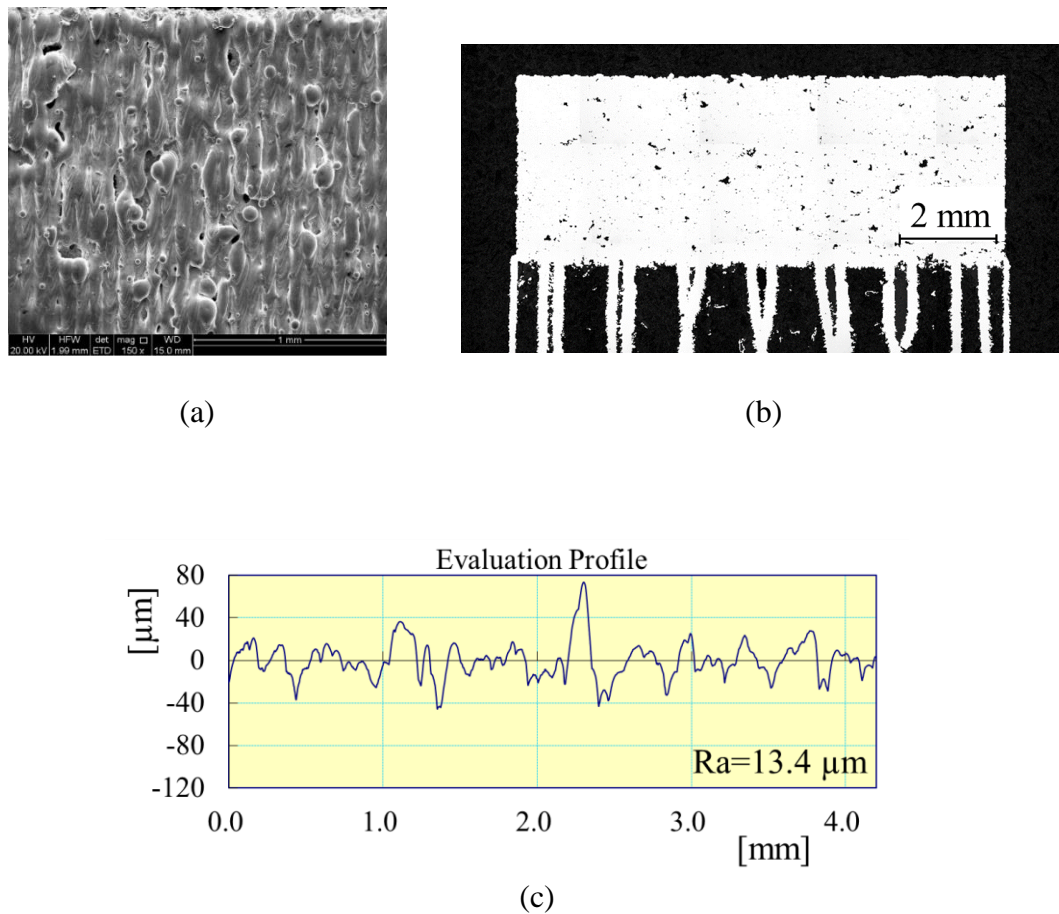


Figure 3-8: a) SEM micrograph of top surface, b) optical microscopy of transverse section and c) surface profile of sample C2 ($P=90$ W, $h=75$ μm , $v=833$ mm/s, $\text{VED}=48$ J/mm^3).

The R_a values for meso-rough samples are not the determining criteria for comparison of the surface quality of the samples, because the R_a values in this study were not filtered from the R_a numbers specific to waviness. For that reason, in the first step of screening for surface quality, the samples with meso-roughness were separated from those with micro-roughness. The samples with meso-rough surfaces are not desired for the following reasons:

- Their surface requires greater machining to achieve dimensional accuracy and a smoother surface.

- They generally require higher energy density, i.e., $VED > 100 \text{ J/mm}^3$ to be fabricated, which is not preferable as explained next.
- Although their overall internal porosities may be low, some large pores, as big as $250 \mu\text{m}$, can be observed, as shown with an arrow in Figure 3-9. These large pores are the outcome of high energy density and heat accumulation, which may cause metal evaporation and formation of keyhole [30-32]. Also, large pores can be the result of excessive shrinkage as an outcome of high energy density [4].

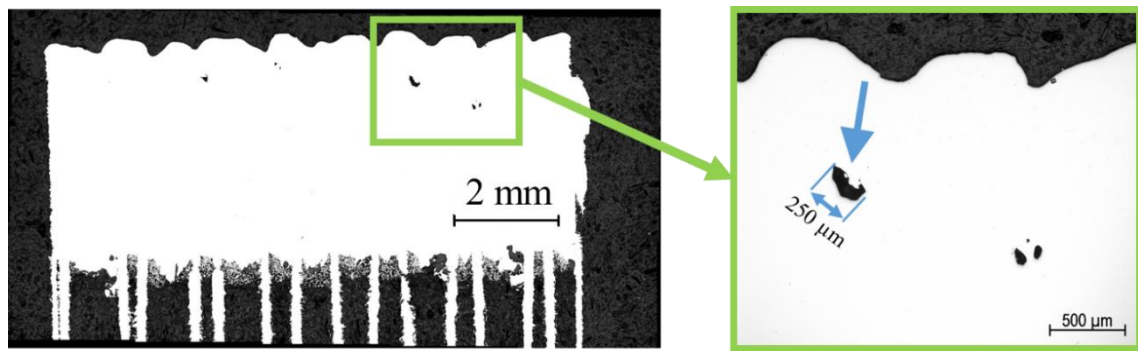


Figure 3-9: Sample A11 with keyhole pores near its surface.

After initial characterisation of the surfaces and discarding of samples with wavy surfaces, the effects of each process parameters on R_a (the micro-roughness of non-wavy surfaces) were investigated to discover the best procedure for optimising the process parameters.

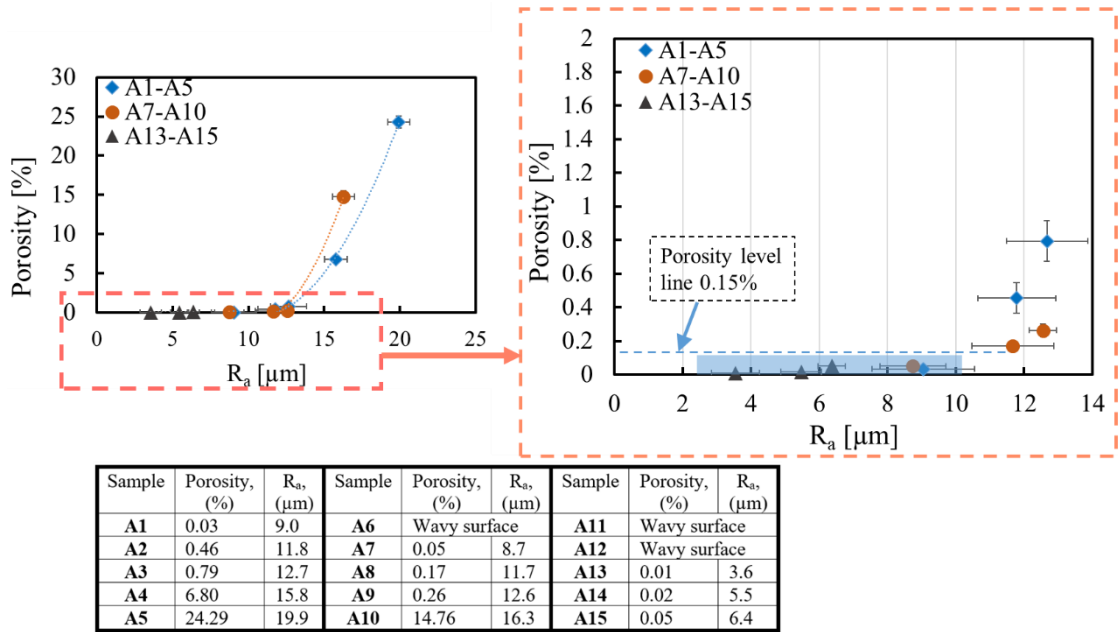
3.3.2 Correlation between surface roughness and porosity

Porosity is the second parameter as a quality target after surface roughness, which should be as low as practically achievable. After measuring the porosity level of each sample and comparing it with their corresponding micro-roughness, a non-linear correlation between porosity and micro-roughness of the sample was observed, Figure 3-10. As shown,

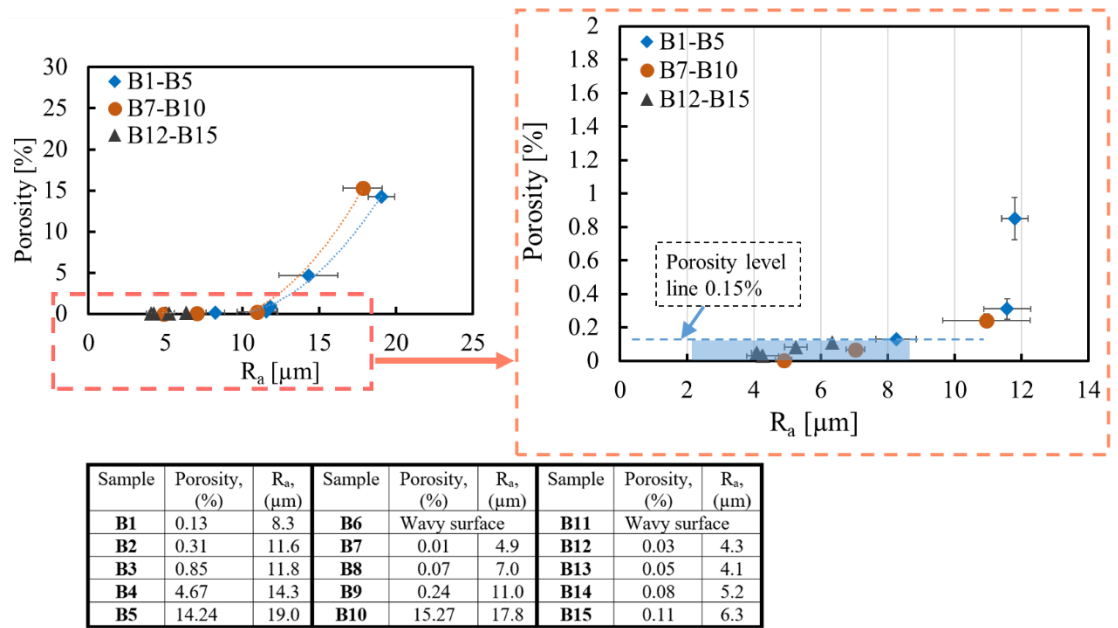
porosity increases with increasing micro-roughness in an exponential way. The magnified graphs in Figure 3-10 reveals that the samples with $R_a < 13 \mu\text{m}$ have a level of porosity less than 1% in groups A and B, and 2% in group C. The porosity level of all parts dramatically increases to nearly 25% when R_a rises to maximum of $20 \mu\text{m}$.

The magnified graph in Figure 3-10c shows that the lowest micro-roughness (R_a) and minimum achievable porosity in group C belongs to sample C14 with $R_a = 11.2 \mu\text{m}$ and porosity level of 0.53%. However, the shaded areas in magnified graphs in Figure 3-10a and 3-10b reveal that the micro-roughness of some samples in groups A and B, can be less than $10 \mu\text{m}$ and their porosity can reach a minimum level of, or less than, 0.15%. So, $R_a \leq 10 \mu\text{m}$ should be a target for fabricating the samples in groups A and B for the lowest porosity.

This correlation between the roughness and porosity level of L-PBF parts is associated with the melting process of the new layer of powder on the rough surface. When the surface is rough, the powder particles of a new layer cannot completely fill in the gaps between the peaks of the surface asperities or penetrate inside the open pores on the surface. This problem can be exacerbated when the particles of $40 \mu\text{m}$ or beyond (refer to Figure 3-1) are located between two peaks, making bigger cavities. Once the new layered powder (with some previous solidified layers) are melted, the cavities (of non-filled gaps) underneath the top layer, are entrapped, leading to closed internal pores.



(a)



(b)

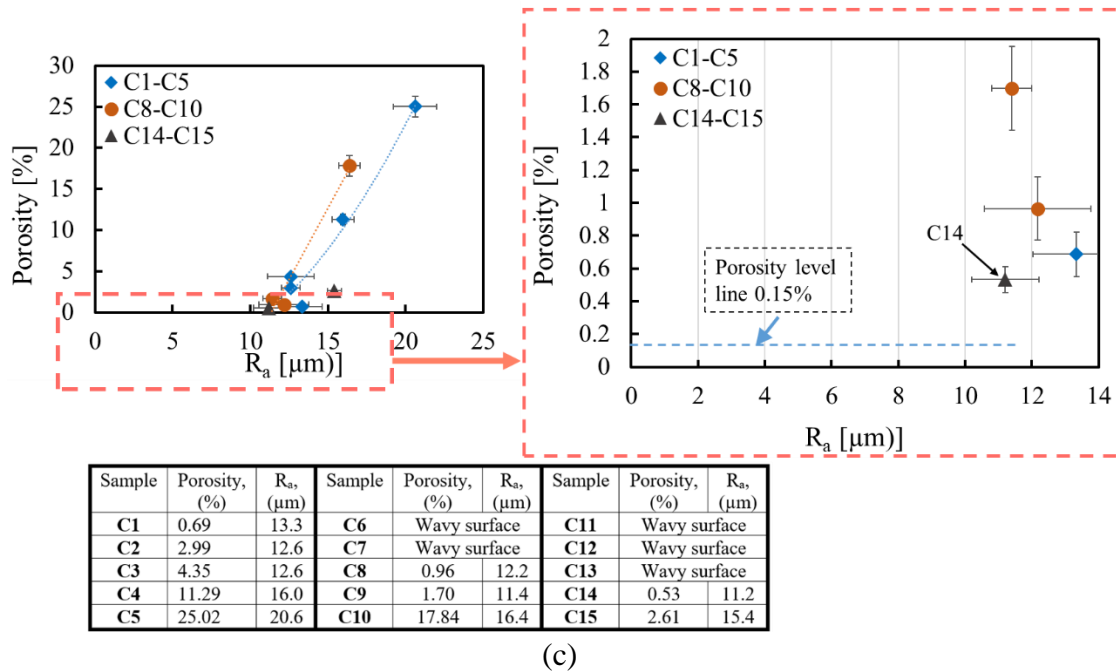


Figure 3-10: Porosity versus roughness in samples of a) group A, b) group B and c) group C. The right graphs are the magnified part of left graphs.

By discovering this correlation between the bulk porosity and micro-roughness, the procedure for measuring porosity can be eliminated in manufacturing or optimisation process since the surface quality could be used as a valid representation of the internal integrity of the L-PBF fabricated parts. Therefore, in the next sections, the effect of each process parameters on the surface morphology and micro-roughness is discussed to highlight the effect of process parameters on the quality of L-PBF parts.

3.3.3 Surface quality and process parameters

3.3.3.1 Laser power

Figure 3-11, demonstrates the micro-roughness of all samples in groups A, B, and C with respect to their series numbers, 1 to 15. The reason some data for some series numbers (like 6 and 11) are missing, is because of the meso-roughness of those series which are disregarded. As seen in Figure 3-11, the majority of the samples in group C, show poorer

micro-roughness than their A and B counter parts. A similar comparison between samples in groups A and B shows that the R_a values of most samples in the group B series ($P=180$ W) are lower than the roughness average of group A ($P=270$ W); however, there are some exceptions where group A samples have a smoother surface.

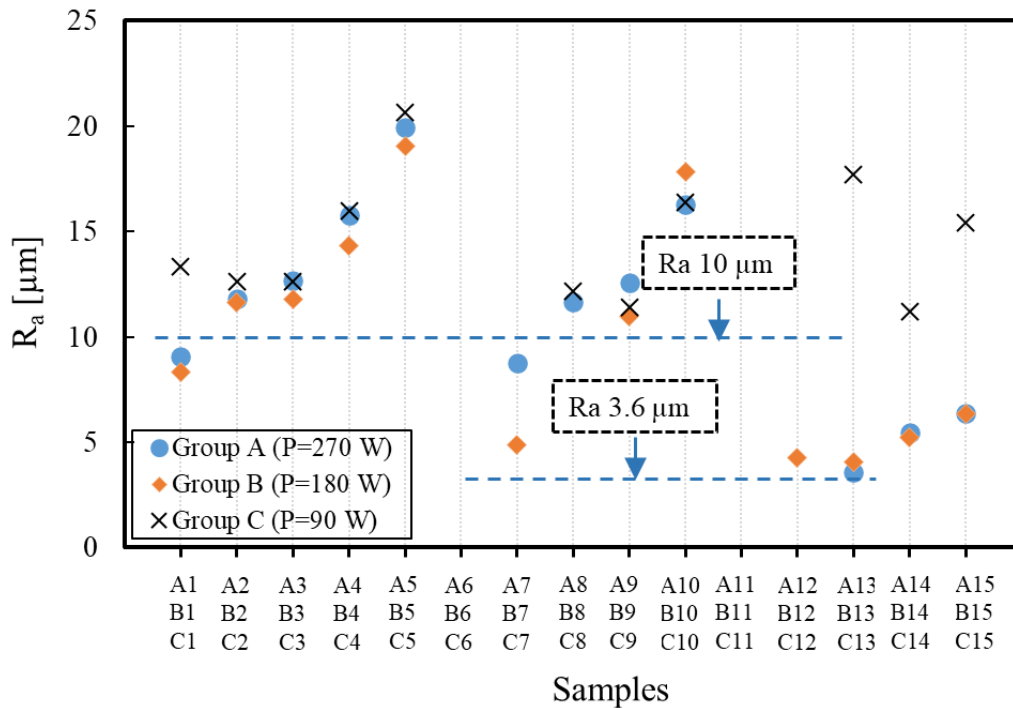


Figure 3-11: Graph of micro-roughness R_a of all samples.

This means that in a constant energy density trial (samples with the same series numbers), using a higher laser power favors a smoother surface finish. However, there are some thresholds for high laser power beyond which the surface roughness deteriorates. In this study, it was noticed that laser power 180 W and 270 W were competing in terms of fabrication of samples with smoother surfaces. So, laser power 270 W may be considered as the top threshold, going beyond which is not recommended. Laser power 90 W appears to be on or below the bottom threshold since the parts fabricated with 90 W exhibited

greater micro-roughness. They also showed higher porosity content, Figure 3-10c, to confirm the correlation between porosity and surface micro-roughness. In groups A and B, some samples can be found with $3.6 \mu\text{m} < R_a < 10 \mu\text{m}$, but in group C, the minimum micro-roughness R_a is $11.2 \mu\text{m}$.

This observation, for the bottom threshold of laser power at 90 W in group C, may be explained by the duration of time given to the system to absorb the energy density. The low scan speed for group C makes the delivery time for the same amount of energy level longer than those for groups A and B. This may result in some dissipation of heat rather than absorption of thermal energy for melting the powder particles and solidified layers. In other words, the melt pool in the samples with low laser power of 90 W can suffer from unbalanced viscosity and difference in surface tension. In such condition the molten material cannot spread properly and therefore, the solidified liquids with curvature form is produced as reported by [29]. This may explain the observation of more samples with wavy surface, when compared with groups A and B. For a very high laser power, like 270 W or higher, it seems the melt pool depth does not change significantly from increasing the laser power but the temperature of the melt pool increases [33, 34]. Keshavarzkermani et al [34] reported that when the laser power is doubled from 150 W to 300 W, the melt pool depth and width at constant LED increases around 25% and 4% respectively. After increasing the laser power at a constant energy density, the melt pool size does not change considerably, but its temperature raises, leading to overheating of the melt pool and the most volatile element, such as aluminium in Ti64, may evaporate [35] and cause turbulence in the melt pool, resulting in a rougher surface at higher laser power.

3.3.3.2 Scan speed

The SEM micrographs of the top surface of all samples exhibit a range of morphological features composed of solidified tracks joined laterally to form fused lines parallel to each

other. Figure 3-12 shows the typical SEM images of the surface morphology for C4, C9, and C14 ($P=90$ W, $h=125$ μm) samples fabricated with different scan speeds of 833 mm/s, 600 mm/s, and 333 mm/s respectively. The morphology of the individual tracks in each sample appears to have changed with the scan speed. As the scan speed decreases, the tracks become more uniform and continuous which is associated with the melt pool lifetime. The lower scan speed in sample C14, Figure 3-12c, increases the melt pool lifetime where the melt pool and its interface with solid powder can be carried forward without any breakage. In contrast with sample C14, where the liquid-powder interface continuously pushes forward, C4 with high scan speed is faced with intermittent melt pool solidification resulting in broken tracks. The necks evident in each track of sample C4 (some shown with arrows in Figure 3-12a) supports this hypothesis. Apart from necking, some large individual spherical beads, like the 112 μm one shown in Figure 3-12a, are built by joining partially melted particles. Before these large beads solidify, they are unable to wet the other particles to develop a bigger melt pool, hence, they instantly solidified into large beads.

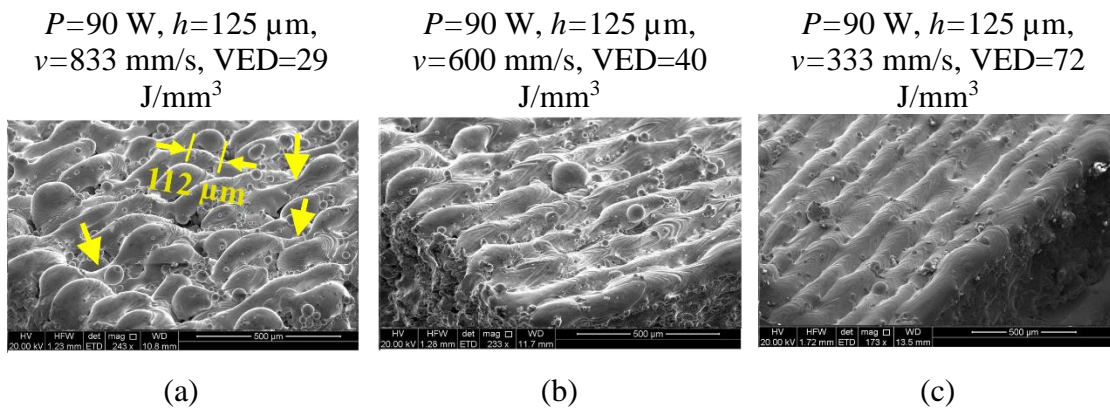


Figure 3-12: SEM images of the top surface of three samples of group C; a) C4, b) C9 and, c) C14.

In addition to the melt pool lifetime, it is postulated that the resulting morphology of the tracks is also due to the shape of the melt pool, which then correlates with the applied scan speed. As the scan speed decreases, the melt pool geometry is expected to change from a long tear shape to an oval, similar to that reported for welding [36], Figure 3-13. The only difference between L-PBF and welding is the melt pool lifetime of L-PBF fabricated parts, 1.47-2 ms, estimated by Yali Li et al [37], promoting the preservation of the melt pool geometry at a time.

Another reason that can explain the surface morphology of parts at very high scan speed, is based on Plateau-Rayleigh conditions in which, the melt pool becomes unstable; breaking and forming beads attributed to the surface energy of the melt pool streak [38].

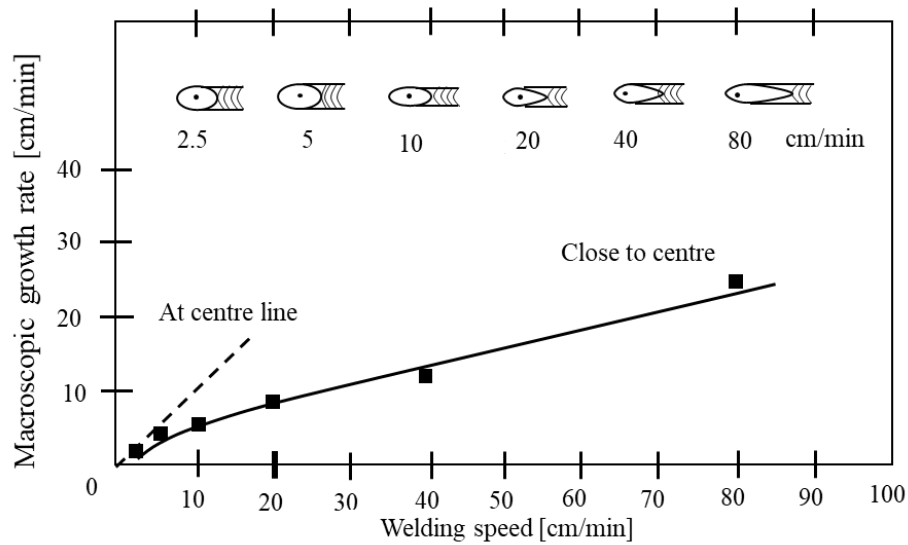


Figure 3-13: Effect of welding speed on the geometry of weld pool due to growth rate, adapted from N. Suutala, [36].

Figure 3-14 shows the SEM images of A3, A8 and A13, which were fabricated under the same laser power and hatch spacing ($P=270$ W, $h=100$ μm), but different scan speeds. When the laser scan speed decreases, the dwell time of laser beam and the lifetime of the melt pool increases, Therefore the melt can wet the powder substrate and spread beyond the laser spot size to overlap with the adjacent track.

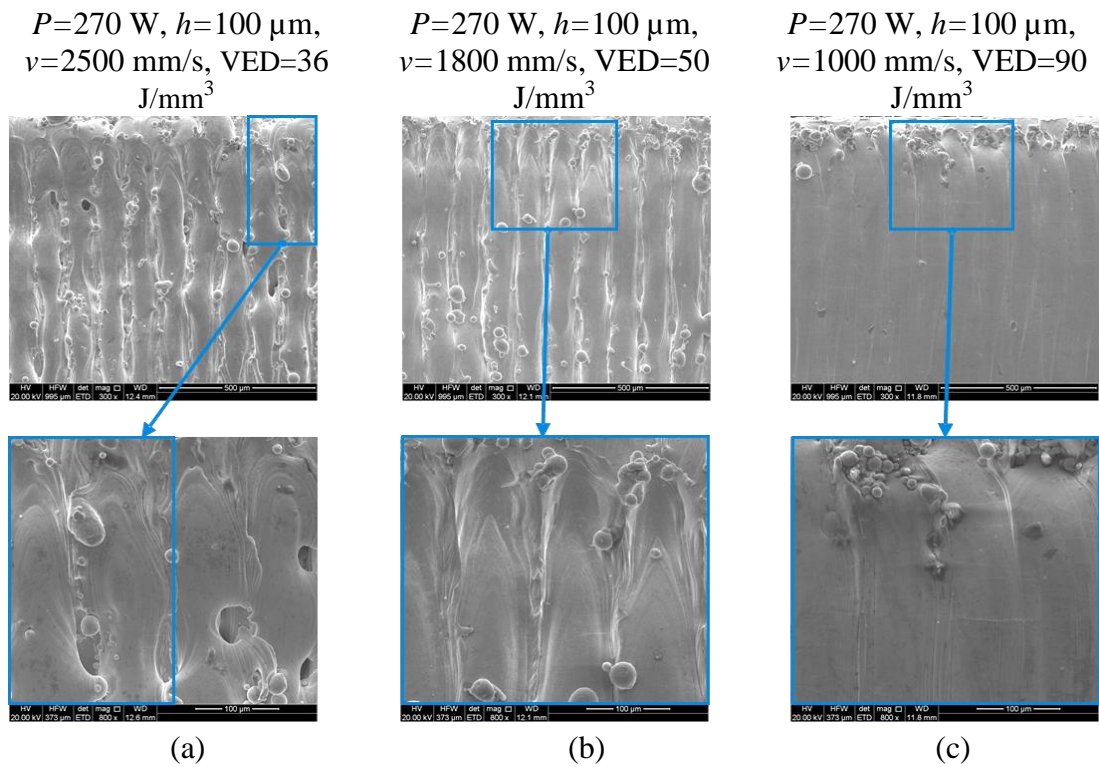
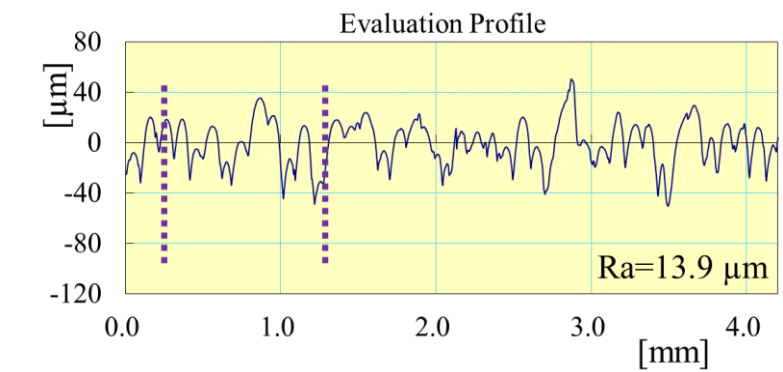


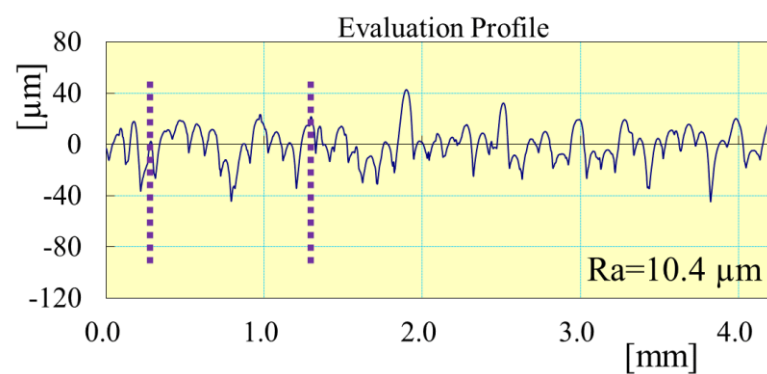
Figure 3-14: Top surface morphology of three samples of group A; a) A3, b) A8 and, c) A13.

The surface profiles shown in Figure 3-15 correspond to the same SEM images as samples A3, A8 and A13, illustrated in Figure 3-14. As seen from Figure 3-15, the average micro-roughness R_a decreases with decreasing scan speed, indicating the formation of a smoother surface, as qualitatively shown by the SEM micrographs in Figure 3-14.

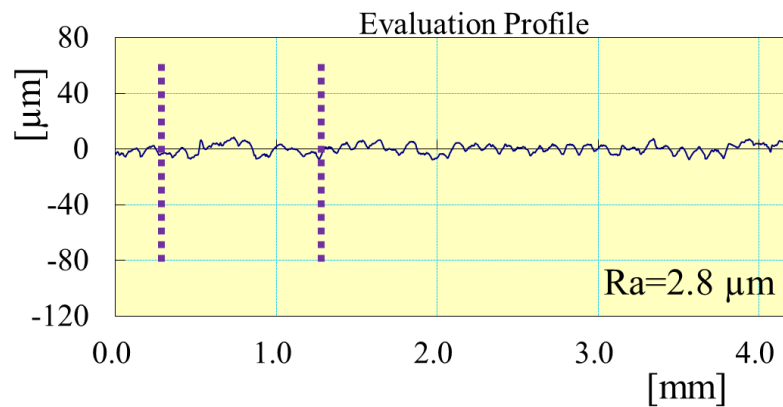
Each peak in the surface profiles shown in Figure 3-15a to 3-15c, represents a laser track. In any span of 1mm of the profile, like the dash lines shown in Figure 3-15, almost ten peaks can be counted, confirming the hatch spacing $100 \mu\text{m}$ in these series of the samples. By decreasing the scan speed from sample A3 to A13, the number of peaks does not change; however, the heights of the peaks to the valleys drop, resulting in smoother surfaces with lower R_a .



(a)



(b)



(c)

Figure 3-15: Typical surface profiles of samples; a) A3 ($P=270$ W, $h=100$ μm , $v=2500$ mm/s, $\text{VED}=36$ J/mm³), b) A8 ($P=270$ W, $h=100$ μm , $v=1800$ mm/s, $\text{VED}=50$ J/mm³) and c) A13 ($P=270$ W, $h=100$ μm , $v=1000$ mm/s, $\text{VED}=90$ J/mm³). (The distance between the dash lines represents a span of 1mm on the surface).

The graphs in Figure 3-16, which illustrate the effect of scan speed on the surface micro-roughness R_a for all samples in three groups of A, B and C, confirm that a lower scan speed renders a smoother surface. It should be noted that the samples with meso-rough surfaces are not included in these graphs. Also, in each category of the samples shown in the legend of each graph in Figure 3-16, higher sample series number like A15 has lower scan speed compared to those samples which have lower series number, like A5.

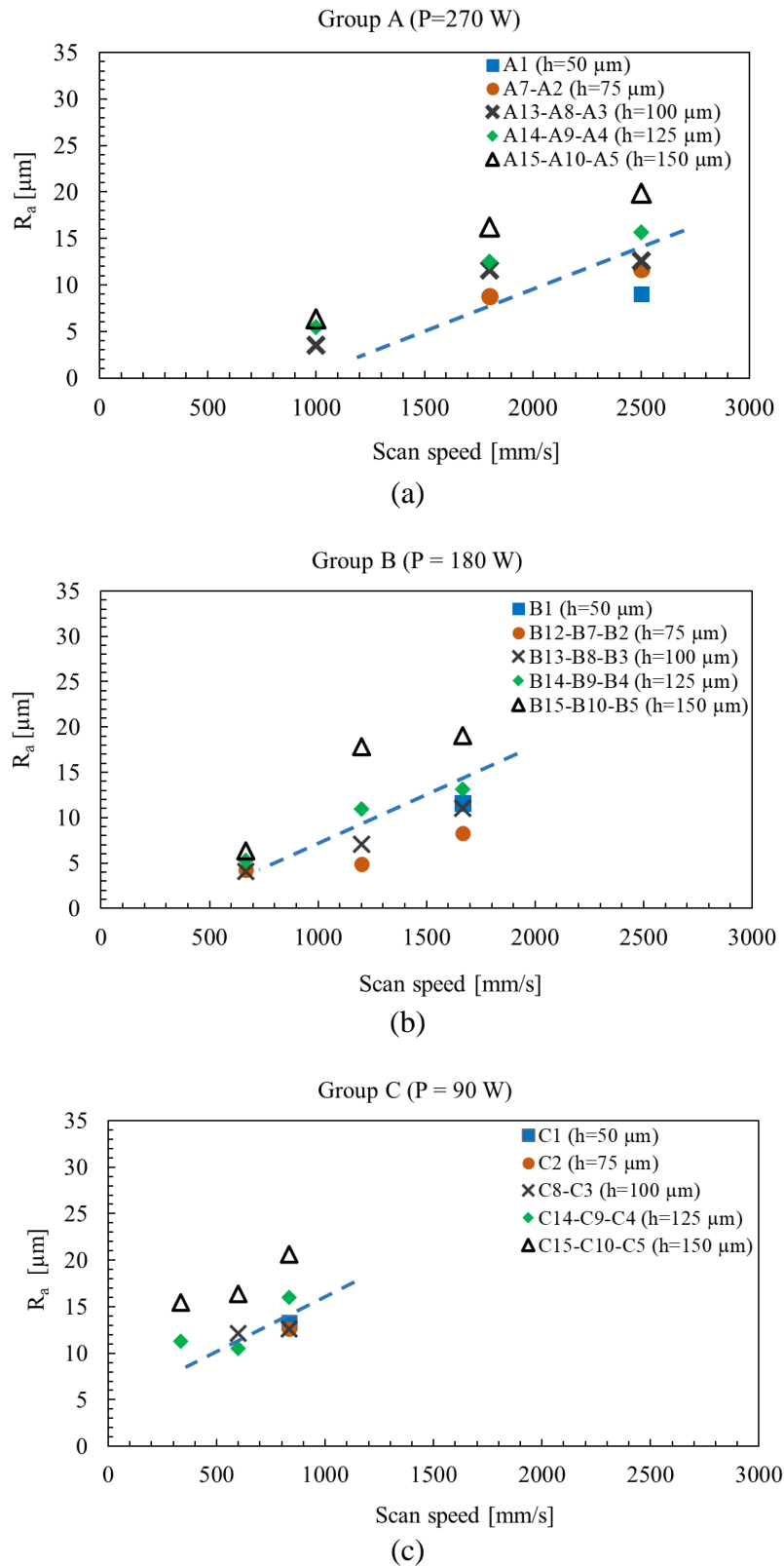


Figure 3-16: Graphs of R_a vs. laser scan speed of, a) group A, b) group B and c) group C (Higher series number of the samples in the legend of the graphs are corresponding to lower scan speed).

3.3.3.3 Hatch spacing

Figure 3-17 shows the graphs of micro-roughness of each subgroup of the three groups against hatch spacing. In each subgroup of the samples in all graphs of Figure 3-17, higher number in samples series are related to higher hatch spacing. As can be seen from all the graphs in Figure 3-17, for each subgroup there is a hatch spacing, called optimum hatch spacing, where the roughness has the lowest value. In most cases, the optimum hatch spacing is equal to or beyond $75\ \mu\text{m}$ which is close to the laser beam spot size, $70\ \mu\text{m}$. The deterioration of surface quality for hatch spacing below the employed laser spot size is associated with laser beam overlap, which has already been discussed in section 3.3.1. By increasing the hatch spacing beyond the optimum, the micro-roughness R_a increases since the inter-track gaps start appearing due to lack of fusion between each track.

Figure 3-17 also shows that for a constant R_a value, the value of optimum hatch spacing increases with decreasing scan speed. In other words, to achieve the same R_a value when decreasing the scan speed, a higher hatch spacing is needed. Also, Figure 3-17 reveals that for fixed hatch spacing, the R_a decreases with scan speed, which was already discussed in the previous section. When the scan speed lowers from one subgroup to another, the minimum hatch spacing in which the tracks bond together, shifts to a higher value due to the higher dwelling times of the laser and consequently widening of the laser track and melt pool. Thus, there is an interdependency between the hatch spacing and the scan speed.

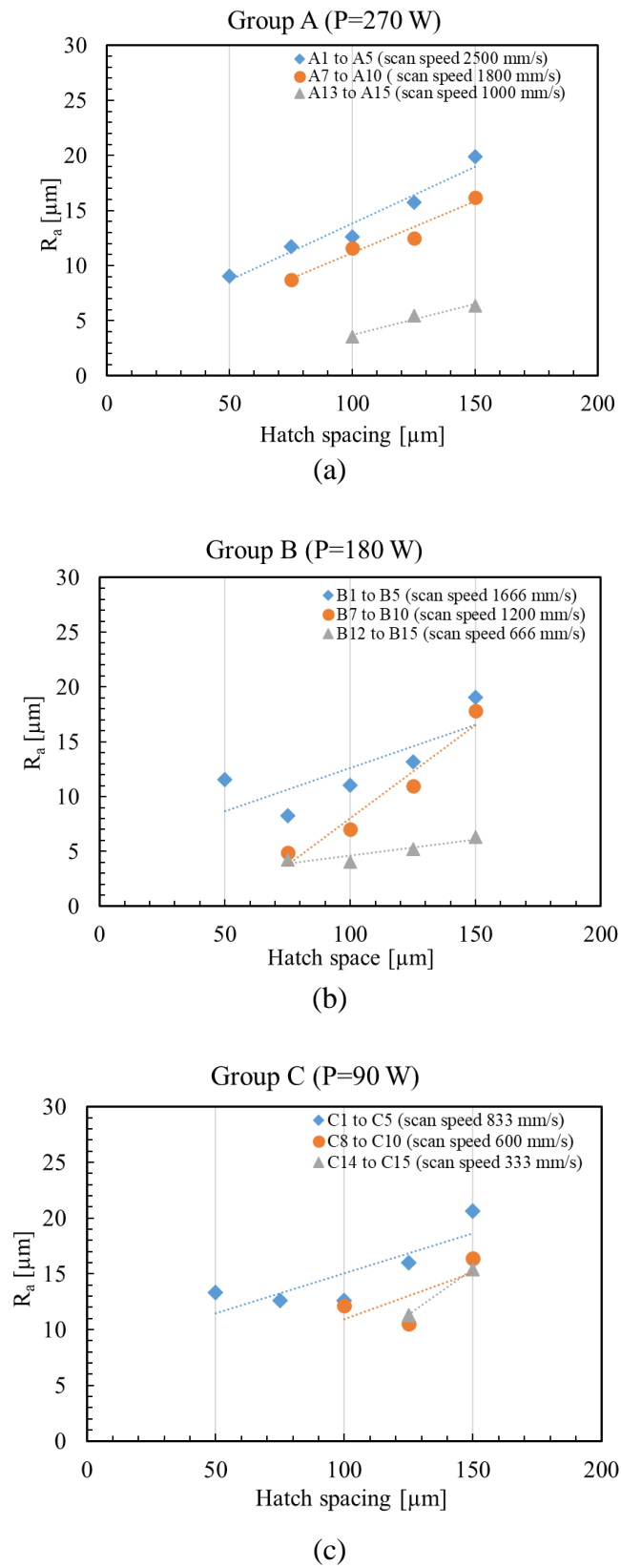


Figure 3-17: Graphs of R_a vs hatch spacing of a) group “A” b) group “B” and c) group “C” (In each subgroup, higher series numbers of the sample are related to higher hatch spacing).

By lowering the scan speed from one subgroup to the other, the corresponding R_a of the optimum hatch spacing generally decreases. In Figure 3-17a, the optimum hatch spacing of subgroup A7 to A10 is 75 μm (with corresponding roughness $R_a=8.7 \mu\text{m}$); however, by lowering the scan speed and moving to the next subgroup, A13 to A15, the optimum hatch spacing shifts to 100 μm with corresponding $R_a=3.5 \mu\text{m}$. This effect whereby the lowered scan speed lowers the R_a , is owing to the increased energy density, which will be discussed in the next section, 3.3.3.4.

3.3.3.4 Volumetric Energy Density, VED

This section presents the main focus of this study, where the soundness of VED as a combined process parameter is investigated. The graph of micro-roughness R_a versus VED, Figure 3-18, reveals that the roughness of the samples in group C is generally higher than that of the A and B groups' samples. This has already been observed in previous graphs, like Figure 3-10 and Figure 3-11, and was attributed to the low laser power 90W, which was explained earlier in section 3.3.3.1. Almost all samples in groups A and B fabricated with $\text{VED} > 50 \text{ J/mm}^3$ have a roughness average of $R_a < 10 \mu\text{m}$, which was determined as a target to fabricate samples with a minimum porosity of 0.15%.

Sample B12 (with VED of 120 J/mm^3) with R_a of 4.3 μm can be seen in enlarged graph (on the right-hand side) of Figure 3-18. But as no samples of group A with VED beyond 100 J/mm^3 appeared in enlarged graph of Figure 3-18, the optimum range of energy density can be determined as $50 \text{ J/mm}^3 < \text{VED} < 100 \text{ J/mm}^3$.

It should be noted that the VED parameter alone does not suffice for optimisation of the L-PBF process, and the individual parameters must fall in acceptable ranges. The samples in group C are a good example, where the low laser power does not satisfy the requirements of their roughness or porosity criteria.

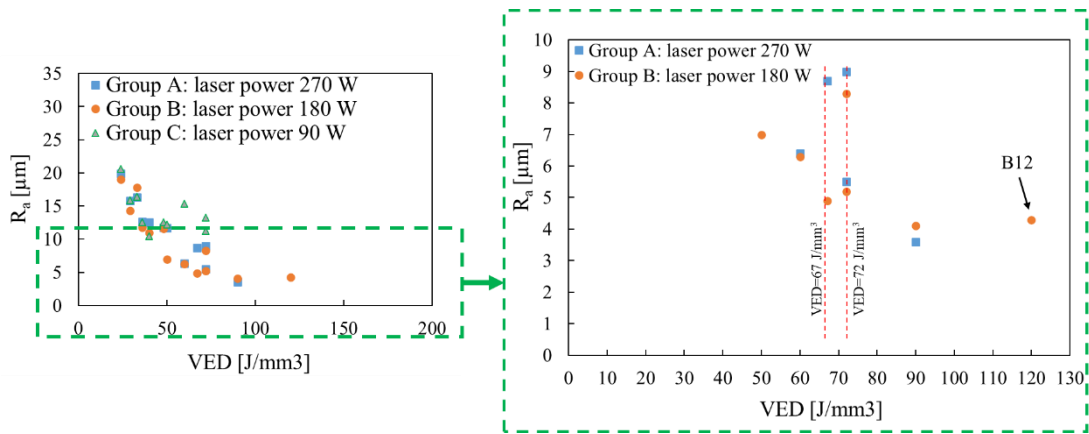


Figure 3-18: Micro-roughness R_a versus VED. (The graph on the right is the enlarged part of the left graph.)

Table 3-4 summarises all values of R_a and their corresponding porosity level for the samples in groups A and B fabricated within $50 \text{ J/mm}^3 < \text{VED} < 100 \text{ J/mm}^3$. These samples satisfy all defined targets of porosity less than 0.15%. The samples in group C are disregarded because they could not meet the defined quality of surface and porosity.

Table 3-4: All samples in group A and B with micro-roughness $R_a < 10 \mu\text{m}$.

Sample series number	VED, (J/mm^3)	Group A (P=270 W)		Group B (P=180 W)	
		R_a , (μm)	Porosity, (%)	R_a , (μm)	Porosity, (%)
15	60	6.4	0.05	6.3	0.11
7	67	8.7	0.05	4.9	0.01
1	72	9	0.03	8.3	0.13
14	72	5.5	0.02	5.2	0.08
13	90	3.6	0.01	4.1	0.05

3.3.4 Production rate and Volumetric Energy Density

Apart from surface roughness and porosity, production rate as the third target parameter should be considered when optimising the process parameters. The production rate of samples (for layers melting) can be calculated based on the equation below:

$$\text{Production rate (cm}^3\text{/hr)} = 3600 \times h \cdot v \cdot t / 10^9 \quad (4)$$

where h , is hatch spacing in μm , v is scan speed in mm/s , and t is layer thickness in μm . It should be noted that the time consumed for spreading the powder over previous layers and the travel time when laser beam is off, are not considered in equation (4). Laser power is not a parameter in equation (4), but it is clear that, when the laser power increases, to keep the VED constant, it is recommended to increase the scan speed to keep the melt pool lifetime constant. So, increasing laser power is indirectly in favour of production rate.

Figure 3-19 illustrates the correlation between the production rate and VED at different laser powers: 270 W, 180 W and 90 W. Samples in group C could not be included in the graph as an optimum process parameter. Although the required energy for fabricating the samples with the same VED is constant, their production rate is different owing to different scan speeds. So, samples in group A are preferred over their group B counterparts due to the higher production rate. The shaded area in Figure 3-19 covers all samples shown in Table 3-4.

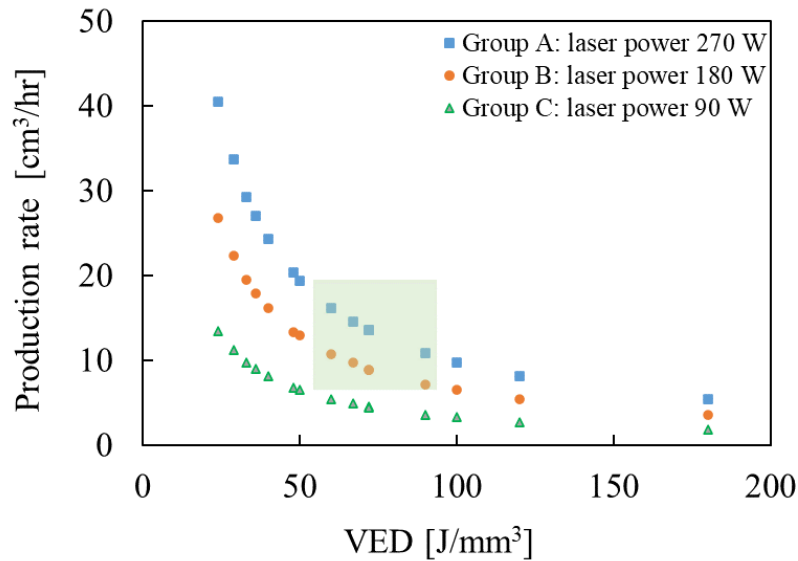


Figure 3-19: Graph of production rate versus VED of all samples fabricated with laser power 270 W, 180 W.

Based on the micro-roughness and porosity of A13, the process parameters of A13 can be chosen as the optimum parameters but it is obvious that A15, with its higher production rate, can satisfy all the outcome parameters of roughness, its correlated porosity, and production rate.

3.4 Conclusions

The results presented are based on the material, fabrication equipment and experimental conditions implemented in this research work. The outcome and values stated below may be a guideline for other researchers using different powder distribution, machines, or process parameters. In this study the feasibility of employing VED as a merit tool for quality assessment of printed parts was explored with its limitations. Besides, it is reported that the individual parameters comprising VED must fall in a pre-determined ranges. Surface roughness, porosity and production rate of the parts are the outcome parameters for assessment of the quality.

It was confirmed that by categorising the surface morphology of the samples into wavy (with meso-roughness) and non-wavy patterns (with micro-roughness), a reasonable correlation between micro-roughness and porosity could be established. The parts with smoother surfaces and low micro-roughness fall at the lower level of porosity. In the samples fabricated with laser power 270 W and 180 W (groups A and B), when the micro-roughness $R_a \leq 10 \mu\text{m}$, the expected porosity should be $\leq 0.15\%$. The minimum achievable micro-roughness and porosity in the samples fabricated with laser power 90 W (group C), was $11.2 \mu\text{m}$ and 0.53% respectively.

The correlation between the individual process parameters and micro-roughness R_a is held as below:

- By lowering the laser scan speed in each subgroup of samples, the average micro-roughness R_a reduces.
- There is an optimum hatch spacing in each subgroup of samples where the R_a is minimum. In most cases, the optimum hatch spacing is beyond the laser spot size of $70 \mu\text{m}$. For initial optimisation, it is recommended that the hatch spacing should not be below the laser spot size, which results in an overlap between the laser beam and the previously solidified track. Hatch spacing below the optimum value causes a wavy surface, which is not desirable.
- Higher laser power induces a smoother surface, but it cannot be beyond or below some limits, as it causes surface deterioration. Laser power 270 W was found to be the top threshold. The laser power 90 W was not preferable, as the minimum achievable micro-roughness was $R_a > 10 \mu\text{m}$, with minimum porosity beyond 0.5% .

In this study, it has been demonstrated when a laser power of 180 W or 270 W is chosen, with hatch spacing beyond the beam spot size $70 \mu\text{m}$ and energy density range of 50

$J/mm^3 < VED < 100 J/mm^3$, the Ti6Al4V parts with $R_a \leq 10 \mu m$ and porosity less than 0.15% can be fabricated via the L-PBF process.

3.5 Acknowledgements

This work was undertaken in part at the OptoFab node of the Australian National Fabrication Facility (ANFF), utilising Commonwealth and South Australian State Government funding. Adelaide Microscopy is gratefully acknowledged for the access provided to its electron microscopy facilities. Thanks to PhD student, John Daniel Arputharaj for some supplementary experiments he performed to support this article. A. Dareh Baghi is grateful to the Australian Government and Adelaide University for his Ph.D. scholarship.

References:

1. Banerjee, D. and J.C. Williams, *Perspectives on Titanium Science and Technology*. Acta Materialia, 2013. **61**(3): p. 844-879.
2. Murr, L., S. Quinones, S. Gaytan, M. Lopez, A. Rodela, E. Martinez, D. Hernandez, E. Martinez, F. Medina, and R. Wicker, *Microstructure and mechanical behavior of Ti-6Al-4V produced by rapid-layer manufacturing, for biomedical applications*. Journal of the mechanical behavior of biomedical materials, 2009. **2**(1): p. 20-32.
3. Enneti, R.K., R. Morgan, and S.V. Atre, *Effect of process parameters on the Selective Laser Melting (SLM) of tungsten*. International Journal of Refractory Metals and Hard Materials, 2018. **71**: p. 315-319.
4. Song, B., S. Dong, B. Zhang, H. Liao, and C. Coddet, *Effects of processing parameters on microstructure and mechanical property of selective laser melted Ti6Al4V*. Materials & Design, 2012. **35**: p. 120-125.
5. Kuai, Z., Z. Li, B. Liu, Y. Chen, S. Lu, X. Tang, and T. Liu, *Selective laser melting of CuCrZr alloy: processing optimisation, microstructure and mechanical properties*. Journal of Materials Research and Technology, 2022. **19**: p. 4915-4931.
6. Sun, Y.Y., S. Gulizia, C.H. Oh, D. Fraser, M. Leary, Y.F. Yang, and M. Qian, *The Influence of As-Built Surface Conditions on Mechanical Properties of Ti-6Al-4V Additively Manufactured by Selective Electron Beam Melting*. Jom, 2016. **68**(3): p. 791-798.
7. Dareh Baghi, A., S. Nafisi, R. Hashemi, H. Ebendorff-Heidepriem, and R. Ghomashchi, *Effective post processing of SLM fabricated Ti-6Al-4 V alloy*:

- Machining vs thermal treatment*. Journal of Manufacturing Processes, 2021. **68**: p. 1031-1046.
8. Kasperovich, G., J. Haubrich, J. Gussone, and G. Requena, *Correlation between porosity and processing parameters in TiAl6V4 produced by selective laser melting*. Materials & Design, 2016. **105**: p. 160-170.
 9. Han, J., J. Yang, H. Yu, J. Yin, M. Gao, Z. Wang, and X. Zeng, *Microstructure and mechanical property of selective laser melted Ti6Al4V dependence on laser energy density*. Rapid Prototyping Journal, 2017.
 10. Jiang, C.-P., A.T. Wibisono, S.-H. Wang, T. Pasang, and M. Ramezani, *Selective Laser Melting of Free-Assembled Stainless Steel 316L Hinges: Optimization of Volumetric Laser Energy Density and Joint Clearance*. Metals, 2022. **12**(7): p. 1223.
 11. Qiu, C., C. Panwisawas, M. Ward, H.C. Basoalto, J.W. Brooks, and M.M. Attallah, *On the role of melt flow into the surface structure and porosity development during selective laser melting*. Acta Materialia, 2015. **96**: p. 72-79.
 12. Yasa, E., J. Deckers, and J.-P. Kruth, *The investigation of the influence of laser re-melting on density, surface quality and microstructure of selective laser melting parts*. Rapid Prototyping Journal, 2011. **17**(5): p. 312-327.
 13. Carter, L.N., X. Wang, N. Read, R. Khan, M. Aristizabal, K. Essa, and M.M. Attallah, *Process optimisation of selective laser melting using energy density model for nickel based superalloys*. Materials Science and Technology, 2016. **32**(7): p. 657-661.
 14. Wang, L., Q.S. Wei, Y.S. Shi, J.H. Liu, and W.T. He. *Experimental Investigation into the Single-Track of Selective Laser Melting of IN625*. in *Advanced Materials Research*. 2011. Trans Tech Publ.
 15. Kumar, S. and A. Shahi, *Effect of heat input on the microstructure and mechanical properties of gas tungsten arc welded AISI 304 stainless steel joints*. Materials & Design, 2011. **32**(6): p. 3617-3623.
 16. Bertoli, U.S., A.J. Wolfer, M.J. Matthews, J.-P.R. Delplanque, and J.M. Schoenung, *On the limitations of volumetric energy density as a design parameter for selective laser melting*. Materials & Design, 2017. **113**: p. 331-340.
 17. Ciurana, J., L. Hernandez, and J. Delgado, *Energy density analysis on single tracks formed by selective laser melting with CoCrMo powder material*. The International Journal of Advanced Manufacturing Technology, 2013. **68**(5-8): p. 1103-1110.
 18. Prashanth, K., S. Scudino, T. Maity, J. Das, and J. Eckert, *Is the energy density a reliable parameter for materials synthesis by selective laser melting?* Materials Research Letters, 2017. **5**(6): p. 386-390.
 19. Koutiri, I., E. Pessard, P. Peyre, O. Amlou, and T. De Terris, *Influence of SLM process parameters on the surface finish, porosity rate and fatigue behavior of as-built Inconel 625 parts*. Journal of Materials Processing Technology, 2018. **255**: p. 536-546.
 20. Attar, H., M. Calin, L.C. Zhang, S. Scudino, and J. Eckert, *Manufacture by selective laser melting and mechanical behavior of commercially pure titanium*. Materials Science and Engineering A, 2014. **593**: p. 170-177.

21. Gong, H., K. Rafi, H. Gu, T. Starr, and B. Stucker, *Analysis of defect generation in Ti-6Al-4V parts made using powder bed fusion additive manufacturing processes*. Additive Manufacturing, 2014. **1-4**: p. 87-98.
22. Santos, L.V., V.J. Trava-Airoldi, E.J. Corat, J. Nogueira, and N.F. Leite, *DLC cold welding prevention films on a Ti6Al4V alloy for space applications*. Surface and Coatings Technology, 2006. **200**(8): p. 2587-2593.
23. Blakey-Milner, B., P. Gradl, G. Snedden, M. Brooks, J. Pitot, E. Lopez, M. Leary, F. Berto, and A. du Plessis, *Metal additive manufacturing in aerospace: A review*. Materials & Design, 2021. **209**: p. 110008.
24. Geetha, M., A.K. Singh, R. Asokamani, and A.K. Gogia, *Ti based biomaterials, the ultimate choice for orthopaedic implants – A review*. Progress in Materials Science, 2009. **54**(3): p. 397-425.
25. Vandenbroucke, B. and J.P. Kruth, *Selective laser melting of biocompatible metals for rapid manufacturing of medical parts*. Rapid Prototyping Journal, 2007. **13**(4): p. 196-203.
26. *ASTM F2924-14, Standard Specification for Additive Manufacturing Titanium-6 Aluminum-4 Vanadium with Powder Bed Fusion*. 2014.
27. *ASME B46.1-2019, Surface Texture (Surface Roughness, Waviness, and Lay)*. 2019, The American Society of Mechanical Engineers: USA.
28. Sahay, C. and S. Ghosh. *Understanding surface quality: beyond average roughness (Ra)*. in *2018 ASEE Annual Conference & Exposition*. 2018.
29. Dai, D. and D. Gu, *Tailoring surface quality through mass and momentum transfer modeling using a volume of fluid method in selective laser melting of TiC/AlSi10Mg powder*. International Journal of Machine Tools and Manufacture, 2015. **88**: p. 95-107.
30. Krakhmalev, P. and I. Yadroitsev, *Microstructure and properties of intermetallic composite coatings fabricated by selective laser melting of Ti-SiC powder mixtures*. Intermetallics, 2014. **46**: p. 147-155.
31. Attar, H., M. Bonisch, M. Calin, L.-C. Zhang, S. Scudino, and J. Eckert, *Selective laser melting of in situ titanium-titanium boride composites: Processing, microstructure and mechanical properties*. Acta Materialia, 2014. **76**: p. 13-22.
32. Khorasani, A.M., I. Gibson, A. Ghaderi, and M.I. Mohammed, *Investigation on the effect of heat treatment and process parameters on the tensile behaviour of SLM Ti-6Al-4V parts*. The International Journal of Advanced Manufacturing Technology, 2019. **101**(9): p. 3183-3197.
33. Pulugurtha, S.R., J. Newkirk, F. Liou, and H.-N. Chou. *Functionally graded materials by laser metal deposition*. in *2009 International Solid Freeform Fabrication Symposium*. 2009. University of Texas at Austin.
34. Keshavarzkermani, A., E. Marzbanrad, R. Esmaeilzadeh, Y. Mahmoodkhani, U. Ali, P.D. Enrique, N.Y. Zhou, A. Bonakdar, and E. Toyserkani, *An investigation into the effect of process parameters on melt pool geometry, cell spacing, and grain refinement during laser powder bed fusion*. Optics & Laser Technology, 2019. **116**: p. 83-91.

35. Mukherjee, T., J.S. Zuback, A. De, and T. DebRoy, *Printability of alloys for additive manufacturing*. Sci Rep, 2016. **6**: p. 19717.
36. Suutala, N., *Effect of solidification conditions on the solidification mode in austenitic stainless steels*. Metallurgical Transactions A, 1983. **14**(1): p. 191-197.
37. Li, Y. and D. Gu, *Thermal behavior during selective laser melting of commercially pure titanium powder: Numerical simulation and experimental study*. Additive Manufacturing, 2014. **1**: p. 99-109.
38. Yadroitsev, I., A. Gusarov, I. Yadroitsava, and I. Smurov, *Single track formation in selective laser melting of metal powders*. Journal of Materials Processing Technology, 2010. **210**(12): p. 1624-1631.

Chapter 4

Microstructural characteristics


Chapter overview

In this chapter the microstructural characteristics of two fabrication routes of laser powder bed fusion (LPBF) and powder metallurgy (PM) is compared. In this comparison, it is revealed that two phases of α (as a constituent of PM microstructure) and martensite α' (as a single phase in microstructure of LPBF parts) have nearly the same the nano-hardness but different micro-hardness. This difference between the micro-hardness and nano-hardness is attributed to the morphology and refinement of α' . This chapter is based on a published paper in the journal of “Metals”.

Statement of Authorship

Title of Paper	Microstructural development of Ti-6Al-4V alloy via Powder Metallurgy and Laser Powder Bed Fusion
Publication status	<input checked="" type="checkbox"/> Published <input type="checkbox"/> Accepted for Publication <input type="checkbox"/> Submitted for Publication <input type="checkbox"/> Unpublished and Unsubmitted work written in manuscript style
Publication Details	A. Dareh Baghi , S. Nafisi, H. Ebendorff-Heidepriem, and R. Ghomashchi, "Microstructural Development of Ti-6Al-4V Alloy via Powder Metallurgy and Laser Powder Bed Fusion", <i>Metals</i> , 2022. 12(9): p. 1462.


Principal Author


Name of Principal Author (Candidate)	Alireza Dareh Baghi		
Contribution to the Paper	Developed the ideas and concepts, designed 3D models of the samples, conducted the experiments, acquired the data, interpreted results and drafted the manuscript		
Overall percentage (%)	85%		
Certification:	This paper reports on original research I conducted during the period of my Higher Degree by Research candidature and is not subject to any obligations or contractual agreements with a third party that would constrain its inclusion in this thesis. I am the primary author of this paper.		
Signature		Date	23/09/2022


Co-Author Contributions

By signing the Statement of Authorship, each author certifies that:

- I. the candidate's stated contribution to the publication is accurate (as detailed above);
- II. permission is granted for the candidate to include the publication in the thesis; and
- III. the sum of all co-author contributions is equal to 100% less the candidate's stated contribution.

Name of Co-Author	Reza Ghomashchi		
Contribution to the Paper	Supervised the work, participated in developing ideas, evaluated, and edited the discussion and manuscript.		
Signature		Date	27/09/2022

Name of Co-Author	Shahrooz Nafisi		
Contribution to the Paper	Supervised the work and reviewed the manuscript.		
Signature		Date	28/10/2022

Name of Co-Author	Heike Ebendorff-Heidepriem		
Contribution to the Paper	Supervised the work and reviewed the manuscript.		
Signature		Date	27/09/2022

Microstructural development of Ti-6Al-4V alloy via Powder Metallurgy and Laser Powder Bed Fusion

Alireza Dareh Baghi, Shahrooz Nafisi, Heike Ebendorff-Heidepriem, Reza Ghomashchi

Abstract

A detailed study was carried out to gain a better understanding of the microstructural differences between Ti-6Al-4V parts fabricated via the conventional powder metallurgy (PM) and the laser powder bed fusion (L-PBF) 3D printing routes. The parts were compared in terms of the constituent phases in the microstructure and their effects on the micro- and nano-hardness. In L-PBF parts, the microstructure has a single phase of martensitic α' with hcp crystal structure and acicular laths morphology, transformed from prior parent phase β formed upon solidification of the melt pool. However, for the sintered parts via powder metallurgy, two phases of α and β are noticeable and the microstructure is composed of α grains and $\alpha + \beta$ Lamellae. The microhardness of L-PBF processed Ti-6Al-4V samples is remarkably higher than that of the PM samples but, surprisingly, the nano-hardness of the bulk martensitic phase α' (6.3 GPa) is almost the same as α (i.e., 6.2 GPa) in PM samples. This confirms the rapid cooling of the β phase does not have any effect on the hardening of the bulk martensitic hcp α' . The high microhardness of L-PBF parts is due to the fine lath morphology of α' , with a large concentration of low angle boundaries of α' . Furthermore, it is revealed that for the α phase in PM samples, a higher level of vanadium concentration lowers the nano-hardness of the α phase. In addition, as expected, the compacting pressure and sintering temperature during the PM process led to variations in the porosity level as well as the microstructural morphology of the fabricated specimens, which will in turn have a significant effect on the mechanical properties.

4.1 Introduction

Titanium and titanium-based alloys have emerged as appealing materials for numerous applications due to their adequate strength, high specific strength, excellent corrosion resistance, and exceptional biocompatibility [1, 2]; however, conventional manufacturing technologies often utilized for the fabrication of titanium based alloy products are generally high energy and materials intensive, and time consuming [3]. Therefore, emerging digitized and automated manufacturing techniques, known as additive manufacturing (AM), are receiving increased attention and starting to play a significant role in the manufacture of titanium parts.

The laser powder bed fusion (L-PBF) technique, also known as selective laser melting (SLM), for titanium alloys has attracted increasing global interest due to its distinctive characteristics and a range of notable advantages over conventional manufacturing techniques. During the L-PBF fabrication process, materials are added layer by layer rather than subtracted as is the case for conventional manufacturing. The layer-wise build technology provides a unique advantage in design freedom for complex geometry without the need for tooling. The other attraction of the L-PBF near-net-shape production route is the ability to simplify production feasibility for fabrication of low quantities of manufactured parts, even down to a batch size of one. The basic working principle and the mechanics of the L-PBF process are widely available in the open literature [4-8].

L-PBF is also capable of processing high melting temperature materials, such as ceramics, and it accurately produces complex features, which is impossible to achieve using conventional fabrication techniques [9-12]. The more traditional near-net-shape manufacturing route, powder metallurgy (PM), is comparable with L-PBF as both have their starting materials in the powder form, generate near-net shape outcome parts, have high material utilization rates, and create minimum waste [13]. In the L-PBF process, the

alloy powder is exposed to rapid melting and solidification, whereas, in the PM route, powder particles are sintered during or after compaction at moderate heating and cooling rates. Since the starting feedstock is the same and the level of net shaping and materials used are comparable for these two manufacturing routes, it is interesting to explore the differences in microstructure and mechanical properties of the fabricated parts.

Ti-6Al-4V (also known as Ti64) is among the titanium alloys to offer a wide range of applications in aerospace [14, 15] and biomedical applications [16-18]. For this reason, there are many research articles about the mechanical properties of Ti64 fabricated via L-PBF in the open literature, reporting a higher strength of L-PBF that is attributed to the formation of martensitic α' . However, it has not been clarified if the higher hardness of L-PBF parts is related to the martensitic crystal structure or the morphology and refinement of the α' phase. In addition, the morphology and crystal structure resulting in L-PBF has not yet been compared with the traditional near-net-shape powder metallurgy technique.

In this paper, the constituent phases in the microstructure of Ti64 alloy processed by the two near-net-shape manufacturing routes of L-PBF and PM were studied using micro- and nano-hardness testing of the identified phases of α , β and α' to highlight the reasons underlying the higher strength reported for L-PBF fabricated Ti64 parts.

4.2 Materials and experimental procedures

The starting material for both L-PBF and PM processes was Ti64 (grade 5) gas atomized pre-alloyed powder obtained from TLS, Technik GmbH & Co (TLS, Technik GmbH & Co is a subsidiary of ALTANA's ECKART division (www.eckart.net)). The powder used in this investigation exhibited particle diameters between 11.9 μm and 41.3 μm (percentile values d_{10} and d_{90} respectively) with a median size d_{50} of 22.7 μm . The powder size

distribution is shown in Figure 4-1 based on the analysis performed using a laser particle size analyzer, the Malvern Mastersizer 2000.

SEM micrographs of powder particles displayed in Figure 4-2 exhibits spherical morphology, which is due to the gas atomization process and makes the powders suitable for the LPBF process because of their high flowability [19]. The satellite particles are also identifiable from the SEM image.

For the chemical composition of the powder, the ICP-AES technique was employed to measure the weight percentages of vanadium, iron and aluminum. To analyze the content of the carbon a LECO CS200 instrument was used, whilst to measure the percentage of hydrogen, nitrogen, and oxygen, a LECO ONH836 analyzer was utilized. Table 4-1 confirms that the chemical composition of Ti-6Al-4V powder complies with the ASTM F2924-14 standard [20]. For fabrication of specimens via L-PBF routes, the powder did not have any treatment; however, for the PM samples, the powder was mixed up with 1.5 wt.% binders, as explained later.

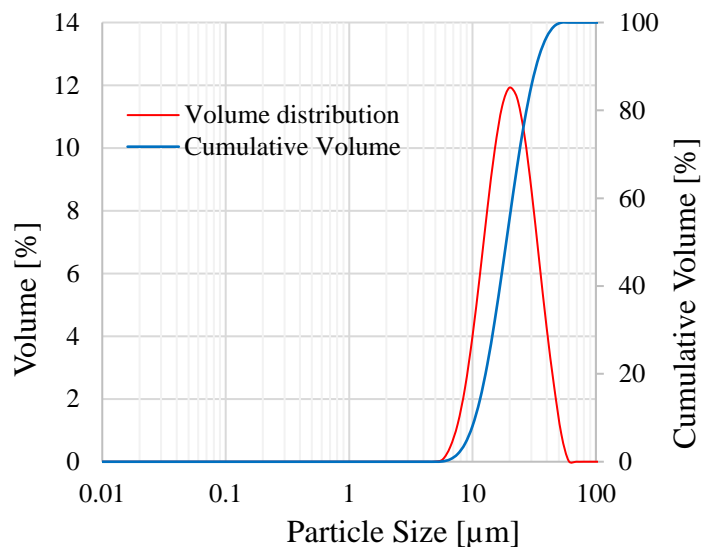


Figure 4-1: Size distribution of Ti64 powder particles.

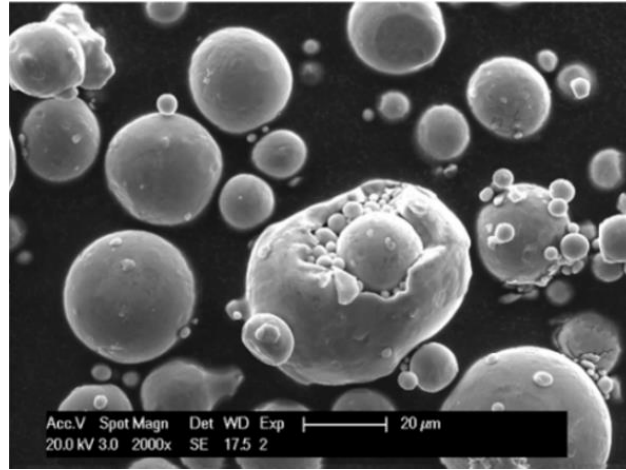


Figure 4-2: spherical morphology of Ti64 powder with satellite and particles inside particles.

Table 4-1: Chemical composition of Ti64 powder (wt.%).

Element	Al	V	Fe	O	C	N	H	Ti
Ti64 powder	6.15	3.94	0.18	0.098	0.005	0.01	< 0.002	Bal.
ASTM F2924-14	5.50– 6.75	3.50– 4.50	Max 0.3	Max 0.2	Max 0.08	Max 0.05	Max 0.015	Bal.

The LPBF machine used in this investigation was a 3D SYSTEMS ProX DMP 200, which employs a laser source with a maximum power of 300W in continuous laser mode. The laser beam diameter of the machine is 70 μ m, with a wavelength (λ) of 1070 nm. The atmosphere of the LPBF chamber is high purity argon, maintained during the course of deposition at atmospheric pressure (101 KPa) to prevent potential oxidation of the molten pool. The maximum allowed oxygen content of the chamber is regulated at 500 ppm. The L-PBF process parameters, shown in Table 4-2 are from the previous study [21], where the authors could fabricate Ti64 parts with a relatively high density of 99.86%. The cylindrical samples with a diameter of 9 mm and a length of 20 mm were built

horizontally and vertically, i.e., the axis of the cylindrical samples was parallel and perpendicular to the substrate respectively. For the laser scan strategy, a bi-directional laser vector for each layer was selected, while the bi-direction laser pattern was rotating 90° between each consecutive layer.

Table 4-2: LPBF processing parameters for fabrication of Ti64 samples.

Laser Power (W)	Scan Speed (mm/s)	Layer Thickness (µm)	Hatch Spacing (µm)
270	1800	30	85

For fabrication of PM samples, the Ti64 powder was ball-mill treated before being poured in a double-action die set with a punch diameter of Ø11 mm to produce 10 mm long specimens. In ball-mill treatment, the powder was mixed with 1.5 wt.% Acrawax (Acrawax™ C Atomized is N, N' Ethylene bis-stearamide (EBS)) lubricant/binder and poured into a stainless steel ball-mill container. The ball milling process was carried out at a constant rotation speed of 100 RPM for 1 h using stainless steel balls with a diameter of 6 mm. The ball-to-powder weight ratio was 5:1 and the milled powder was used as the starting powder for the PM process. The powder mixture was compacted using a Mohr & Federhaff AG Mannheim-Germany (M&F 2) 20-ton hydraulic press, at two different compaction pressures of 450 and 735 MPa, at room temperature.

The sintering process was conducted in a horizontal resistance heating tube furnace, model AY-TF-80-175, with a high purity grade argon atmosphere and heating rate of 5 °C/min. The as-compacted green samples were sintered at 1100 °C and 1250 °C. However, before reaching sintering temperatures, a dwell time of 30 min at 450 °C was employed to burn out the Acrawax lubricant added to the powder. The samples were heated to sintering temperatures and held isothermally for 1 h at these temperatures, followed by a furnace cooling rate of 3 °C/min to room temperature.

For metallographic examinations, all the PM and L-PBF cylindrical samples were sectioned transversally (perpendicular to the axis of samples). However, for the statistical significance of nano-hardness results, it was necessary to section further sites of the L-PBF samples, as will be explained later in this section.

All metallographic samples were mounted in Bakelite and polished conventionally with a fine final polishing of 0.04 μm colloidal silica under 15 N force for 25 min on a Struers Tegramin-25 machine. For microstructural analysis, the Zeiss Axio optical microscope Imager2 and an FEI Quanta 450 FEG-SEM were used. Porosity level of all polished samples were examined on the images obtained from the Zeiss optical microscope via ImageJ software. It should be noted that the percentage of porosity was measured on the as-polished surface.

X-ray Diffraction (XRD) was performed for phase identification purposes for the powder, as well as the PM and the L-PBF-fabricated samples. The XRD machine (MiniFlex 600-Rigaku) employed a Cu radiation operating at 40kV and 15mA, in a continuous scan mode with scan speed of 10°/min and 2θ ranging from 30° to 80°. A Vickers micro-hardness measurement of all samples was performed with a LECO LM700AT. A load of 300 g with a dwelling time of 10 s was chosen for all the measurements. Ten measurements were taken for each sample and the average values were calculated as the microhardness.

For nano-indentation testing, a Fisher-Cripps IBIS system with a Berkovich indenter was utilized. The maximum penetration depth of the indenter was set at 300 nm (depth control) for all samples and the indenter was held for 2 s at the maximum penetration depth before unloading. The loading and unloading rate of the indenter was 60 nm/s; therefore, each loading and unloading procedure took 5 s.

For the PM samples, 120 nano-indentations were performed on unetched metallographic

samples where all constituent phases could be observed and identified. The inter-center distances of the nano-hardness impressions for the PM samples were at least 10 μ m apart to ensure no interference occurred between the indentations.

For nano-hardness of L-PBF samples, each sample of horizontal and vertical was equally sectioned into four short cylindrical discs, as displayed in Figure 4-3a. Then, on each disc, 130 indents with a 60 μ m space between the centers of the indents were impressed in two directions, as illustrated in Figure 4-3b. The reason for impressing nano-indentations in two directions was to obtain more representative data from each section, with better statistical significance and representation of the results. To eliminate any effect of an unstable melt pool or induced residual stress near the peripheral surface, the nano-indentations started and ended approximately 0.6 mm away from any surface of the L-PBF samples, Figure 4-3b. As the final polishing for 25 min with a low load of 15 N left minor polishing-related etching on the samples, the traces of the phases were visible in the micrographs, even in the unetched condition. This minor polishing-related etching helped the nano-indentations with their corresponding results be categorized accurately for each specific phase. It has already been shown [22] that the micro-hardness results in the unetched and etched conditions are nearly the same, meaning that the values of micro-hardness in the etched condition are still valid and reliable. However, nano-indentations should be conducted on polished (unetched) samples only to ensure reliable results.

After the microhardness and nano-hardness experiments, all the samples were etched with Kroll's reagent, (3% HF + 5% HNO₃ + 92% distilled water) for 30 s for microstructural characterization by optical and scanning electron microscopy. Energy Dispersive X-Ray Spectroscopy (EDS) was performed using Aztec analysis software with an SDD detector released by Oxford Instruments fixed on Quanta 450 FEG-SEM.

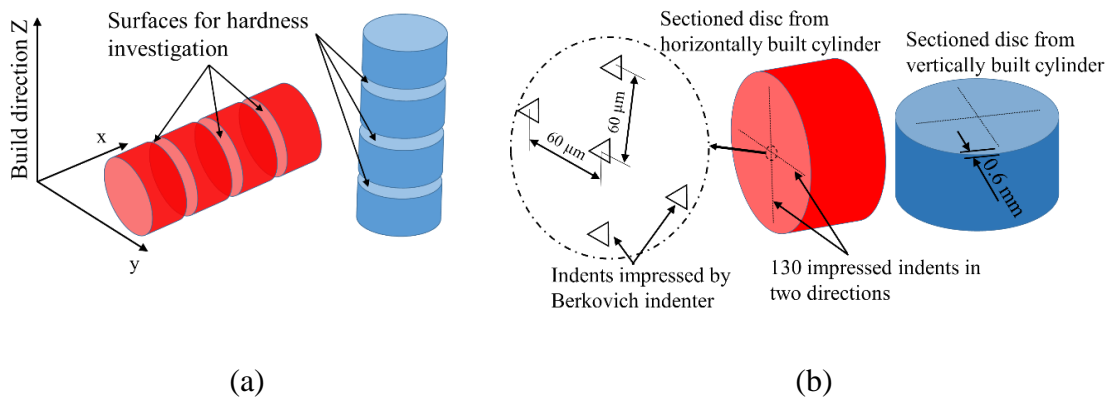


Figure 4-3: a) sectioning plan for hardness measurement of L-PBF fabricated vertical and horizontal samples, b) nano-indentation maps for sectioned discs from vertical and horizontal samples.

After micro-hardness and nano-hardness experiments, all samples were etched with Kroll's reagent, (3% HF + 5% HNO₃ + 92% distilled water) for 30 seconds for microstructure characterisation by microscopy. Energy Dispersive X-Ray Spectroscopy (EDS) was performed using Aztec analysis software with SDD detectors released by Oxford Instruments fixed on Quanta 450 FEG-SEM.

4.3 Results and discussion

4.3.1 Microstructural constituents

Microstructural characterization was initially carried out on the as-received powder particles and then continued on the L-PBF fabricated samples. Due to rapid solidification occurring during the fabrication of powder and L-PBF parts, they were expected to exhibit similar constituent phases. From the SEM micrograph in Figure 4-4a and 4-4b, it is evident that a fully acicular, i.e., tiny needle shape, the martensitic microstructure of α' , has evolved in both the starting powder and the L-PBF fabricated specimens, as reported by other researchers [21, 23-25]. However, when the L-PBF micrograph (Figure 4-4b) is

examined closely, there are some light contrast features (encircled) different from martensite needles. The arrowed encircled feature in Figure 4b is termed the “fish scale” as reported in a previous study [26]. The fish scale feature is not a new phase. It is the same hcp α' phase observed in other regions of the microstructure, but its aluminum content has dropped from its nominal value, due to possible localized overheating and vaporization of aluminum, as a volatile alloying element in Ti64 [27].

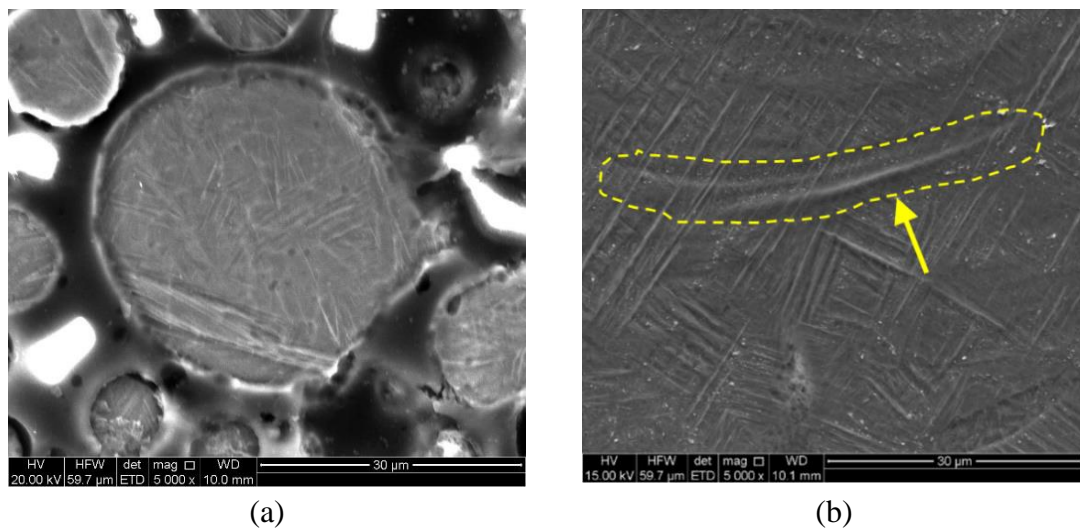


Figure 4-4: SEM of micrographs of etched a) starting powder particles and b) L-PBF sample.

As seen in Figure 4-5, it seems the formation of porosities is the main defect in the PM parts. It is quite evident that the sintering temperature is the key parameter on the microstructural development as the specimens sintered at 1100 °C have still preserved their powder morphology character, while this is not the case for samples sintered at 1250 °C, regardless of compaction pressure. However, when the microstructure at 1100 °C is examined closely, it becomes evident that the two mechanisms of Ostwald ripening (smaller particles dissolve and deposit on larger particles) and particle coalescing (joining of particles) [28] are active during the sintering process. In addition to sintering

temperature, the application of a higher compaction pressure also imparts some improvement on the density of sintered samples if Figure 4-5a and 4-5c is compared. Based on the porosity percentage analysis shown in Table 4-3, under the same sintering temperature (either 1100 °C or 1250 °C), the samples compacted at 450 MPa exhibit higher percentages of porosity than those compacted at 735 MPa.

The XRD phase analysis of both L-PBF and PM samples is given in Figure 4-6 as a stacked graph of XRD spectra of starting powder, as-built L-PBF and PM samples. The XRD spectrum of the PM belongs to the sample fabricated under 750 MPa compacting pressure and sintering temperature of 1250 °C. As seen in Figure 4-6, the hcp α / α' phase exists in all samples, while the formation of the β phase is only observed in the PM samples. Martensitic phase α' and phase α have not been differentiated in the XRD spectra, as both α and α' have the same hcp crystal structure and their lattice parameters are very [26, 29-32]. The α phase has transformed from the parent β (bcc) phase in a diffusion-controlled transformation in the PM sample, while the α' martensitic phase has experienced a diffusionless transformation from the β (bcc) phase, resulting in supersaturation of vanadium in α' [33, 34].

The evolution of martensitic microstructure in the L-PBF samples is attributed to the rapid cooling [35, 36] in which the cooling rate may vary between 10^3 and 10^6 K/s [37-40]. This is true for the α' martensitic phase in Ti64 powder since the particles experience a high cooling rate during gas atomization of molten alloy [41]. For PM samples in Figure 4-5, however, the martensitic needle shape α' observed in the as-atomized powder particles is no longer observed; instead, grains of α have been developed in the matrix of β phase for all PM samples leading to a lamellar morphology.

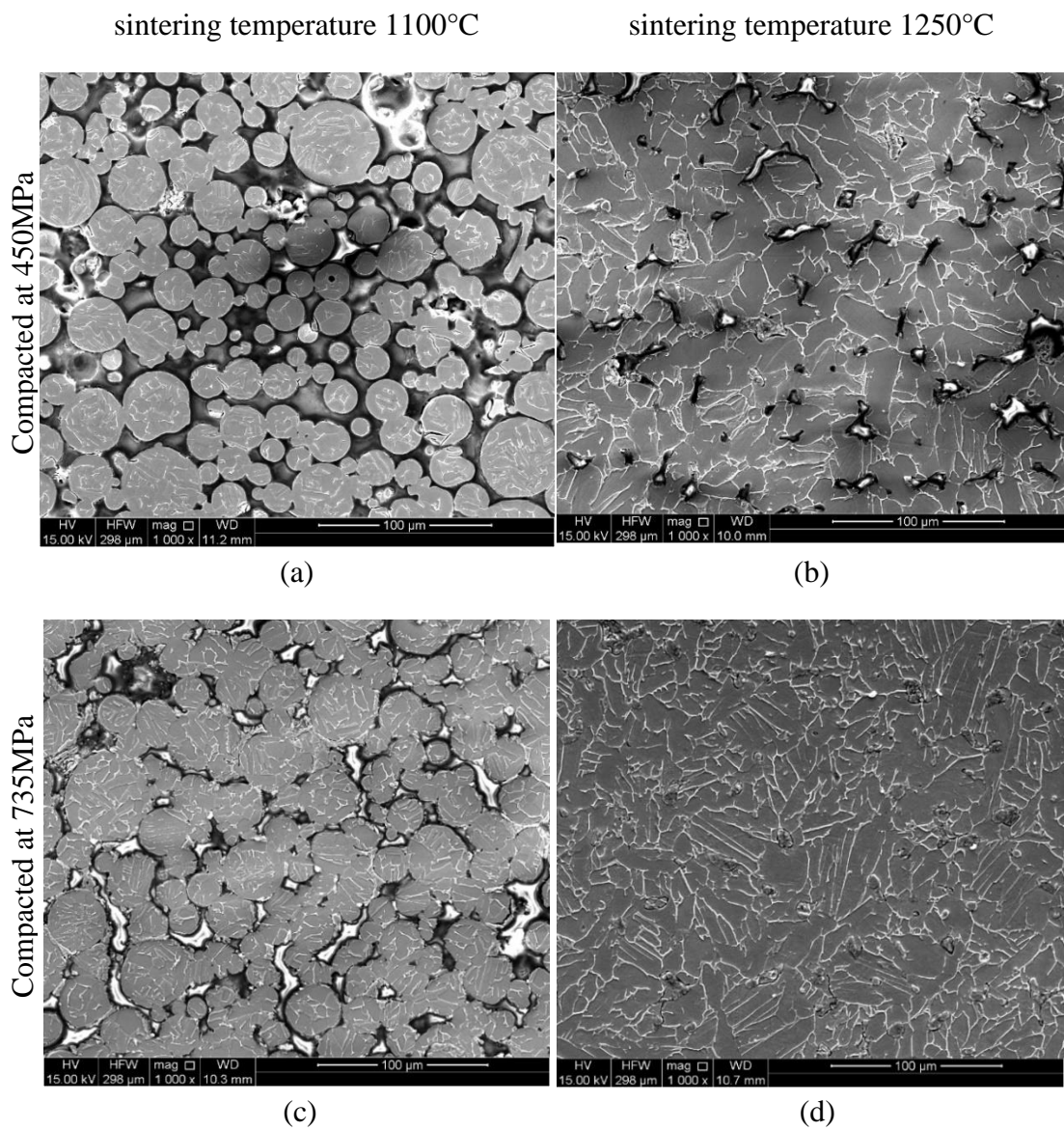


Figure 4-5: SEM images of PM samples sintered at 1100°C: a) compacted at 450 MPa and c)735 MPa and PM samples sintered at 1250°C: b) compacted at pressure 450 MPa and d)735 MPa.

Table 4-3: Porosity percentage of PM samples.

Sample	Compacting pressure, (MPa)	Sintering temperature, (°C)	Sintering time, (hour)	Porosity, (%)
Powder metallurgy (PM)	450	1100	1	26.0 ± 1.2
		1250		9.0 ± 0.5
	735	1100		13.0 ± 1.6
		1250		4.0 ± 0.2

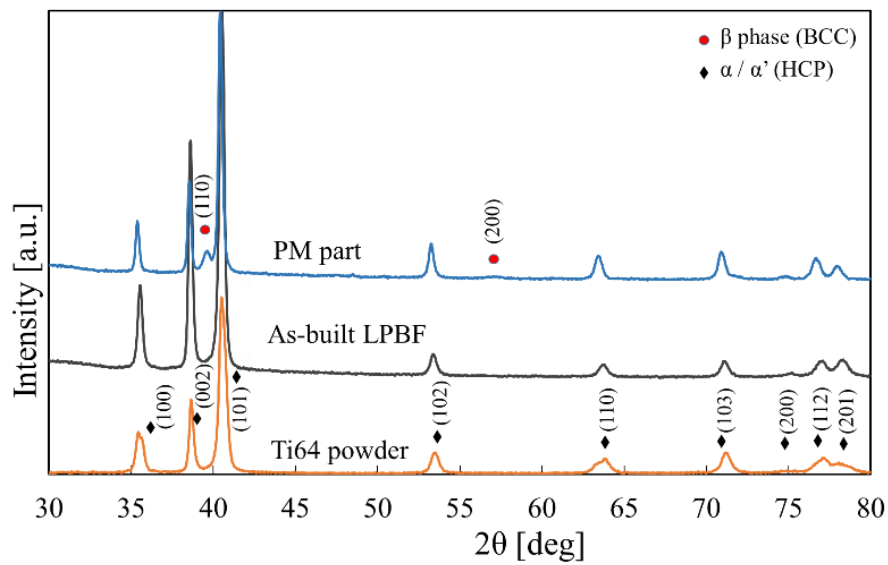


Figure 4-6: XRD spectra of Ti64 powder, as-built LPBF and PM sample.

The nearly equiaxed α grains with $\alpha + \beta$ lamellae in PM samples are the result of diffusion-controlled transformation promoted by the slow cooling rate of 3 °C/min. This is well demonstrated in PM samples sintered at 1250 °C whereas in PM samples sintered at 1100 °C the particles are still in their original morphology, which is believed to be entirely due to a lower diffusion rate resulting from the lower sintering temperature. The presence of some remaining thick laths morphology demonstrated in Figure 4-5a and 4-5c, confirms the coarsening of the lath morphology and their transformation to lamellae. The formation of lamellar structure, Figure 4-5b, and 4-5d, was also observed by others

[42-44]. It is worth mentioning that the highly charged white inter-particle regions, more distinctly seen in Figure 4-5c, are the metallographic consumables' residue employed for sample preparation. They have accumulated within the pores.

EDS (Energy dispersive spectroscopy) examination of the microstructure, shown by the high magnification SEM micrographs in Figure 4-7, confirms that the light grey regions in the PM samples are rich in vanadium. The weight percentage of vanadium in three selected points (1–3), displayed in Figure 4-7b, is between 8.3% and 16.6%, which is beyond the vanadium nominal concentration of 4% in the Ti64 alloy examined in this study. Although it is a well-known fact that EDS analysis is a semi-quantitative method for measuring chemical composition, especially when the concentration of the element is very low, certainly confirms the localized segregation of vanadium. Since vanadium is a β -stabilizer, the formation of the vanadium-rich region in the Ti64 alloy could be an indication of the β phase [45, 46]; so, the bright spots in the PM samples are evidence of the β phase. EDS analysis results of the L-PBF sample, Figure 4-7a, do not show drastic changes in the weight percentages of either aluminum or vanadium compared with their nominal values of 6% and 4%, respectively.

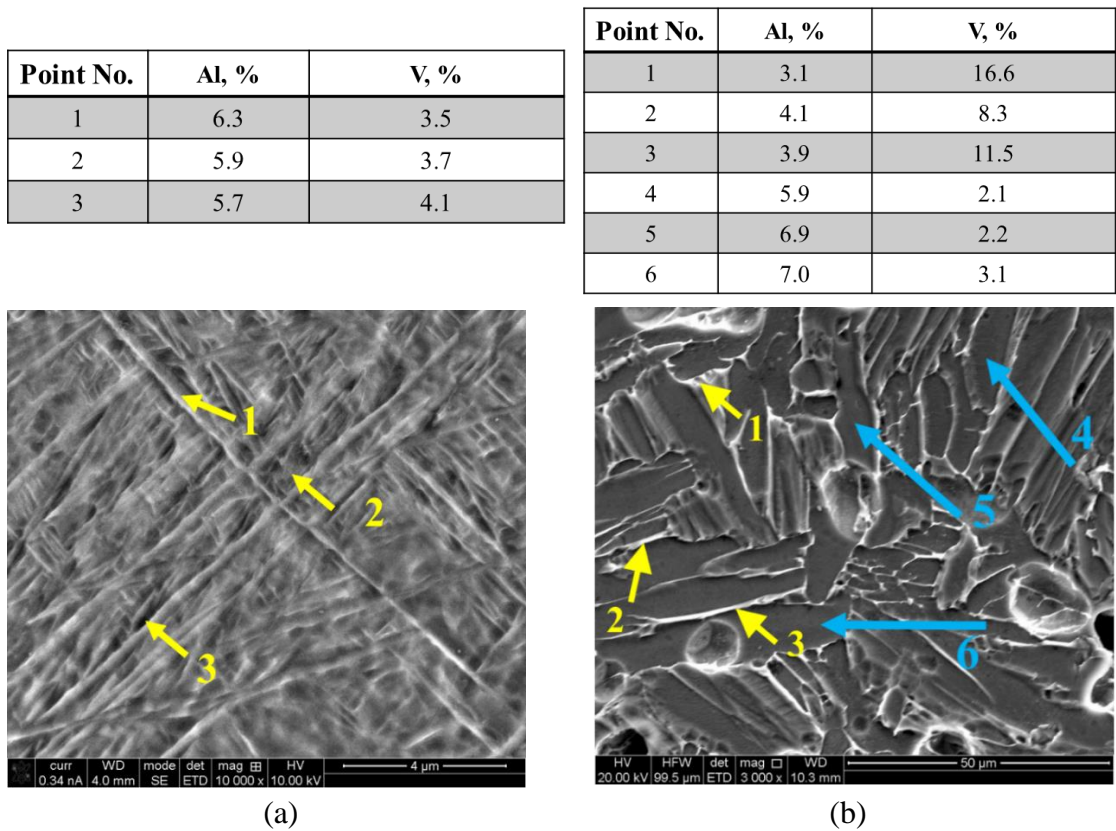


Figure 4-7: EDS analysis of a) as-built L-PBF fabricated part, b) PM sample (750 MPa/1250 °C).

This is expected as the rapid cooling encountered during L-PBF does not allow diffusion to take place. Optical micrographs of the L-PBF parts illustrated in Figure 4-8a reveal the columnar grain architecture of the martensitic microstructure, which is parallel with the L-PBF build direction. The chessboard pattern micrograph shown in Figure 4-8b is, indeed, a section perpendicular to the columnar grains. The prior phase grain boundaries are observed in both micrographs of Figure 4-8a and 4-8b.

This architecture of the microstructure is typically unique for L-PBF parts, as reported by other researchers [24, 47], and is due to the layer-wise building mechanism in L-PBF where a thermal gradient of 10^4 - 10^5 °C/cm along the build direction exists within the very small melt pool [48].

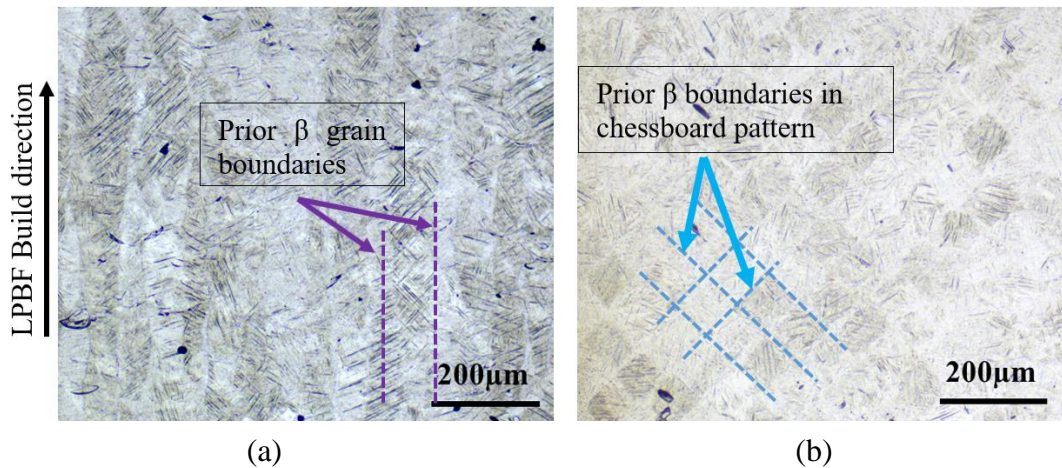
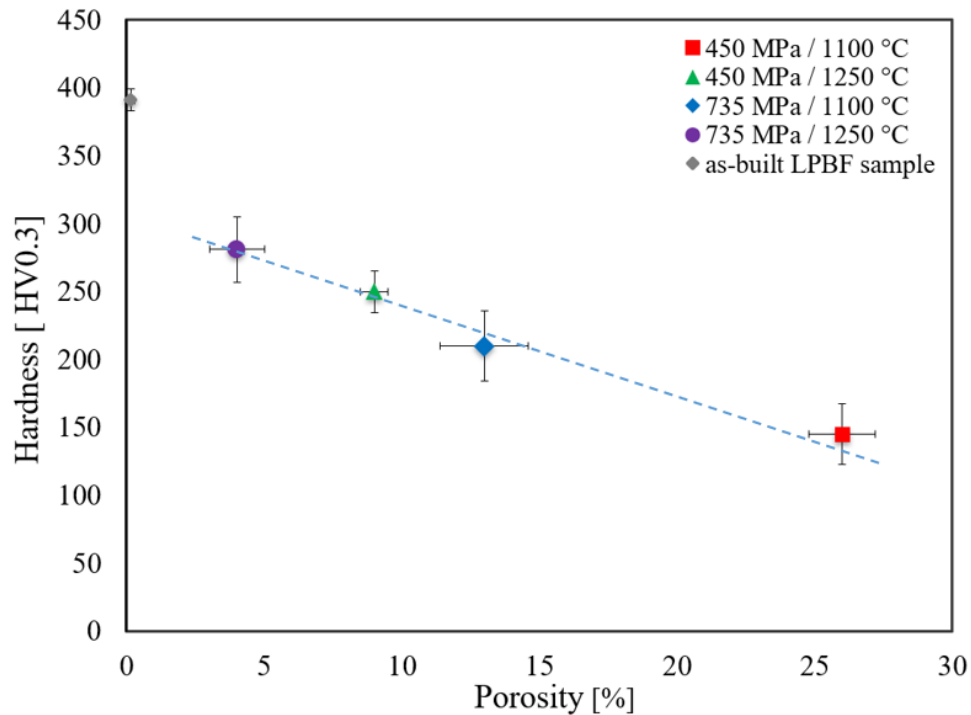


Figure 4-8: Optical micrographs of transverse sections of LPBF parts after etching a) horizontally built cylinder and b) vertically built cylinder.

4.3.2 Micro and nano-hardness characteristics

In addition, as seen from Figure 4-9, the values of Vickers hardness are in the inverse correlation with the samples' porosity as expected. If the fitted line in Figure 4-9 is extrapolated to 100% dense PM samples, the highest achievable micro-hardness would be ~ 310 HV. This hardness value for PM sample, in a fully dense condition, is not far from the hardness (304 ± 12 HV) of the almost fully dense L-PBF sample (relative density of 99.86%) cooled from β -region at a rate of $0.1 \text{ }^\circ\text{C s}^{-1}$ [49]. The reason as why that specific sample ($0.1 \text{ }^\circ\text{C s}^{-1}$) with that hardness value was used as a comparison with the fully dense PM estimated hardness is based on the phases that are present in that near equilibrium L-PBF sample cooled from temperatures above the β transus temperature of this alloy, i.e., it contains $\alpha + \beta$ phases, the same phases form in the sintered PM samples. Any other L-PBF sample, whether as-printed or reheated, may have a combination of α , α' , and β and are not valid since the phases will be different to those of PM samples and therefore hardness value will be different. For the as-printed L-PBF sample, with an

almost fully dense microstructure, the micro-hardness is 22% higher than in the extrapolated fully dense PM sample, which is a noticeable increase in the hardness.



	Vickers Hardness (HV0.3)	Porosity (%)
■ 450 MPa / 1100 °C	145 ± 22.4	26.0 ± 1.2
▲ 450 MPa / 1250 °C	250 ± 15.5	9.0 ± 0.5
◆ 735 MPa / 1100 °C	210 ± 25.6	13.0 ± 1.6
● 735 MPa / 1250 °C	281 ± 14	4.0 ± 0.2
◆ as-built LPBF sample	391 ± 8.0	0.15 ± 0.02

Figure 4-9: Hardness of PM and L-PBF samples vs. their porosity contents.

This improvement in the hardness of L-PBF samples is attributed to different constituent phases in L-PBF (α') and PM parts ($\alpha + \beta$), as observed and discussed earlier, alongside the formation of the lath martensitic structure and microstructural refinement in L-PBF [50, 51]. In order to clarify whether the increase in hardness value is indeed due to the formation of a martensitic structure or the resulting refinements initiated by rapid cooling

during the L-PBF process or both, nano-hardness testing of the PM and L-PBF samples was carried out for in situ measurement of hardness of individual phases.

For a nano-indentation examination, it is critical to perform the hardness measurement on an unetched high-quality surface finish, but the phase's recognition of the samples in the indented region through optical microscopy is a challenge. It has already been reported [22] that even light etching, can affect the nano-indentation results. As explained in Section 4.2, the final polishing step with colloidal silica for 25 min helped the phases of the samples be visible through SEM in unetched conditions. As seen from Figure 4-10a, the differentiation between the two phases of β and α in the PM sample is more pronounced than the thin needle shape α' in the L-PBF sample, Figure 4-10b. EDS analysis of the regions at the vicinity of the nano-indentations, which is explained later, confirms that the light grey strips in Figure 4-10a are β phase, while the dark grey areas, covering the main part of the image, are α phase. This has already been confirmed in the etched PM sample, Figure 4-7b.

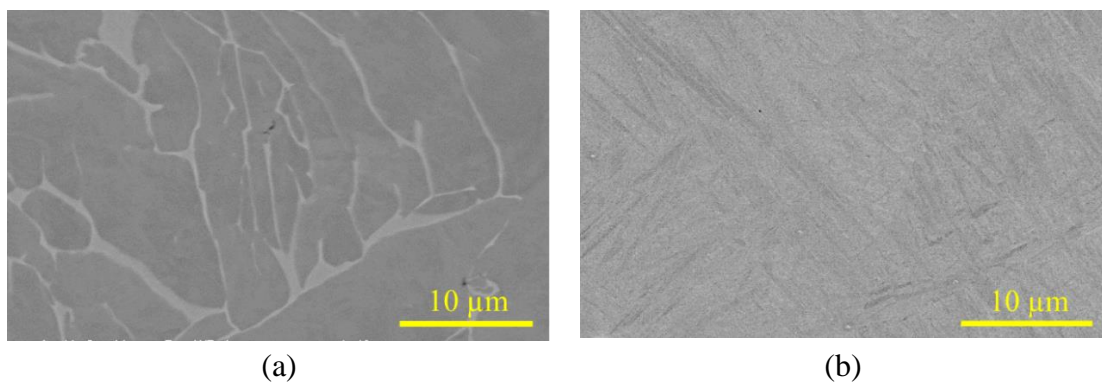


Figure 4-10: Backscatter electron image of polished samples in unetched conditions, a) PM and b) L-PBF sample.

Figure 4-11 shows the nano-indentation maps conducted on the PM sample. In order to increase the validity of the nano-indentation test results of a specific single phase like β , the regions of mixed phases, where the nano-indentations have been impressed, are disregarded. In this way, the contribution of different phases to each other (like the effect of the β phase on α or vice versa), is removed from the nano-indentation results. For example, impression 106 in Figure 4-11 is one of the points in which the indentation impression has included both phases of α and β . For that reason, the data of any impressions, like 106, were invalid and removed from the data analysis. Impressions 12 and 76 in Figure 4-11 are examples of the indentations having valid data because they were fully impressed on individual phases of α and β , respectively. For each individual impression, there is nano-characterization data besides the EDS spectrum, showing the elements of a phase on each indentation.

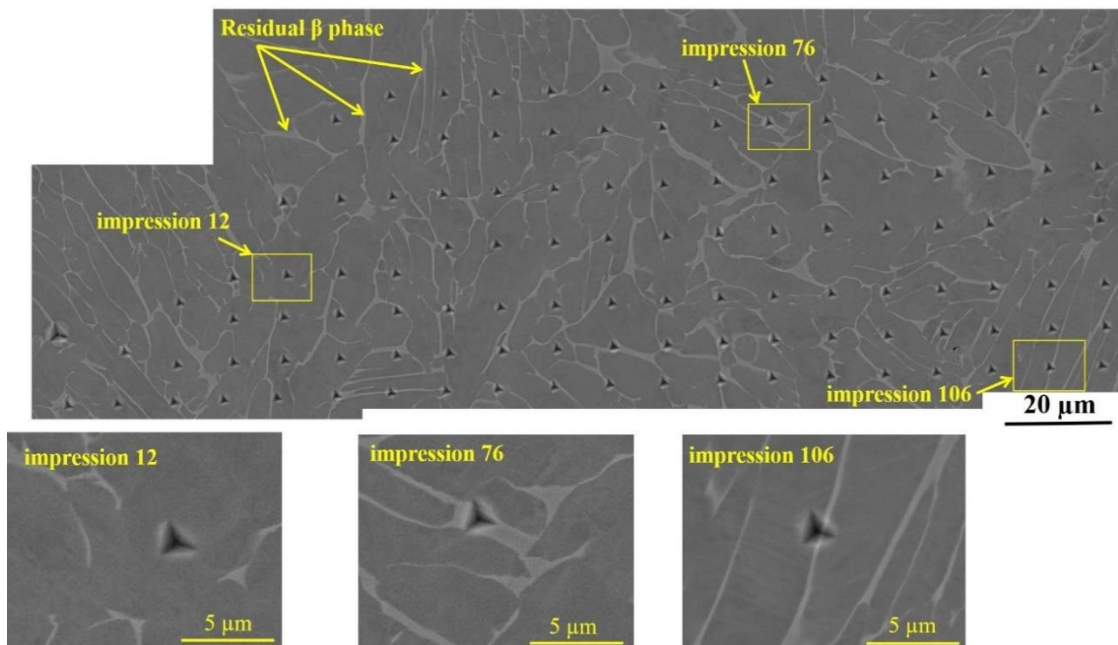


Figure 4-11: Backscatter electron images of 120 indents on the PM sample in unetched condition.

The EDS spectrum of PM sample showed that the amount of vanadium in α phase (the dark grey regions in Figure 4-10) varies between nearly 0% and 4.9%, whereas in the β phase (light grey areas in Figure 4-10), it changes from 5% to 16.6%. This variation of vanadium in either the α or β phases is related to the segregation phenomenon [52], confirming that the microstructure of the PM sample, made with a furnace cooling rate of 3 °C/min, is a quasi-equilibrium, not a fully equilibrium transformation.

In contrast with the PM sample, the variation of the amount of vanadium in the microstructure of the L-PBF sample was much narrower, i.e., 3.5% to 4.2%. This observation reconfirms that the rapid cooling experienced by the β -phase transformation to martensitic phase α' prevented the vanadium atoms diffusion. For measuring the percentage of vanadium in L-PBF, more than ten spots were chosen according to the brightness and darkness of the regions, as observed in Figure 4-10b, but it was noticed the different contrast between acicular α' in the L-PBF samples was not associated with the percentage of vanadium. This suggests that the different contrast observed in the α' needles shape in Figure 4-10b is related to the crystallographic orientation differences between α' laths. The different orientations of the α' -laths can be observed in other studies where crystallographic texture is presented via EBSD analysis [53-55].

Based on the EDS analysis of the regions adjacent to individual indents and the nano-hardness value of each indent in the PM samples, the α phase has been categorized into four groups, based on the amount of dissolved vanadium and aluminum in α . As seen from the graph and tabulated data in Figure 4-12, it seems there is a decreasing trend of nano-hardness of α when the vanadium content increases and aluminum decreases. Aluminum is a well-known substitutional strengthening element in titanium alloy [56-58] and its effect on the nano-hardness of titanium alloy has been reported in [59], but the changes in aluminum weight percentage in the α phase shown in Figure 4-12, compared

with vanadium changes, is very little. So, the decreasing trend in nano-hardness of the α phase, observed in Figure 4-12, is believed to be more related to the higher vanadium concentration than trace reduction in aluminum. The hypothesis that may explain this observation is related to the radius of the vanadium atom ($R_V = 0.134$ nm), which is smaller compared to aluminum ($R_{Al} = 0.143$ nm) and titanium ($R_{Ti} = 0.145$ nm) atoms. When the vanadium atoms substitute the titanium atoms in the crystal lattice, the smaller size of the V atoms reduces lattice frictional forces (Peierls load) necessary for slip systems to activate. This makes it easier for the dislocations to move to initiate plastic deformation, i.e., lower hardness. In a way, it is hypothesized that the smaller size of substituting vanadium atoms relaxes the Ti crystal lattice and therefore the atomic displacement necessary for hardness measurement is easier, i.e., reduction in hardness.

Nano-hardness of Ti64 alloys with a bimodal microstructure of α and β phases has already been reported by other researchers [60, 61] and the wide variation of nano-hardness of α , like 4.57 GPa to 6.84 GPa in [61], has been attributed to α grain orientation [61-63]. However, they have not investigated whether these changes in nano-hardness can be associated with variations in chemical composition and segregation. In addition to the effect of α -grain orientation on nano-hardness value, the mechanics of nano-indentation testing could introduce some variation in the reported results. The indentation size effect (known as ISE) [64-66] and tip radius of indenter [67-69] are some parameters that could be responsible for different values of the nano-hardness reported in the open literature.

The nano-hardness of α in this study, Figure 4-12, fits well in the range found in the open literature, see

Table 4-4, and the slight difference may be due to phase chemistry and the mechanics of nano-hardness measurement mentioned above.

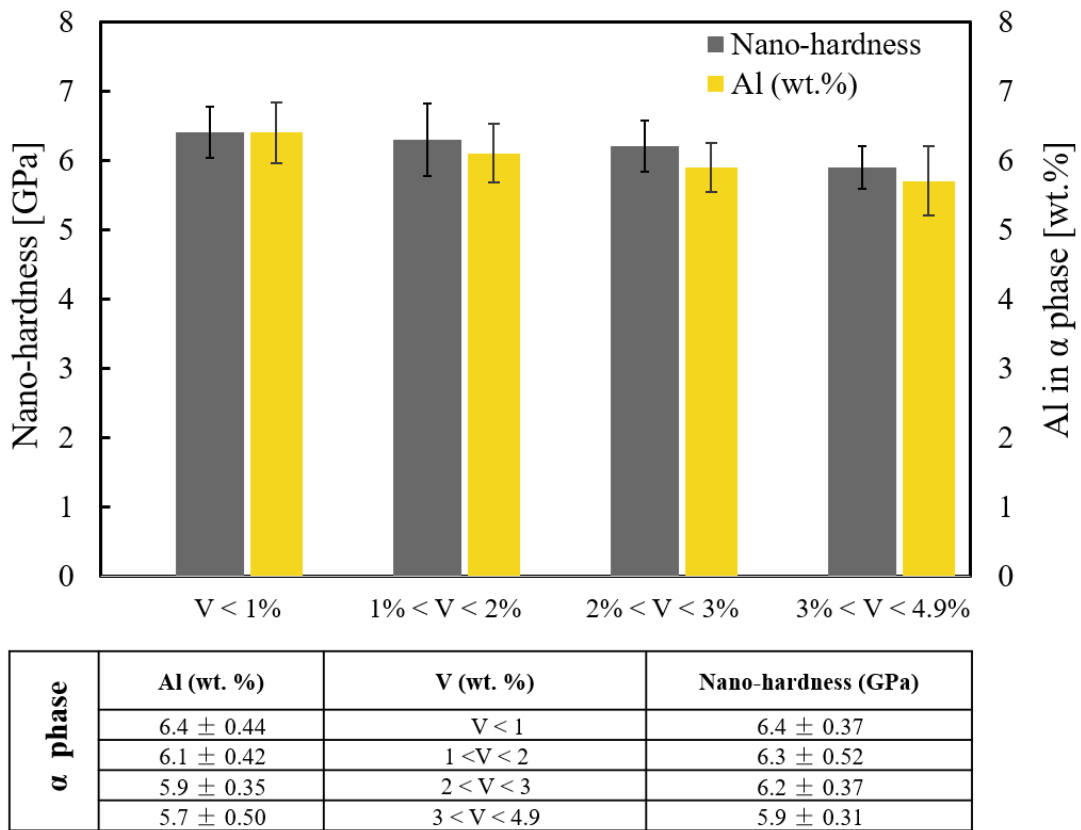


Figure 4-12: Nano-hardness values of the α phase with different contents of vanadium and aluminium.

Figure 4-13 displays the graphs of load (P) vs. penetration depth (h) of nano-indentations of the L-PBF and the two phases of α and β in the PM samples. The graph shows the rate of loading and unloading, with the loading dwell time of 2 s as specified in the experimental procedure (Figure 4-13c). It is important to point out that the loading and unloading rates along with the dwell time and applied load plus the geometry of the indenter, all affect the value of nano-hardness.

Table 4-4 summarizes the average of all the results of nano-hardness of all the phases observed in the microstructure of all the samples in this study. The graphs in Figure 4-13

reveal that the bcc structure of β phase is softer than the hcp phase of α and α' , confirming previous reports [46, 58, 70]. This is due to the fact that the bcc crystal structure has more slip systems than the hcp and consequently should exhibit better movement of dislocations and greater ductility. However, by comparison of the graphs for α and α' , Figure 4-13a, and 13b as well as the values in

Table 4-4, it seems α' does not really require greater loads for the same degree of plastic deformation, i.e., a penetration depth of 300 nm. The nano-hardness of the α phase is the average hardness of all the values of α discussed in Figure 4-12. Although in some articles [62, 71] the effect of β phase and its grain boundaries (with the α phase) on nano-indentation results has been discussed, it is hard to find any reports in the open literature in which they have explicitly differentiated the nano-hardness of each phase of α and β of Ti64 alloy.

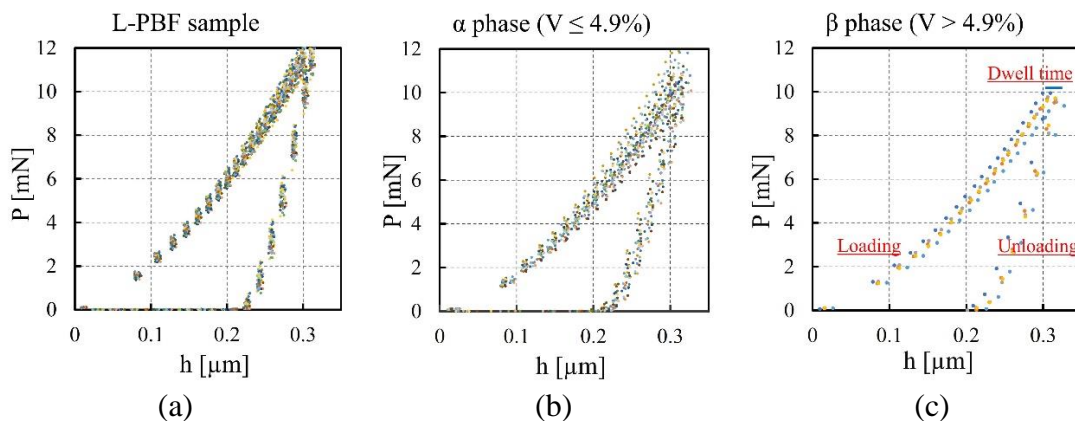


Figure 4-13: Loading and unloading indentations graphs of a) L-PBF, b) α phase-PM and c) β phase-PM samples.

Table 4-4: Nano-hardness of α' , α and β in L-PBF and PM samples.

Phase	Nano-indentation Load (mN)	Indenter Penetration Depth (nm)	Nano-Hardness (GPa)	Reference
α' phase of L-PBF sample	10.3 ± 0.4	300	6.3 ± 0.27	This study
	500	2500	3.9	[72]
α phase	10.13 ± 0.72	300	6.2 ± 0.51	This study
	50	550–675	4.4–6.2	[60]
	2	110–150	4.09–4.71	[62]
	2	–	4.1–10.0	[73]
	8–10.6	300	4.57–6.84	[61]
β phase	9.6 ± 0.2	300	5.9 ± 0.37	This study

It is interesting to note that the standard deviation of nano-hardness value for α' , i.e., ± 0.27 as shown in

Table 4-4, is lower than in α . It is related to the nearly constant concentration of aluminium and vanadium in α' , which is not the case for the α as explained in Figure 4-12. By comparing the nano-hardness values of α' and α (6.3 ± 0.27 GPa and 6.2 ± 0.51 GPa, respectively) it is clear that their nano-hardness values are nearly the same. Moreover, the refined laths structure of α' martensite, with a greater area of low angle boundaries as barriers for movement of dislocations, can increase the nano-hardness. This is illustrated in Figure 4-14, where a 300 nm deep indentation with a semi-equilateral triangle has encountered a few laths boundaries. Apart from α' laths' size and associated boundaries, the existence of the dislocations network, stacking faults, and twinning in α' martensite, as reported by Kurdi et al. [74], are expected to increase the nano-hardness of the L-PBF printed sample. In other words, the negligible increase in the nano-hardness value of α' (1.6%) is due to the opposing issues of defects in α' (hardening) and supersaturation of vanadium in α' (softening).

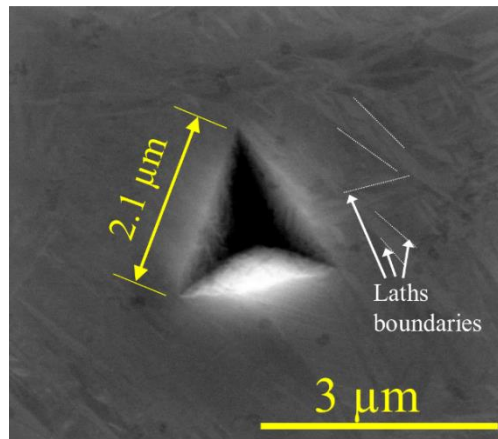


Figure 4-14: A 300nm deep penetrated nano-indentation in L-PBF sample.

4.4 Conclusion

- The microstructural characterization of Ti64 parts fabricated by L-PBF reconfirms columnar growth of prior β grains upon solidification that transforms to acicular martensite hcp α' in contrast with Ti64 parts fabricated via the conventional powder metallurgy route, exhibiting diffusional transformation of β to a bimodal microstructure of α and β phases with nearly equiaxed α grains and $\alpha + \beta$ lamellae.
- The average micro-hardness of L-PBF fabricated parts is 391 HV compared with an estimated hardness of 310 HV of fully dense PM samples. The higher micro-hardness of L-PBF parts is associated with the laths' morphology and refinement of the microstructure of a single phase of α' in L-PBF parts, whereas in PM samples two phases of α and β are influencing the micro-hardness.
- The nano-hardness measurement enables isolation of the grains boundaries from interfering in the hardness measurement and thus rendering the true bulk hardness of individual phases of α' , α , and β .
- Almost the same bulk nano-hardness values of α' and α , i.e., 6.3 GPa and 6.2 GPa, respectively, supports the hypothesis that only the morphology and refinement of α' are responsible for the greater microhardness values of L-PBF parts.

- The bulk nano-hardness of α in PM samples seems to be dependent on the concentration of vanadium solute atoms. A higher concentration of vanadium in the hcp crystal structure of α , lowers its hardness.
- It is hypothesized that the space created by smaller vanadium atoms substituting titanium atoms in α phase crystal lattice allows for the dislocations to move with lesser frictional stresses, leading to a softer α phase.

4.5 Acknowledgements

This work has been supported by the Australian Government Research Training Program Scholarship and The University of Adelaide. This work was performed in part at the Optofab node of the Australian National Fabrication Facility (ANFF) utilizing Commonwealth and South Australian State Government Funding.

References:

1. Banerjee, D. and J.C. Williams, *Perspectives on Titanium Science and Technology*. Acta Materialia, 2013. **61**(3): p. 844-879.
2. Geetha, M., A.K. Singh, R. Asokamani, and A.K. Gogia, *Ti based biomaterials, the ultimate choice for orthopaedic implants – A review*. Progress in Materials Science, 2009. **54**(3): p. 397-425.
3. Peters, M. and C. Leyens, *Fabrication of Titanium Alloys*, in *Titanium and Titanium Alloys*. 2005, Wiley-VCH Verlag GmbH & Co. KGaA. p. 245-261.
4. Kruth, J.P., G. Levy, F. Klocke, and T.H.C. Childs, *Consolidation phenomena in laser and powder-bed based layered manufacturing*. CIRP Annals, 2007. **56**(2): p. 730-759.
5. Brandt, M., *Laser Additive Manufacturing: Materials, Design, Technologies, and Applications*. 2016: Woodhead Publishing.
6. Gu, D., X. Shi, R. Poprawe, D.L. Bourell, R. Setchi, and J. Zhu, *Material-structure-performance integrated laser-metal additive manufacturing*. Science, 2021. **372**(6545).
7. Papazoglou, E.L., N.E. Karkalos, P. Karmiris-Obratański, and A.P. Markopoulos, *On the modeling and simulation of SLM and SLS for metal and polymer powders: A review*. Archives of Computational Methods in Engineering, 2021: p. 1-33.

8. Singh, D.D., T. Mahender, and A.R. Reddy, *Powder bed fusion process: A brief review*. *Materials Today: Proceedings*, 2021. **46**: p. 350-355.
9. Hu, Y. and W. Cong, *A review on laser deposition-additive manufacturing of ceramics and ceramic reinforced metal matrix composites*. *Ceramics International*, 2018. **44**(17): p. 20599-20612.
10. Hegab, H.A., *Design for additive manufacturing of composite materials and potential alloys: a review*. *Manufacturing Rev.*, 2016. **3**: p. 11.
11. Yap, C.Y., C.K. Chua, Z.L. Dong, Z.H. Liu, D.Q. Zhang, L.E. Loh, and S.L. Sing, *Review of selective laser melting: Materials and applications*. *Applied Physics Reviews*, 2015. **2**(4): p. 041101.
12. Yeong, W., C. Yap, M. Mapar, and C. Chua. *State-of-the-art review on selective laser melting of ceramics*. in *High Value Manufacturing: Advanced Research in Virtual and Rapid Prototyping, Proceedings of the 6th International Conference on Advanced Research in Virtual and Rapid Prototyping. Portugal: Leiria*. 2014.
13. Randall, M.G., *Powder metallurgy science* 2nd ed. 1994, USA: Metal Powder Industries Federation.
14. Santos, L.V., V.J. Trava-Airoldi, E.J. Corat, J. Nogueira, and N.F. Leite, *DLC cold welding prevention films on a Ti6Al4V alloy for space applications*. *Surface and Coatings Technology*, 2006. **200**(8): p. 2587-2593.
15. Blakey-Milner, B., P. Gradl, G. Snedden, M. Brooks, J. Pitot, E. Lopez, M. Leary, F. Berto, and A. du Plessis, *Metal additive manufacturing in aerospace: A review*. *Materials & Design*, 2021. **209**: p. 110008.
16. Murr, L., S. Quinones, S. Gaytan, M. Lopez, A. Rodela, E. Martinez, D. Hernandez, E. Martinez, F. Medina, and R. Wicker, *Microstructure and mechanical behavior of Ti-6Al-4V produced by rapid-layer manufacturing, for biomedical applications*. *Journal of the mechanical behavior of biomedical materials*, 2009. **2**(1): p. 20-32.
17. Salmi, M., *Additive manufacturing processes in medical applications*. *Materials*, 2021. **14**(1): p. 191.
18. Ghomi, E.R., F. Khosravi, R.E. Neisiany, S. Singh, and S. Ramakrishna, *Future of additive manufacturing in healthcare*. *Current Opinion in Biomedical Engineering*, 2021. **17**: p. 100255.
19. Kumar, S., *Selective Laser Sintering/Melting*, in *Comprehensive Materials Processing*. 2014, Elsevier. p. 93-134.
20. *ASTM F2924-14, Standard Specification for Additive Manufacturing Titanium-6 Aluminum-4 Vanadium with Powder Bed Fusion*. 2014.
21. Dareh Baghi, A., S. Nafisi, R. Hashemi, H. Ebendorff-Heidepriem, and R. Ghomashchi, *Experimental realisation of build orientation effects on the mechanical properties of truly as-built Ti-6Al-4V SLM parts*. *Journal of Manufacturing Processes*, 2021. **64**: p. 140-152.
22. Dareh Baghi, A., R. Ghomashchi, R.H. Oskouei, and H. Ebendorff-Heidepriem, *Nano-mechanical characterization of SLM-fabricated Ti6Al4V alloy: etching and precision*. *Metallography, Microstructure, and Analysis*, 2019. **8**(5): p. 749-756.

23. Xie, B., Y. Fan, and S. Zhao, *Characterization of Ti6Al4V powders produced by different methods for selective laser melting*. Materials Research Express, 2021. **8**(7): p. 076510.
24. Thijs, L., F. Verhaeghe, T. Craeghs, J.V. Humbeeck, and J.-P. Kruth, *A study of the microstructural evolution during selective laser melting of Ti-6Al-4V*. Acta Materialia, 2010. **58**(9): p. 3303-3312.
25. Rafi, H.K., N.V. Karthik, H. Gong, T.L. Starr, and B.E. Stucker, *Microstructures and Mechanical Properties of Ti6Al4V Parts Fabricated by Selective Laser Melting and Electron Beam Melting*. Journal of Materials Engineering and Performance, 2013. **22**(12): p. 3872-3883.
26. Dareh Baghi, A., S. Nafisi, R. Hashemi, H. Ebendorff-Heidepriem, and R. Ghomashchi, *Effective post processing of SLM fabricated Ti-6Al-4 V alloy: Machining vs thermal treatment*. Journal of Manufacturing Processes, 2021. **68**: p. 1031-1046.
27. Mukherjee, T., J.S. Zuback, A. De, and T. DebRoy, *Printability of alloys for additive manufacturing*. Sci Rep, 2016. **6**: p. 19717.
28. Martin, J.W., R.D. Doherty, and B. Cantor, *Stability of microstructure in metallic systems*. 2010: Cambridge University Press.
29. Facchini, L., E. Magalini, P. Robotti, A. Molinari, S. Höges, and K. Wissenbach, *Ductility of a Ti-6Al-4V alloy produced by selective laser melting of prealloyed powders*. Rapid Prototyping Journal, 2010. **16**(6): p. 450-459.
30. Kubiak, K. and J. Sieniawski, *Development of the microstructure and fatigue strength of two phase titanium alloys in the processes of forging and heat treatment*. Journal of Materials Processing Technology, 1998. **78**(1-3): p. 117-121.
31. Jovanović, M.T., S. Tadić, S. Zec, Z. Mišković, and I. Bobić, *The effect of annealing temperatures and cooling rates on microstructure and mechanical properties of investment cast Ti-6Al-4V alloy*. Materials & Design, 2006. **27**(3): p. 192-199.
32. Malinov, S., W. Sha, Z. Guo, C.C. Tang, and A.E. Long, *Synchrotron X-ray diffraction study of the phase transformations in titanium alloys*. Materials Characterization, 2002. **48**(4): p. 279-295.
33. Thöne, M., S. Leuders, A. Riemer, T. Tröster, and H.A. Richard, *Influence of heat-treatment on Selective Laser Melting products-e.g. Ti6Al4V*. 2012.
34. Sallica-Leva, E., R. Caram, A.L. Jardini, and J.B. Fogagnolo, *Ductility improvement due to martensite α' decomposition in porous Ti-6Al-4V parts produced by selective laser melting for orthopedic implants*. Journal of the Mechanical Behavior of Biomedical Materials, 2016. **54**: p. 149-158.
35. R. Boyer, E.W.C., and G. Welsch, *Materials Properties Handbook: Titanium Alloys*. 1994: ASM International. 1169.
36. T. Ahmed and H.J. Rack, *Phase transformations during cooling in $\alpha + \beta$ titanium alloys*. Materials Science and Engineering A, 1998.

37. Das, M., V.K. Balla, D. Basu, S. Bose, and A. Bandyopadhyay, *Laser processing of SiC-particle-reinforced coating on titanium*. Scripta Materialia, 2010. **63**(4): p. 438-441.
38. Prashanth, K.G., S. Scudino, H.J. Klauss, K.B. Surreddi, L. Löber, Z. Wang, A.K. Chaubey, U. Kühn, and J. Eckert, *Microstructure and mechanical properties of Al-12Si produced by selective laser melting: Effect of heat treatment*. Materials Science and Engineering: A, 2014. **590**: p. 153-160.
39. Li, Y. and D. Gu, *Parametric analysis of thermal behavior during selective laser melting additive manufacturing of aluminum alloy powder*. Materials & design, 2014. **63**: p. 856-867.
40. Hooper, P.A., *Melt pool temperature and cooling rates in laser powder bed fusion*. Additive Manufacturing, 2018. **22**: p. 548-559.
41. Gianoglio, D., N. Ciftci, S. Armstrong, V. Uhlenwinkel, and L. Battezzati, *On the Cooling Rate-Microstructure Relationship in Molten Metal Gas Atomization*. Metallurgical and Materials Transactions A, 2021. **52**(9): p. 3750-3758.
42. Bolzoni, L., E.M. Ruiz-Navas, and E. Gordo, *Feasibility study of the production of biomedical Ti-6Al-4V alloy by powder metallurgy*. Materials Science and Engineering: C, 2015. **49**: p. 400-407.
43. Dunstan, M.K., J.D. Paramore, and Z.Z. Fang, *The effects of microstructure and porosity on the competing fatigue failure mechanisms in powder metallurgy Ti-6Al-4V*. International Journal of Fatigue, 2018. **116**: p. 584-591.
44. Fang, Z.Z., J.D. Paramore, P. Sun, K.R. Chandran, Y. Zhang, Y. Xia, F. Cao, M. Koopman, and M. Free, *Powder metallurgy of titanium—past, present, and future*. International Materials Reviews, 2018. **63**(7): p. 407-459.
45. Molchanova, E.K., *Phase diagrams of titanium alloys*. 1965: Israel Program for Scientific Translations.
46. Peters, M., J. Hemptenmacher, J. Kumpfert, and C. Leyens, *Structure and Properties of Titanium and Titanium Alloys*, in *Titanium and Titanium Alloys*. 2005, Wiley-VCH Verlag GmbH & Co. KGaA. p. 1-36.
47. Murr, L.E., S.M. Gaytan, D.A. Ramirez, E. Martinez, J. Hernandez, K.N. Amato, P.W. Shindo, F.R. Medina, and R.B. Wicker, *Metal Fabrication by Additive Manufacturing Using Laser and Electron Beam Melting Technologies*. Journal of Materials Science & Technology, 2012. **28**(1): p. 1-14.
48. Zhang, L.-C. and H. Attar, *Selective Laser Melting of Titanium Alloys and Titanium Matrix Composites for Biomedical Applications: A Review* Advanced Engineering Materials, 2016. **18**(4): p. 463-475.
49. Dareh Baghi, A., J.D. Arputharaj, S. Nafisi, and R. Ghomashchi, *L-PBF 3D printing of Ti64 alloy, unpublished results, University of Adelaide, Adelaide*. 2022.
50. Gu, D., Y.-C. Hagedorn, W. Meiners, G. Meng, R.J.S. Batista, K. Wissenbach, and R. Poprawe, *Densification behavior, microstructure evolution, and wear performance of selective laser melting processed commercially pure titanium*. Acta Materialia, 2012. **60**(9): p. 3849-3860.

51. Attar, H., M. Calin, L.C. Zhang, S. Scudino, and J. Eckert, *Manufacture by selective laser melting and mechanical behavior of commercially pure titanium*. Materials Science and Engineering A, 2014. **593**: p. 170-177.
52. Callister, W.D. and D.G. Rethwisch, *Materials science and engineering: an introduction*. Vol. 7. 2007: Wiley New York.
53. Medvedev, A.E., E.W. Lui, D. Edwards, M. Leary, M. Qian, and M. Brandt, *Improved ballistic performance of additively manufactured Ti6Al4V with α - β lamellar microstructures*. Materials Science and Engineering: A, 2021. **825**: p. 141888.
54. Liu, J., G. Li, Q. Sun, H. Li, J. Sun, and X. Wang, *Understanding the effect of scanning strategies on the microstructure and crystallographic texture of Ti-6Al-4V alloy manufactured by laser powder bed fusion*. Journal of Materials Processing Technology, 2022. **299**: p. 117366.
55. Simonelli, M., Y.Y. Tse, and C. Tuck, *On the Texture Formation of Selective Laser Melted Ti-6Al-4V*. Metallurgical and Materials Transactions A, 2014. **45**(6): p. 2863-2872.
56. Truax, D. and C. McMahon Jr, *Plastic behavior of titanium-aluminum alloys*. Materials Science and Engineering, 1974. **13**(2): p. 125-139.
57. Fitzner, A., D.L. Prakash, J.Q. Da Fonseca, M. Thomas, S.-Y. Zhang, J. Kelleher, P. Manuel, and M. Preuss, *The effect of aluminium on twinning in binary alpha-titanium*. Acta Materialia, 2016. **103**: p. 341-351.
58. Donachie, M.J., *Titanium: a technical guide*. 2000: ASM international.
59. Fitzner, A., J. Palmer, B. Gardner, M. Thomas, M. Preuss, and J.Q. da Fonseca, *On the work hardening of titanium: new insights from nanoindentation*. Journal of Materials Science, 2019. **54**(10): p. 7961-7974.
60. Wen, Y., L. Xie, Z. Wang, L. Wang, W. Lu, and L.-C. Zhang, *Nanoindentation characterization on local plastic response of Ti-6Al-4V under high-load spherical indentation*. Journal of Materials Research and Technology, 2019. **8**(4): p. 3434-3442.
61. Viswanathan, G.B., E. Lee, D.M. Maher, S. Banerjee, and H.L. Fraser, *Direct observations and analyses of dislocation substructures in the α phase of an α/β Ti-alloy formed by nanoindentation*. Acta Materialia, 2005. **53**(19): p. 5101-5115.
62. Han, F., B. Tang, H. Kou, J. Li, and Y. Feng, *Experiments and crystal plasticity finite element simulations of nanoindentation on Ti-6Al-4V alloy*. Materials Science and Engineering: A, 2015. **625**: p. 28-35.
63. Zambaldi, C., Y. Yang, T.R. Bieler, and D. Raabe, *Orientation informed nanoindentation of α -titanium: Indentation pileup in hexagonal metals deforming by prismatic slip*. Journal of Materials Research, 2012. **27**(1): p. 356-367.
64. Peng, Z., J. Gong, and H. Miao, *On the description of indentation size effect in hardness testing for ceramics: Analysis of the nanoindentation data*. Journal of the European Ceramic Society, 2004. **24**(8): p. 2193-2201.
65. Durst, K., B. Backes, O. Franke, and M. Göken, *Indentation size effect in metallic materials: Modeling strength from pop-in to macroscopic hardness using geometrically necessary dislocations*. Acta Materialia, 2006. **54**(9): p. 2547-2555.

66. Rodriguez, R. and I. Gutierrez, *Correlation between nanoindentation and tensile properties: influence of the indentation size effect*. Materials Science and Engineering: A, 2003. **361**(1-2): p. 377-384.
67. Lu, C.-J. and D.B. Bogy, *The effect of tip radius on nano-indentation hardness tests*. International Journal of Solids and Structures, 1995. **32**(12): p. 1759-1770.
68. Shih, C.W., M. Yang, and J.C.M. Li, *Effect of tip radius on nanoindentation*. Journal of Materials Research, 1991. **6**(12): p. 2623-2628.
69. Sagadevan, S. and P. Murugasen, *Novel Analysis on the Influence of Tip Radius and Shape of the Nanoindenter on the Hardness of Materials*. Procedia Materials Science, 2014. **6**: p. 1871-1878.
70. Lei, X., L. Dong, Z. Zhang, M. Hu, Z. Wang, Y. Hao, and R. Yang, *Microtexture and nanoindentation of α and β Phases in Ti-6Al-1.5 Cr-2.5 Mo-0.5 Fe-0.3 Si titanium alloy*. Science of Advanced Materials, 2017. **9**(9): p. 1476-1483.
71. Weaver, J.S. and S.R. Kalidindi, *Mechanical characterization of Ti-6Al-4V titanium alloy at multiple length scales using spherical indentation stress-strain measurements*. Materials & Design, 2016. **111**: p. 463-472.
72. Hadadzadeh, A., E. Asadi, S.I. Shakil, B.S. Amirkhiz, M. Mohammadi, and M. Haghshenas, *Indentation-derived mechanical properties of Ti-6Al-4V: Laser-powder bed fusion versus electron beam melting*. Materials Letters, 2021. **301**: p. 130273.
73. Li, R., L. Riestler, T.R. Watkins, P.J. Blau, and A.J. Shih, *Metallurgical analysis and nanoindentation characterization of Ti-6Al-4V workpiece and chips in high-throughput drilling*. Materials Science and Engineering: A, 2008. **472**(1): p. 115-124.
74. Kurdi, A. and A. Basak, *Micro-mechanical behaviour of selective laser melted Ti6Al4V under compression*. Materials Science and Engineering: A, 2021. **826**: p. 141975.

Chapter 5

Effects of build orientations and surface on LPBF parts

Chapter overview

This chapter which is based on a published paper in “Journal of Manufacturing Processes”, presents the effect of two build directions of vertical and horizontal on the fabricated parts in their truly as-built condition. Then by machining the surface of the horizontal and vertical sample, the effect of build direction in surface treated condition was investigated as well. The challenge in this study was fabricating the undistorted horizontal tensile samples without any post processes. In this chapter it is demonstrated how we overcome this difficulty with a developed design for fabrication truly as-built straight horizontal tensile sample.

Statement of Authorship

Title of Paper	Experimental realisation of build orientation effects on the mechanical properties of truly as-built Ti-6Al-4V SLM parts
Publication status	<input checked="" type="checkbox"/> Published <input type="checkbox"/> Accepted for Publication <input type="checkbox"/> Submitted for Publication <input type="checkbox"/> Unpublished and Unsubmitted work written in manuscript style
Publication Details	A. Dareh Baghi , S. Nafisi, R. Hashemi, H. Ebendorff-Heidepriem, and R. Ghomashchi, "Experimental realisation of build orientation effects on the mechanical properties of truly as-built Ti-6Al-4V SLM parts", <i>Journal of Manufacturing Processes</i> , vol. 64, pp. 140-152, 2021/04/01/ 2021.

Principal Author

Name of Principal Author (Candidate)	Alireza Dareh Baghi		
Contribution to the Paper	Developed the ideas and concepts, designed 3D models of the samples, conducted the experiments, acquired the data, interpreted results, and drafted the manuscript		
Overall percentage (%)	80%		
Certification:	This paper reports on original research I conducted during the period of my Higher Degree by Research candidature and is not subject to any obligations or contractual agreements with a third party that would constrain its inclusion in this thesis. I am the primary author of this paper.		
Signature		Date	11/05/2022

Co-Author Contributions

By signing the Statement of Authorship, each author certifies that:

- I. the candidate's stated contribution to the publication is accurate (as detailed above);
- II. permission is granted for the candidate to include the publication in the thesis; and
- III. the sum of all co-author contributions is equal to 100% less the candidate's stated contribution.

Name of Co-Author	Reza Ghomashchi		
Contribution to the Paper	Supervised the work, participated in developing ideas, evaluated and edited the manuscript.		
Signature		Date	11/05/2022

Name of Co-Author	Shahrooz Nafisi		
Contribution to the Paper	Helped in developing the concept and experimental design and manuscript review.		
Signature		Date	28/10/2022

Name of Co-Author	Reza Hashemi		
Contribution to the Paper	contributed to experimental setup, academic discussion and manuscript review		
Signature		Date	13/05/2022

Name of Co-Author	Heike Ebendorff-Heidepriem		
Contribution to the Paper	Supervised the research, provided access to LPBF machine for sample preparation and reviewed the manuscript.		
Signature		Date	16/05/2022

Experimental realisation of build orientation effects on the mechanical properties of truly as-built Ti-6Al-4V SLM parts

Alireza Dareh Baghi, Shahrooz Nafisi, Reza Hashemi, Heike Ebendorff-Heidepriem, Reza Ghomashchi

Abstract

Studying the mechanical properties of Selective Laser Melting (SLM) fabricated titanium parts built in a horizontal direction, parallel to the substrate, in a truly as-built condition, has always been a challenge. The problem is mainly related to the stress relaxation of horizontal parts after removal from the substrate, which causes a noticeable level of distortion when compared with vertically printed parts with no observable distortion. In this study, a novel design has been developed that enables fabrication of straight undistorted horizontal parts via an SLM route with no post-processing steps, and thus the mechanical properties of horizontal Ti-6Al-4V (Ti64) samples in their truly as-built condition have been reported and compared with their vertically built counterparts. The study reveals that the vertical samples suffer from premature fracture in their truly as-built condition, while the horizontal parts perform similarly to post-treated samples. The analysis of the tensile test results shows that the fracture stress (maximum stress) of the truly as-built vertical parts is below the yield stress (YS) of the horizontal parts in their truly as-built condition, i.e., nearly 38% of the Ultimate Tensile Strength (UTS). In addition to the truly as-built condition, the effect of machining was also studied to further highlight the effect of as-built surface removal on the mechanical properties of both vertically and horizontally deposited Ti-6Al-4V(Ti64) SLM parts.

5.1 Introduction

Ti-6Al-4V (Ti64) has attracted significant interest for fabricating high integrity parts using additive manufacturing techniques, like SLM [1-3]. The alloy is widely used in diverse industrial fields, such as aerospace [4, 5] and biomedical applications [6, 7]. This has led to considerable study of the mechanical properties of Ti64 parts fabricated via SLM under different process parameters [3, 8, 9]. There is a large body of work in the open literature reporting on the mechanical properties of SLM fabricated parts, including Ti64, to highlight the anisotropic behaviour in mechanical properties with respect to the build directions, both vertical and horizontal [10-13]. SLM fabricated parts generally suffer from residual stresses originating from the very high temperature gradients and extreme cooling rates experienced during the process [14-16]. The residual stresses could be problematic in Ti64 parts [17, 18]; compromising their mechanical performance. The horizontally built long parts (such as tensile test samples) experience severe residual stresses, causing deflection to occur in the test pieces immediately upon support removal. For this reason, as-built horizontal parts must be stress relieved before being removed from the substrate [19, 20] or they will need to be machined afterwards to eliminate distortion. The stress relieving process helps the horizontal parts stay straight and remain acceptable for tensile tests. Some researchers have made straight horizontal samples out of the deflected horizontal parts [13] or cut from horizontally-built blocks via machining [21, 22]. In other words, there are no tensile properties available in the open literature for the as-built horizontal samples having no post fabrication treatment, i.e., being “*truly as-built*”, since the actual as-built horizontal samples are not straight and cannot be tested properly. Both processes of stress relieving and machining alter the condition of the SLM samples from their “*truly as-built*” conditions. ASTM F2924-14 states that “as-built refers to the state of components made by an additive process before any post processing

employed, except where the removal from a build platform is necessary or powder removal or support removal is required” [23]. Thus, according to this standard, neither the stress relieved parts nor the machined components could be considered as having a “*truly as-built*” condition.

Furthermore, it is obvious that any post fabrication treatment will increase the cost of production, while at the same time there is market pressure on cost reduction [24-27]. Therefore, by eliminating any post processes of machining, heat treatment or other treatments like hot-isostatic pressing (Hipping) [28] the final production cost should reduce significantly. However, since there is no reported mechanical characterization comparison between the *truly as-built* horizontal and vertical samples, it is required to evaluate whether as-built vertical or horizontal parts meet the expected mechanical characteristics of Ti64 manufactured by other processes than SLM, and to see if the as-built parts can exhibit reliable performance in their applications. In the current work, “*truly as-built*” SLM fabricated Ti-6Al-4V undistorted horizontal tensile test pieces were realized by implementing an innovative design approach. The fabrication of the undistorted tensile test pieces made it possible to study the effect of the build direction on the tensile properties of the *truly as-built* Ti-6Al-4V samples fabricated by SLM experimentally. Also, the as-built samples were machined to show how machining can improve the mechanical properties of both vertical and horizontal samples. It is important to specify the terminology used in this report. Hereafter, “as-built” signifies the “*truly as-built*” condition: test pieces fabricated with no post processes, including surface machining or heat treatment. The machined samples have their surface machined only, without any heat treatment.

5.2 Materials and experimental procedures

To fabricate the as-built straight horizontal samples, a 3D model of the samples was designed, such that the long axis of the samples is slightly arched (according to a pre-calculated radius). After removing this part from the substrate, the SLM-induced residual stresses relax and the curved sample obtains a straight-line profile, which is suitable for tensile tests. By fabricating both straight horizontal samples (via the above-mentioned innovative approach) and vertical samples, it becomes possible to study the effect of the build direction on the tensile properties of SLM-fabricated Ti-6Al-4V experimentally in their as-built conditions. The machined tensile samples in this paper are made from vertical and horizontal SLM-fabricated cylindrical rods.

5.2.1 Materials

The gas atomized pre-alloyed powder Ti64 (grade 5) was supplied by TLS, Technik GmbH & CoTM, Germany [29]. The particle size distribution of the powder and its chemical analysis were provided through the powder manufacturer's certificate. Since the powder used in this investigation had already been used for parts' production, it was necessary to re-examine the powder for its chemical composition and particle morphology. Table 5-1 presents the results of the chemical analysis of the powder in its as-received, new condition and after being used. The ICP-AES technique was used for the elemental chemical analysis of Iron (Fe), Aluminium (Al), and Vanadium (V). The elemental percentages of Hydrogen (H), Nitrogen (N), and Oxygen (O) were measured using a LECO ONH836 analyser. Also, Carbon (C) elements were analysed by the LECO CS200 instrument.

Table 5-1: Chemical composition (wt. %) of Ti64 (grade5) powder.

Element	Al	V	Fe	O	C	N	H	Ti
ASTM F2924-14	5.50- 6.75	3.50- 4.50	Max 0.3	Max 0.2	Max 0.08	Max 0.05	Max 0.015	Bal.
New powder according to the powder manufacturer's certificate	6.39	3.88	0.2	0.077	0.011	0.005	<0.002	Bal.
Used powder according to the chemical analysis in this study	6.15	3.94	0.18	0.098	0.005	0.010	<0.002	Bal.
SLM-fabricated bulk sample	6.14	3.97	0.19	0.114	0.005	0.011	<0.002	Bal.

Although there is an increase in the level of oxygen and a decrease in the level of aluminium in the used powder and bulk fabricated samples, these elements are still within the acceptable range provided in the standard, ASTM F2924-14 [23]. Figure 5-1a shows the size distribution of the new and used powders, which were examined using a laser particle size analyser, Malvern Mastersizer 2000. The new powder shows a volume median size of $d(0.5)=22.73 \mu\text{m}$, while the used powder exhibits an increase in median size, $30.00 \mu\text{m}$. This is probably due to a minor agglomeration of loose, small particles in the SLM chamber during fabrication, leading to a slight increase in the median size of the whole batch. The oxygen pick-up and change of the particle size distribution (PSD) of the reused powder in this study is in agreement with other studies [30, 31]. The morphology of the used powder was examined using an FEI Quanta 450 FEGSEM. Ti64 powder exhibits a spherical morphology, as shown in Figure 5-1b, which makes the powders suitable for the SLM process because of their high flowability [32]. The cluster of small particles and partially sintered small particles in Figure 5-1b explains the peak shift in the particles' size distribution graph of the used powder (Figure 5-1a). Satellite

phenomena can also be seen from the typical SEM image of the powder particles, Figure 5-1b.

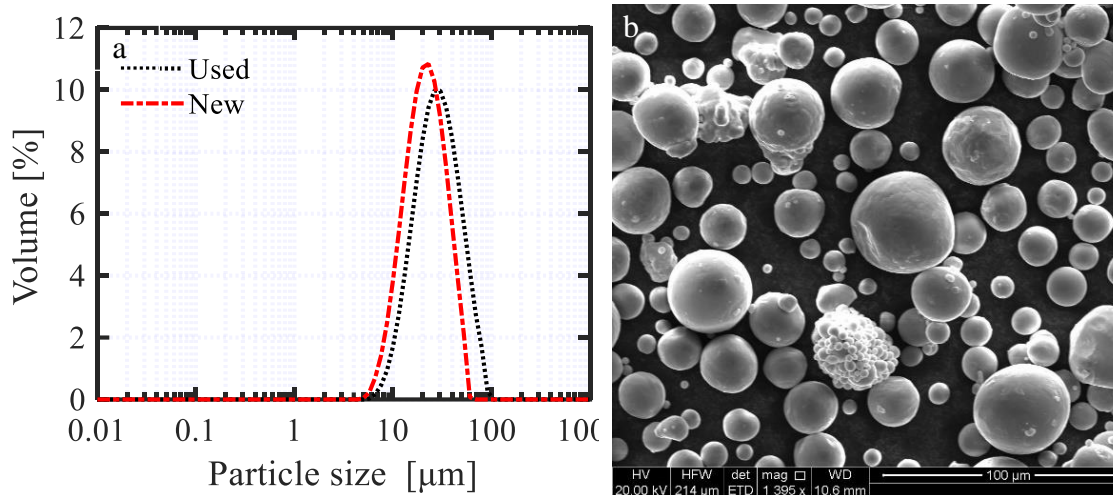


Figure 5-1: a) Ti64 particle diameter distribution of new powder and used powder, b) Typical SEM image of used Ti64 powder particles after being sieved.

5.2.2 Experimental procedures

In this study, a 3D SYSTEMS ProX DMP 200 machine was used. This machine employs a 1070 nm wavelength (λ) laser source in continuous mode, with a maximum power capacity of 300W. The SLM chamber is filled with argon at atmospheric pressure (101 KPa) during deposition. The level of oxygen in the chamber was kept as low as 500 ppm and the substrate was not pre-heated. Table 5-2 summarises the optimised SLM process parameters [33] used in this investigation. A bi-directional laser scanning strategy with a 90° interlayer rotation (criss-cross) was chosen for fabricating the tensile samples on a 12mm thick substrate. Figure 5-2 shows the schematic of the first batch of the horizontal samples used to measure the deflection after support removal, immediately after deposition.

Table 5-2: SLM process parameters to fabricate Ti64 samples.

Laser Power, P (W)	Scanning velocity, v (mm/s)	Layer thickness, t (μm)	hatch spacing, h (μm)	Laser beam spot size, w_0 (μm)
270	1800	30	85	70

The coloured arrows in Figure 5-2 show the laser path in alternating layers employed for the horizontal samples. The build direction is perpendicular to the plane of this page and the laser path has an alternating angle of $\pm 45^\circ$ with respect to the tensile axis of the test pieces.

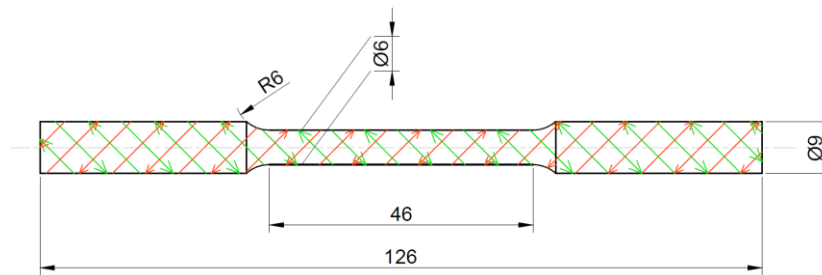


Figure 5-2: Geometry of first batch of the horizontal samples.

The deflection of the first batch of the horizontal samples were measured, by a dial gauge, on the centre axis of both ends to the centre of test piece. That was approximately 1 mm as depicted in Figure 5-3. The deflection distribution of the individual points along the tensile axis of two typical horizontal samples is shown in Figure 5-4.

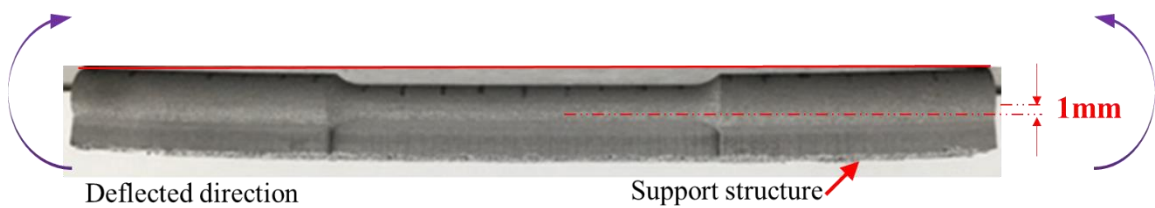


Figure 5-3: Typical sample of the first batch of the horizontally-built parts after being removed from the substrate.

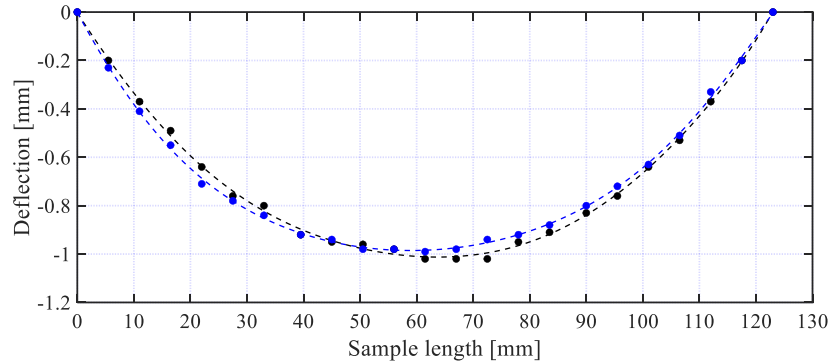


Figure 5-4: Deflection curve of two typical horizontal samples from the first batch

Once the deflection values of the fabricated samples (length=126 mm) was determined (Figure 5-4), a reversed design was considered to fabricate the samples with a maximum length of 80 mm. The selection of this length, 80mm, was based on the maximum allowable height of the vertical parts to be built by the ProX-200 3D printing machine. As demonstrated in Figure 5-4, a deflection of 0.5mm was calculated for the samples with 80 mm length. In the next step, the samples were designed to be fabricated with a deflection of 0.5 mm, as shown in Figure 5-5a. After removing the curved horizontal dumbbell samples from the substrate, they formed a straight profile shape. This confirmed the expected deflection analysed from Figure 5-4. This design was used to fabricate both as-built parts (Figure 5-5a) and rods for further machining (Figure 5-5b). Moreover, three samples in each direction, vertical and horizontal, in the shape of dumbbells and cylindrical rods, were fabricated for the tensile tests. The machining process in this study for removing the as-built surface from rods was a turning process with an NC lathe machine. It is noteworthy that the final shape of the as-built and machined samples (Figure 5-5c), complies with the small size specimens specified by ASTM E8 [34], for which the gauge length must be four times the gauge diameter. A universal tensile testing machine (Instron, model 5969 with a 50kN load cell) was used in this study. All tensile

tests were conducted at room temperature with a cross-head speed (displacement rate) of 0.2 mm/min.

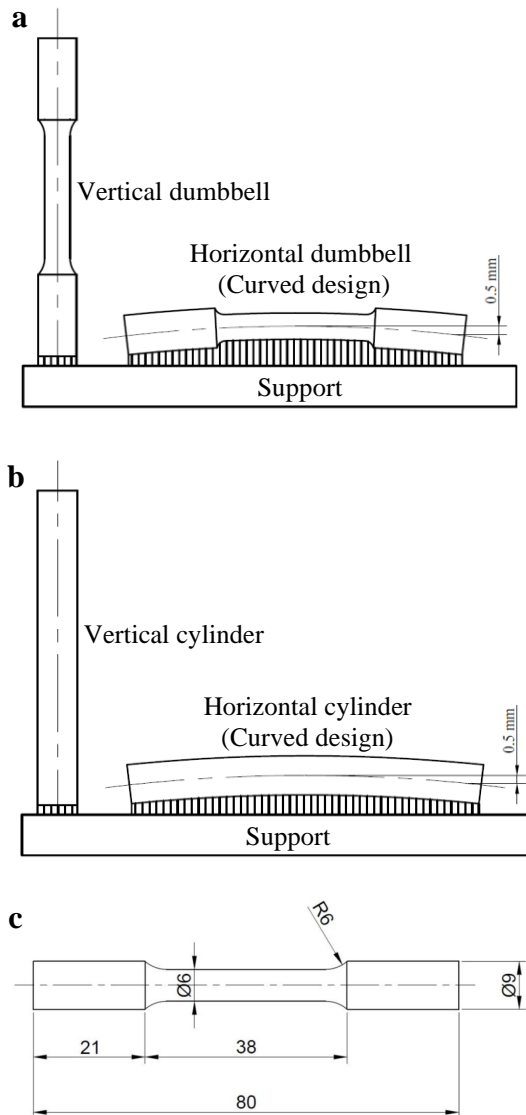


Figure 5-5: a) Vertical sample and reversed deflected design of a horizontal dumbbell shape sample attached to the substrate, b) Vertical and horizontal cylinder to be machined, and c) Final test specimen dimensions, (all units in mm).

For metallographic examinations, horizontal and vertical tensile test samples were sectioned transversally from their grip sections. All the metallographic samples were mounted in Bakelite and polished conventionally, with a final polish of 0.04 μm colloidal silica and hydrogen peroxide (30%) solution. Prior to etching, the metallographic samples

were examined for both pore morphology and the level of porosity using optical microscopy and image analysis software, ImageJ⁷. More than 30 fields of view were examined for porosity measurements, to render a statistically viable result. Vickers' microhardness tests (LECO LM700AT machine) were also performed on unetched samples at a 300g applied load with 10 s dwell time on all samples. The final microhardness result for each sample was the average value of more than 6 indentations around the centre of the samples. The Rigaku MiniFlex 600 XRD machine used in this study, employed Cu radiation, operating at 40kV and 15mA, with a scan speed of 10°/min over a range of 2θ from 30° to 85°. All the metallographic samples were etched for microstructure and phase characterisation using Kroll's reagent (3% HF + 5% HNO₃ + 92% distilled water) for 50 seconds. For microstructural analysis, a Zeiss Axio optical microscope Imager2 and a FEI Quanta 450 FEG-SEM were used.

5.3 Results and discussion

5.3.1 Microstructural characterisation

It is worth emphasizing again that the examined metallographic samples are both transverse sections to the tensile axis for both horizontal and vertical test pieces. However, the transverse cut of the grip section for the horizontal samples is actually a plane parallel to the build direction; whereas it is a plane perpendicular to the build direction in the vertical samples, Figure 5-6a. Optical microscopy of polished samples reveals that the morphology of the pores appears to vary: semi-equiaxed in the horizontal samples and generally elongated in the vertical test pieces. The pores' morphologies are easily recognizable after the polished samples are etched (see Figure 5-6b and c). The elongated pores shown in Figure 5-6c have the same direction as the laser vector strategy, i.e., $\pm 45^\circ$

⁷ ImageJ is a trademark; (<https://imagej.net/Welcome>)

criss-cross, perhaps suggesting that there is a minor lack of fusion in the solidifying molten pool with its adjacent solidified track or with the previously-solidified layers, i.e., inter-track pores or inter-layer pores. Some of the semi-equiaxed pores observed in the horizontal samples could be the same elongated pores appearing in the vertical samples, given that sectioning the architecture and viewing the samples from a different angle could have altered their morphology. The porosity content of the transverse sections of the horizontal and vertical samples are summarised in Table 5-3. The very low content of porosity of 0.14%, confirms the selection of appropriate process parameters to render SLM fabricated Ti64 parts with nearly full density (99.86%). The magnitude of the standard deviation may also suggest the distribution of pores examined by 2D image analysis is nearly the same in two directions.

Table 5-3: Results of 2D image analysis of two different sections of an SLM sample to measure the porosity distribution.

	Parallel to build direction (transverse cut from horizontal)	Perpendicular to build direction (transverse cut from vertical)	Average
Porosity, (%)	0.12 ± 0.08	0.16 ± 0.07	0.14 ± 0.07

The microstructure of the etched transverse section of the horizontal sample, Figure 5-6b, exhibits a columnar pattern; whereas the transverse section of the vertical sample, Figure 5-6c, shows a chessboard pattern, which is the consequence of criss-cross alternating layering. The chessboard side length of 85 μm and diagonal length of 120 μm displayed in Figure 5-6c or the $\sim 120 \mu\text{m}$ of columnar grain width in Figure 5-6b, all correspond with the laser hatch spacing of 85 μm , Table 5-2. The columnar architecture of the microstructure parallel to the build direction and the formation of a chessboard pattern perpendicular to the build direction are consistent with other studies [3, 22, 35]. Figure 5-6d illustrates a schematic representation of the 3D architecture of the SLM fabricated

Ti64 parts according to the criss-cross alternating layering and with respect to the direction of applied tensile load for horizontal and vertical samples. It could be expected that this architecture, with respect to the applied loading direction, results in an anisotropy of the mechanical properties. The boundaries separating the individual columnar grains are believed to be the grain boundaries of the prior β phase upon solidification of the Ti64 [36]. The martensitic lath structure in the columnar or chessboard grains in Figure 5-6b and c are due to the steep thermal gradient experienced during the SLM process, i.e., cooling rates of 10^4 - 10^6 [37-39], by which the β phase directly transforms to a martensitic α' phase.

The SEM micrographs in Figure 5-7 show the lath morphology of the martensitic phase (α') is almost similar for both vertical and horizontal samples. The XRD spectrum in Figure 5-8 confirms there is no trace of the bcc structure β -titanium phase in the SLM fabricated part, or, at least, it is below the detection limit of the XRD method. In the event that any β phase exists, the first peak of bcc should have appeared between planes (002) and (101) of hcp α' ($2\theta \sim 39^\circ$) and its second peak between planes (102) and (110) of hcp ($2\theta \sim 57^\circ$), specified with the red dashed lines in Figure 5-8 [40-42].

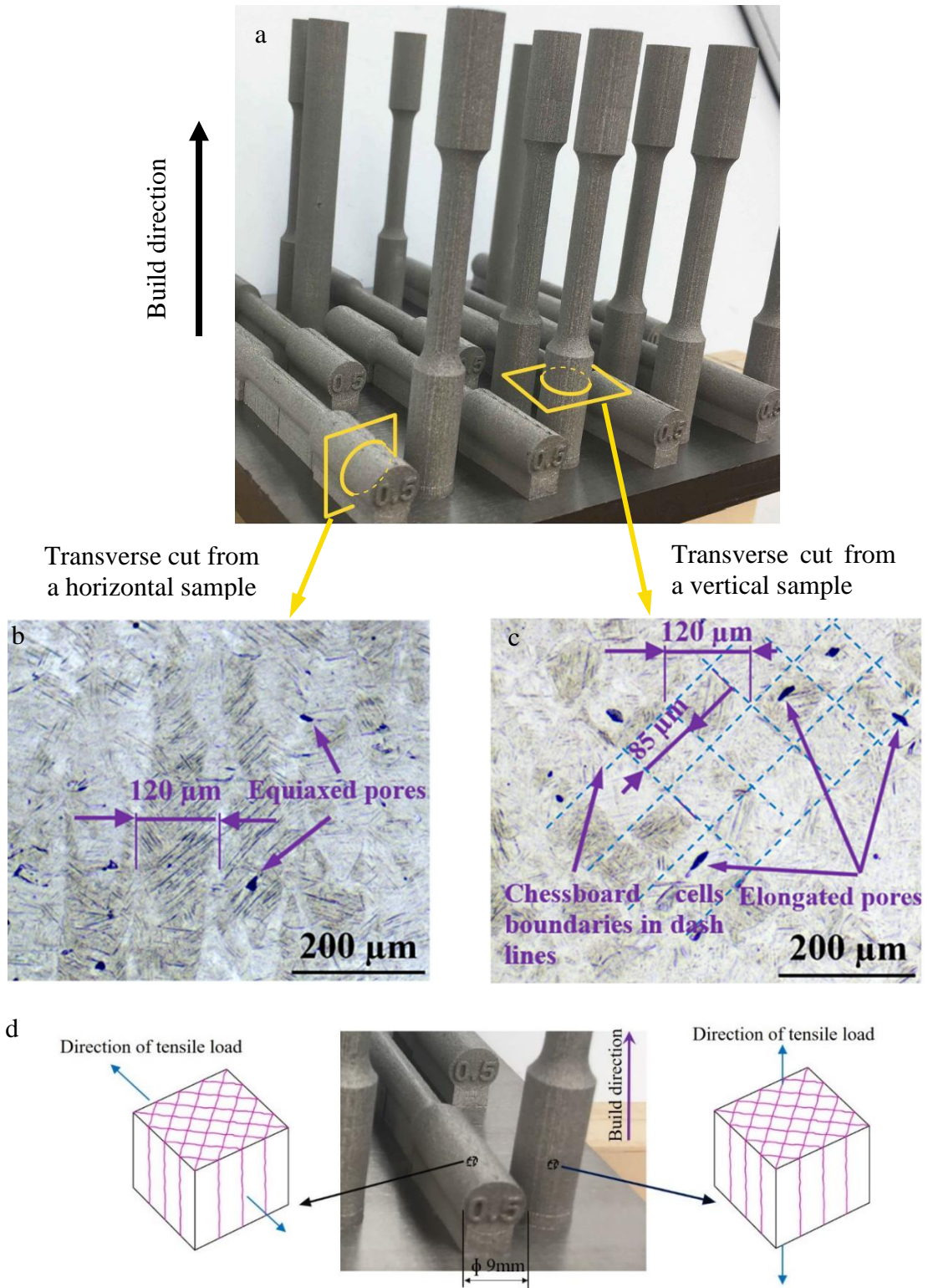


Figure 5-6: a) Transverse cutting of horizontal and vertical tensile samples from the “grip section”. b and c) Optical micrographs of etched transverse sections of horizontal and vertical samples, respectively, and d) Schematic 3D model of microstructure architecture, according to the applied tensile load direction.

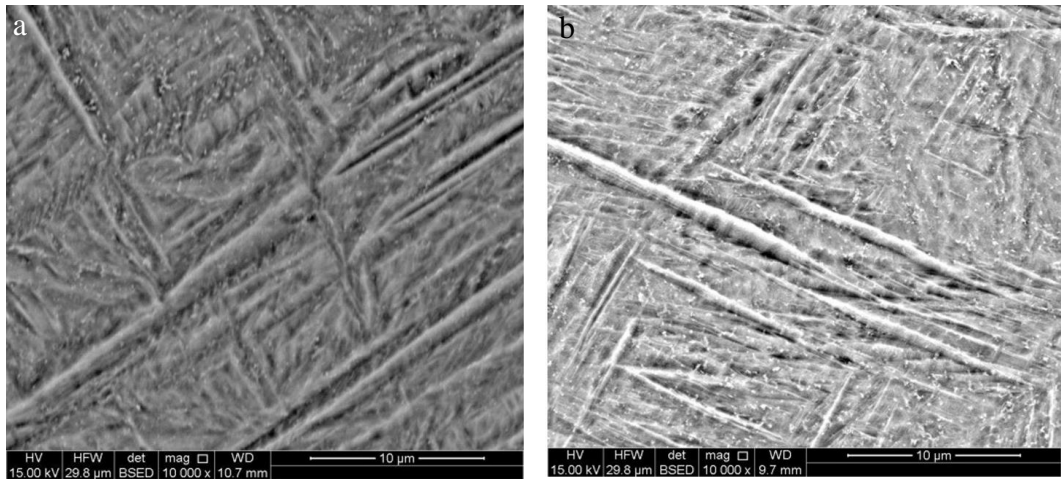


Figure 5-7: Backscattered Electron micrographs of the etched samples sectioned transversely from; a) a horizontal sample, and b) a vertical sample.

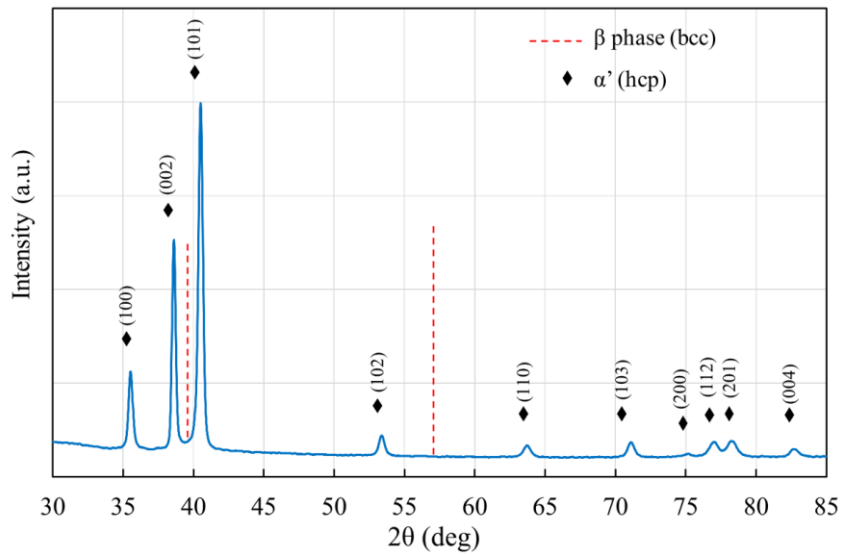


Figure 5-8: The XRD spectrum of the SLM sample shows no trace of β phase, (the red dashed lines show the position of the expected peaks of the β phase).

5.3.2 Mechanical properties

Figure 5-9a - d exhibits the engineering stress-strain graphs for all the SLM samples built in the horizontal and vertical directions, and in two separate conditions: as-built and machined. The tensile results extracted from the stress-strain graphs in Figure 5-9a - d are

summarised in Figure 5-9e. The effect of surface machining on the tensile properties varies greatly, depending on the build direction. By comparing the tensile properties of the machined horizontal samples with those of the as-built horizontals in Figure 5-9a, it is obvious that the machining of the surface played a role in improving the tensile properties of the horizontally-built samples. This improvement is about 15% for YS, almost 11% for UTS and nearly 34% for ductility (elongation), Figure 5-9e. A similar trend is also true for the machined vertically-built tensile samples, Figure 5-9b and Figure 5-9e; however the surface machining of the verticals drastically improved the UTS and elongation at fracture by 180% and 460%, respectively. The build direction appears to have a significant effect on the tensile properties of as-built parts. The vertical samples in their as-built surface condition experienced premature fracture at an average stress of 482 MPa, still within the linear elastic region, as seen in Figure 5-9b. Since the horizontal samples, in which the tensile loading is nearly parallel to the deposited layers, do not suffer from any early failures compared with the verticals, this makes the horizontal samples the better candidates to be used directly in service in the as-built condition. This is not the case for the verticals. From the graphs of stress-strain of the as-built vertical and horizontal samples shown in Figure 5-9c, it is clear that the tensile properties of as-built verticals are far less than their horizontal counterparts. However, Figure 5-9d shows that the machined verticals and horizontals are very similar in their strengths but the strain at fracture of the machined verticals is still nearly half that of the horizontal samples, which will be discussed later in this section. The variation of Young's modulus for all samples, according to Figure 5-9.e, is approximately 4%. This means the build direction and associated surface condition of the samples does not have any significant effect on the elasticity (stiffness), which is not the case for YS and UTS. As explained in the section on microstructural characterisation, the direction of tensile loading with respect

to the columnar architecture (Figure 5-6d) can result in anisotropy of the mechanical properties but there are other factors affecting the mechanical properties, especially in the as-built vertical. The different behaviour of vertical samples under two conditions of as-built and machined, Figure 5-9b, may suggest that the interrelationship between the surface topography of the test pieces and the loading axis needs to be examined closely to verify if the build direction has any effect on the directionality of the valleys and hills of the roughness profile with respect to the loading axis. Figure 5-10 shows the surface topography of the as-built horizontal and vertical samples prepared longitudinally with respect to the applied tensile load. The peaks to valleys patterns on the outer surface of the horizontal sample in Figure 5-10b is completely different from those observed in the vertical samples, Figure 5-10c. The wavelength (peak to peak distance) on the outer surface of horizontal samples is greater compared with that of the as-built vertical. The short wavelength of the asperities on the outer surface of an as-built vertical sample is mainly correlated to the 30 μ m layer thickness. This short wavelength, beside the unfused layers near the outer surface of the as-built vertical sample, leads to sharp, deep valleys (notches), as can be seen from Figure 5-10c. The sharp valleys on the surface of the as-built vertical sample could act as stress concentration points, magnifying the applied stress at the surface and thus encouraging crack initiation. The high level of stress may then guide the crack towards the centre at a faster rate, causing premature fracture. It is also possible that the induced residual stress along the build direction, which is the tension on the edge of sample [15, 43], may contribute to the stress concentration at the sharp notches. It should also be mentioned that the outer side surface of vertical samples is actually the edge of the sample where the laser track finishes. The higher stress level is then responsible for faster crack growth, resulting in a flat fracture surface for the as-built vertical samples. As has already been discussed for tensile properties, Figure 5-9e shows

that, by removing the surface layer of the vertical samples via machining, a considerable improvement in the mechanical properties could be achieved. Further investigation is required to show whether the surface characteristics (the sharp notches on the surface) of the as-built vertical samples alone are responsible for the premature failure or the residual stresses, or both. The observed lower ductility of machined vertical samples with respect to their horizontal counterparts could partially be attributed to the sharp angles of inter-layered pores, appearing perpendicular to the applied tensile load, Figure 5-6c. In other words, anisotropy of pores with respect to the direction of applied load could be a potential cause of anisotropy of the mechanical properties. Porosities, which are inevitable SLM-induced defects [11, 44], often limit the ductility of Ti64 parts [45]. In some studies, [12, 20], it is shown that these thin flattened pores, which are due to the lack of fusion between layers, may act as local stress risers, with some role played in the early fracture of the vertical samples. Moletsane et al. [46] reported that the elongated (inter-layer) pores contribute to the residual stress and can lower the ductility of as-built samples. This may explain the lower elongation of the machined vertical samples with elongated pores, compared with the machined horizontal samples. The average Vickers' microhardness of the transverse cut of the tensile samples from their grip sections were measured at 407 ± 12 (HV) and 423 ± 17 (HV) for the horizontal and vertical specimens, respectively. The microhardness values reveal that the hardness in both directions is nearly the same; however, the tensile load results show that there is a considerable anisotropy between the vertical and horizontal samples. Thus, Vickers' hardness is an indication of the hardness of the microstructure fabricated by the SLM process, but serious attention must be paid not to be misled by the hardness, as it does not reveal any effects of induced defects and the architecture of the microstructure on the mechanical properties and the anisotropy. A possible parameter which may influence the anisotropy

of mechanical properties of SLM fabricated parts is the crystallographic texture. Some researchers [39, 47] found that although the columnar prior grains show a strong $\langle 001 \rangle \beta$ texture parallel to the build direction, the α' martensitic phase formed from β during cooling exhibits just a random texture. This means that the crystallographic texture in SLM-fabricated Ti64 parts is weak. Beladi et al. [40] reported that the overall texture strength of α' martensitic structure is considerably weaker compared with the $(\alpha + \beta)$ microstructure produced in a diffusional transformation. This is further confirmed by the measured microhardness values for the two orientations of vertical and horizontal with only 4% difference. Therefore, texture appears not to be the main contributor of the anisotropy in mechanical properties, such as the observed difference in elongation of vertical and horizontal samples in current study. Although differences in ductility have been reported between the two deposition directions of machined samples, in some studies, the ductility was the opposite, i.e. the vertical samples showed higher ductility [13, 48]. Therefore, it may be concluded that the anisotropic mechanical properties are an intrinsic feature of the SLM 3D printing process, affected by a range of parameters including component size and geometry, microstructure architecture and phases, solidification mechanism affecting crystallographic planes, porosity content and morphology and, of course, the process parameters. They pose a considerable challenge to the design and fabrication process for SLM components.

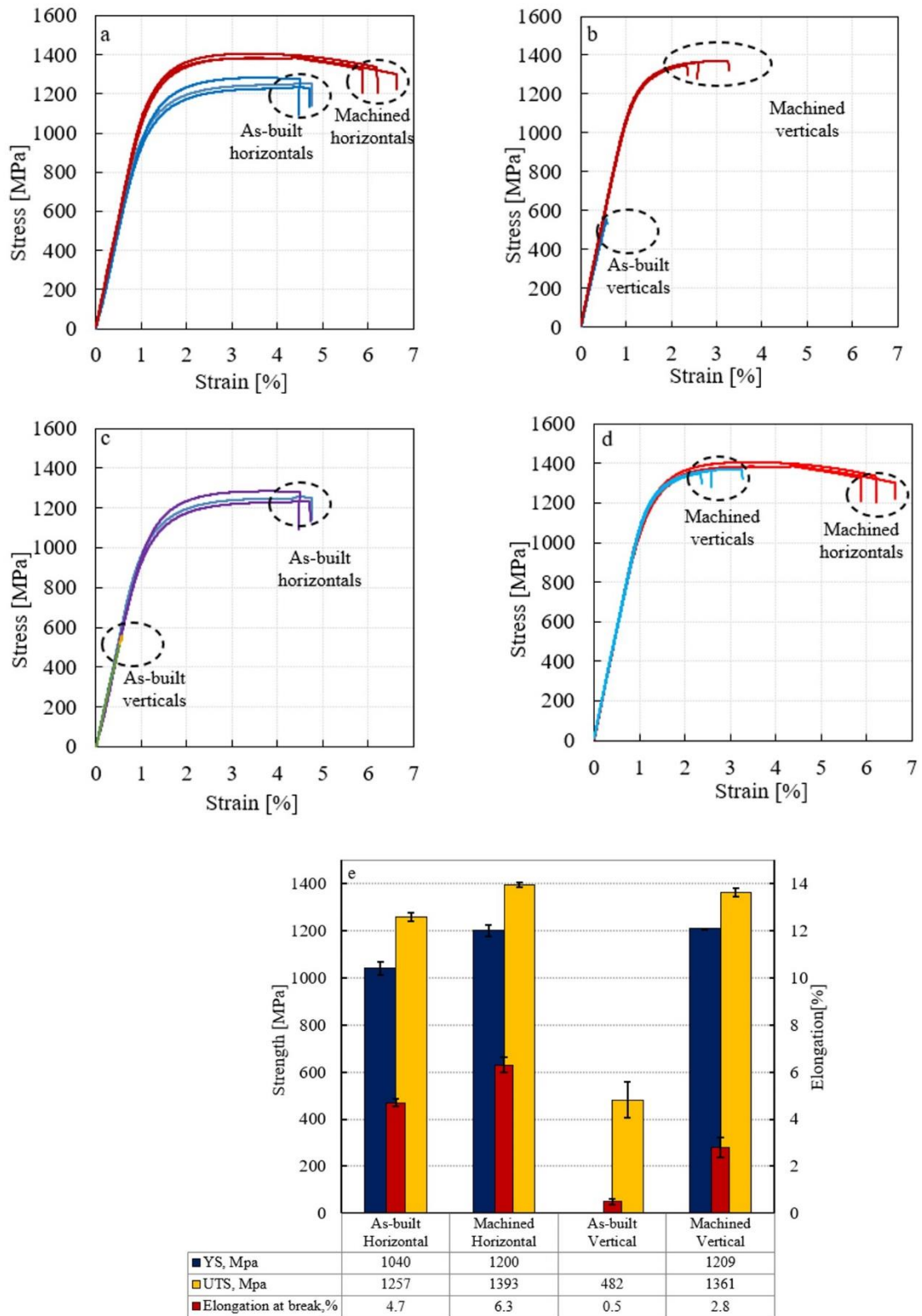


Figure 5-9: The stress-strain plots, a) machined and as-built horizontals, b) machined and as-built verticals, c) as-built horizontals and verticals, d) machined horizontals and verticals, e) tensile properties of horizontal and vertical samples in two conditions of as-built and machined.

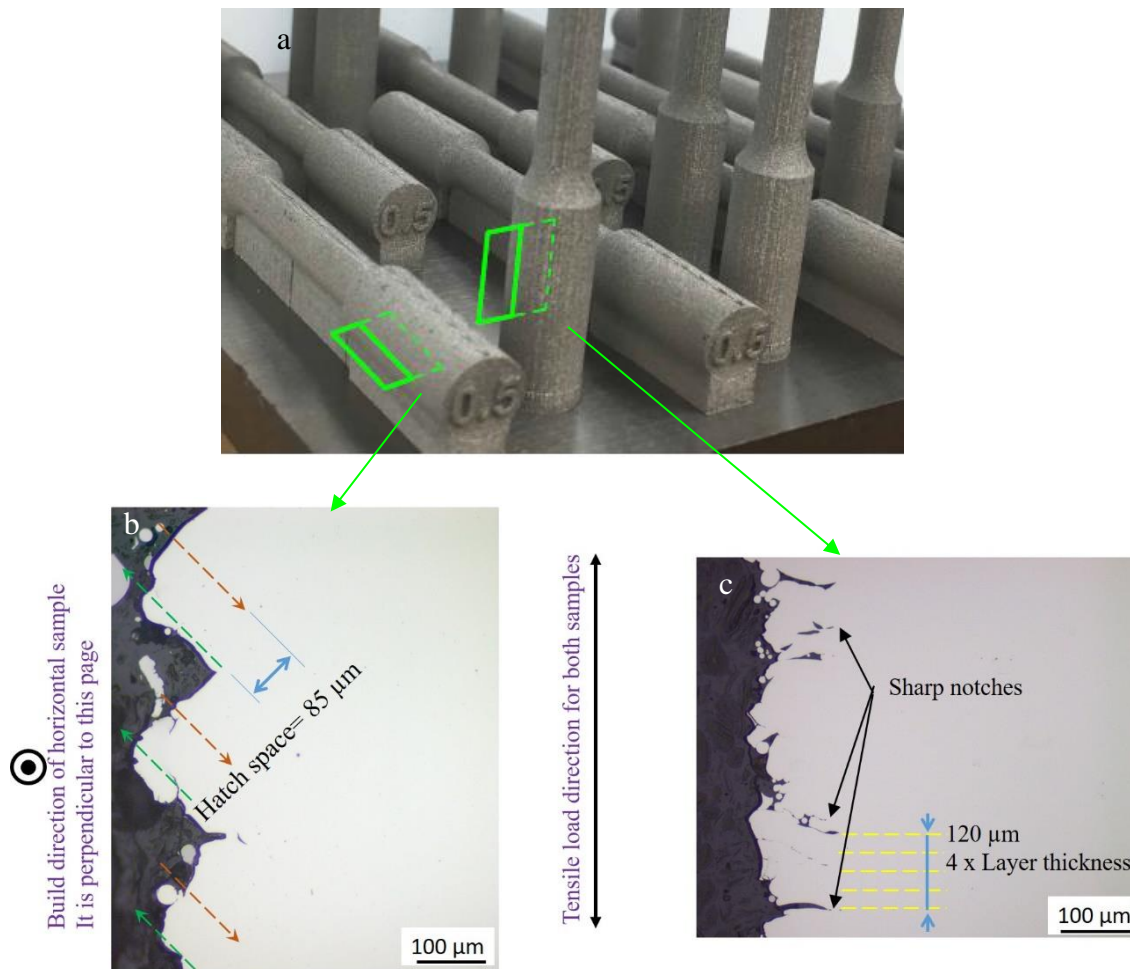


Figure 5-10: a) Longitudinal cutting direction for outer surface morphology, b) Optical microscopy of an as-built horizontal sample, and c) an as-built vertical sample.

Figure 5-11 shows the graphs of the UTS versus elongation of the machined horizontal (Figure 5-11a) and vertical (Figure 5-11b) samples in this study, compared with the results reported in the literature for the non-heat treated but machined samples [2, 3, 12, 13, 22, 35, 49-52]. Also, the SLM machines used by the researchers are specified in Figure 5-11. The elongation of the machined horizontal samples in Figure 5-11a shows a variation between 2% to 11.8%, while the UTS varies between 1143 MPa and 1393 MPa, which is not as wide as for the elongation. It can be noted that the highest elongation is related to the part with the lowest UTS. Also, Figure 5-11a reveals that the tensile

strength, UTS, and ductility of Ti64 parts fabricated with different SLM machines and different process parameters approximate to a trend that shows an interrelationship between the ductility and strength of the samples, i.e., the ductility and strength vary inversely with respect to each other. This relationship between strength and ductility is very common in most materials fabricated with other manufacturing routes. However, the mechanical strength versus the elongation of the vertical samples in Figure 5-11b shows the widely dispersed results in the open literature, making it hard to conclude confidently that UTS and ductility vary inversely, regardless of the machine and process parameters. The scattered mechanical properties of vertical samples noticed in the literature, may be due to the direction of applied load with respect to orientation of defects which results in magnification of applied stress more acutely for vertical samples. In another words, regardless of the SLM machine and the process parameters, the mechanical properties of SLM fabricated Ti64 parts in the machined condition can be predicable to some extent when the parts are supposed to carry the load parallel to the deposited layer (horizontal samples), but it is not true for vertical samples.

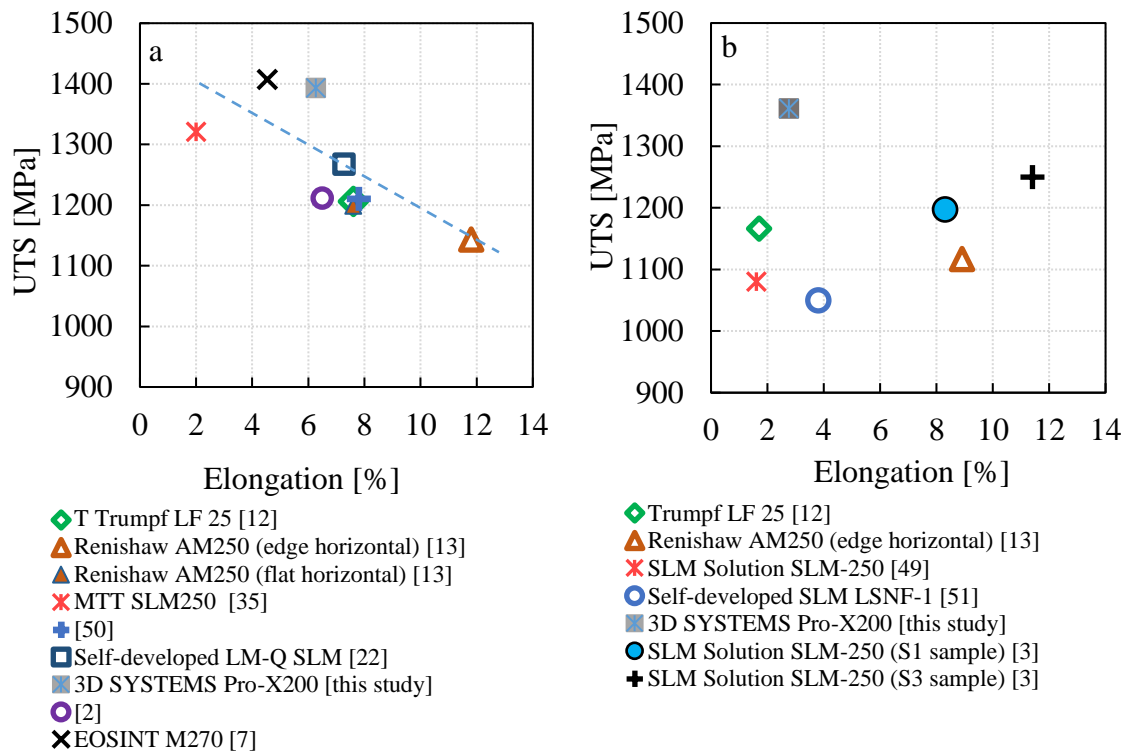


Figure 5-11: UTS versus Elongation of SLM fabricated Ti64 parts, a) machined horizontals, and b) machined verticals.

5.3.3 Fracture analysis

A visual inspection of the fracture surface is summarised in Figure 5-12. As mentioned earlier, for statistical significance, three tensile samples of each group were fabricated and tested. Figure 5-12 only displays the cut sections of one typical sample from each group. The fracture surface of the as-built horizontal sample (Figure 5-12a), machined horizontal (Figure 5-12c) and machined vertical (Figure 5-12d) with the shear lips around the edge periphery, indicate the ductile fracture mode for these samples, whereas the flat fracture surface of the as-built vertical, Figure 5-12b, without a well-developed shear lip on a portion of the edge periphery of the fracture surface, resembles the brittle fracture mode. Having two different modes of fracture (brittle and ductile) is inconceivable for

the SLM parts fabricated and tested at the same conditions. The flatness of the fracture surface for the as-built vertical sample may be attributed to the crack initiation site, propagation, and speed of crack growth; otherwise, the mode of fracture is the same for both the horizontal and vertical samples. It means that the flat fracture surface of an as-built vertical sample does not represent the brittle fracture mode, but instead displays a catastrophic failure caused by overload, i.e., fast ductile fracture. The fact that the vertical as-built sample does not show well-developed shear lips may be an indication that the crack initiates at the surface for vertical samples. This observation supports the hypothesis in the previous section, where the sharp valleys on the surface of the as-built vertical were suggested as acting as stress raiser and crack initiation sites.

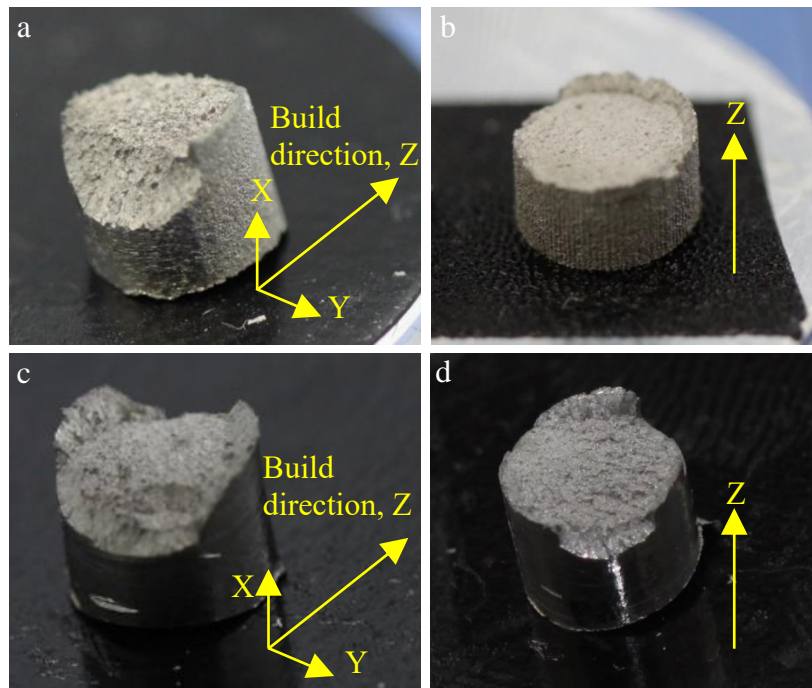


Figure 5-12: Typical fracture surfaces of (a) as-built horizontal sample, (b) as-built vertical sample, (c) machined horizontal sample and (d) machined vertical sample.

Optical microscopy of the etched longitudinal section of the fracture surface is shown in Figure 5-13. The flat fracture surface of the as-built vertical sample has been further

highlighted in Figure 5-13a. In addition, Figure 5-13b, confirms the effectiveness of the sharp rooted surface profile of the as-built vertical sample in crack initiation from the surface of the as-built verticals. In contrast with the vertical samples, Figure 5-14 displays the uneven fracture surface of the as-built horizontal samples. The shear lips on each side of the as-built horizontal sample confirm the last stage of fracture takes place near the surface of the horizontal samples, i.e., gives an indication of crack initiation at the centre of the test pieces, propagating towards the surface. This is the classic mechanism of ductile fracture through void coalescence that takes place in a horizontal sample.

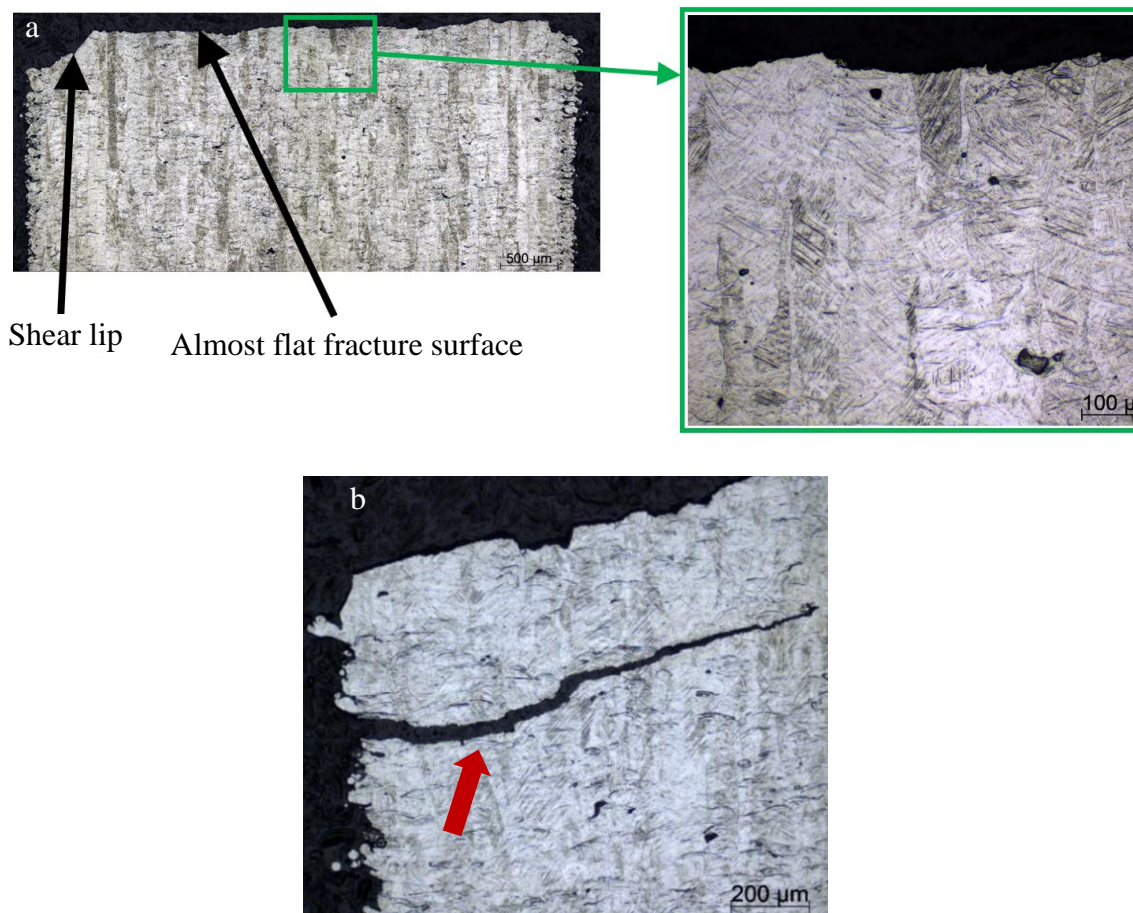


Figure 5-13: Optical micrographs of the longitudinal section of the as-built vertical samples to show a) its flat fracture surface and b) the formation of surface initiated crack as a result of the sharp-rooted surface profile.

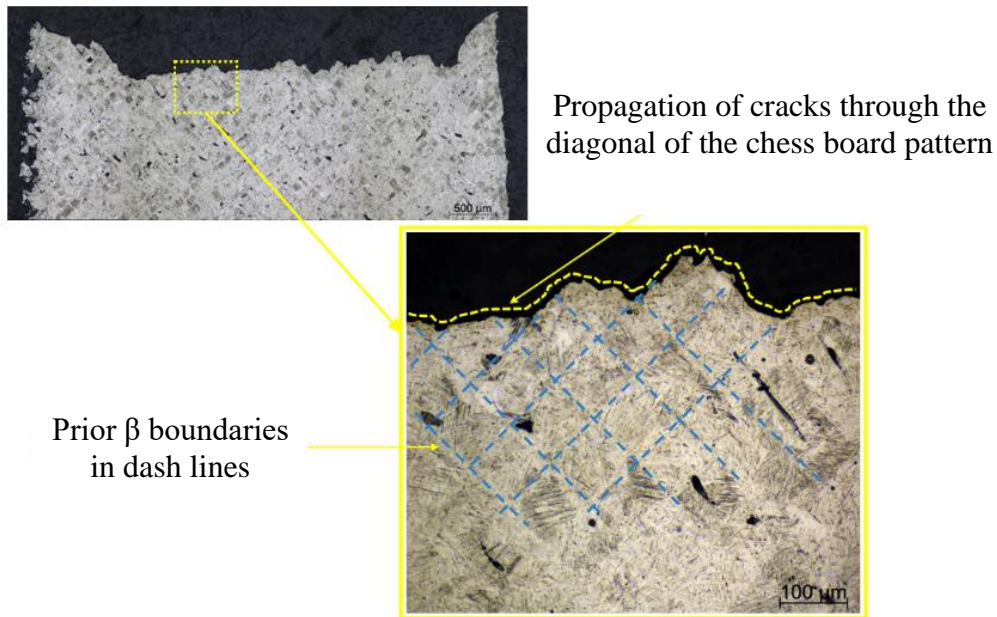


Figure 5-14: Optical micrograph of a crack path for the fracture surface of the as-built horizontal sample with well-developed shear lips.

The fracture surfaces of the machined horizontal and vertical samples are presented in Figure 5-15, showing bulk fractures in the middle of the samples and shear lips around the periphery. The fracture surface of the vertical sample, Figure 5-15a, exhibits a layered topography, meaning that the fracture surface seems to alternate between layers whilst propagating. The quasi-cleavage features with dimples in both the horizontal and vertical samples may indicate a mixed mode of ductile and brittle fracture. A typical microcrack, which connects an inter-layer unfused site to the fracture surface, is clearly seen from the magnified inset in Figure 5-15a; while in the magnified inset of Figure 5-15b, showing a horizontal sample, typical inter-track voids and microcracks are visible. The fracture surface of the machined vertical sample is completely different from the as-built vertical shown in Figure 5-13a. For the machined samples, regardless of the deposition direction (horizontal or vertical), the cracks seem to be initiated within the specimens by void coalescence which then propagates towards the surface. The fracture regions in shear lips are bordered with broken lines in both the vertical and horizontal samples.

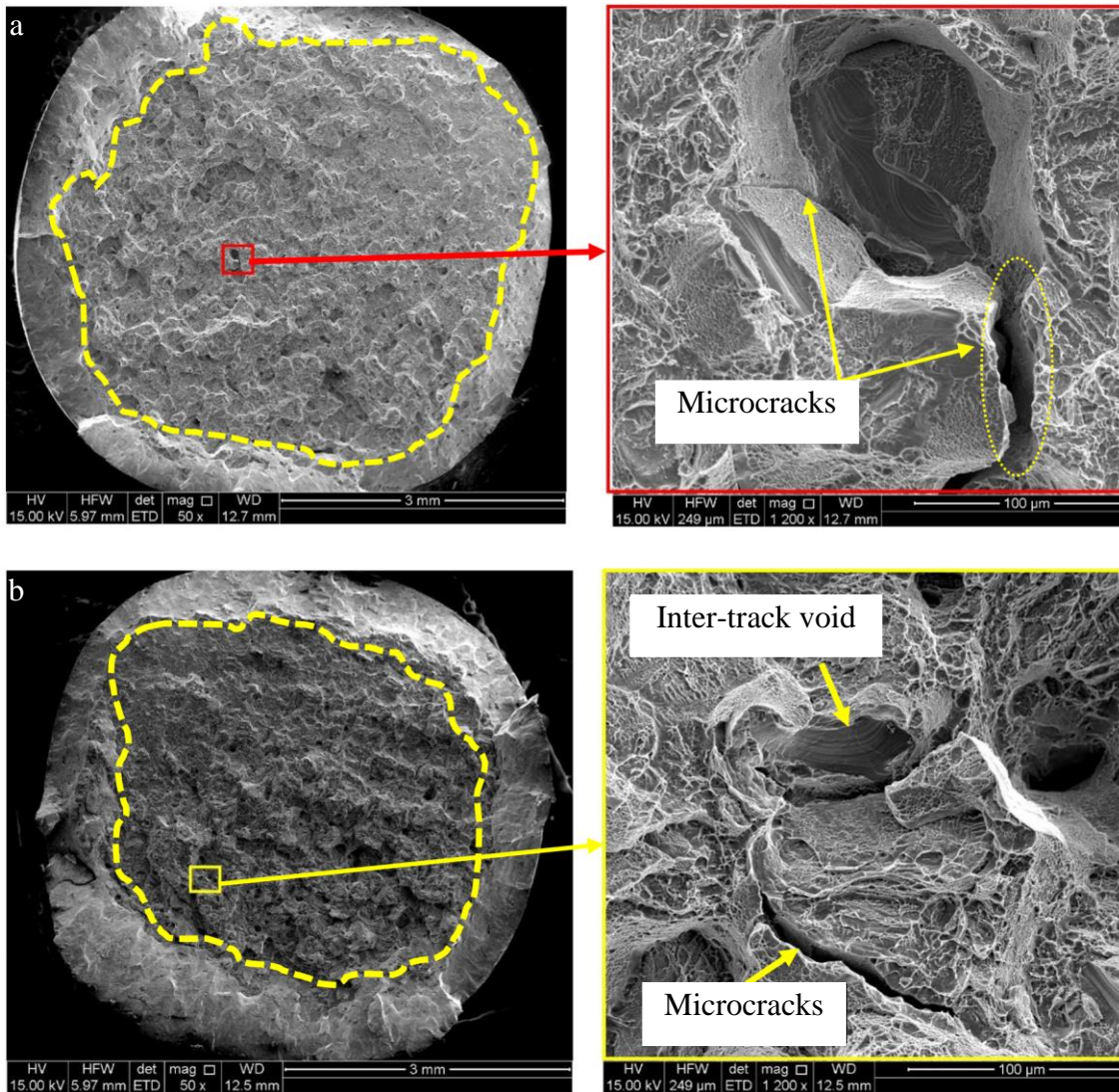


Figure 5-15: SEM micrographs of the fracture surfaces of a) machined vertical with microcracks inter-connecting between layers. The broken lines show the borderline of the shear lips regions and bulk fracture surfaces on the machined tensile samples, and b) machined horizontal with a typical inter-track void and microcrack.

In order to confirm the hypothesis of fast fracture in the as-built vertical due to the lack of micro-void coalescence in contrast with the other samples, the porosity contents of the fractured test pieces at the vicinity of the fracture surface within the gauge length were measured and plotted in Figure 5-16. As shown in Figure 5-16, the levels of porosity developed in the gauge section of both horizontal samples (machined and as-built), are

almost the same, meaning that void coalescence is taking place in both the machined and as-built horizontal samples. This confirms the fracture mechanism is the same for both conditions. There is an increase of around five folds to the average porosity in their grip sections. Although the porosity in the gauge section of the machined vertical exhibits nearly three times increase to its grip section (which confirms the void coalescence mechanism), the as-built vertical behaved completely differently. In fact, the as-built vertical sample did not show any changes in the porosity level near the fracture surface when compared with its grip section. These results reconfirm that the fracture of the as-built vertical sample did not initiate from the centre of the part by coalescence of the voids and development of pores, but from its periphery surface. In addition, Figure 5-16 reveals that the porosity increase in the gauge section of the machined vertical sample is far less than both the machined and as-built horizontal samples. This result means that the pores' coalescence in machined vertical samples is not as prevalent as for the horizontal samples and, if related to the anisotropy of pores, it may justify a lower elongation value for the machined vertical samples when compared with both the machined and as-built horizontal samples.

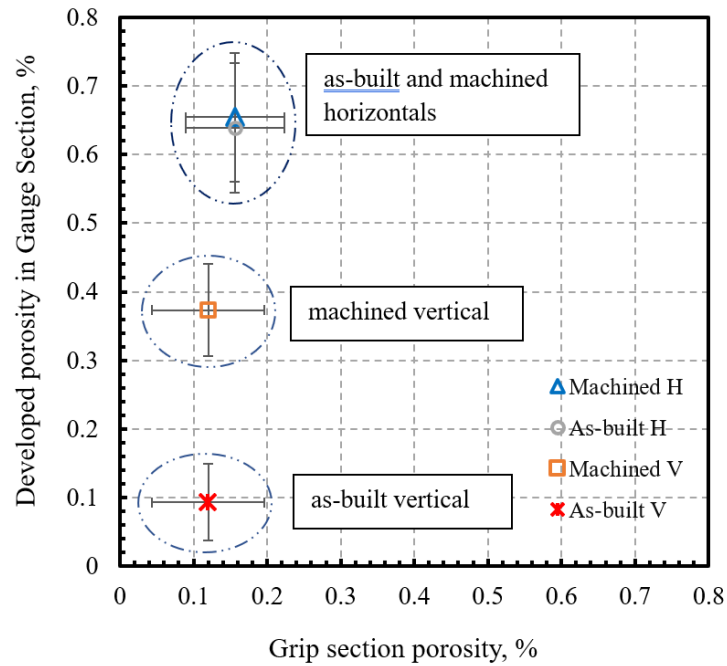


Figure 5-16: Developed porosity in the gauge section of all samples near the fracture surface (gauge section) vs the porosity in the grip section.

5.4 Conclusions

This work reports a novel design approach to fabricate undistorted “truly as-built” Ti-6Al-4V horizontal samples via an SLM technique where the samples are not treated under any post-fabrication processes, such as machining and/or heat treatment. These horizontal samples are now valid for tensile tests and can be compared with their vertical counterparts. This study highlights that alignment of the SLM layering direction with respect to the tensile loading direction in as-built samples is critical. This research paper shows that “truly as-built” samples, in which the applied load is aligned with deposited layers like in the horizontal samples, can be acceptable for some applications, without any post process treatments. But vertical samples, in which the applied load is perpendicular to the deposited layers, suffer from premature failure under just 38% of the nominal load that their horizontal counterparts can carry before failure. This means that the vertical samples are not suitable to be used directly in any applications prior to post processing, which was the machining process in this paper. It is believed that this

shortcoming in vertical samples is related to the deficiencies in the vertical as-built surfaces, which in turn, can be correlated to the quality of the surface and/or induced residual stress on the surface. Furthermore, it is shown that a relationship between the strength along the deposited layer (as for horizontal samples) and ductility of SLM fabricated Ti64 can be established, regardless of the SLM machine and process parameters: i.e., they vary inversely with respect to each other. However, such interrelationships between the strength perpendicular to the deposited layers and ductility remain rather uncertain.

5.5 Declaration of competing interest

We wish to confirm that there are no known conflicts of interest associated with this publication.

5.6 Acknowledgements

This work was performed in part at the OptoFab node of the Australian National Fabrication Facility (ANFF) utilizing Commonwealth and South Australian State Government funding. Adelaide Microscopy is gratefully acknowledged for providing access to electron microscopy facilities. A. Dare Baghi is grateful to the Australian Government and Adelaide University for the PhD scholarship.

References

1. Shipley, H., D. McDonnell, M. Culleton, R. Lupoi, G. O'Donnell, and D. Trimble, *Optimisation of process parameters to address fundamental challenges during selective laser melting of Ti-6Al-4V: A review*. International Journal of Machine Tools and Manufacture, 2018. **128**: p. 1-20.
2. Hollander, D.A., M. von Walter, T. Wirtz, R. Sellei, B. Schmidt-Rohlfing, O. Paar, and H.-J. Erli, *Structural, mechanical and in vitro characterization of individually structured Ti-6Al-4V produced by direct laser forming*. Biomaterials, 2006. **27**(7): p. 955-963.
3. Xu, W., M. Brandt, S. Sun, J. Elambasseril, Q. Liu, K. Latham, K. Xia, and M. Qian, *Additive manufacturing of strong and ductile Ti-6Al-4V by selective laser melting via in situ martensite decomposition*. Acta Materialia, 2015. **85**: p. 74-84.
4. Banerjee, D. and J.C. Williams, *Perspectives on Titanium Science and Technology*. Acta Materialia, 2013. **61**(3): p. 844-879.
5. Santos, L.V., V.J. Trava-Airoldi, E.J. Corat, J. Nogueira, and N.F. Leite, *DLC cold welding prevention films on a Ti6Al4V alloy for space applications*. Surface and Coatings Technology, 2006. **200**(8): p. 2587-2593.
6. Geetha, M., A.K. Singh, R. Asokamani, and A.K. Gogia, *Ti based biomaterials, the ultimate choice for orthopaedic implants – A review*. Progress in Materials Science, 2009. **54**(3): p. 397-425.
7. Murr, L., S. Quinones, S. Gaytan, M. Lopez, A. Rodela, E. Martinez, D. Hernandez, E. Martinez, F. Medina, and R. Wicker, *Microstructure and mechanical behavior of Ti-6Al-4V produced by rapid-layer manufacturing, for biomedical applications*. Journal of the mechanical behavior of biomedical materials, 2009. **2**(1): p. 20-32.
8. Song, B., S. Dong, B. Zhang, H. Liao, and C. Coddet, *Effects of processing parameters on microstructure and mechanical property of selective laser melted Ti6Al4V*. Materials & Design, 2012. **35**: p. 120-125.
9. Gong, H., K. Rafi, H. Gu, G.D. Janaki Ram, T. Starr, and B. Stucker, *Influence of defects on mechanical properties of Ti-6Al-4V components produced by selective laser melting and electron beam melting*. Materials & Design, 2015. **86**: p. 545-554.
10. Hartunian, P. and M. Eshraghi, *Effect of Build Orientation on the Microstructure and Mechanical Properties of Selective Laser-Melted Ti-6Al-4V Alloy*. Journal of Manufacturing and Materials Processing, 2018. **2**(4): p. 69.
11. Rafi, H.K., N.V. Karthik, H. Gong, T.L. Starr, and B.E. Stucker, *Microstructures and Mechanical Properties of Ti6Al4V Parts Fabricated by Selective Laser Melting and Electron Beam Melting*. Journal of Materials Engineering and Performance, 2013. **22**(12): p. 3872-3883.
12. Vilaro, T., C. Colin, and J.D. Bartout, *As-Fabricated and Heat-Treated Microstructures of the Ti-6Al-4V Alloy Processed by Selective Laser Melting*. Metallurgical and Materials Transactions A, 2011. **42**(10): p. 3190-3199.

13. Simonelli, M., Y.Y. Tse, and C. Tuck, *Effect of the build orientation on the mechanical properties and fracture modes of SLM Ti-6Al-4V*. Materials Science and Engineering: A, 2014. **616**: p. 1-11.
14. Zaeh, M.F. and G. Branner, *Investigations on residual stresses and deformations in selective laser melting*. Production Engineering, 2010. **4**(1): p. 35-45.
15. Mercelis, P. and J.P. Kruth, *Residual stresses in selective laser sintering and selective laser melting*. Rapid Prototyping Journal, 2006. **12**(5): p. 254-265.
16. Kruth, J.-P., J. Deckers, E. Yasa, and R. Wauthlé, *Assessing and comparing influencing factors of residual stresses in selective laser melting using a novel analysis method*. Proceedings of the institution of mechanical engineers, Part B: Journal of Engineering Manufacture, 2012. **226**(6): p. 980-991.
17. Yadroitsev, I. and I. Yadroitsava, *Evaluation of residual stress in stainless steel 316L and Ti6Al4V samples produced by selective laser melting*. Virtual and Physical Prototyping, 2015. **10**(2): p. 67-76.
18. Yadroitsava, I., S. Grewar, D. Hattingh, and I. Yadroitsev. *Residual stress in SLM Ti6Al4V alloy specimens*. in *7th International Light Metals Technology Conference, LMT 2015, July 27, 2015 - July 29, 2015*. 2015. Port Elizabeth, South africa: Trans Tech Publications Ltd.
19. Greitemeier, D., C. Dalle Donne, F. Syassen, J. Eufinger, and T. Melz, *Effect of surface roughness on fatigue performance of additive manufactured Ti-6Al-4V*. Materials Science and Technology, 2016. **32**(7): p. 629-634.
20. Rafi, H.K., T.L. Starr, and B.E. Stucker, *A comparison of the tensile, fatigue, and fracture behavior of Ti-6Al-4V and 15-5 PH stainless steel parts made by selective laser melting*. The International Journal of Advanced Manufacturing Technology, 2013. **69**(5-8): p. 1299-1309.
21. Facchini, L., E. Magalini, P. Robotti, A. Molinari, S. Höges, and K. Wissenbach, *Ductility of a Ti-6Al-4V alloy produced by selective laser melting of prealloyed powders*. Rapid Prototyping Journal, 2010. **16**(6): p. 450-459.
22. Vrancken, B., L. Thijs, J.-P. Kruth, and J. Van Humbeeck, *Heat treatment of Ti6Al4V produced by Selective Laser Melting: Microstructure and mechanical properties*. Journal of Alloys and Compounds, 2012. **541**: p. 177-185.
23. *ASTM F2924-14, Standard Specification for Additive Manufacturing Titanium-6 Aluminum-4 Vanadium with Powder Bed Fusion*. 2014.
24. *Qiang Li, Kucukkoc Ibrahim, David Z. Zhang, Production planning in additive manufacturing and 3D printing, Computers & Operations Research, Volume 83, July 2017, Pages 157-172.*
25. *Aini Zuhra Abdul Kadir, Yusri Yusof, Md Saidin Wahab, Additive manufacturing cost estimation models—a classification review, The International Journal of Advanced Manufacturing Technology (2020) 107:4033–4053.*
26. *C.R.Cunningham, S.Wikshåland, F.Xu, N.Kemakolam, A.Shokrani, V.Dhokia, S.T.Newman, Cost Modelling and Sensitivity Analysis of Wire and Arc Additive Manufacturing, Procedia Manufacturing, Volume 11, 2017, Pages 650-657.*
27. *Huang, Runze, Ulu, Erva, Kara, Levent Burak, and Whitefoot, Kate S. "Cost Minimization in Metal Additive Manufacturing Using Concurrent Structure and*

- Process Optimization." Proceedings of the ASME 2017 International Design Engineering Technical Conferences and Computers and Information in Engineering Conference. Volume 2A: 43rd Design Automation Conference. Cleveland, Ohio, USA. August 6–9, 2017. V02AT03A030. ASME. <https://doi.org/10.1115/DETC2017-67836>.*
28. Jamshidi, P., M. Aristizabal, W. Kong, V. Villapun, S.C. Cox, L.M. Grover, and M.M. Attallah, *Selective laser melting of Ti-6Al-4V: the impact of post-processing on the tensile, fatigue and biological properties for medical implant applications*. Materials, 2020. **13**(12): p. 2813.
 29. Antonysamy, A.A., J. Meyer, and P.B. Prangnell, *Effect of build geometry on the β -grain structure and texture in additive manufacture of Ti6Al4V by selective electron beam melting*. Materials Characterization, 2013. **84**: p. 153-168.
 30. Tang, H., M. Qian, N. Liu, X. Zhang, G. Yang, and J. Wang, *Effect of powder reuse times on additive manufacturing of Ti-6Al-4V by selective electron beam melting*. Jom, 2015. **67**(3): p. 555-563.
 31. Quintana, O.A. and W. Tong, *Effects of Oxygen Content on Tensile and Fatigue Performance of Ti-6Al-4 V Manufactured by Selective Laser Melting*. JOM, 2017. **69**(12): p. 2693-2697.
 32. Kumar, S., *Selective Laser Sintering/Melting*, in *Comprehensive Materials Processing*. 2014, Elsevier. p. 93-134.
 33. Baghi, A.D., *Additive Manufacturing of Titanium-Based Biomedical Alloys*, in *School of Mechanical Engineering*. 2016-2020, The University of Adelaide.
 34. *ASTM E8/E8M -16a Standard Test Methods for Tension Testing of Metallic Materials*. 2016.
 35. Mertens, A., S. Reginster, H. Paydas, Q. Contrepolis, T. Dormal, O. Lemaire, and J. Lecomte-Beckers, *Mechanical properties of alloy Ti-6Al-4V and of stainless steel 316L processed by selective laser melting: Influence of out-of-equilibrium microstructures*. Powder Metallurgy, 2014. **57**(3): p. 184-189.
 36. Yang, J., J. Han, H. Yu, J. Yin, M. Gao, Z. Wang, and X. Zeng, *Role of molten pool mode on formability, microstructure and mechanical properties of selective laser melted Ti-6Al-4V alloy*. Materials & Design, 2016. **110**: p. 558-570.
 37. Yasa, E., J. Deckers, J.-P. Kruth, M. Rombouts, and J. Luyten, *Experimental investigation of Charpy impact tests on metallic SLM parts*. Innovative Developments in Design and Manufacturing Advanced Research in Virtual and Rapid Prototyping, 2009: p. 207-214.
 38. Thijs, L., F. Verhaeghe, T. Craeghs, J.V. Humbeeck, and J.-P. Kruth, *A study of the microstructural evolution during selective laser melting of Ti-6Al-4V*. Acta Materialia, 2010. **58**(9): p. 3303-3312.
 39. Simonelli, M., Y.Y. Tse, and C. Tuck, *On the Texture Formation of Selective Laser Melted Ti-6Al-4V*. Metallurgical and Materials Transactions A, 2014. **45**(6): p. 2863-2872.
 40. Beladi, H., Q. Chao, and G.S. Rohrer, *Variant selection and intervariant crystallographic planes distribution in martensite in a Ti-6Al-4V alloy*. Acta Materialia, 2014. **80**: p. 478-489.

41. Galarraga, H., R.J. Warren, D.A. Lados, R.R. Dehoff, M.M. Kirka, and P. Nandwana, *Effects of heat treatments on microstructure and properties of Ti-6Al-4V ELI alloy fabricated by electron beam melting (EBM)*. Materials Science and Engineering: A, 2017. **685**: p. 417-428.
42. Li, B., Y. Shen, W. Hu, and L. Luo, *Surface modification of Ti-6Al-4V alloy via friction-stir processing: microstructure evolution and dry sliding wear performance*. Surface and Coatings Technology, 2014. **239**: p. 160-170.
43. Rangaswamy, P., T. Holden, R. Rogge, and M. Griffith, *Residual stresses in components formed by the laserengineered net shaping (LENS®) process*. The Journal of strain analysis for engineering design, 2003. **38**(6): p. 519-527.
44. Hrabe, N. and T. Quinn, *Effects of processing on microstructure and mechanical properties of a titanium alloy (Ti-6Al-4V) fabricated using electron beam melting (EBM), Part 2: Energy input, orientation, and location*. Materials Science and Engineering: A, 2013. **573**: p. 271-277.
45. Carroll, B.E., T.A. Palmer, and A.M. Beese, *Anisotropic tensile behavior of Ti-6Al-4V components fabricated with directed energy deposition additive manufacturing*. Acta Materialia, 2015. **87**: p. 309-320.
46. Moletsane, M., P. Krakhmalev, N. Kazantseva, A. Du Plessis, I. Yadroitsava, and I. Yadroitsev, *Tensile properties and microstructure of direct metal laser-sintered Ti6Al4V (ELI) Alloy*. South African Journal of Industrial Engineering, 2016. **27**(3): p. 110-121.
47. Sridharan, N., A. Chaudhary, P. Nandwana, and S.S. Babu, *Texture evolution during laser direct metal deposition of Ti-6Al-4V*. Jom, 2016. **68**(3): p. 772-777.
48. Frey, M., M. Shellabear, and L. Thorsson, *Mechanical testing of DMLS parts*. EOS whitepaper, EOS GmbH, Munich, 2009.
49. Leuders, S., M. Thöne, A. Riemer, T. Niendorf, T. Tröster, H.A. Richard, and H.J. Maier, *On the mechanical behaviour of titanium alloy TiAl6V4 manufactured by selective laser melting: Fatigue resistance and crack growth performance*. International Journal of Fatigue, 2013. **48**: p. 300-307.
50. Zhao, J.-R., F.-Y. Hung, T.-S. Lui, and Y.-L. Wu, *The Relationship of Fracture Mechanism between High Temperature Tensile Mechanical Properties and Particle Erosion Resistance of Selective Laser Melting Ti-6Al-4V Alloy*. Metals, 2019. **9**(5): p. 501.
51. Yang, J., H. Yu, Z. Wang, and X. Zeng, *Effect of crystallographic orientation on mechanical anisotropy of selective laser melted Ti-6Al-4V alloy*. Materials Characterization, 2017. **127**: p. 137-145.
52. Murr, L.E., S.A. Quinones, S.M. Gaytan, M.I. Lopez, A. Rodela, E.Y. Martinez, D.H. Hernandez, E. Martinez, F. Medina, and R.B. Wicker, *Microstructure and mechanical behavior of Ti-6Al-4V produced by rapid-layer manufacturing, for biomedical applications*. J Mech Behav Biomed Mater, 2009. **2**(1): p. 20-32.

Chapter 6

Surface machining versus thermal treatment


Chapter overview

In this chapter two post process of surface machining and thermal treatments is studied. Two individual thermal treatments of stress relieving at temperature of 670 and annealing at 850 are compared. It is presented that any kind of treatments of either surface machining or thermal treatments (of stress relieving or annealing) can prevent premature failure observed in as-built vertical samples. This chapter highlights the higher effectiveness of annealing compared to the other thermal treatment of stress relieving besides surface machining treatment. The following section presents the word format of a published paper in the “Journal of Manufacturing Processes”.

Statement of Authorship

Title of Paper	Effective post processing of SLM fabricated Ti-6Al-4 V alloy: Machining vs thermal treatment
Publication status	<input checked="" type="checkbox"/> Published <input type="checkbox"/> Accepted for Publication <input type="checkbox"/> Submitted for Publication <input type="checkbox"/> Unpublished and Unsubmitted work written in manuscript style
Publication Details	A. Dareh Baghi , S. Nafisi, R. Hashemi, H. Ebendorff-Heidepriem, and R. Ghomashchi, "Effective post processing of SLM fabricated Ti-6Al-4 V alloy: Machining vs thermal treatment", <i>Journal of Manufacturing Processes</i> , vol. 68, pp. 1031-1046, 2021/08/01/ 2021.


Principal Author


Name of Principal Author (Candidate)	Alireza Dareh Baghi		
Contribution to the Paper	Developed the ideas and concepts, designed 3D models of the samples, conducted the experiments, acquired the data, interpreted results and drafted the manuscript		
Overall percentage (%)	85%		
Certification:	This paper reports on original research I conducted during the period of my Higher Degree by Research candidature and is not subject to any obligations or contractual agreements with a third party that would constrain its inclusion in this thesis. I am the primary author of this paper.		
Signature		Date	11/05/2022

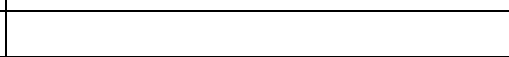
Co-Author Contributions

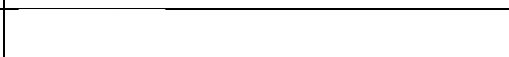
By signing the Statement of Authorship, each author certifies that:

- I. the candidate's stated contribution to the publication is accurate (as detailed above);
- II. permission is granted for the candidate to include the publication in the thesis; and
- III. the sum of all co-author contributions is equal to 100% less the candidate's stated contribution.

Name of Co-Author	Reza Ghomashchi		
Contribution to the Paper	Supervised the work, participated in developing ideas, evaluated the results and discussion, and edited the manuscript.		
Signature		Date	11/05/2022

Name of Co-Author	Shahrooz Nafisi		
Contribution to the Paper	Helped and encouraged in developing the experimental design, feedback on manuscript.		
Signature		Date	28/10/2022

Name of Co-Author	Reza Hashemi		
Contribution to the Paper	Helped in running the experiments, academic discussion, and manuscript review		
Signature		Date	13/05/2022

Name of Co-Author	Heike Ebendorff-Heidepriem		
Contribution to the Paper	Supervised the research, provided the 3D printed samples and reviewed the manuscript.		
Signature		Date	16/05/2022

Effective post processing of SLM fabricated Ti-6Al-4V alloy:

Machining vs thermal treatment

Alireza Dareh Baghi, Shahrooz Nafisi, Reza Hashemi, Heike Ebendorff-Heidepriem,
Reza Ghomashchi

Abstract

Anisotropy in the mechanical properties with respect to the build direction of Selective Laser Melting (SLM) fabricated titanium parts is a known, challenging problem, which can be mitigated using a post processing method such as heat treatment. This paper investigates the potential sources of anisotropy associated with SLM fabricated Ti64 parts and studies the influence of heat treatment on the anisotropy in mechanical properties' behaviour in two directions: vertical and horizontal. SLM fabricated samples were machined and stress-relieved at 670°C. In addition, annealing at 850°C was performed on the machined samples to investigate the effect of heat treatment at a higher temperature on the anisotropy behaviour of the machined parts. The tensile test results showed that the difference in elongation at fracture between the vertical and horizontal samples (elongation anisotropy) will reduce from 125% in non-heat treated samples to 36% when the samples are annealed.

Microstructural analyses revealed an anomaly, which is named the fish scale feature in this work. This newly-found type of defect was significantly identifiable in non-heat treated samples; however, after annealing it completely disappeared from the microstructure. It is believed that the fish scale defect plays a role in the failure of vertical samples.

The same stress-relieving and annealing processes were then investigated on as-built vertical samples. The outcome revealed that the annealing process provides a greater improvement than machining. The results demonstrate that each post process, either machining or annealing, can eliminate the premature failure problem of as-built vertical samples, which occurs at a fracture strain of 0.5% under 482 MPa stress. Machining improves the fracture strength of the non-machined vertical samples to 1361 MPa at a strain of 2.8%; whereas annealing can enhance the fracture stress (premature) from 482 MPa to 1069 MPa, with a significant increase in fracture strain from 0.5% to 4%. The observations were found to be correlated to the phase change in the microstructure, mitigating the influence of defects such as the fish scale feature and full removal of the residual stress during annealing.

6.1 Introduction

The selective laser melting (SLM) fabrication method, as one of the additive manufacturing (AM) techniques, has drawn extensive attention because of its ability to produce intricate parts in one single manufacturing process. One of the advantages of the SLM route is its ability to process high melting temperature materials, such as Ti-based light alloys [1, 2], where conventional methods, such as casting and machining, may be neither viable for the required mechanical and physical properties nor cost effective. Ti-6Al-4V (Ti64), with its wide applications in the aerospace [3, 4] and biomedical [5, 6] fields, is among the titanium alloys shaped by SLM with some interesting outcomes. Despite the high strength offered by SLM-fabricated Ti64 parts, the ductility is inferior when compared with conventionally manufactured components. This is due to the non-equilibrium martensitic phase α' appearing in the microstructure, which is associated with the rapid solidification rates encountered during the SLM process [7-11].

In addition, there may be a certain degree of undesirable anisotropy in the mechanical properties, depending on the build direction, for vertically- or horizontally-built parts [11-15]. In a previous study by the authors [16], the effect of build orientation on the tensile properties of as-built vertical and horizontal Ti64 samples was studied for which the unwanted distortion that normally occurs in as-built horizontal parts was eliminated through a novel design. It was reported that the post machining process can improve the mechanical properties of truly as-built vertical and horizontal parts in terms of ductility and strength, but they still suffer from anisotropy in ductility (elongation % at fracture), i.e., 6.3% for machined horizontal as against 2.8% for machined vertical parts.

This raises an important question as to whether or not a post heat treatment would be able to effectively resolve the problem of anisotropy in mechanical properties observed in the SLM fabricated Ti64 alloy (both horizontal and vertical parts). Despite a reasonable number of reports in the literature studying the mechanical strength and elongation (with and without heat treatment) [17-19], there is still limited information available in terms of how and why an applied thermal treatment might mitigate the influence of build orientation and the resultant anisotropy on the mechanical properties of SLM fabricated Ti64 parts [11].

Also, it has already been reported that the as-built (non-machined surface) vertical parts suffer from premature failure; and importantly, the mechanical strength vs the elongation of vertical sample reviewed in open literature, showed widely-dispersed results compared with horizontally built parts [16]. Chlebus et al. [20] discuss how the drastic decrease in the ultimate tensile strength (UTS) of their vertical samples, compared with two series of horizontal samples, is mainly related to the high level of residual stresses and the orientation of flat-shape pores (with their small tip radii) with respect to the applied tensile

load. Thus, the vertical samples are susceptible to fail under lower stresses and strains, resulting in premature failure in the as-built (non-machined surface) condition.

In the absence of generally optimised process parameters to fabricate the parts with the most consistent mechanical properties, especially in as-built vertical parts, finding an effective post process, to save the vertical parts from premature failure, is vital. It has been reported that the premature failure of as-built vertical samples may be resolved by machining the outer surface [16]. However, a post machining process may not be preferable as additive manufacturing aims to produce parts in one step without the need for another fabrication process such as machining. Also, machining may not be feasible for complex parts that are conveniently fabricated using additive manufacturing. This highlights the need to explore if a post heat treatment can be an effective substitute for machining, with the aim of preventing the occurrence of premature failure in as-built vertical parts.

This paper therefore aims to study how and why a post heat treatment can first reduce anisotropy and then make significant improvements in the mechanical properties of SLM fabricated Ti64 alloy with an emphasis on as-built vertical parts. This will be accomplished through a careful investigation of the microstructure (including phase analysis and defects).

The findings of this study will be useful in manufacturing applications where machining of the as-built SLM titanium parts is very costly or may not be feasible, especially for parts carrying the service load along the layer deposition (as happens in vertically built parts).

6.2 Materials and experimental procedures

6.2.1 Materials

The gas atomized pre-alloyed powder Ti64 (grade 5) was supplied by TLS, Technik GmbH & Co, Germany [21]. The ICP-AES technique was used for the elemental chemical analysis of iron (Fe), aluminium (Al), and vanadium (V). The elemental percentages of hydrogen (H), nitrogen (N), and oxygen (O) were measured using a LECO ONH836 analyser. In addition, the carbon (C) content was analysed by the LECO CS200 instrument. Table 6-1 presents the results of the chemical analysis of the powder and SLM fabricated sample. All elements, especially the impurities and oxygen in both the Ti64 powder and bulk sample, are within the acceptable range recommended by ASTM F2924-14 [22].

The morphology of the powder was examined using an FEI Quanta 450 FEGSEM. The powder exhibits a spherical morphology, Figure 6-1a, which confirms the suitability of the powder for SLM processing. Figure 6-1b shows the powder size distribution measured by a laser particle size analyser, Malvern Mastersizer 2000.

Table 6-1: Chemical composition (wt. %) of Ti64 (grade5) powder.

Item	Al	V	Fe	O	C	N	H	Ti
ASTM F2924-14	5.50- 6.75	3.50- 4.50	Max 0.3	Max 0.2	Max 0.08	Max 0.05	Max 0.015	Bal.
Powder	6.15	3.94	0.18	0.098	0.005	0.010	<0.002	Bal.
SLM fabricated bulk samples	6.14	3.97	0.19	0.114	0.005	0.011	<0.002	Bal.

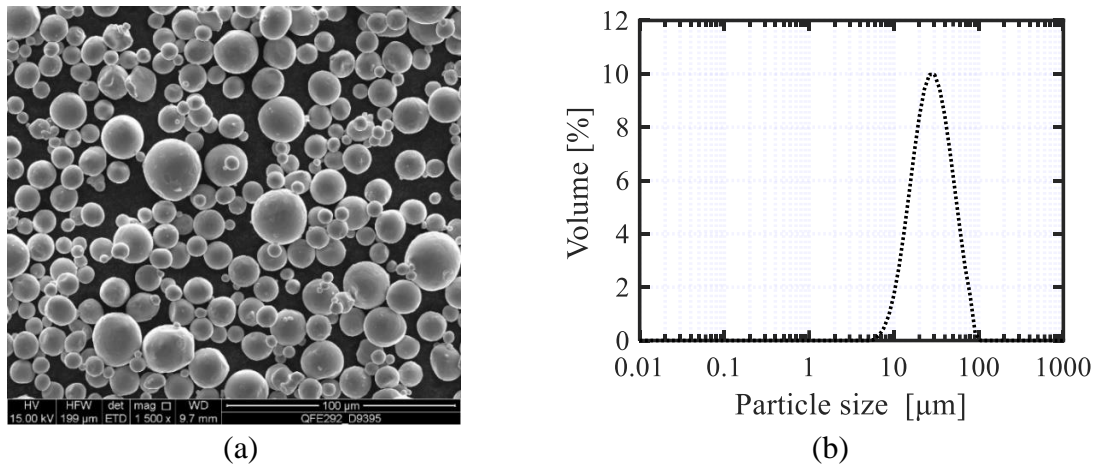


Figure 6-1: a) Typical SEM image of Ti64 powder particles, b) Ti64 particle diameter distribution of powder.

6.2.2 SLM fabrication equipment and method

A 3D SYSTEMS ProX DMP 200 machine was used to fabricate the tensile samples. This machine has a build platform of 140mm x 140mm and is equipped with a laser as the heat source, with a maximum power of 300W in continuous mode and 1070nm wavelength. Argon at atmospheric pressure (101 KPa) filled the build chamber of the machine, while the oxygen level was kept below 500 ppm. Table 6-2 presents the SLM process parameters, optimised to fabricate almost fully dense Ti64 parts. Also, a bi-directional laser strategy with an interlayer 90° rotation ($\pm 45^\circ$ with respect to the X and Y axes) was chosen, Figure 6-2.

Table 6-2: SLM process parameters to fabricate Ti64 samples.

Laser Power, P (W)	Layer thickness, t (μm)	Scanning velocity, v (mm/s)	hatch spacing, h (μm)
270	30	1800	85

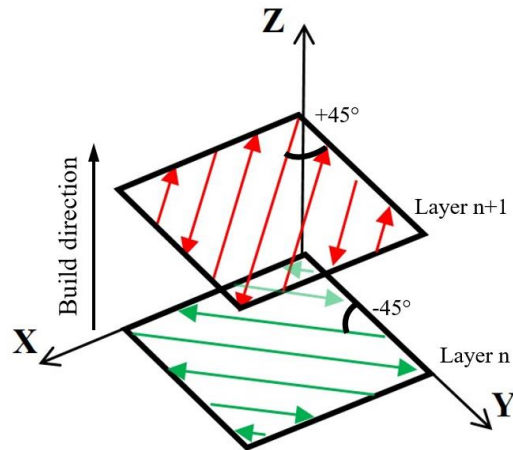


Figure 6-2: Laser scan strategy and build direction.

6.2.3 Tensile samples preparation and heat treatment cycles

In the previous report [16] it was shown that surface machining can significantly improve the mechanical properties of as-built parts, especially in vertical samples. As a result, machined samples are a suitable candidate for investigation of heat treatment on the anisotropy in mechanical properties for both horizontal and vertical samples. By machining the outer surface of the as-built samples, the surface imperfections are removed, and the heat treatment results will not be influenced by surface defects.

In addition to the heat treatment of the machined samples, the effect of heat treatment on the mechanical properties of non-machined (as-built) vertical samples is also investigated. This extra investigation on as-built vertical samples alone aims to compare the effect of surface machining and heat treatment separately and identify the most influential post process in eliminating premature failure in the as-built vertical samples. Therefore, the tensile test samples studied in this research are summarised as below in three groups:

- **MH: Machined Horizontal** samples made from cylindrical rods deposited horizontally, (Figure 6-3a).

- **MV: Machined Vertical** samples made from SLM fabricated vertical rods, (Figure 6-3b).
- **NMV: Non-Machined Vertical** samples, which are as-built tensile test samples, deposited vertically, (Figure 6-3c).

For the MH and MV tensile samples, horizontal and vertical cylindrical rods were initially heat treated, followed by a turning process to make machined tensile test samples, Figure 6-4. It is noteworthy that the shape of the final tensile test samples (MH, MV and NMV), shown in Figure 6-4, complies with the ASTM E8 [23] standard, where the gauge length is 4D (four times the gauge diameter “D”).

Two heat treatments cycles; i.e., stress-relieving and annealing, were conducted in a horizontal resistance heating tube furnace model AY-TF-80-175, with a heating rate of 5°C /min under an inert gas (argon) atmosphere. Temperature control was performed according to SAE AMS 2801B [24] (Table 6-3).

Table 6-3: Heat treatments performed on the cylindrical samples prior to machining.

Heat treatment	Temperature, °C	Soaking time, hr	Cooling type
Stress-relieving	670°C (±10)	5	Controlled furnace cooling from 670°C to 250 °C in 12 hours
Annealing	850°C (±10)	2	Controlled furnace cooling from 850°C to 250 °C in 12 hours

Due to the statistical significance of tensile test results, three samples of each group of MH, MV and NMV were allocated for each heat treatment cycle, i.e., stress relieving and annealing. Apart from the samples dedicated to two cycles of heat treatments, three tensile samples of each group were also assigned to the non-heat treated condition as reference samples. Therefore, nine samples of each group of MH, MV and NMV and ultimately twenty seven samples in total, have been fabricated for this study.

To prepare metallographic samples, transverse cuts (planes shown in Figure 6-3a and b) were collected from the grip section of the MH and MV tensile samples. To investigate the effect of the as-built surface of the NMV on the tensile properties, the metallographic samples were prepared by longitudinally sectioning the NMV sample, Figure 6-3c. Alongside the metallographic samples collected from transverse sections of the MV and MH samples, the fractured surfaces of the MH and MV samples were sectioned longitudinally (along the tensile axis) as demonstrated in Figure 6-5, for crack path characterisation.

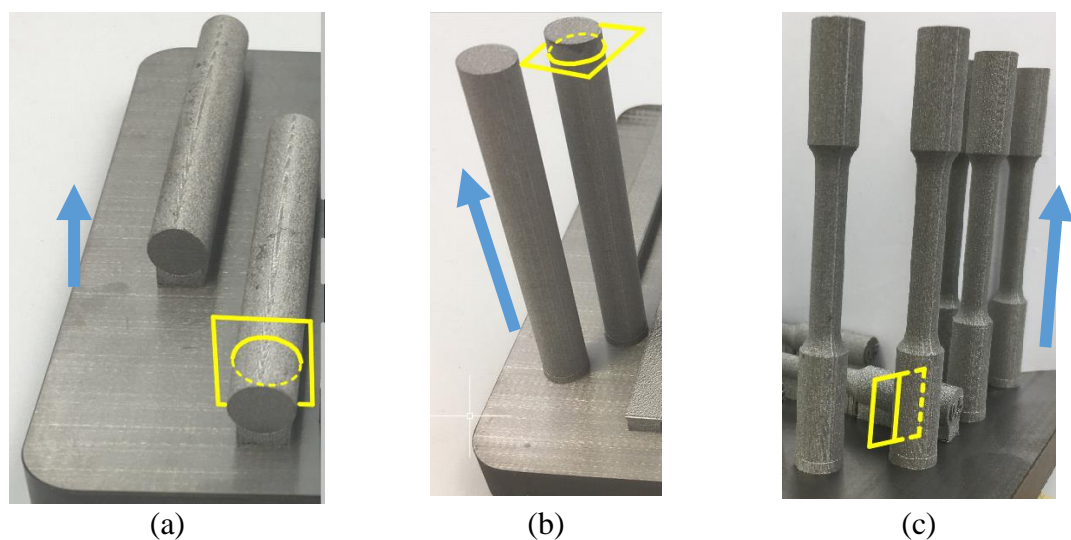


Figure 6-3: a) horizontal deposited rods, b) vertical deposited rods and c) non-machined vertical samples (NMV). (Arrows show the SLM build direction; and the sketched planes demonstrate sectioning for preparation of the metallographic samples).

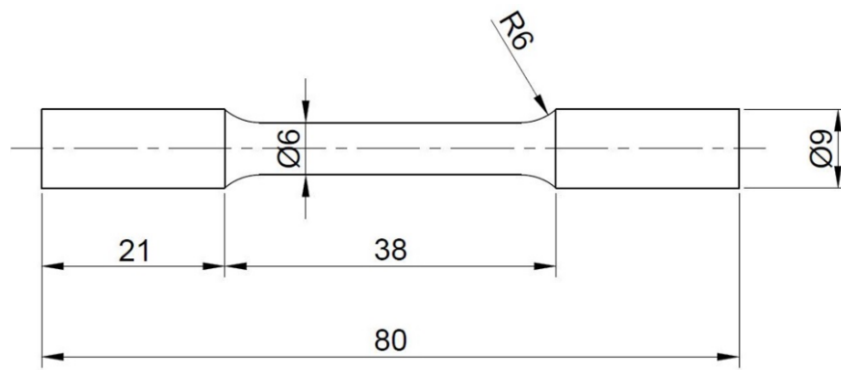


Figure 6-4: Dimensions of the tensile test samples (in mm) according to ASTM E8 [27].

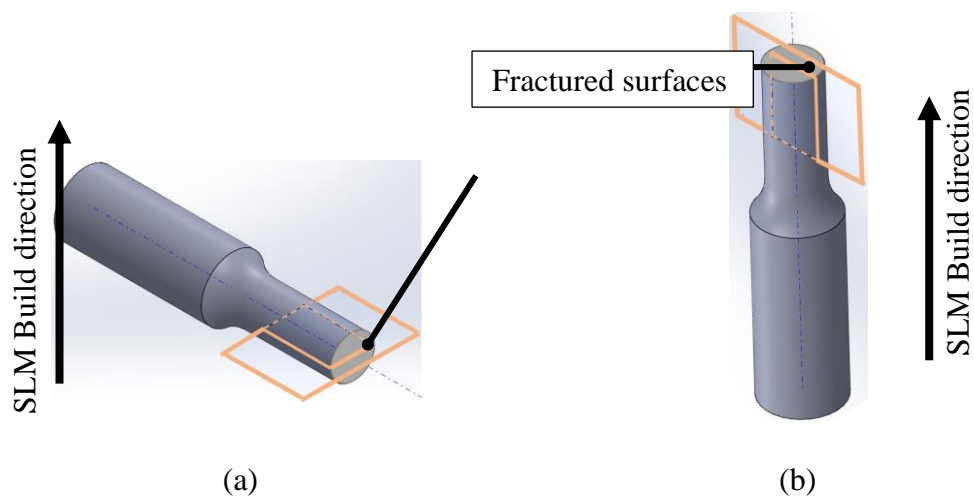


Figure 6-5: Longitudinal sectioning through the fractured surfaces of a) MH and b) MV samples.

6.2.4 Analysis methods

All metallographic samples were etched using Kroll's reagent (3% HF + 5% HNO₃ + 92% distilled water) for 50 seconds. Prior to etching, all samples in the polished condition were examined for porosity content via the 2D area fraction method, employing optical microscopy and image analysis software, ImageJ⁸. Phase identifications of the sectioned samples were conducted with X-ray diffraction in a Rigaku MiniFlex 600 XRD machine with Cu radiation, operating at 40kV and 15mA, with a scan speed of 10°/min over a range of 2 θ from 30° to 80°. For the microstructural analysis, a Zeiss optical microscope Imager2, an FEI Quanta 450 FEG-SEM, and FIB SEM Helios Nanolab FEI Dual Beam were used. Hardness of all sectioned samples from the grip sections (Figure 6-3a and b) were measured by a Vickers microhardness device (LECO, LM-700AT) with a 300g load and dwell time of 10s. Six indentations were performed near the centre of each sample and the average microhardness is reported. An Instron testing machine model 5969 with a load capacity of 50kN was used for conducting the tensile tests with a displacement of 0.20 mm/min at room temperature.

6.3 Results and discussion

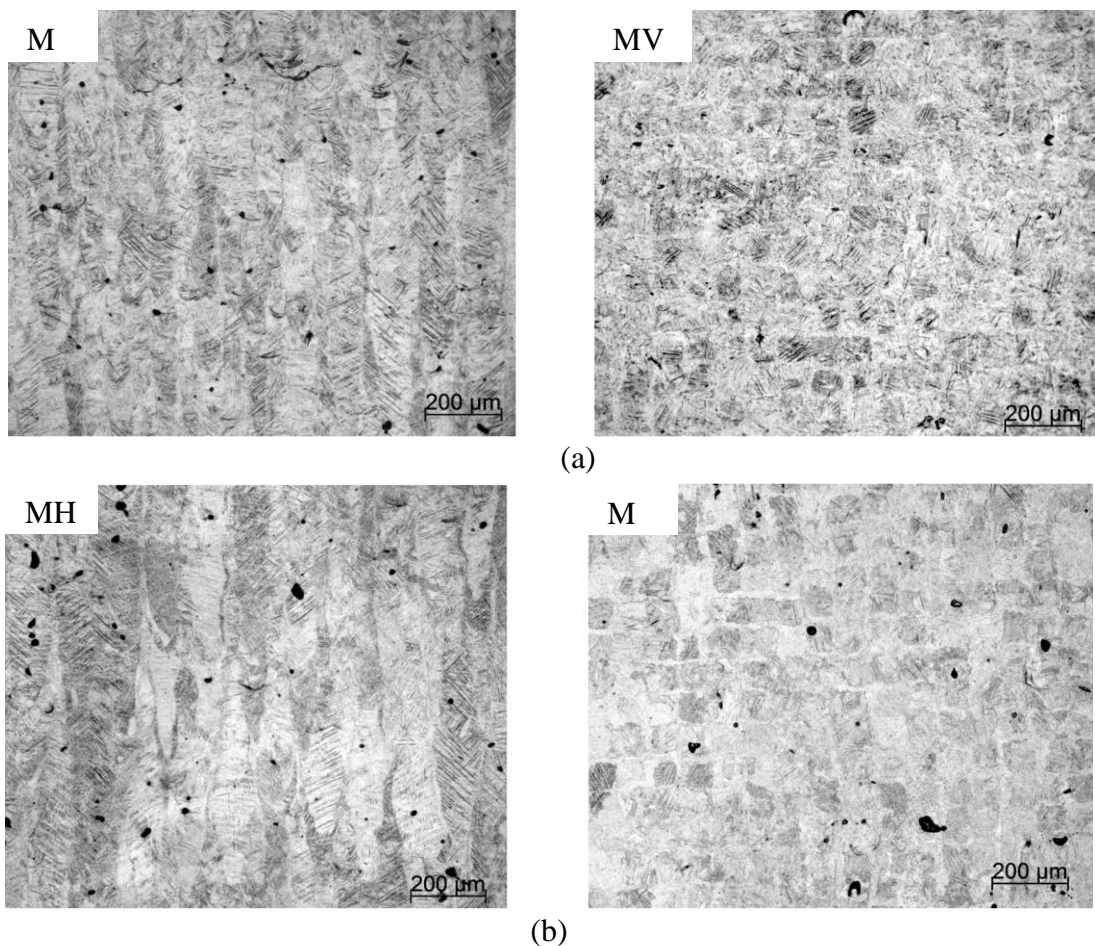
6.3.1 Microstructural characterisation

The optical micrographs in Figure 6-6 reveal the formation of a columnar structure in non-heat treated, stress-relieved and annealed MH samples. The chessboard patterns observed for the MV samples, Figure 6-6, are further confirmation of columnar grains formation in Ti64 SLM printed samples. The columnar grains in non-heat treated SLM fabricated Ti64 parts, has already been reported by other researchers [1, 25-27]. The boundaries separating the columnar grains are the prior β grains boundaries. Since the

⁸ ImageJ is a trade mark; (<https://imagej.net>)

temperatures of both stress-relieving and annealing treatments are below the β transus temperature, i.e., $1000 \pm 20^\circ\text{C}$ [28], it is expected to find the columnar grain architecture with the prior β boundaries preserved [11, 17].

The 3D sketch of the columnar architecture of the microstructure (macrostructure) in all samples of MH and MV, shown in Figure 6-7, confirms that the microstructure in vertical and horizontal samples is the same but the direction of applied load on their microstructure is different. In vertical samples, the tensile load is aligned with the columnar grains, while in horizontal samples the load is along the diagonal of the cubic columnar grains.



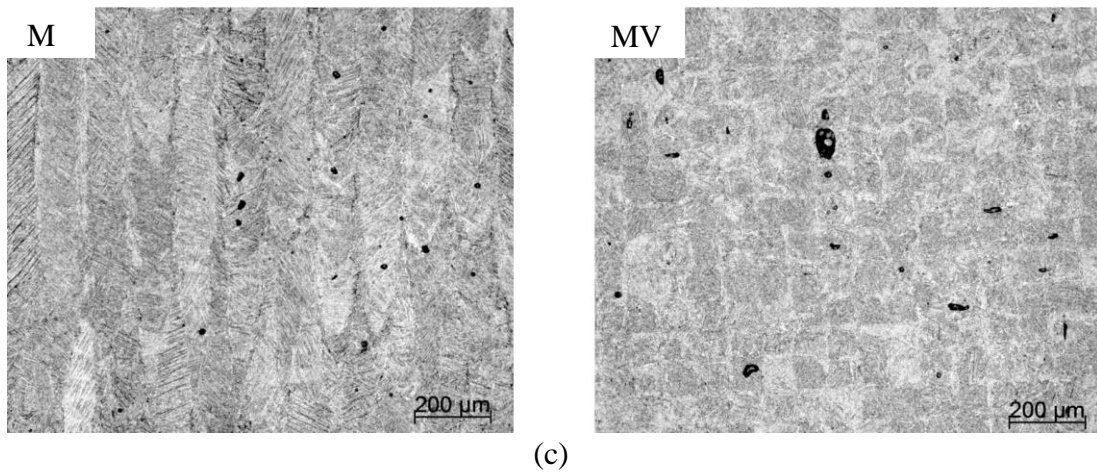


Figure 6-6: Optical micrographs of the grains architecture in MH and MV samples: a) non-heat treated, b) stress-relieved and c) annealed.

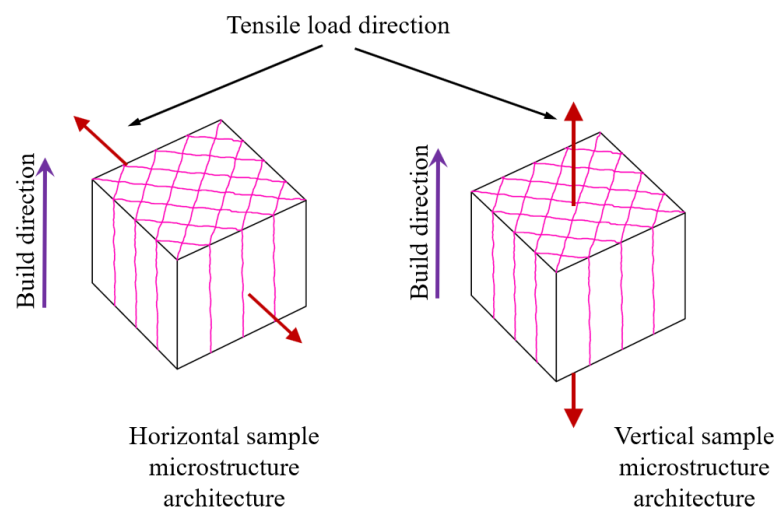


Figure 6-7: 3D Schematic of a columnar microstructure in SLM fabricated samples.

Figure 6-8, which is the stacked XRD spectra of three metallographic samples, reveals the existence of (HCP) α and/or α' phase in all samples, while the phase of β (BCC) is observed only in stress-relieved and annealed samples. It is hard to differentiate the HCP α from the α' martensitic phase via the XRD technique, as both α and α' have the same crystal structure with very similar lattice parameters [7, 29-31]. The main difference between α and α' is related to crystal distortion, which is due to the supersaturation of vanadium in the diffusionless transformation of β to the α' martensitic phase [32, 33].

In addition, the XRD spectrum in Figure 6-8 for non-heat treated samples are somewhat broadened, compared with other samples. Broadening of XRD peaks is related to the small crystal size (or particles) and strain [34]. Although non-heat treated SLM fabricated Ti64 samples usually suffer from residual stresses, it cannot be positively confirmed that the broadening of non-heat treated samples can be related to strain, but may be due to the small acicular shape of the α' martensitic phase, which will be discussed later. The full width at half maximum (FWHM) of the main peak of the HCP phase α/α' of all samples, which is associated with plane (101), shown in

Table 6-4, presents a maximum broadening value of 0.40° for the non-heat treated sample. Jovanovic et al [30] reported that an FWHM above 0.20° is evidence of a martensitic phase. The lowest value of FWHM in

Table 6-4 for annealed samples, 0.09° , may represent the value of FWHM for the HCP α phase without any α' phases in the structure. It has already been reported [11, 35, 36] that any heat treatment above 800°C fully decomposes the α' phase to α . So, it is confirmed that the value of FWHM, 0.09° , for annealed samples is associated with a fully HCP α phase. The FWHM value of 0.12° in the stress-relieved samples may indicate that the microstructure contains both α' and α phases.

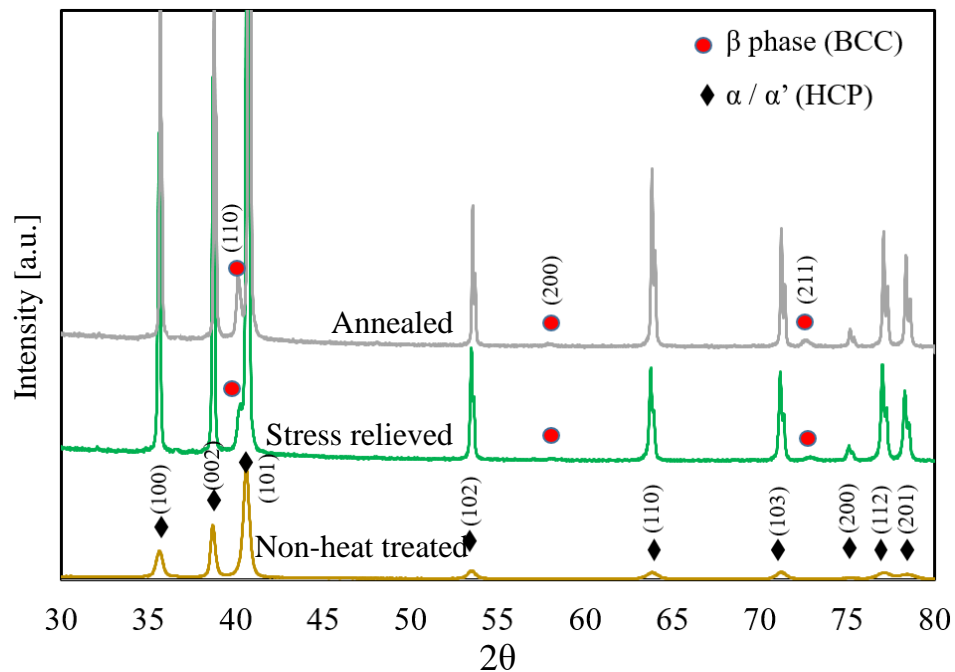


Figure 6-8: XRD spectra of three sample sections from differently-treated MH samples.

Table 6-4: FWHM of the peak of the HCP phase of the samples at 2θ diffraction nearly 40.6° , plane (101).

Sample	non-heat treated	Stress relieved	Annealed
FWHM, ($^\circ$)	0.40	0.12	0.09

For further microstructure characterisation, optical and SEM micrographs of the samples with higher magnification is required. As the microstructure of the columnar architecture for both MH and MV samples are very similar, only MH metallographic samples are examined under higher magnification, Figure 6-9.

Optical and SEM micrographs of non-heat treated samples, Figure 6-9a, exhibit the acicular (tiny needle shape) martensitic phase of α' (HCP), which is the result of rapid cooling and diffusionless transforming of the β phase to α' . There is some degree of coarsening of needle shape HCP phase due to the stress-relieving and annealing processes. The width of acicular α' in stress-relieved and annealed samples appears to have increased, as shown in the optical micrographs, the left images of Figure 6-9b and c. Also, some new fine particles, (bright spots in the SEM micrographs of Figure 6-9b and c), precipitated within the α' matrix, particularly at the lath boundaries.

The EDS examinations of the precipitated bright spots in stress-relieved and annealed samples confirmed them as rich in vanadium. The EDS of a few bright spots in stress-relieved and annealed samples, displayed in Figure 6-10, shows that the percentage of vanadium varies from 5.0% to 10.2%, which is above the nominal 4% V in the Ti64 powder. As the vanadium rich phase in Ti64 alloy is the β phase [37, 38], the bright spots in stress-relieved and annealed samples are also β phase, which was earlier confirmed in the XRD spectra, Figure 6-8. It should be noted that the scale of the SEM image in Figure 6-10a is different from Figure 6-10b. Apart from the β phase observed in the stress-relieved and annealed samples, very few white particles are also detectable in the SEM of non-heat treated samples, Figure 6-9a. These white particles in the non-heat treated sample could be β phase, which are precipitated from α' when a deposited layer with α' microstructure is reheated by the following deposited layers [20, 39], but neither the XRD spectrum nor the EDS analysis confirm the existence of any β phase. However, it does not necessarily mean that there is no β phase in the non-heat treated samples, since the β phase fraction might be below the detection limit of the XRD technique. Thus, it is assumed that the non-heat treated sample is fully composed of the α' martensitic phase.

As seen from the SEM micrographs in Figure 6-9b and c, the bright spots' sizes, β phase, are larger but fewer in the annealed sample compared with that of those that are stress-relieved, as has already been reported by other researchers [33]. The β phase in the stress-relieved samples looks like short needle-shaped particles; however, in the annealed samples, they appear to have coarsened, with wider and elongated needles along (α/α') phase boundaries with some globular β particles. The optical micrograph of the annealed sample, Figure 6-9c, reveals the lamellar microstructure of α (white laths) with β (in black), alongside some globular α phases (shown with arrows). The prior β boundary, which appears as a coarsened α -lath (displayed with a dash line), confirms the prior β boundaries as the preferred sites for diffusion and phase nucleation during annealing.

The image analysis of SEM micrographs in Figure 6-9b and c, exhibits about 4% and 13% of β constituent in stress-relieved and annealed samples respectively. It should be mentioned that, although image analysis is not an accurate method for measurement of the percentages of existing phases with different crystal structures (HCP and BCC) in the microstructure, it can be a good indication for comparing the volume fraction of the β phase existing in stress-relieved and annealed samples.

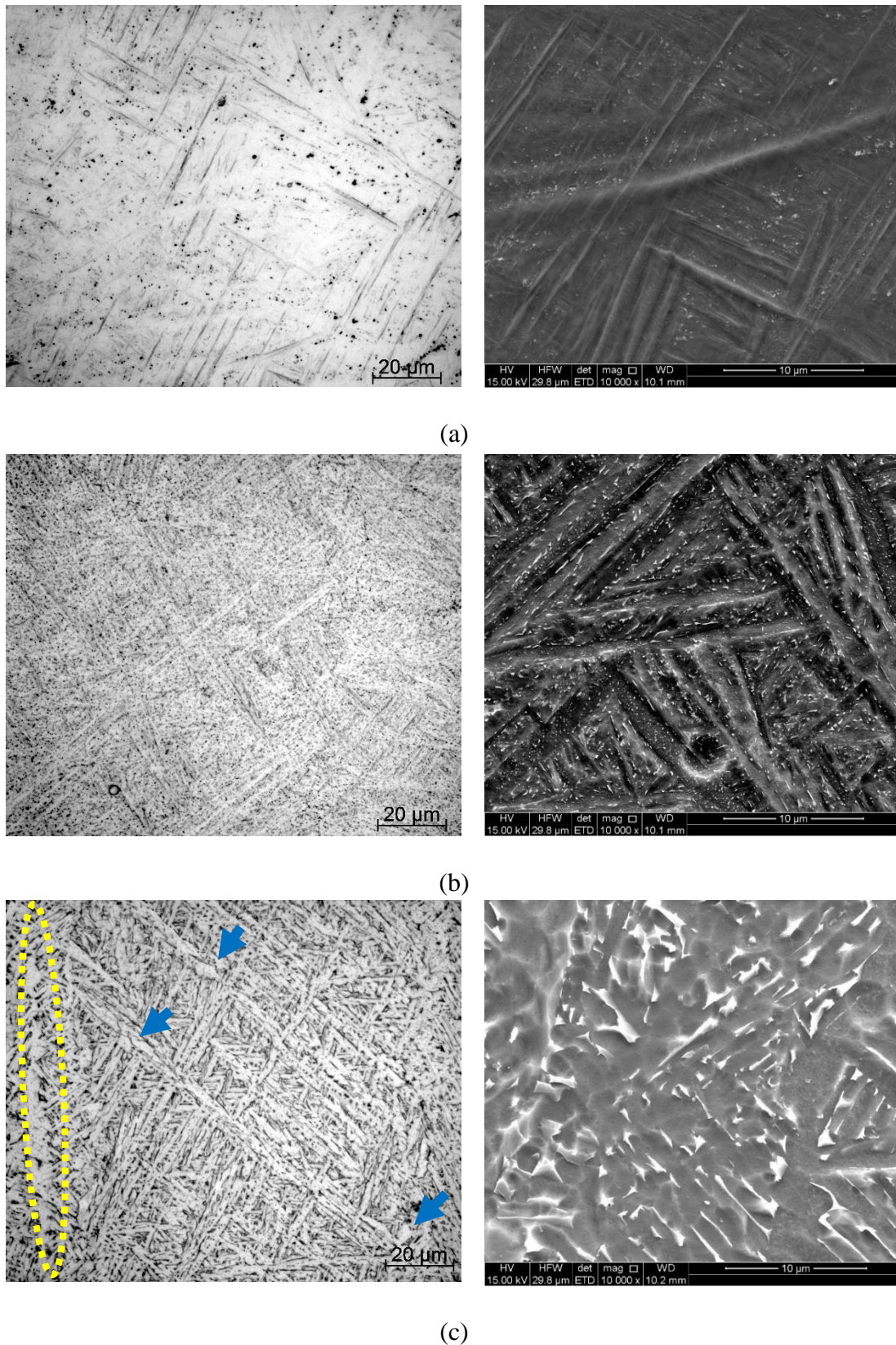


Figure 6-9: Optical micrographs (left) and SEM (right images) of MH samples; a) non-heat treated, b) stress-relieved and c) annealed. (Arrows show the globular α phase)

From the equilibrium phase diagram of Ti64 [38], it is expected to observe a 13.7% β phase, which is similar to the image analysis of 13%. The estimated β content of 4% in stress-relieved samples, which is far less than the expected 13.7% β in equilibrium conditions, confirms that the microstructure of stress-relieved samples still contains the α' phase. This is in good agreement with the FWHM of XRD spectrum in the stress-relieved samples discussed earlier.

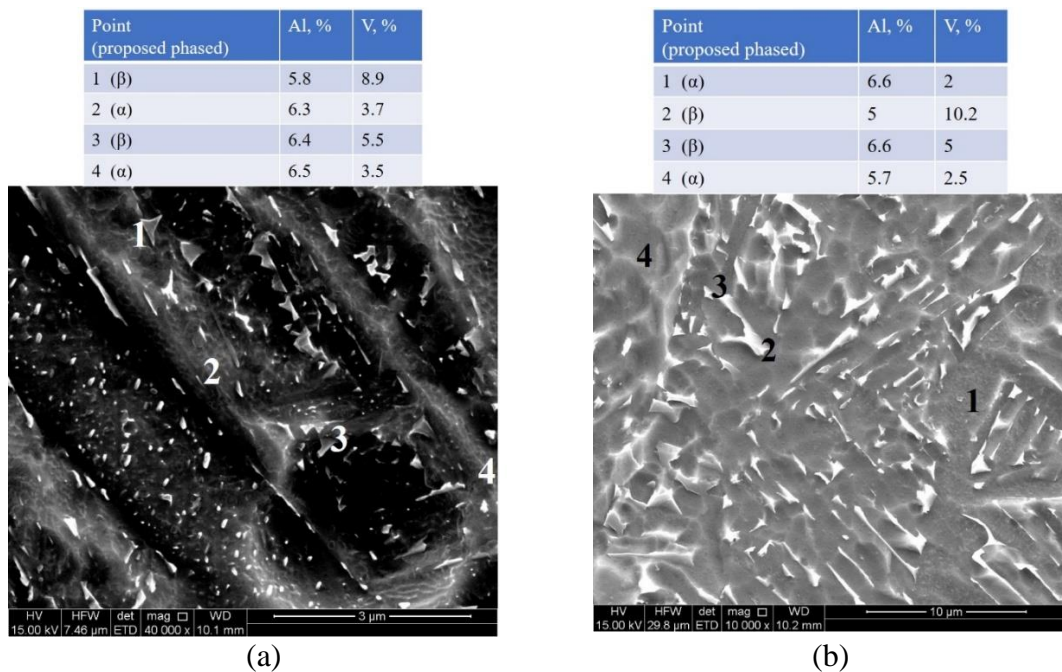


Figure 6-10: EDS point analysis of a) a stress-relieved sample, b) an annealed sample.

Table 6-5 shows the porosity content of the non-heat treated MH and MV samples measured via optical microscopy using ImageJ software. The average porosity of 0.14% shows that the SLM fabricated samples in this study were nearly fully dense, around 99.85%. There is a small difference between the porosity contents in the two samples that is believed to be due to the build direction.

Table 6-5: Porosity content in vertical and horizontal samples.

	Transverse section from MH sample	Transverse section from MV sample	Average
Porosity content, (%)	0.12 ± 0.08	0.16 ± 0.07	0.14 ± 0.07

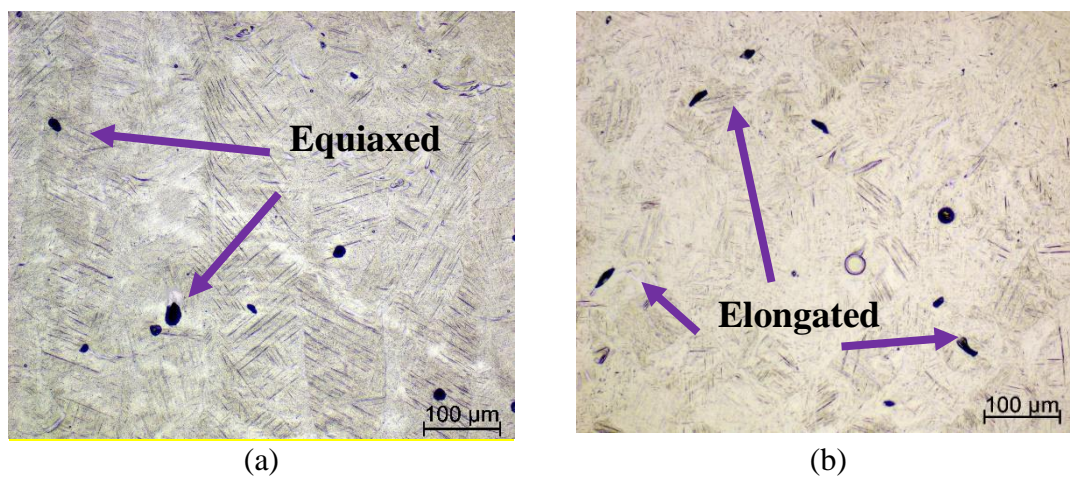


Figure 6-11: Optical micrographs of the transverse section of a) MH and b) MV samples.

The arrows in Figure 6-11 show the equiaxed and elongated pores observed in non-heat treated MH and MV samples, respectively. The axes of elongated pores in Figure 6-11 are aligned with the criss-cross laser vector, i.e., $\pm 45^\circ$, Figure 6-2. These elongated pores are associated with a minor lack of fusion either between the adjacent solidified tracks or between the previously-solidified layers.

In addition to porosity defects, there are some anomalies detected within the non-heat treated and stress-relieved test piece. In Figure 6-12a, some fish scale features are shown (arrows) in the transverse section of the non-heat treated MH sample. Interestingly, these features cannot be found in the annealed samples.

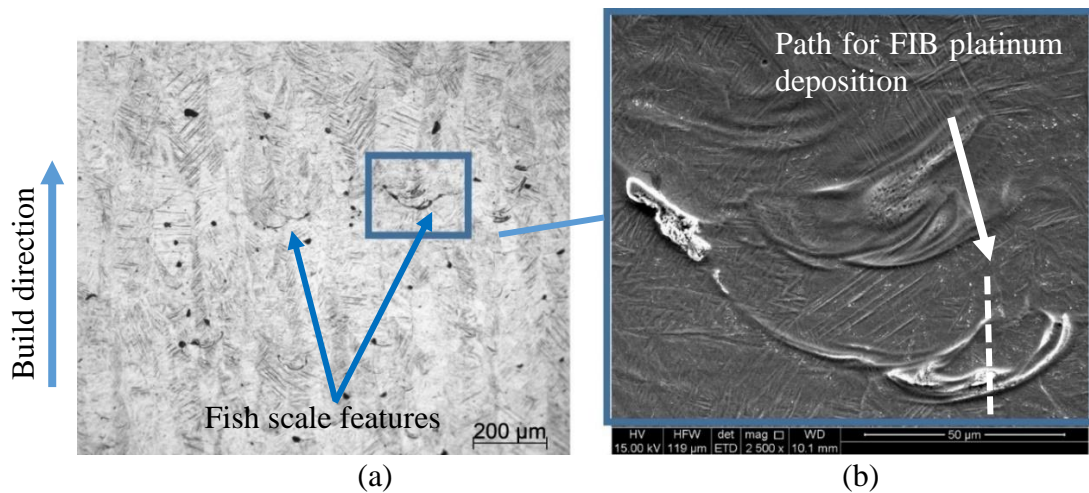


Figure 6-12: a) Optical microscopy of a non-heat treated sample, b) the SEM image of inset in the optical microscopy image.

The fish scale features depict the melt pool boundaries and for that reason, their orientations can identify the build direction. After performing the stress-relieving process, the number of detectable fish scale features decreases, while in annealed samples these features completely disappear. It is important to note that the fish scale phenomenon, which has not been clearly reported or characterised previously, has different morphology to melt pool boundaries reported in some studies [40-43]. Figure 6-12b shows a SEM image of the inset in Figure 6-12a where this feature appears as an uneven surface topography, possibly caused by different reactions of the material composition of this feature to Kroll's reagent. Figure 6-13a displays a portion of the area shown in Figure 6-12b but from a different angle viewed in FIB. The arrows in Figure 6-13a and b show the platinum deposited path, which has already been represented by a dash line in Figure 6-12b, where the cross section is created by Ga ion beam sputtering. Figure 6-13b reveals the results of an EDS line scan in different areas: two horizontal lines close to the surface, where platinum has been deposited, and two vertical lines perpendicular to the etched surface. All results have been normalised to remove the element of platinum from the weight percentage analysis of the main elements: titanium, aluminium, and vanadium.

The EDS results of all four lines reveal the fact that the fish scale feature is a result of negative segregation of the melt pool tip, where the aluminium percentage has dropped from its nominal 6% to an average of 3.5%. Thus, the fish scale phenomenon can be described as an HCP α' / α phase with a lack of aluminium. It has already been reported that Ti64 is a material susceptible to composition change during SLM fabrication and that the aluminium in Ti64 is the most volatile element [44].

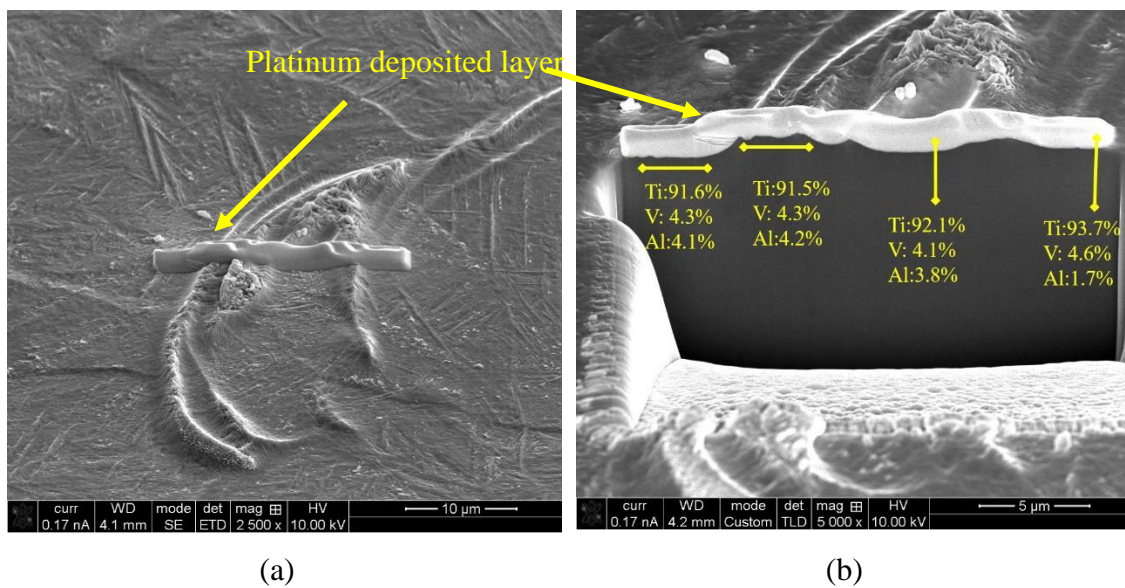


Figure 6-13: a) Platinum deposited layer according to the dash line in Figure 6-12, as a preparation for sectioning with FIB, b) location of the EDS lines and the average results of each line.

Figure 6-14a reveals some bright areas (shown with arrows) in the optical microscopy of an annealed sample that has similar shapes of melt pool boundaries to the fish scale feature. The inset in Figure 6-14a has been displayed with higher magnification in Figure 6-14b. The globular and coarse α phase, enclosed in the crescent in Figure 6-14b, confirms that the fish scale features in non-heat treated samples act in the same way as the prior β boundaries for any phase nucleation during phase transformation. In other words, fish scale features, because of the negative segregation in their aluminium

compositions, are preferred diffusion sites for receiving aluminium atoms and releasing the super-saturated vanadium.

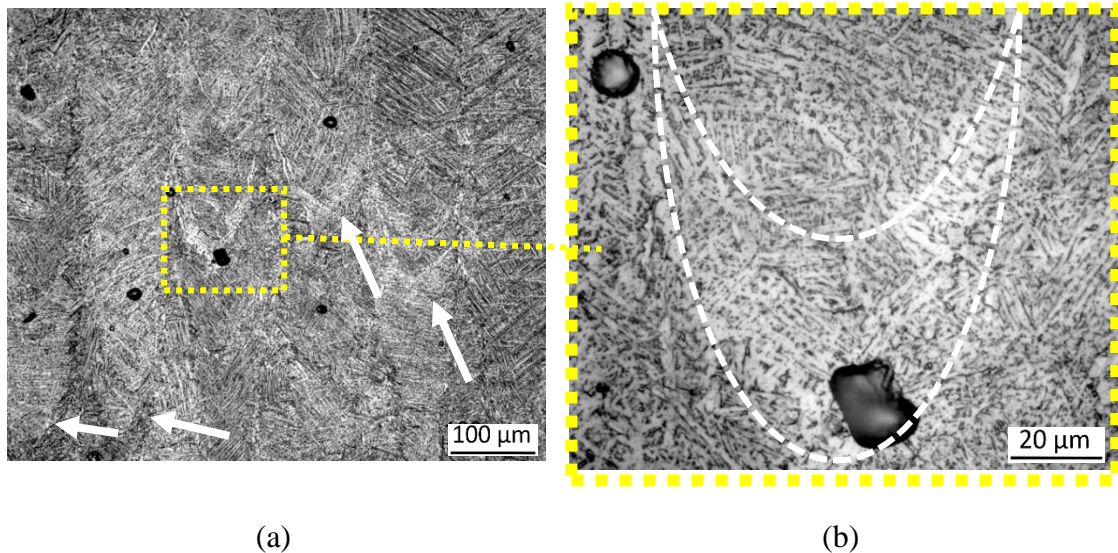


Figure 6-14: a) Optical micrograph of columnar grains in an annealed sample and b) the magnified inset with coarse and globular α phase. (Arrows show the melt pool boundaries)

As mentioned in Section 6.2, apart from the investigation into the anisotropy of mechanical properties for MH and MV samples, the influence of heat treatment on the tensile properties of NMV has also been studied. As the microstructure of an NMV sample is the same as the other samples, the polished metallographic sample of the NMV sample does not require etching, but the outer surface of the NMV sample should be examined. Figure 6-15 displays a micrograph of the longitudinal section of the outer surface of an NMV sample in a polished condition. Alongside some sharp valleys, shown with arrows in Figure 6-15, two micro-grooves displayed with dash lines are noticeable. These micro-grooves, with their planes perpendicular to the tensile load and 150 μm deep, could influence the mechanical properties of NMV, as discussed in the next section.

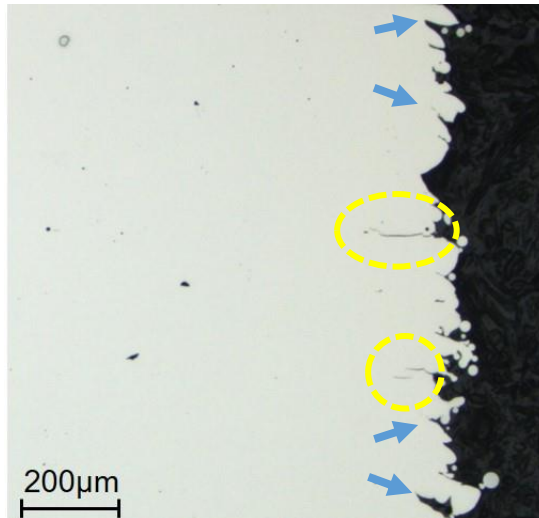


Figure 6-15: Optical microscopy of the outer surface of an NMV sample.

6.3.2 Mechanical properties

Figure 6-16 displays the stress-strain graphs for MH and MV samples in three conditions: non-heat treated, stress-relieved, and annealed while the tabulated tensile results are shown in Figure 6-17. As seen from Figure 6-16 and Figure 6-17, the two heat treatment procedures of stress-relieving and annealing lower the UTS and YS of both MH and MV samples, compared with non-heat treated samples, while the % elongation of most samples increases after being heat treated. In addition, the Young's modulus shows an increase from non-heat treated samples to annealed ones. The change in the modulus is related to phase changes in the samples during heat treatment since, in multi-phase Ti64 alloy, the Young's modulus is affected by the moduli of existing phases and their volume fraction in the microstructure [28]. The average UTS of non-heat treated MH and MV samples, which is 1377 MPa, lowers to an average of 1228 MPa after stress-relieving (which is a 11% drop); however, for annealed samples, the average UTS lowers to 1137 MPa, showing a drop of 17%.

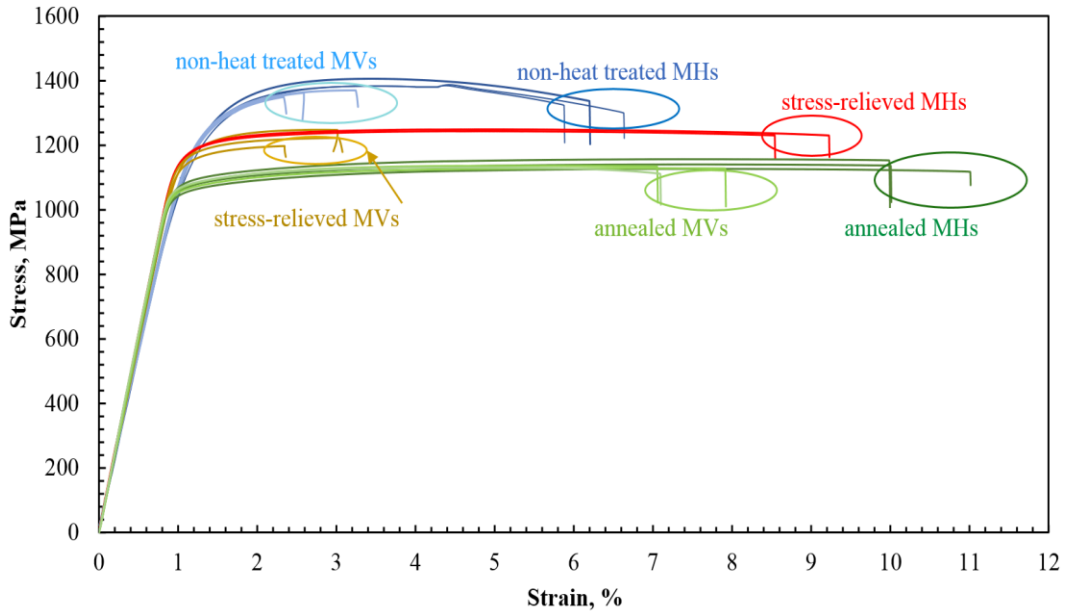


Figure 6-16: The stress-strain graphs of MH and MV samples.

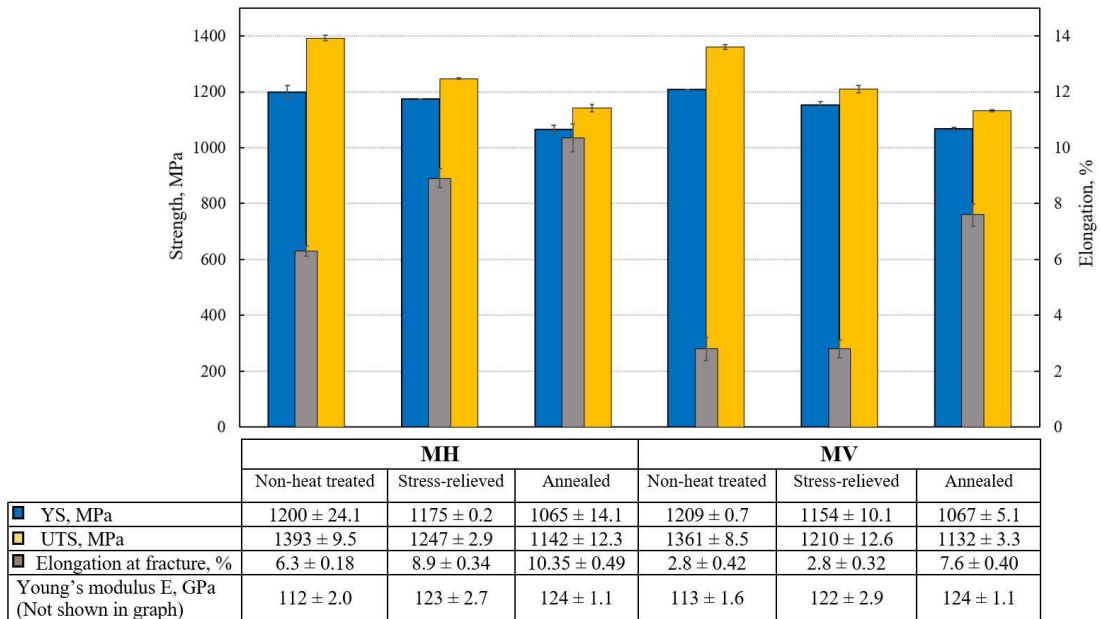


Figure 6-17: Tensile properties histogram of all the machined samples. (MH and MV)

Improvement of ductility (which is the increase of elongation and strain at fracture) in an annealed condition for both build orientations is much higher than for stress-relieving treatment. The improvement of ductility in MH is 41% after stress-relieving and 64% after the annealing process. But for MV samples, stress-relieving does not increase the

ductility; however, a drastic increase of 170% in the elongation is observed after the annealing process.

The difference in elongation between MH and MV samples in non-heat treated conditions is 125%, while by annealing this difference lowered to 36%. In other words, annealing the properties leads to greater uniformity in the sample, irrespective of build direction. It should also be noted that the elongation of MH samples is always higher than that of MV. The difference in YS between MH and MV is 0.19% in an annealed condition and 1.8% in stress-relieved samples, which is negligible compared with the elongation anisotropy revealed from the tensile tests. Thus, this investigation mainly focuses on the effect of heat treatment on the elongation anisotropy observed in MH and MV samples.

Figure 6-18 displays the microhardness of the microstructure of each treatment for both verticals and horizontals, showing that the hardness of MH and MV samples in each condition of treatment is nearly the same, with around 3% difference. Figure 6-18 shows that the non-heat treated sample with a fully martensitic microstructure has the highest average hardness compared with the lowest hardness, which is related to the annealed sample with fully decomposed α' to α and β phases. The average hardness of stress-relieved samples is in between the hardness of non-heat treated and annealed samples. The average results of microhardness in the samples in Figure 6-18 correspond with the UTS of the same samples extracted from tensile tests, Figure 6-17. The decrease in mechanical strength, UTS and YS, after heat treatment processes (which are comparable with their microhardness) are mainly related to the phase transformation from non-heat treated single phase martensite α' with acicular morphology, to β and lamellar α with increased laths size - compared with α' - as observed in stress-relieved and annealed samples.

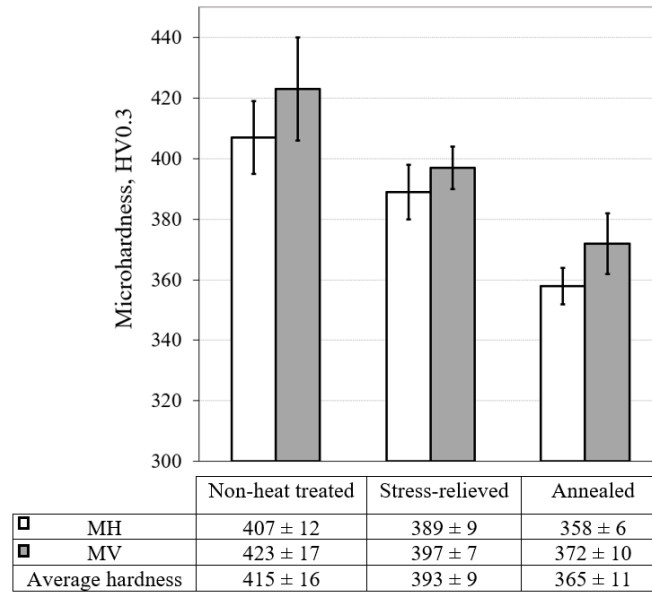


Figure 6-18: Measured microhardness of the transverse sections of all samples.

Since the mechanical properties of titanium alloys are strongly affected by the microstructure which in turn, are influenced by morphology and the sizes of the two phases of β and α , [45, 46], any phase transformation of SLM fabricated Ti64 parts during heat treatment explains any changes in the mechanical properties.

While the UTS and YS decrease through these heat treatment processes, the ductility of most samples increases, which is believed to be associated with the plasticity of the $\alpha + \beta$ microstructure [3]. Although the trends of decrease in the hardness of three different samples, Figure 6-18, are in good agreement with the decrease of UTS in those samples, the hardness cannot explain the anisotropy of elongation between MV and MH samples. This is due to the nature of the microhardness test, which is static and localized; unable to reveal the effects of defects and their orientations' contribution to elongation.

As discussed in Section 3.1, by performing the heat treating processes, either stress-relieving or annealing, the columnar architecture is preserved but at the same time the prior β boundaries, as the preferred nucleation site for the new α and β phases, may reduce

the degree of directionality in annealed samples due to the formation of coarse and semi-equiaxed morphology for the α phase.

The other factor affecting the elongation anisotropy can be related to the pores' morphologies and their orientations with respect to the loading direction. As discussed in a previous publication [16], the sharp edges of flattened pores in MV samples with tensile load perpendicular to the pores' edges and planes could increase cracking susceptibility in MV samples. The increased cracking susceptibility, along with the contribution of residual stress, as reported by [47], could be a potential reason for lowering elongation of non-heat treated MV samples, leading to anisotropy in elongation of non-heat treated parts.

In annealed samples, residual stresses are fully released, as the annealing temperature is 850°C, which is above the temperature recommended for complete stress-relieving, i.e., 730°C [11, 32]. Thus, the improvement in anisotropy of elongation observed in annealed samples is believed to show that the residual stresses on the pores' edges in MV samples are completely removed. In stress-relieved MV samples, the elongation is very similar to the non-heat treated MV, suggesting that the anisotropy in stress-relieved samples does not show any improvement. It is believed that the residual stresses in the stress-relieved samples are not completely released, considering the treatment temperature (670°C) is below 730°C. Thus, the remaining residual stress in stress-relieved samples with the contribution of the sharp edges of (elongated) flattened pores are still dominant in keeping the low elongation of verticals. The partial phase transformation in stress-relieved MV appears to be less effective in improving the ductility. Apart from the elongated pores and their flat sharp edges, fish scale features might also be responsible for lower elongation of the MV samples in non-heat treated and stress-relieved samples. It is suggested that the negative segregation and inhomogeneity observed in the fish scale feature could alter

the wetting angle of the melt-pool for the already deposited layer, rendering a lack of coherency between the stacked layers. These features can be potential sites for void formation in the fracture of non-heat treated and stress-relieved MV samples, which will be discussed in the next section.

Figure 6-19 shows the stress-strain diagrams of MV and NMV (non-machined vertical) samples under different heat treatments. Generally, NMV, when compared with MV, show lower mechanical properties in terms of their strengths (YS and UTS) and also elongation, as shown in the histogram in Figure 6-20a and b. The non-heat treated NMV samples (known as, as-built), suffer from premature failure and they fracture at an average stress of 482 MPa, which is around 35% of the UTS of their machined counterparts, i.e., non-heat treated MV samples. By conducting stress-relieving on NMV samples, all the tensile properties of NMV significantly improve. This confirms that the main reasons for premature failure of non-heat treated NMV is the contribution of sharp valleys and micro grooves on the outer surface and residual tensile stresses (which might be very high on the surface). By removing either the rough surface of NMV (via machining and making MV) or releasing the residual stresses (even partially by stress-relieving), the vertical samples will not suffer from premature failure: see Figure 6-19 and Figure 6-20.

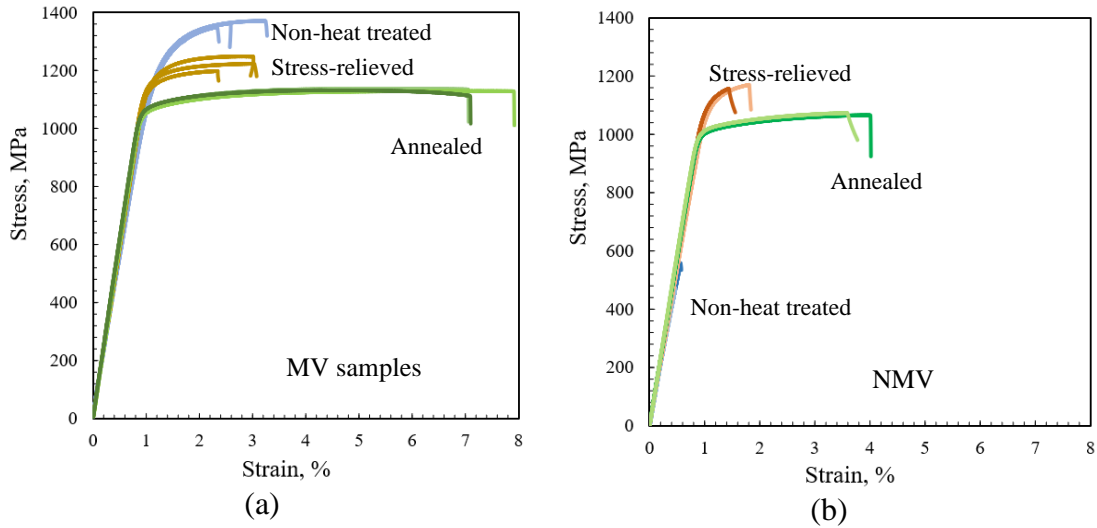


Figure 6-19: The stress-strain graphs of non-heat treated, stress-relieved and annealed: a) MV and b) NMV samples.

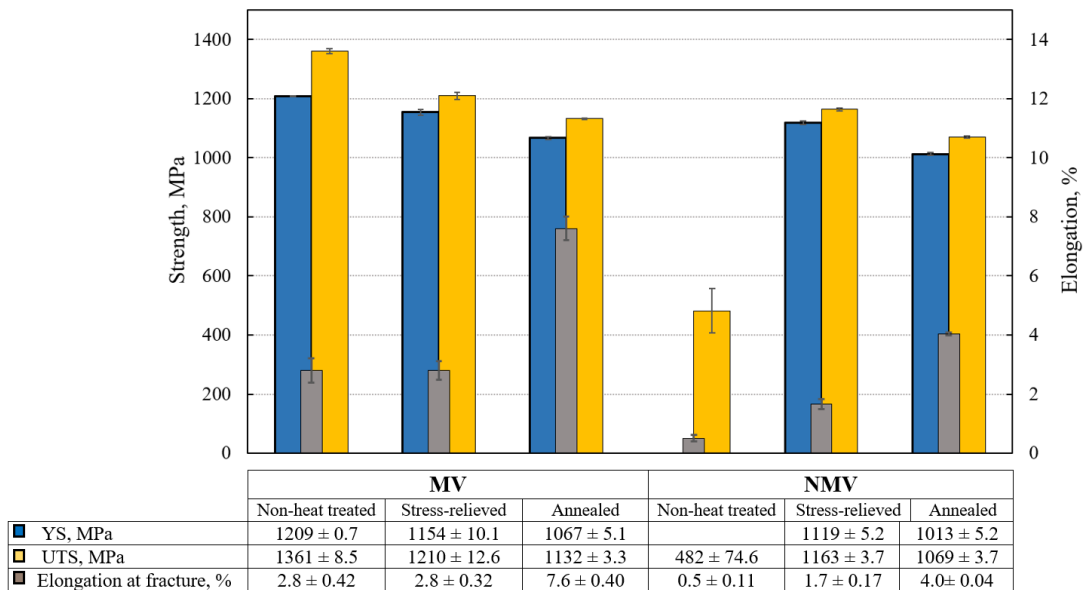


Figure 6-20: Tensile properties histogram of all vertical samples.

Although the elongation of stress-relieved NMV, which is around 1.7% compared with the non-heat treated NMV (0.5%), shows a good improvement, it is not acceptable in comparison with non-heat treated MV. Annealing the NMV can improve the elongation to 4.0%, compared with 1.7% in stress-relieved NMV samples. This can be attributed to

the fully decomposed α' to α and β in the microstructure and consequently fully releasing the residual stresses in the annealed samples. However, it can be noticed that the outer surfaces of NMV samples play a major role in elongation. The effect of sharp valleys (or micro grooves) in annealed NMV samples, even in the absence of residual stress, is so high that it reduces the elongation to nearly 53% of their annealed MV counterparts. Nevertheless, in some applications, where the shape of components is intricate and machining is not viable, the annealing process can improve the as-built mechanical properties even when the loads are applied along the deposition layers, as for NMV samples.

6.3.3 Fracture surface analysis

Figure 6-21 displays the SEM of the fracture surfaces of all MH samples in this study. As seen from Figure 6-21a to c, apart from the shear lip around the periphery of all the samples, the fracture surfaces of non-heat treated and stress-relieved samples are uneven; however, in annealed samples the surface is rather even. Figure 6-21d and e, reveal quasi-cleavage features (as reasons for uneven surfaces) and microcracks in non-heat treated and stress-relieved MH samples, suggesting a mixed mode of ductile and brittle fracture. In the annealed sample, Figure 6-21f, the quasi-cleavage features cannot be observed, meaning that the annealed MH sample behaves like a ductile material. Also, a qualitative comparison of the dimples in all fracture surfaces, Figure 6-21d to f, indicates that in the annealed sample the dimples are larger and more uniform compared with those in the other two samples, which confirms the ductility of the annealed sample is relatively better.

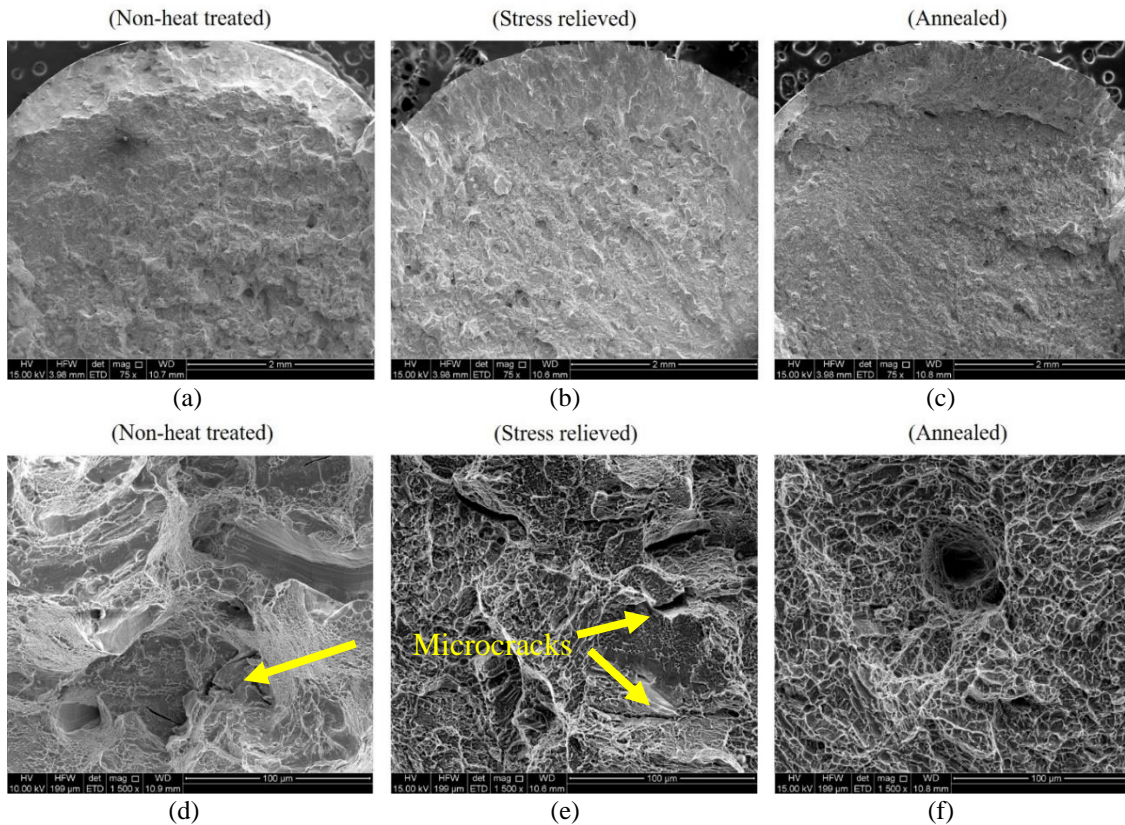


Figure 6-21: SEM micrographs of fractured surfaces of MH samples, to show the formation shear lips and fracture topography a) to c) and the formation of dimples at higher magnification as a measure of ductility d) to f).

Figure 6-22 displays the fracture surfaces of all MH samples sectioned longitudinally along the axis of tensile samples and etched for metallographic examination and analysis of crack paths. Figure 6-22a to c display the images of the entire fracture surfaces. As can be seen in the close-up images, Figure 6-22d to f, the fracture has generally propagated through the chess board pattern in the MH samples, regardless of the heat treatment conditions, meaning that all MH samples had transgranular fractures. Apart from the very few elongated pores in the microstructure near the fracture surfaces of all samples, Figure 6-22d to f, there are no microcracks near the fracture surface, suggesting that the voids' coalescence in MH samples occurred uniformly on the final fracture surface. Also, the

chess board pattern has distorted to a diamond shape (with different lengths of diagonals) confirming lateral plastic deformation of the columnar grains.

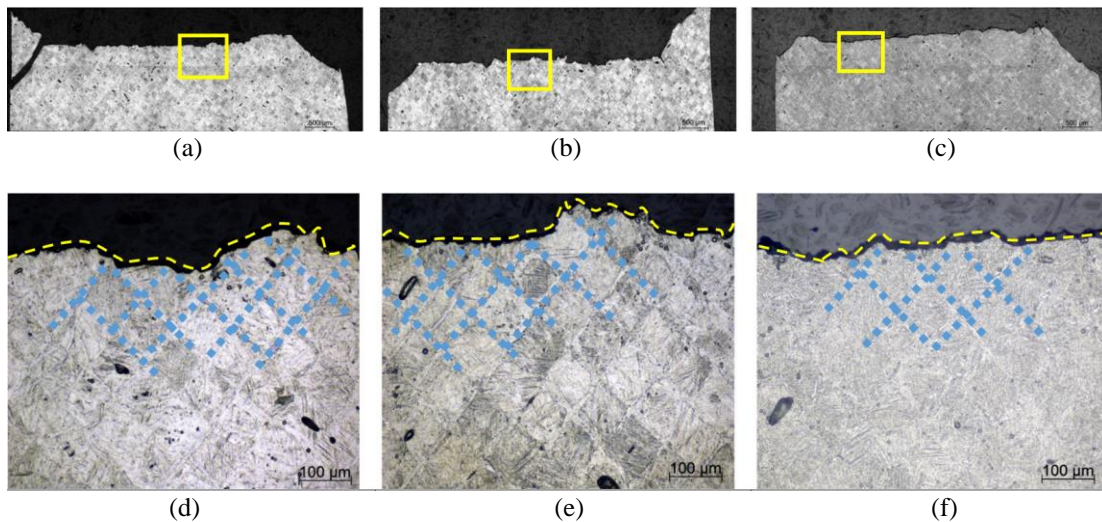


Figure 6-22: Optical micrographs of etched fractured surfaces (longitudinally sectioned) of MH samples; a) to c) whole fracture surface with shear lips, d) to f) magnification of corresponding insets in a) to c).

The SEM micrographs of the fracture surfaces of all MV samples are displayed in Figure 6-23. All machined verticals (MV) exhibit a bulk fracture in the middle due to the coalescence of the voids, which propagate towards the outer surfaces of the samples where the shear lips occur. It should be noticed that the entirety of the shear lips surrounding the fracture surfaces of all MV are not shown in Figure 6-23a to c. The fracture surfaces of non-heat treated, and stress-relieved verticals unveil a layered topography in Figure 6-23a and b, meaning the cracks initiate on different deposited layers; while propagating they then alternate and connect with each other from one layer to another. The layered topography is not dominant in the annealed verticals, compared with the other verticals, explaining the smooth fracture surface in annealed MV samples. The dash lines in Figure 6-23d to f show the inter layer voids as a consequence of the lack

of fusion observed in all verticals; however, in Figure 6-23d an inter-layer void is shown as a crack initiation site, which has connected through a microcrack to the upper fracture surface. Also, the dimples in the annealed MV samples, Figure 6-23f, are more regular than for the other MV samples, Figure 6-23d and e: indeed they are similar to what was observed in the annealed MH samples.

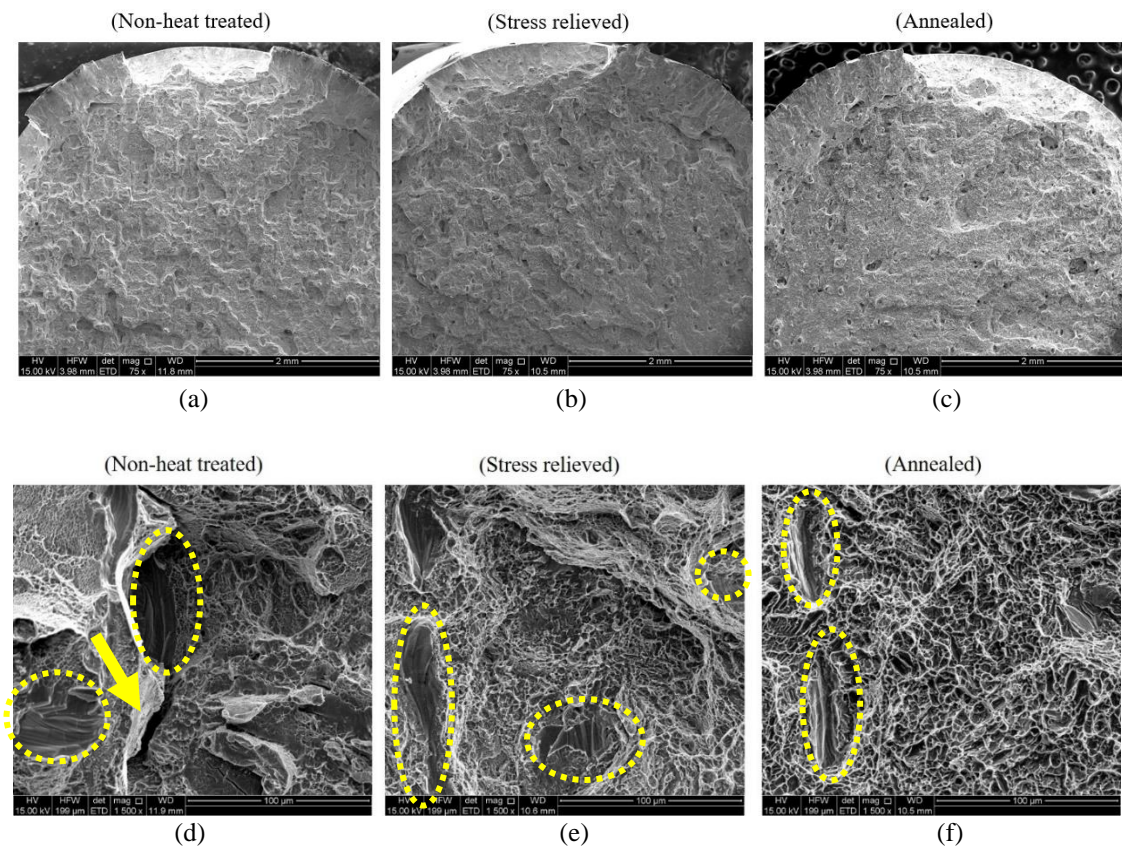


Figure 6-23: SEM micrographs of all MV fractured surfaces; a) to c) fracture topography and partial views of shear lips, d) to f) lack of fusions and dimples formation in all samples. (Arrow shows a microcrack in the non-heat treated MV)

Figure 6-24 displays the optical microscopy of the etched samples longitudinally cut from the fracture surfaces of all MV samples. Figure 6-24a to c shows images of the entire fracture surfaces, confirming the uneven surfaces of non-heat treated and stress-relieved MV samples compared with the relatively even fracture surface of the annealed MV.

Figure 6-24d to f, which contain the corresponding insets to Figure 6-24a to c, shows some microcracks developed underneath the fracture surface in non-heat treated and stress-relieved MV samples. The formation of microcracks may explain the lower ductility (% elongation) in non-heat treated and stress-relieved MV samples compared with MH.

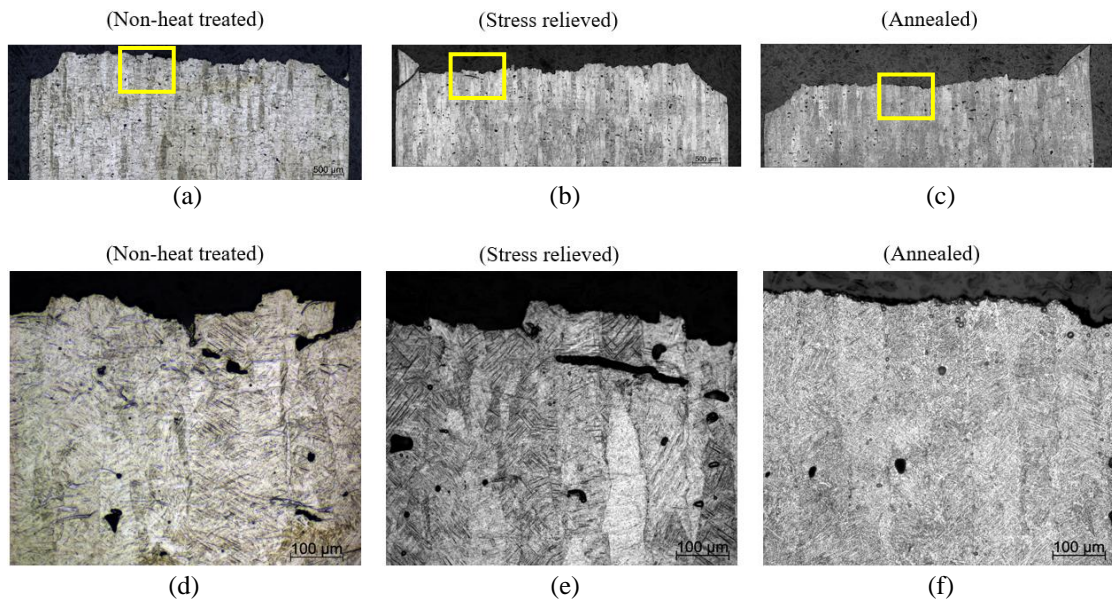


Figure 6-24: Optical micrographs of etched fracture surfaces (longitudinally sectioned) of MV samples; a) to c) shear lips seen under magnification 50, d) to f) magnification of corresponding insets in a) to c).

Figure 6-25 unveils two observed sections of a fractured surface of an MV sample (non-heat treated) in which the crack has propagated through the fish scale features, suggesting that the fish scale features may be the preferred sites for initial voids' or microcracks' formation.

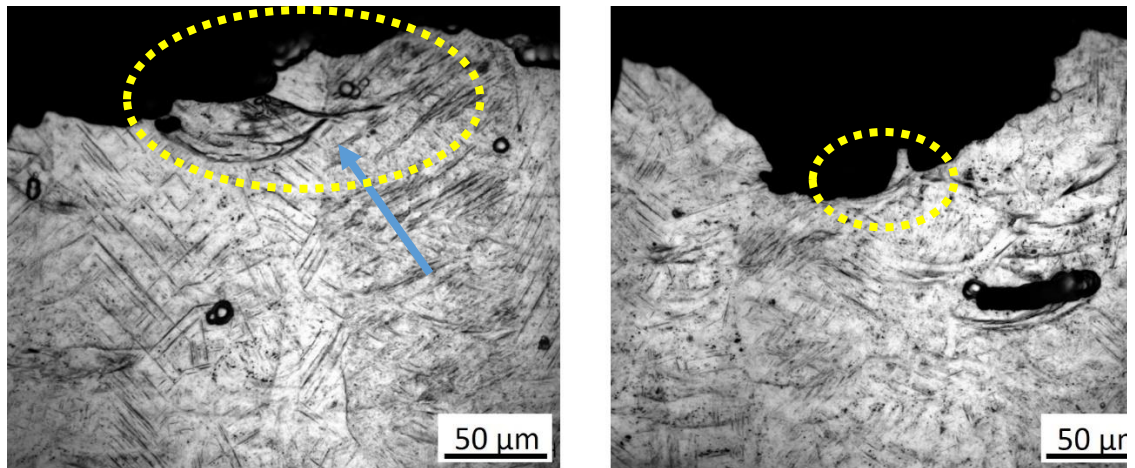


Figure 6-25: Two sites of a fractured surface of a non-heat treated MV sample.

Thus, the microcracks observed in non-heat treated and stress-relieved MV samples are believed to have originated from flattened pores (as inter-layer voids) between the layers or from a lack of coherency between the stacked layers, which is associated with fish scale features. The effect of flattened pores as a stress riser in vertical samples has already been noticed by others [11, 48]; however, the effect of fish scale features as microcrack initiating sites is not yet clear. The drastic improvement in the elongation of verticals during annealing may be attributed to removal of fish scales and complete transformation of α' to $\alpha + \beta$ along with coarsening of lamellar α and β , which are in favour of the higher ductility of annealed verticals. In addition, the release of residual stress could also be instrumental in improving the ductility of annealed verticals.

6.4 Conclusions

This study reveals that the annealing process presents a uniform elongation and lowers anisotropy on Machined Horizontal and Machined Vertical (MH and MV) samples. Furthermore, annealing results in better properties in Non-Machined Vertical (NMV)

samples compared with the machining post process on the non-heat treated verticals. The detailed conclusions are listed below:

- The annealing increases the elongation of both MH and MV samples; however, the stress-relieving increases the elongation of MH samples alone and does not change the elongation of the MV samples.
- After annealing, the elongation of non-heat treated MV (2.8%) and MH (6.3%) increases to 7.6% and 10.35%, respectively. Therefore, the annealing not only increases the ductility of both MV and MH samples, but also helps to mitigate the anisotropy in ductility. All improvements in mechanical properties, with emphasis on the elongation, are attributed to the phase changes (α' to $\alpha + \beta$) and releasing the SLM process-induced residual stresses.
- The fish scale features, as the sites with low coherency between the stacked layers, can potentially contribute to lowering the elongation of non-heat treated and stress-relieved vertical samples.
- The elongation of 4.0% in annealed NMV compared with the elongation of 2.8% of non-heat treated MV proves that the annealing process is more effective than the machining for improving the elongation of verticals where only one post process can be chosen.
- The results of this study can be applied to improve the mechanical properties of as-built verticals, especially where machining is not feasible, such as intricate parts.

6.5 Declaration of competing interest

We wish to confirm that there are no known conflicts of interest associated with this publication.

6.6 Acknowledgements

This work was undertaken in part at the OptoFab node of the Australian National Fabrication Facility (ANFF), utilizing Commonwealth and South Australian State Government funding. Adelaide Microscopy is gratefully acknowledged for the access provided to their electron microscopy facilities. A. Dareh Baghi is grateful to the Australian Government and Adelaide University for his PhD scholarship.

References

1. Xu, W., M. Brandt, S. Sun, J. Elambasseril, Q. Liu, K. Latham, K. Xia, and M. Qian, *Additive manufacturing of strong and ductile Ti–6Al–4V by selective laser melting via in situ martensite decomposition*. *Acta Materialia*, 2015. **85**: p. 74-84.
2. Attar, H., M. Calin, L.C. Zhang, S. Scudino, and J. Eckert, *Manufacture by selective laser melting and mechanical behavior of commercially pure titanium*. *Materials Science and Engineering A*, 2014. **593**: p. 170-177.
3. Banerjee, D. and J.C. Williams, *Perspectives on Titanium Science and Technology*. *Acta Materialia*, 2013. **61**(3): p. 844-879.
4. Santos, L.V., V.J. Trava-Airoldi, E.J. Corat, J. Nogueira, and N.F. Leite, *DLC cold welding prevention films on a Ti6Al4V alloy for space applications*. *Surface and Coatings Technology*, 2006. **200**(8): p. 2587-2593.
5. Geetha, M., A.K. Singh, R. Asokamani, and A.K. Gogia, *Ti based biomaterials, the ultimate choice for orthopaedic implants – A review*. *Progress in Materials Science*, 2009. **54**(3): p. 397-425.
6. Murr, L., S. Quinones, S. Gaytan, M. Lopez, A. Rodela, E. Martinez, D. Hernandez, E. Martinez, F. Medina, and R. Wicker, *Microstructure and mechanical behavior of Ti–6Al–4V produced by rapid-layer manufacturing, for biomedical applications*. *Journal of the mechanical behavior of biomedical materials*, 2009. **2**(1): p. 20-32.
7. Facchini, L., E. Magalini, P. Robotti, A. Molinari, S. Höges, and K. Wissenbach, *Ductility of a Ti-6Al-4V alloy produced by selective laser melting of prealloyed powders*. *Rapid Prototyping Journal*, 2010. **16**(6): p. 450-459.
8. Koike, M., P. Greer, K. Owen, G. Lilly, L.E. Murr, S.M. Gaytan, E. Martinez, and T. Okabe, *Evaluation of Titanium Alloys Fabricated Using Rapid Prototyping Technologies—Electron Beam Melting and Laser Beam Melting*. *Materials*, 2011. **4**(12): p. 1776-1792.
9. Sallica-Leva, E., A.L. Jardini, and J.B. Fogagnolo, *Microstructure and mechanical behavior of porous Ti-6Al-4V parts obtained by selective laser melting*. *J Mech Behav Biomed Mater*, 2013. **26**: p. 98-108.

10. Zhang, L.-C. and H. Attar, *Selective Laser Melting of Titanium Alloys and Titanium Matrix Composites for Biomedical Applications: A Review* Advanced Engineering Materials, 2016. **18**(4): p. 463-475.
11. Vilaro, T., C. Colin, and J.D. Bartout, *As-Fabricated and Heat-Treated Microstructures of the Ti-6Al-4V Alloy Processed by Selective Laser Melting*. Metallurgical and Materials Transactions A, 2011. **42**(10): p. 3190-3199.
12. Rafi, H.K., N.V. Karthik, H. Gong, T.L. Starr, and B.E. Stucker, *Microstructures and Mechanical Properties of Ti6Al4V Parts Fabricated by Selective Laser Melting and Electron Beam Melting*. Journal of Materials Engineering and Performance, 2013. **22**(12): p. 3872-3883.
13. Sercombe, T., N. Jones, R. Day, and A. Kop, *Heat treatment of Ti-6Al-7Nb components produced by selective laser melting*. Rapid Prototyping Journal, 2008. **14**(5): p. 300-304.
14. Simonelli, M., Y.Y. Tse, and C. Tuck, *Effect of the build orientation on the mechanical properties and fracture modes of SLM Ti-6Al-4V*. Materials Science and Engineering: A, 2014. **616**: p. 1-11.
15. Hartunian, P. and M. Eshraghi, *Effect of Build Orientation on the Microstructure and Mechanical Properties of Selective Laser-Melted Ti-6Al-4V Alloy*. Journal of Manufacturing and Materials Processing, 2018. **2**(4): p. 69.
16. Dareh Baghi, A., S. Nafisi, R. Hashemi, H. Ebendorff-Heidepriem, and R. Ghomashchi, *Experimental realisation of build orientation effects on the mechanical properties of truly as-built Ti-6Al-4V SLM parts*. Journal of Manufacturing Processes, 2021. **64**: p. 140-152.
17. Vrancken, B., L. Thijs, J.-P. Kruth, and J. Van Humbeeck, *Heat treatment of Ti6Al4V produced by Selective Laser Melting: Microstructure and mechanical properties*. Journal of Alloys and Compounds, 2012. **541**: p. 177-185.
18. Khorasani, A., I. Gibson, M. Goldberg, and G. Littlefair, *On the role of different annealing heat treatments on mechanical properties and microstructure of selective laser melted and conventional wrought Ti-6Al-4V*. Rapid Prototyping Journal, 2017.
19. Khorasani, A.M., I. Gibson, A. Ghaderi, and M.I. Mohammed, *Investigation on the effect of heat treatment and process parameters on the tensile behaviour of SLM Ti-6Al-4V parts*. The International Journal of Advanced Manufacturing Technology, 2019. **101**(9): p. 3183-3197.
20. Chlebus, E., B. Kuźnicka, T. Kurzynowski, and B. Dybała, *Microstructure and mechanical behaviour of Ti-6Al-7Nb alloy produced by selective laser melting*. Materials Characterization, 2011. **62**(5): p. 488-495.
21. <https://www.tls-technik.de>.
22. *ASTM F2924-14, Standard Specification for Additive Manufacturing Titanium-6 Aluminum-4 Vanadium with Powder Bed Fusion*. 2014.
23. *ASTM E8/E8M -16a Standard Test Methods for Tension Testing of Metallic Materials*. 2016.
24. *SAE AMS 2801B, Heat Treatment of Titanium Alloy Parts (R2014)*. 2014.

25. Wysocki, B., P. Maj, R. Sitek, J. Buhagiar, K.J. Kurzydłowski, and W. Świążkowski, *Laser and electron beam additive manufacturing methods of fabricating titanium bone implants*. Applied Sciences, 2017. **7**(7): p. 657.
26. Yang, J., H. Yu, Z. Wang, and X. Zeng, *Effect of crystallographic orientation on mechanical anisotropy of selective laser melted Ti-6Al-4V alloy*. Materials Characterization, 2017. **127**: p. 137-145.
27. Zhao, X., S. Li, M. Zhang, Y. Liu, T.B. Sercombe, S. Wang, Y. Hao, R. Yang, and L.E. Murr, *Comparison of the microstructures and mechanical properties of Ti-6Al-4V fabricated by selective laser melting and electron beam melting*. Materials & Design, 2016. **95**: p. 21-31.
28. *Heat Treating of Titanium and Titanium Alloys; Revised by Roger Gilbert, IMI Titanium; and C. Richard Shannon, Teledyne Allvac, in ASM handbook. Vol. 4, Heat treatment*. 1991, ASM International. p. 913-923.
29. Kubiak, K. and J. Sieniawski, *Development of the microstructure and fatigue strength of two phase titanium alloys in the processes of forging and heat treatment*. Journal of Materials Processing Technology, 1998. **78**(1-3): p. 117-121.
30. Jovanović, M.T., S. Tadić, S. Zec, Z. Mišković, and I. Bobić, *The effect of annealing temperatures and cooling rates on microstructure and mechanical properties of investment cast Ti-6Al-4V alloy*. Materials & Design, 2006. **27**(3): p. 192-199.
31. Malinov, S., W. Sha, Z. Guo, C.C. Tang, and A.E. Long, *Synchrotron X-ray diffraction study of the phase transformations in titanium alloys*. Materials Characterization, 2002. **48**(4): p. 279-295.
32. Thöne, M., S. Leuders, A. Riemer, T. Tröster, and H.A. Richard, *Influence of heat-treatment on Selective Laser Melting products-e.g. Ti6Al4V*. 2012.
33. Sallica-Leva, E., R. Caram, A.L. Jardini, and J.B. Fogagnolo, *Ductility improvement due to martensite α' decomposition in porous Ti-6Al-4V parts produced by selective laser melting for orthopedic implants*. Journal of the Mechanical Behavior of Biomedical Materials, 2016. **54**: p. 149-158.
34. Cullity, B., *Element of X-ray Diffraction, Addison-Wesley Reading*. MA Google Scholar, 1978.
35. Gil, F.J., M.P. Ginebra, J.M. Manero, and J.A. Planell, *Formation of α -Widmanstätten structure: effects of grain size and cooling rate on the Widmanstätten morphologies and on the mechanical properties in Ti6Al4V alloy*. Journal of Alloys and Compounds, 2001. **329**(1): p. 142-152.
36. *Influence of tempering temperature and time on the α' -Ti-6Al-4V martensite*. Journal of alloys and compounds, 1996. **234**(2): p. 287-289.
37. Molchanova, E.K., *Phase diagrams of titanium alloys*. 1965: Israel Program for Scientific Translations.
38. Peters, M., J. Hemptenmacher, J. Kumpfert, and C. Leyens, *Structure and Properties of Titanium and Titanium Alloys*, in *Titanium and Titanium Alloys*. 2005, Wiley-VCH Verlag GmbH & Co. KGaA. p. 1-36.

39. Agius, D., K.I. Kourousis, C. Wallbrink, and T. Song, *Cyclic plasticity and microstructure of as-built SLM Ti-6Al-4V: The effect of build orientation*. Materials Science and Engineering: A, 2017. **701**: p. 85-100.
40. Yadroitsev, I., P. Krakhmalev, and I. Yadroitsava, *Selective laser melting of Ti6Al4V alloy for biomedical applications: Temperature monitoring and microstructural evolution*. Journal of Alloys and Compounds, 2014. **583**: p. 404-409.
41. Gong, H., K. Rafi, H. Gu, T. Starr, and B. Stucker, *Analysis of defect generation in Ti-6Al-4V parts made using powder bed fusion additive manufacturing processes*. Additive Manufacturing, 2014. **1-4**: p. 87-98.
42. Yang, J., J. Han, H. Yu, J. Yin, M. Gao, Z. Wang, and X. Zeng, *Role of molten pool mode on formability, microstructure and mechanical properties of selective laser melted Ti-6Al-4V alloy*. Materials & Design, 2016. **110**: p. 558-570.
43. Yasa, E. and J.P. Kruth, *Microstructural investigation of Selective Laser Melting 316L stainless steel parts exposed to laser re-melting*. Procedia Engineering, 2011. **19**: p. 389-395.
44. Mukherjee, T., J.S. Zuback, A. De, and T. DebRoy, *Printability of alloys for additive manufacturing*. Sci Rep, 2016. **6**: p. 19717.
45. *Titanium Alloys*, in *Handbook of Advanced Materials*. 2004. p. 271-319.
46. Froes, F., *Titanium alloys*. Handbook of advanced materials, 2004: p. 271.
47. Moletsane, M., P. Krakhmalev, N. Kazantseva, A. Du Plessis, I. Yadroitsava, and I. Yadroitsev, *Tensile properties and microstructure of direct metal laser-sintered TI6AL4V (ELI) Alloy*. South African Journal of Industrial Engineering, 2016. **27(3)**: p. 110-121.
48. Rafi, H.K., T.L. Starr, and B.E. Stucker, *A comparison of the tensile, fatigue, and fracture behavior of Ti-6Al-4V and 15-5 PH stainless steel parts made by selective laser melting*. The International Journal of Advanced Manufacturing Technology, 2013. **69(5-8)**: p. 1299-1309.

Chapter 7

Conclusion and future work

The main findings and significance of the current study on the powder bed fusion 3D printing of Ti6Al4V alloy are summarized below, along with suggested themes for future study.

7.1 Summary and significance

This research presented a practical method for optimisation of the process parameters for fabricating sound parts. Finding the correlation between the surface topography and microstructure was investigated at a fundamental level. Then, surface topography as a criterion for soundness of the parts was established. Furthermore, a maximum and minimum for the required laser power were investigated and a guide for choosing the proper hatch spacing was found.

In principle, conventional powder metallurgy, as another near net shape manufacturing route, was compared with the LPBF technique. We found that the constituent phases in

the microstructure of Ti6Al4V powder metallurgy parts, were α and β phase, but LPBF parts had only the hcp martensitic phase of α' . The martensite phase in Ti6Al4V parts was the outcome of diffusionless transformation from the bcc β phase. Also, the microstructure of the LPBF parts exhibited a columnar architecture as evidence of the epitaxial growth of the parent phase β .

In this work it was demonstrated that, by implementing a novel design, fabrication of undistorted horizontal parts becomes viable for studying the effects of build orientations on mechanical properties of parts under real as-built conditions. The premature failure of as-built verticals was attributed to flattened pores, where their sharp flat edges behaved as stress raisers (stress concentration) when their orientation is aligned with the load direction. It was proved that any post processes of either surface machining, stress relieving or annealing can overcome the challenge of failure of as-built vertical parts. However, it was demonstrated that the most effective post process was annealing at a temperature of 850°C rather than surface machining or stress relieving.

The summary and conclusions of this thesis are as follows:

- 1- A practical approach was implemented for optimisation of the process parameters by considering the effects of three main variables, laser power, laser scan speed and hatch spacing, on the surface quality and bulk integrity of the LPBF fabricated Ti6Al4V parts. It was identified that the morphology of the top surface of the samples falls into two categories: meso-roughness (or wavy surface) and micro-roughness (or non-wavy surface), which is the novel approach proposed for the assessment of Ti6Al4V parts fabricated via LPBF route.
- 2- We highlight the correlation between the bulk porosity of the parts with their surface micro-roughness but not with their meso-roughness.

- 3- We identify the top and bottom thresholds (or ranges) of energy density as a combined parameter, and the two independent parameters: laser power and hatch spacing, through which the optimised scan speed can be calculated. It was postulated that surfaces with meso-roughness quality may be an indication of less harmonized process parameters. Thus, the actual target in the optimization process should be based on achieving parts with micro-roughness (R_a) lower than a certain value of $9\mu\text{m}$ to achieve the highest relative density of 99.85% of parts.
- 4- We consider the production rate as one of the other important measures in optimization process, where appropriate laser power must be chosen.
- 5- Characterisation of the microstructure of 3D printed Ti6Al4V parts revealed that their higher micro-hardness is only attributable to the refinement of the microstructure, evolving during the LPBF process, and the laths morphology of the martensite phase, α' . By comparing the nano-hardness of α' (as a result of diffusionless transformation) with α (as the outcome of diffusional transformation), it was demonstrated that their bulk harnesses are nearly the same, i.e., 6.3GPa and 6.2GPa respectively. In other words, martensite phase α' with hcp crystal structure is not a harder phase than α with the same structure.
- 6- We quantified the bulk nano-hardness of α phase in powder metallurgy samples when the concentration of vanadium solute atoms changes from nearly 1% to less than 4.9%. It has been highlighted that there are lower concentrations of vanadium in the hcp crystal structure of α , increases in the hardness of the α phase and vice versa, so it is hypothesised that substituted vanadium atoms in hcp crystals allow dislocations to move with less friction, resulting in a softer α phase with increasing vanadium.
- 7- We demonstrated a novel design for fabrication of undistorted Ti6Al4V horizontal samples to achieve a “truly as-built” condition. This naming is due to the fact that

the samples were not treated under any sort of post processes. Thus, the measurement of the mechanical properties of the vertical and horizontal parts built in “truly as-built” become viable.

- 8- We highlighted the considerable effect of layering direction with respect to the tensile loading direction in “truly as-built” conditions. By understanding this effect, a fabricated part is determined to be used directly in service with or without post treatment considering the loading condition in the real application.
- 9- We identified the grounds for premature failure of “truly as-built” vertical parts as their shortcomings. It was confirmed that the deficiency of vertical parts (where the load is aligned with the build direction, layering direction) is attributable to two factors, micro-grooves of as-built surfaces and induced residual stress on the surface, together. Therefore, by either machining the outer surface of the as-built vertical or implementing one of the thermal treatments (stress relieving or annealing) the vertical samples stop failing prematurely.
- 10- We highlighted strong anisotropy in the ductility between machined vertical and horizontal samples. It was demonstrated that this anisotropy is associated with residual stress and the orientation of pores in respect of loading direction. It was demonstrated that by annealing, at 850°C, where all the residual stresses are relieved, this anisotropy is significantly removed.
- 11- We identified a new microstructural feature named a “fish scale”, in non-heat treated and stress-relieved vertical samples. It was shown that the formation of fish scales may contribute to lowering the ductility of vertical samples.
- 12- We compared the effect of surface machining and annealing separately on the elongation of the vertical samples. This confirmed that annealing at 850°C is more effective than surface machining. Therefore, in some applications where the

mechanical properties need to be improved by choosing one post process, or where machining is either costly or not viable, the annealing process alone may be the most appropriate solution.

7.2 Recommendations for future work

Experimental tests to study the effect of fabrication process parameters on the quality and integrity of 3D printed Ti6Al4V alloy were successfully conducted with significant outcomes; however, inevitable limitations in this study may create new opportunities for further work and study. To reach a solid conclusion aligned with the outcome of this study, it is recommended that further study be performed with the same 3D printing machine or at least a machine with similar specifications. Some recommendations for future work are summarised below.

7.2.1 Process parameters

- The optimization method for process parameters was performed based on a uni-directional laser scan strategy. However, the scan strategy could have some effect on the integrity of the printed parts. Therefore, it is recommended that researchers examine the role played by the scan strategy on the optimised process parameters.
- The main aim of the optimisation procedure in this study was printing the parts with better surface quality and lower porosity. Such an attempt was mainly based on the selection of a range of acceptable process parameters and energy density. For further study, considering the acceptable range of parameters achieved in this work, the effect of parameters on strength and ductility could be investigated. This may be achieved by studying the effect of parameters on the morphology of flattened pores as one the main factors affecting ductility.

- Premature failure of the “truly as-built” vertical parts was resolved by post processing: either surface machining or thermal treatment. Study is proposed on the effect of depositing a separate contour layer around the outer surface of the “truly as-built” vertical to clarify the role played by the micro-grooves and residual stresses on the mechanical properties of the printed parts.

7.2.2 Experiments

The experiments conducted in this study for mechanical properties were limited to tensile tests and hardness. All the findings in this study regarding the effect of as-built surfaces, machined surfaces, and thermal treatment of 3D printed Ti6Al4V alloys can be re-investigated for other mechanical properties, such as fatigue, creep at elevated temperatures, or the effect of corrosive environments on mechanical properties.

7.2.3 Post processes

The post processes performed in this work were surface machining and two types of thermal treatment. The surface treatments could be expanded to other techniques like laser peening, chemical etching, and surface rolling.

The thermal treatment could be conducted in single stage at higher temperatures beyond beta transus in order to investigate the effect of higher temperatures on blunting the sharp edges of micro-grooves and flattened pores in the as-built verticals. Moreover, the effect of other types of annealing, like duplex or triplex, for improving the anisotropy is another possible avenue for further work.

Appendices: Original published papers as parts of this study

Appendix A: Papers presented in the chapters of this thesis

Article

Microstructural Development of Ti-6Al-4V Alloy via Powder Metallurgy and Laser Powder Bed Fusion

Alireza Dareh Baghi ^{1,*}, Shahrooz Nafisi ^{1,2} , Heike Ebendorff-Heidepriem ³  and Reza Ghomashchi ^{1,3}¹ School of Mechanical Engineering, University of Adelaide, Adelaide, SA 5005, Australia² Relativity Space, Long Beach, CA 90815, USA³ Institute of Photonics and Advanced Sensing, School of Physical Sciences, University of Adelaide, Adelaide, SA 5005, Australia

* Correspondence: alireza.darehbaghi@adelaide.edu.au

Abstract: A detailed study was carried out to gain a better understanding of the microstructural differences between Ti-6Al-4V parts fabricated via the conventional powder metallurgy (PM) and the laser powder bed fusion (L-PBF) 3D printing routes. The parts were compared in terms of the constituent phases in the microstructure and their effects on the micro- and nano-hardness. In L-PBF parts, the microstructure has a single phase of martensitic α' with hcp crystal structure and acicular laths morphology, transformed from prior parent phase β formed upon solidification of the melt pool. However, for the sintered parts via powder metallurgy, two phases of α and β are noticeable and the microstructure is composed of α grains and $\alpha + \beta$ Lamellae. The microhardness of L-PBF processed Ti-6Al-4V samples is remarkably higher than that of the PM samples but, surprisingly, the nano-hardness of the bulk martensitic phase α' (6.3 GPa) is almost the same as α (i.e., 6.2 GPa) in PM samples. This confirms the rapid cooling of the β phase does not have any effect on the hardening of the bulk martensitic hcp α' . The high microhardness of L-PBF parts is due to the fine lath morphology of α' , with a large concentration of low angle boundaries of α' . Furthermore, it is revealed that for the α phase in PM samples, a higher level of vanadium concentration lowers the nano-hardness of the α phase. In addition, as expected, the compacting pressure and sintering temperature during the PM process led to variations in the porosity level as well as the microstructural morphology of the fabricated specimens, which will in turn have a significant effect on the mechanical properties.

Keywords: additive manufacturing; laser powder bed fusion; Ti-6Al-4V (Ti64); powder metallurgy



Citation: Dareh Baghi, A.; Nafisi, S.; Ebendorff-Heidepriem, H.; Ghomashchi, R. Microstructural Development of Ti-6Al-4V Alloy via Powder Metallurgy and Laser Powder Bed Fusion. *Metals* **2022**, *12*, 1462. <https://doi.org/10.3390/met12091462>

Academic Editor: Amir Mostafaei

Received: 28 July 2022

Accepted: 24 August 2022

Published: 31 August 2022

Publisher's Note: MDPI stays neutral with regard to jurisdictional claims in published maps and institutional affiliations.



Copyright: © 2022 by the authors. Licensee MDPI, Basel, Switzerland. This article is an open access article distributed under the terms and conditions of the Creative Commons Attribution (CC BY) license (<https://creativecommons.org/licenses/by/4.0/>).

1. Introduction

Titanium and titanium-based alloys have emerged as appealing materials for numerous applications due to their adequate strength, high specific strength, excellent corrosion resistance, and exceptional biocompatibility [1,2]; however, conventional manufacturing technologies often utilized for the fabrication of titanium-based alloy products are generally high energy and materials intensive, and time-consuming [3]. Therefore, emerging digitized and automated manufacturing techniques, known as additive manufacturing (AM), are receiving increased attention and starting to play a significant role in the manufacture of titanium parts.

The laser powder bed fusion (L-PBF) technique, also known as selective laser melting (SLM), for titanium alloys has attracted increasing global interest due to its distinctive characteristics and a range of notable advantages over conventional manufacturing techniques. During the L-PBF fabrication process, materials are added layer by layer rather than subtracted as is the case for conventional manufacturing. The layer-wise build technology provides a unique advantage in design freedom for complex geometry without the need for tooling. The other attraction of the L-PBF near-net-shape production route is the ability to simplify production feasibility for fabrication of low quantities of manufactured parts, even

down to a batch size of one. The basic working principle and the mechanics of the L-PBF process are widely available in the open literature [4–8]. L-PBF is also capable of processing high melting temperature materials, such as ceramics, and it accurately produces complex features, which is impossible to achieve using conventional fabrication techniques [9–12]. The more traditional near-net-shape manufacturing route, powder metallurgy (PM), is comparable with L-PBF as both have their starting materials in the powder form, generate near-net shape outcome parts, have high material utilization rates, and create minimum waste [13]. In the L-PBF process, the alloy powder is exposed to rapid melting and solidification, whereas, in the PM route, powder particles are sintered during or after compaction at moderate heating and cooling rates. Since the starting feedstock is the same and the level of net shaping and materials used are comparable for these two manufacturing routes, it is interesting to explore the differences in microstructure and mechanical properties of the fabricated parts.

Ti-6Al-4V (also known as Ti64) is among the titanium alloys to offer a wide range of applications in aerospace [14,15] and biomedical applications [16–18]. For this reason, there are many research articles about the mechanical properties of Ti64 fabricated via L-PBF in the open literature, reporting a higher strength of L-PBF that is attributed to the formation of martensitic α' . However, it has not been clarified if the higher hardness of L-PBF parts is related to the martensitic crystal structure or the morphology and refinement of the α' phase. In addition, the morphology and crystal structure resulting in L-PBF has not yet been compared with the traditional near-net-shape powder metallurgy technique.

In this paper, the constituent phases in the microstructure of Ti64 alloy processed by the two near-net-shape manufacturing routes of L-PBF and PM were studied using micro- and nano-hardness testing of the identified phases of α , β , and α' to highlight the reasons underlying the higher strength reported for L-PBF fabricated Ti64 parts.

2. Materials and Experimental Procedures

The starting material for both L-PBF and PM processes was Ti64 (grade 5) gas atomized pre-alloyed powder obtained from TLS, Technik GmbH & Co (Wilhelmshaven, Germany) (TLS, Technik GmbH & Co (Wilhelmshaven, Germany) is a subsidiary of AL-TANA's ECKART division (www.eckart.net) accessed on 28 July 2022). The powder used in this investigation exhibited particle diameters between 11.9 μm and 41.3 μm (percentile values d_{10} and d_{90} , respectively) with a median size d_{50} of 22.7 μm . The powder size distribution is shown in Figure 1, based on the analysis performed using a laser particle size analyzer, the Malvern Mastersizer 2000 (Malvern Instruments Ltd., Worcestershire, UK). SEM micrographs of the powder particles displayed in Figure 2 exhibit spherical morphology, which is due to the gas atomization process and makes the powders suitable for the L-PBF process because of their high flowability [19]. The satellite particles are also identifiable from the SEM image.

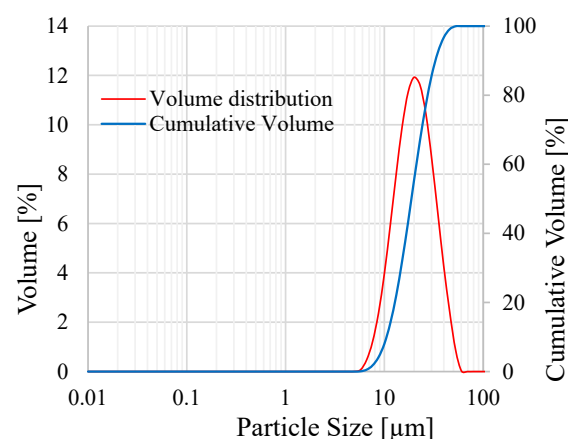


Figure 1. Size distribution of Ti64 powder particles.

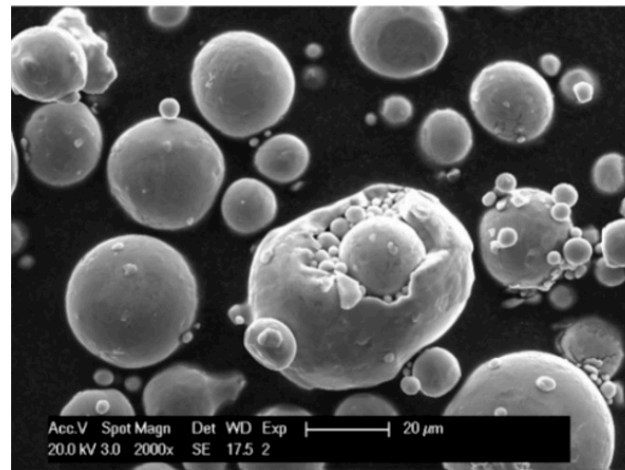


Figure 2. Spherical morphology of Ti64 powder with satellite particles and particles inside particles.

For the chemical composition of the powder, the ICP-AES technique was employed to measure the weight percentages of vanadium, iron and aluminum. To analyze the content of the carbon a LECO CS200 instrument (LECO corporation, St. Joseph, MI, USA) was used, whilst to measure the percentage of hydrogen, nitrogen, and oxygen, a LECO ONH836 analyzer (LECO corporation, St. Joseph, MI, USA) was utilized. Table 1 confirms that the chemical composition of Ti-6Al-4V powder complies with the ASTM F2924-14 standard [20]. For fabrication of specimens via L-PBF routes, the powder did not have any treatment; however, for the PM samples, the powder was mixed up with 1.5 wt.% binders, as explained later.

Table 1. Chemical composition of Ti64 powder (wt.%).

Element	Al	V	Fe	O	C	N	H	Ti
Ti64 powder	6.15	3.94	0.18	0.098	0.005	0.01	<0.002	Bal.
ASTM F2924-14	5.50–6.75	3.50–4.50	Max 0.3	Max 0.2	Max 0.08	Max 0.05	Max 0.015	Bal.

The L-PBF machine used in this investigation was a 3D SYSTEMS ProX DMP 200(3D Systems, Rock Hill, South Carolina, SC, USA), which employs a laser source with a maximum power of 300 W in continuous laser mode. The laser beam diameter of the machine is 70 μm , with a wavelength (λ) of 1070 nm. The atmosphere of the L-PBF chamber is high purity argon, maintained during the course of deposition at atmospheric pressure (101 KPa) to prevent potential oxidation of the molten pool. The maximum allowed oxygen content of the chamber is regulated at 500 ppm. The L-PBF process parameters, shown in Table 2, are from the previous study [21], where the authors could fabricate Ti64 parts with a relatively high density of 99.86%. The cylindrical samples with a diameter of 9 mm and a length of 20 mm were built horizontally and vertically, i.e., the axis of the cylindrical samples was parallel and perpendicular to the substrate respectively. For the laser scan strategy, a bi-directional laser vector for each layer was selected, while the bi-direction laser pattern was rotating 90° between each consecutive layer.

Table 2. L-PBF processing parameters for fabrication of Ti64 samples.

Laser Power (W)	Scan Speed (mm/s)	Layer Thickness (μm)	Hatch Spacing (μm)
270	1800	30	85

For fabrication of PM samples, the Ti64 powder was ball-mill treated before being poured in a double-action die set with a punch diameter of $\text{\O}11$ mm to produce 10 mm

long specimens. In ball-mill treatment, the powder was mixed with 1.5 wt.% Acrawax (Acrawax™ C Atomized is N, N' Ethylene bis-stearamide (EBS)) lubricant/binder and poured into a stainless steel ball-mill container. The ball milling process was carried out at a constant rotation speed of 100 RPM for 1 h using stainless steel balls with a diameter of 6 mm. The ball-to-powder weight ratio was 5:1 and the milled powder was used as the starting powder for the PM process. The powder mixture was compacted using a Mohr & Federhaff AG Mannheim-Germany (M&F 2) 20-ton hydraulic press, at two different compaction pressures of 450 and 735 MPa, at room temperature.

The sintering process was conducted in a horizontal resistance heating tube furnace, model AY-TF-80-175, with a high purity grade argon atmosphere and heating rate of 5 °C/min. The as-compacted green samples were sintered at 1100 °C and 1250 °C. However, before reaching sintering temperatures, a dwell time of 30 min at 450 °C was employed to burn out the Acrawax lubricant added to the powder. The samples were heated to sintering temperatures and held isothermally for 1 h at these temperatures, followed by a furnace cooling rate of 3 °C/min to room temperature.

For metallographic examinations, all the PM and L-PBF cylindrical samples were sectioned transversally (perpendicular to the axis of samples). However, for the statistical significance of nano-hardness results, it was necessary to section further sites of the L-PBF samples, as will be explained later in this section.

All metallographic samples were mounted in Bakelite and polished conventionally with a fine final polishing of 0.04 µm colloidal silica under 15 N force for 25 min on a Struers Tegramin-25 machine (Struers, Copenhagen, Denmark). For microstructural analysis, the Zeiss Axio optical microscope Imager2 (Zeiss, Wetzlar, Germany) and an FEI Quanta 450 FEG-SEM (FEI, Hillsbor, Oregon, OR, USA) were used. The porosity level of all polished samples was examined on the images obtained from the Zeiss optical microscope via ImageJ software (Zeiss, Wetzlar, Germany). It should be noted that the percentage of porosity was measured on the as-polished surface.

X-ray diffraction (XRD) was performed for phase identification purposes for the powder, as well as the PM and the L-PBF-fabricated samples. The XRD machine (MiniFlex 600-Rigaku, Rigaku, Tokyo, Japan) employed Cu radiation operating at 40 kV and 15 mA, in continuous scan mode with a scan speed of 10°/min and 2θ ranging from 30° to 80°. A Vickers microhardness measurement of all samples was performed with a LECO LM700AT (LECO corporation, St. Joseph, MI, USA). A load of 300 g with a dwelling time of 10 s was chosen for all the measurements. Ten measurements were taken for each sample and the average values were calculated as the microhardness.

For nano-indentation testing, a Fisher-Cripps IBIS system with a Berkovich indenter was utilized. The maximum penetration depth of the indenter was set at 300 nm (depth control) for all samples and the indenter was held for 2 s at the maximum penetration depth before unloading. The loading and unloading rate of the indenter was 60 nm/s; therefore, each loading and unloading procedure took 5 s.

For the PM samples, 120 nano-indentations were performed on unetched metallographic samples where all constituent phases could be observed and identified. The inter-center distances of the nano-hardness impressions for the PM samples were at least 10 µm apart to ensure no interference occurred between the indentations.

For the nano-hardness of L-PBF samples, each sample of the horizontal and vertical builds was equally sectioned into four short cylindrical discs, as displayed in Figure 3a. Then, on each disc, 130 indents with a 60 µm space between the centers of the indents were impressed in two directions, as illustrated in Figure 3b. The reason for impressing nano-indentations in two directions was to obtain more representative data from each section, with better statistical significance and representation of the results. To eliminate any effect of an unstable melt pool or induced residual stress near the peripheral surface, the nano-indentations started and ended approximately 0.6 mm away from any surface of the L-PBF samples, Figure 3b. As the final polishing for 25 min with a low load of 15 N left minor polishing-related etching on the samples, the traces of the phases were visible in

the micrographs, even in the unetched condition. This minor polishing-related etching helped the nano-indentations with their corresponding results be categorized accurately for each specific phase. It has already been shown [22] that the micro-hardness results in the unetched and etched conditions are nearly the same, meaning that the values of micro-hardness in the etched condition are still valid and reliable. However, nano-indentations should be conducted on polished (unetched) samples only to ensure reliable results.

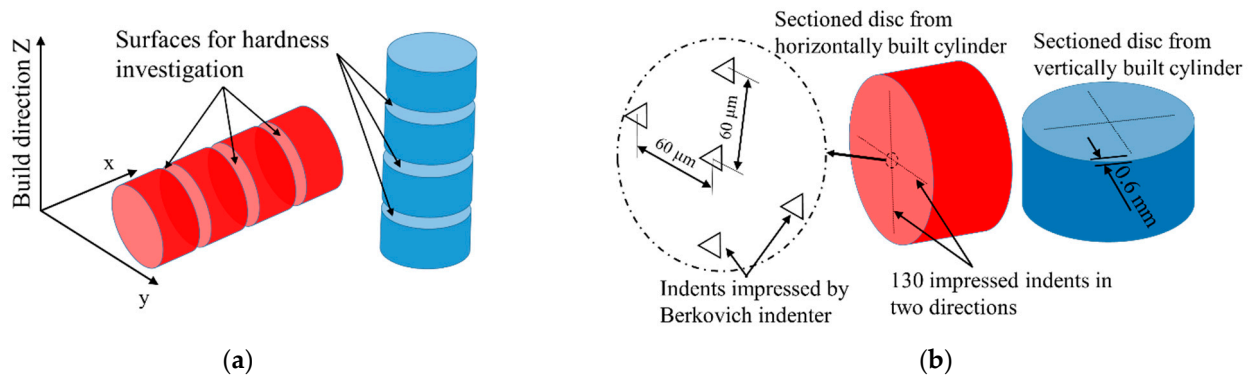


Figure 3. (a) sectioning plan for hardness measurement of L-PBF fabricated vertical and horizontal samples, (b) nano-indentation maps for sectioned discs from vertical and horizontal samples.

After the microhardness and nano-hardness experiments, all the samples were etched with Kroll's reagent, (3% HF + 5% HNO₃ + 92% distilled water) for 30 s for microstructural characterization by optical and scanning electron microscopy. Energy Dispersive X-Ray Spectroscopy (EDS) was performed using Aztec analysis software (Oxford Instruments, Abingdon, UK) with an SDD detector released by Oxford Instruments fixed on Quanta 450 FEG-SEM (FEI, Hillsbor, Oregon, OR, USA).

3. Results and Discussion

3.1. Microstructural Constituents

Microstructural characterization was initially carried out on the as-received powder particles and then continued on the L-PBF fabricated samples. Due to rapid solidification occurring during the fabrication of powder and L-PBF parts, they were expected to exhibit similar constituent phases. From the SEM micrographs in Figure 4a,b, it is evident that a fully acicular, i.e., tiny needle shape, the martensitic microstructure of α' , has evolved in both the starting powder and the L-PBF fabricated specimens, as reported by other researchers [21,23–25]. However, when the L-PBF micrograph (Figure 4b) is examined closely, there are some light contrast features (encircled) different from martensite needles. The arrowed encircled feature in Figure 4b is termed the “fish scale” as reported in a previous study [26]. The fish scale feature is not a new phase. It is the same hcp α' phase observed in other regions of the microstructure, but its aluminum content has dropped from its nominal value, due to possible localized overheating and vaporization of aluminum, as a volatile alloying element in Ti64 [27].

As seen in Figure 5, it seems the formation of porosities is the main defect in the PM parts. It is quite evident that the sintering temperature is the key parameter on the microstructural development as the specimens sintered at 1100 °C have still preserved their powder morphology character, while this is not the case for samples sintered at 1250 °C, regardless of compaction pressure. However, when the microstructure at 1100 °C is examined closely, it becomes evident that the two mechanisms of Ostwald ripening (smaller particles dissolve and deposit on larger particles) and particle coalescing (joining of particles) [28] are active during the sintering process. In addition to sintering temperature, the application of a higher compaction pressure also imparts some improvement on the density of sintered samples if Figure 5a,c is compared. Based on the porosity percentage analysis shown in Table 3, under the same sintering temperature (either 1100 °C or 1250 °C),

the samples compacted at 450 MPa exhibit higher percentages of porosity than those compacted at 735 MPa.

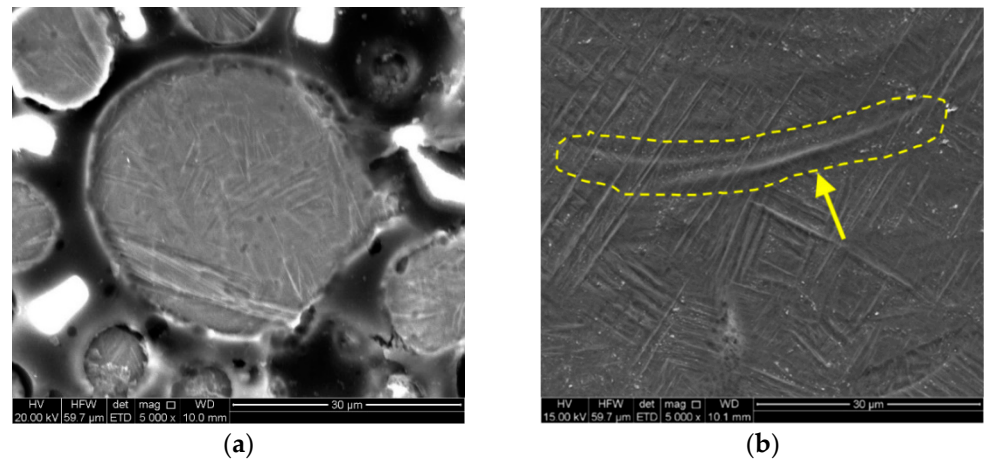


Figure 4. SEM micrographs of etched (a) starting powder particles and (b) L-PBF sample.

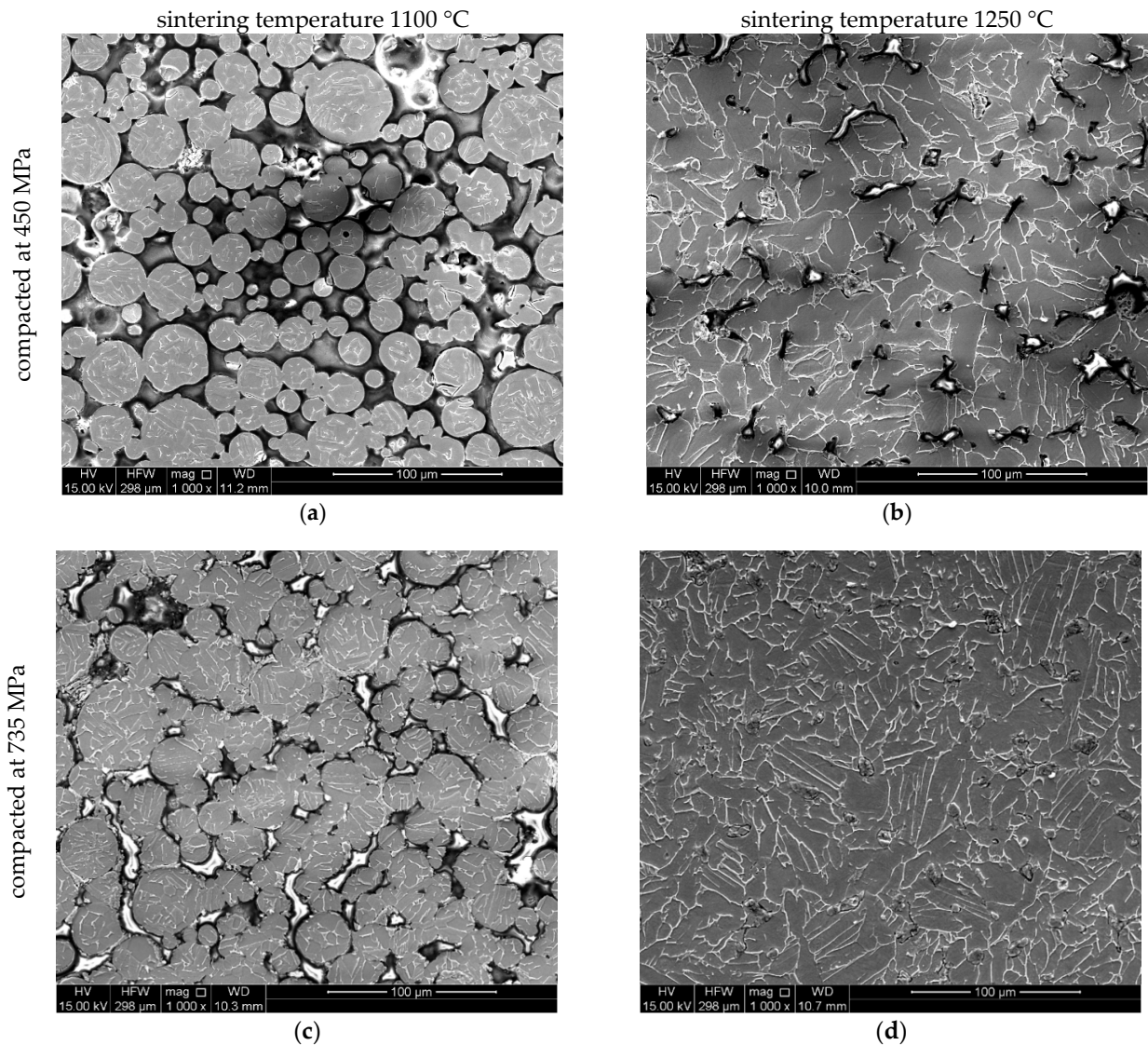
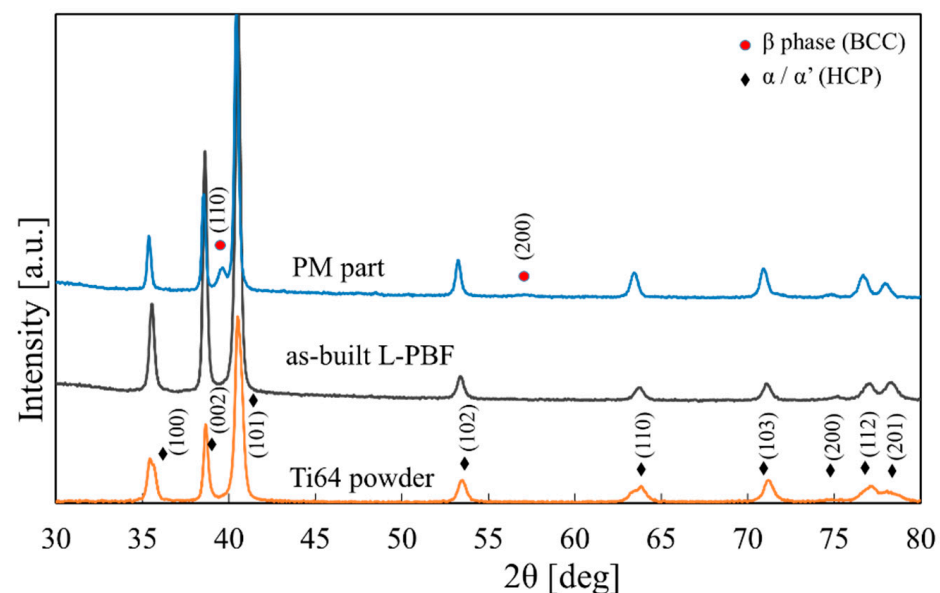


Figure 5. SEM images of PM samples sintered at 1100 °C: (a) compacted at 450 MPa and (c) 735 MPa, and PM samples sintered at 1250 °C: (b) compacted at pressure 450 MPa and (d) 735 MPa.

Table 3. Porosity percentage of PM samples.

Sample	Compacting Pressure (MPa)	Sintering Temperature (°C)	Sintering Time (h)	Porosity (%)
Powder metallurgy (PM)	450	1100	1	26.0 ± 1.2
		1250		9.0 ± 0.5
	735	1100		13.0 ± 1.6
		1250		4.0 ± 0.2

The XRD phase analysis of both L-PBF and PM samples is given in Figure 6 as a stacked graph of XRD spectra of starting powder, as-built L-PBF, and PM samples. The XRD spectrum of the PM belongs to the sample fabricated under 750 MPa compacting pressure and sintering temperature of 1250 °C. As seen in Figure 6, the hcp α/α' phase exists in all samples, while the formation of the β phase is only observed in the PM samples. Martensitic phase α' and phase α have not been differentiated in the XRD spectra, as both α and α' have the same hcp crystal structure and their lattice parameters are very close [26,29–32]. The α phase has transformed from the parent β (bcc) phase in a diffusion-controlled transformation in the PM sample, while the α' martensitic phase has experienced a diffusionless transformation from the β (bcc) phase, resulting in supersaturation of vanadium in α' [33,34].

**Figure 6.** XRD spectra of Ti64 powder, as-built L-PBF, and PM sample.

The evolution of martensitic microstructure in the L-PBF samples is attributed to the rapid cooling [35,36] in which the cooling rate may vary between 10^3 and 10^6 K/s [37–40]. This is true for the α' martensitic phase in Ti64 powder since the particles experience a high cooling rate during gas atomization of molten alloy [41]. For PM samples in Figure 5, however, the martensitic needle shape α' observed in the as-atomized powder particles is no longer observed; instead, grains of α have been developed in the matrix of β phase for all PM samples leading to a lamellar morphology. The nearly equiaxed α grains with $\alpha + \beta$ lamellae in PM samples are the result of diffusion-controlled transformation promoted by the slow cooling rate of 3 °C/min. This is well demonstrated in PM samples sintered at 1250 °C whereas in PM samples sintered at 1100 °C the particles are still in their original morphology, which is believed to be entirely due to a lower diffusion rate resulting from the lower sintering temperature. The presence of some remaining thick laths morphology demonstrated in Figure 5a,c, confirms the coarsening of the lath morphology and their

transformation to lamellae. The formation of lamellar structure, Figure 5b,d, was also observed by others [42–44]. It is worth mentioning that the highly charged white interparticle regions, more distinctly seen in Figure 5c, are the metallographic consumables' residue employed for sample preparation. They have accumulated within the pores.

EDS(Energy dispersive spectroscopy) examination of the microstructure, shown by the high magnification SEM micrographs in Figure 7, confirms that the light grey regions in the PM samples are rich in vanadium. The weight percentage of vanadium in three selected points (1–3), displayed in Figure 7b, is between 8.3% and 16.6%, which is beyond the vanadium nominal concentration of 4% in the Ti64 alloy examined in this study. Although it is a well-known fact that EDS analysis is a semi-quantitative method for measuring chemical composition, especially when the concentration of the element is very low, certainly confirms the localized segregation of vanadium. Since vanadium is a β -stabilizer, the formation of the vanadium-rich region in the Ti64 alloy could be an indication of the β phase [45,46]; so, the bright spots in the PM samples are evidence of the β phase. EDS analysis results of the L-PBF sample, Figure 7a, do not show drastic changes in the weight percentages of either aluminum or vanadium compared with their nominal values of 6% and 4%, respectively.

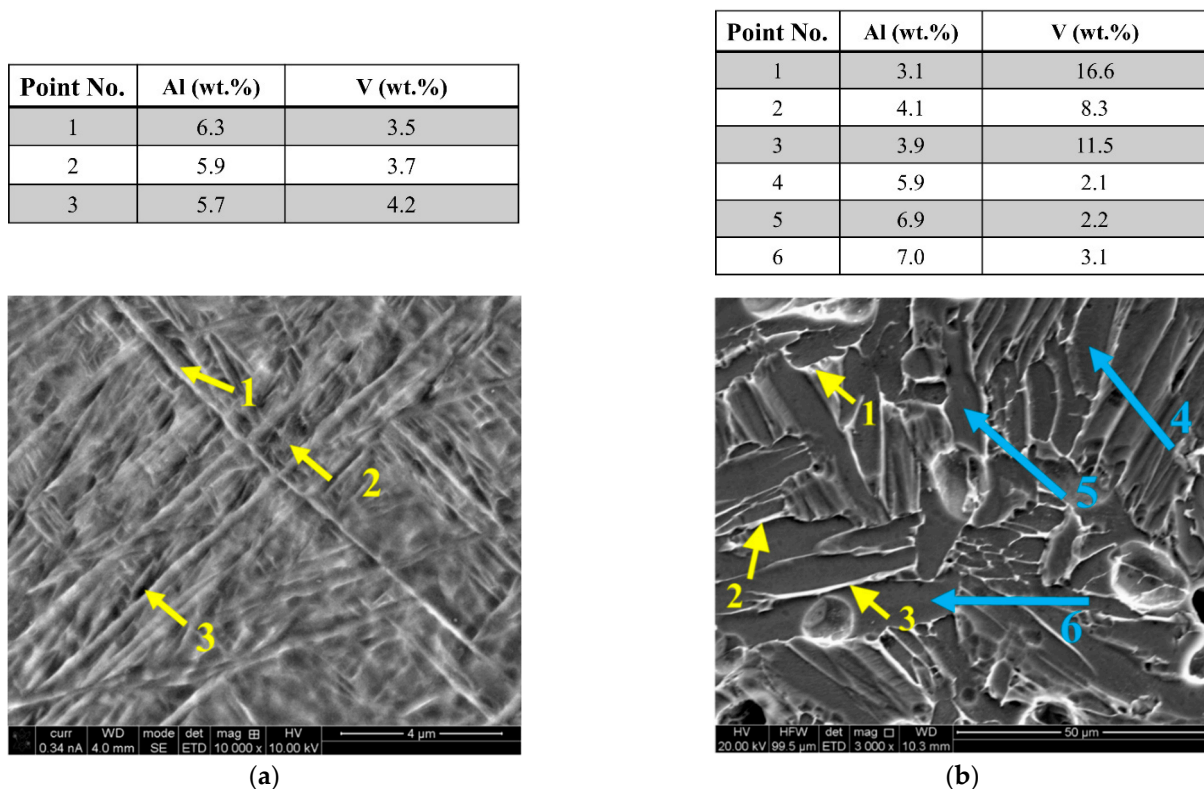


Figure 7. EDS analysis of (a) as-built L-PBF fabricated part, (b) PM sample (750 MPa/1250 °C).

This is expected as the rapid cooling encountered during L-PBF does not allow diffusion to take place. Optical micrographs of the L-PBF parts illustrated in Figure 8a reveal the columnar grain architecture of the martensitic microstructure, which is parallel with the L-PBF build direction. The chessboard pattern micrograph shown in Figure 8b is, indeed, a section perpendicular to the columnar grains. The prior β phase grain boundaries are observed in both micrographs of Figure 8a,b. This architecture of the microstructure is typically unique for L-PBF parts, as reported by other researchers [24,47], and is due to the layer-wise building mechanism in L-PBF where a thermal gradient of 10^4 – 10^5 °C/cm along the build direction exists within the very small melt pool [48].

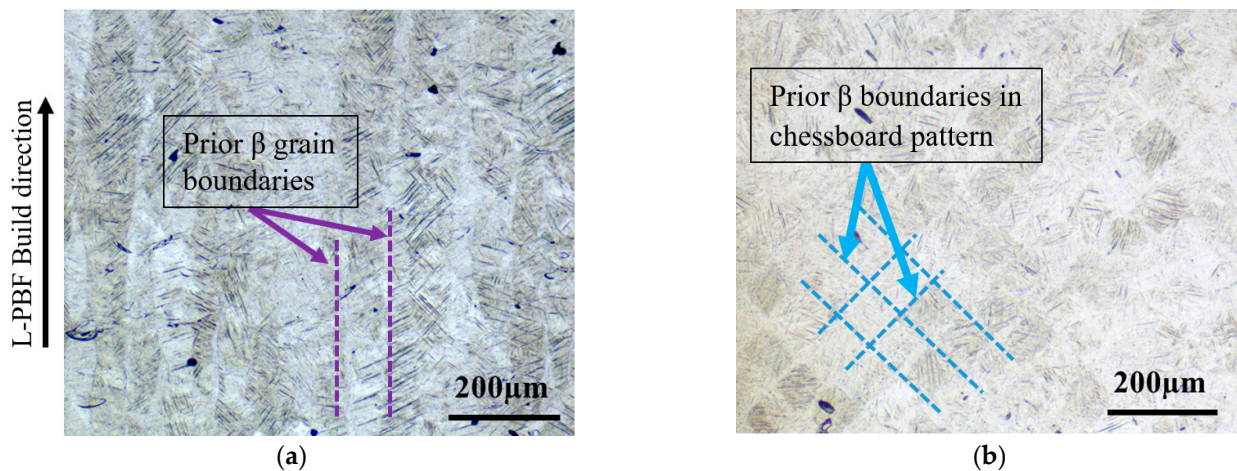


Figure 8. Optical micrographs of transverse sections of L-PBF parts after etching (a) horizontally built cylinder and (b) vertically built cylinder.

3.2. Micro and Nano-Hardness Characteristics

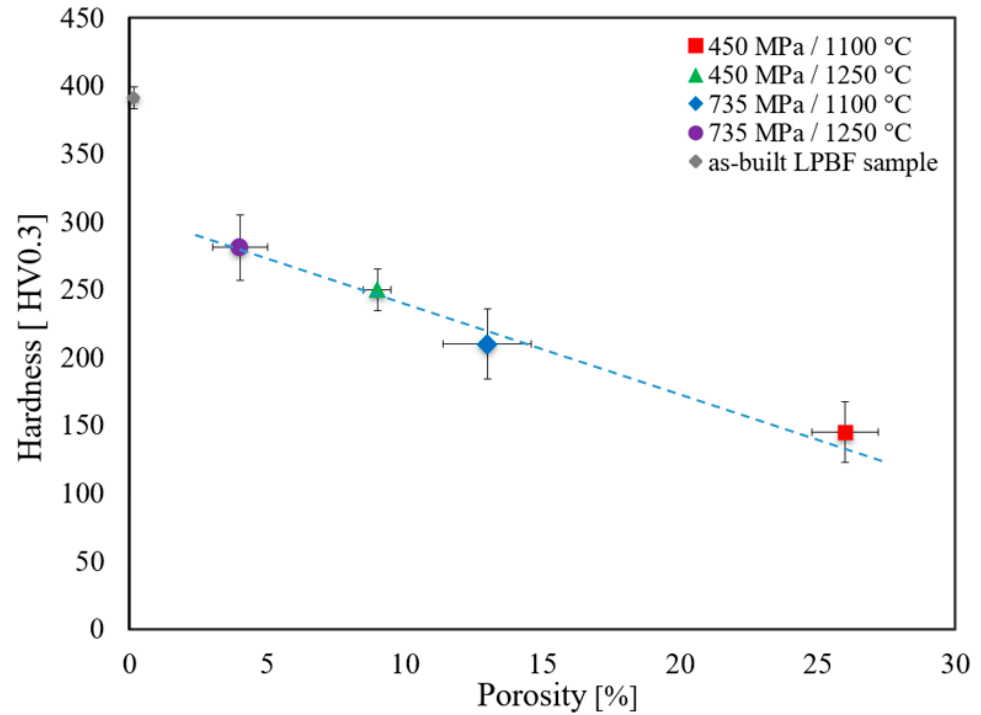
Figure 9 shows the tabulated results and a graph of the micro-hardness versus the porosity content for both the PM and L-PBF samples. For PM samples, the hardness increases with increasing compaction pressure and sintering temperature. At the same sintering temperature, the hardness value of a specimen compacted at a pressure of 435 MPa is lower than specimens compacted at a higher pressure of 735 MPa; this is attributed to the various levels of porosity content, Table 3, induced by various compacting pressures in the green samples. However as previously explained, the sintering temperature seems to be more effective in lowering the level of porosity than the compacting pressure.

In addition, as seen from Figure 9, the values of Vickers hardness are in the inverse correlation with the samples' porosity as expected. If the fitted line in Figure 9 is extrapolated to 100% dense PM samples, the highest achievable micro-hardness would be ~ 310 HV. This hardness value for PM sample, in a fully dense condition, is not far from the hardness (304 ± 12 HV) of the almost fully dense L-PBF sample (relative density of 99.86%) cooled from β -region at a rate of 0.1 $^{\circ}\text{Cs}^{-1}$ [49]. The reason as why that specific sample (0.1 $^{\circ}\text{Cs}^{-1}$ with that hardness value was used as a comparison with the fully dense PM estimated hardness is based on the phases that are present in that near equilibrium LPBF sample cooled from temperatures above the β transus temperature of this alloy, i.e., it contains $\alpha + \beta$ phases, the same phases form in the sintered PM samples. Any other LPBF sample, whether as-printed or reheated, may have a combination of α , α' , and β and are not valid since the phases will be different to those of PM samples and therefore hardness value will be different. For the as-printed L-PBF sample, with an almost fully dense microstructure, the micro-hardness is 22% higher than in the extrapolated fully dense PM sample, which is a noticeable increase in the hardness.

This improvement in the hardness of L-PBF samples is attributed to different constituent phases in L-PBF (α') and PM parts ($\alpha + \beta$), as observed and discussed earlier, alongside the formation of the lath martensitic structure and microstructural refinement in L-PBF [50,51]. In order to clarify whether the increase in hardness value is indeed due to the formation of a martensitic structure or the resulting refinements initiated by rapid cooling during the L-PBF process or both, nano-hardness testing of the PM and L-PBF samples was carried out for in situ measurement of hardness of individual phases.

For a nano-indentation examination, it is critical to perform the hardness measurement on an unetched high-quality surface finish, but the phase's recognition of the samples in the indented region through optical microscopy is a challenge. It has already been reported [22] that even light etching, can affect the nano-indentation results. As explained in Section 2, the final polishing step with colloidal silica for 25 min helped the phases of the samples be visible through SEM in unetched conditions. As seen from Figure 10a, the differentiation

between the two phases of β and α in the PM sample is more pronounced than the thin needle shape α' in the L-PBF sample, Figure 10b. EDS analysis of the regions at the vicinity of the nano-indentations, which is explained later, confirms that the light grey strips in Figure 10a are β phase, while the dark grey areas, covering the main part of the image, are α phase. This has already been confirmed in the etched PM sample, Figure 7b.



	Vickers Hardness (HV0.3)	Porosity (%)
■ 450 MPa / 1100 °C	145 ± 22.4	26.0 ± 1.2
▲ 450 MPa / 1250 °C	250 ± 15.5	9.0 ± 0.5
◆ 735 MPa / 1100 °C	210 ± 25.6	13.0 ± 1.6
● 735 MPa / 1250 °C	281 ± 14	4.0 ± 0.2
◆ as-built LPBF sample	391 ± 8.0	0.15 ± 0.02

Figure 9. Hardness of PM and L-PBF samples vs. their porosity contents.

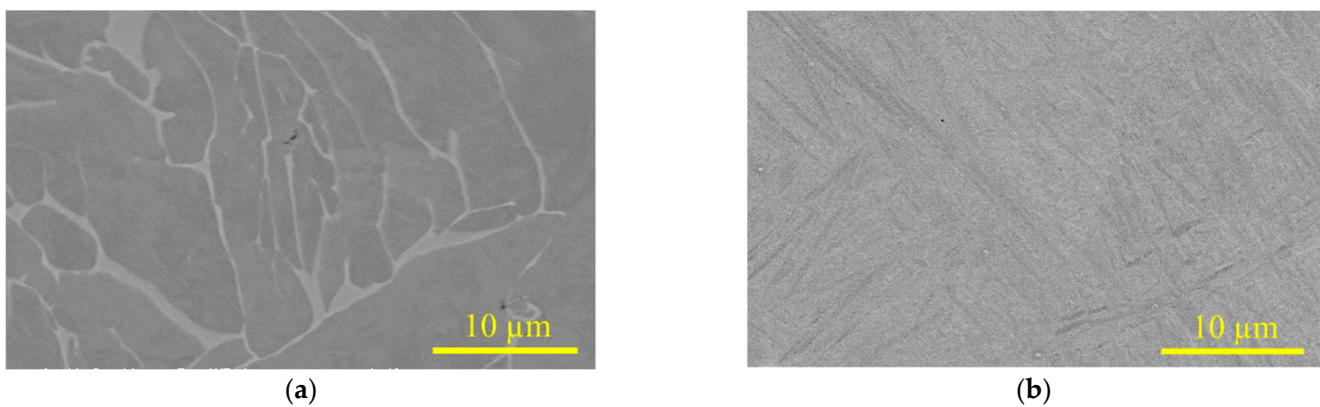


Figure 10. Backscatter electron image of polished samples in unetched conditions, (a) PM and (b) L-PBF sample.

Figure 11 shows the nano-indentation maps conducted on the PM sample. In order to increase the validity of the nano-indentation test results of a specific single phase like β , the regions of mixed phases, where the nano-indentations have been impressed, are disregarded. In this way, the contribution of different phases to each other (like the effect of the β phase on α or vice versa), is removed from the nano-indentation results. For example, impression 106 in Figure 11 is one of the points in which the indentation impression has included both phases of α and β . For that reason, the data of any impressions, like 106, were invalid and removed from the data analysis. Impressions 12 and 76 in Figure 11 are examples of the indentations having valid data because they were fully impressed on individual phases of α and β , respectively. For each individual impression, there is nano-characterization data besides the EDS spectrum, showing the elements of a phase on each indentation.

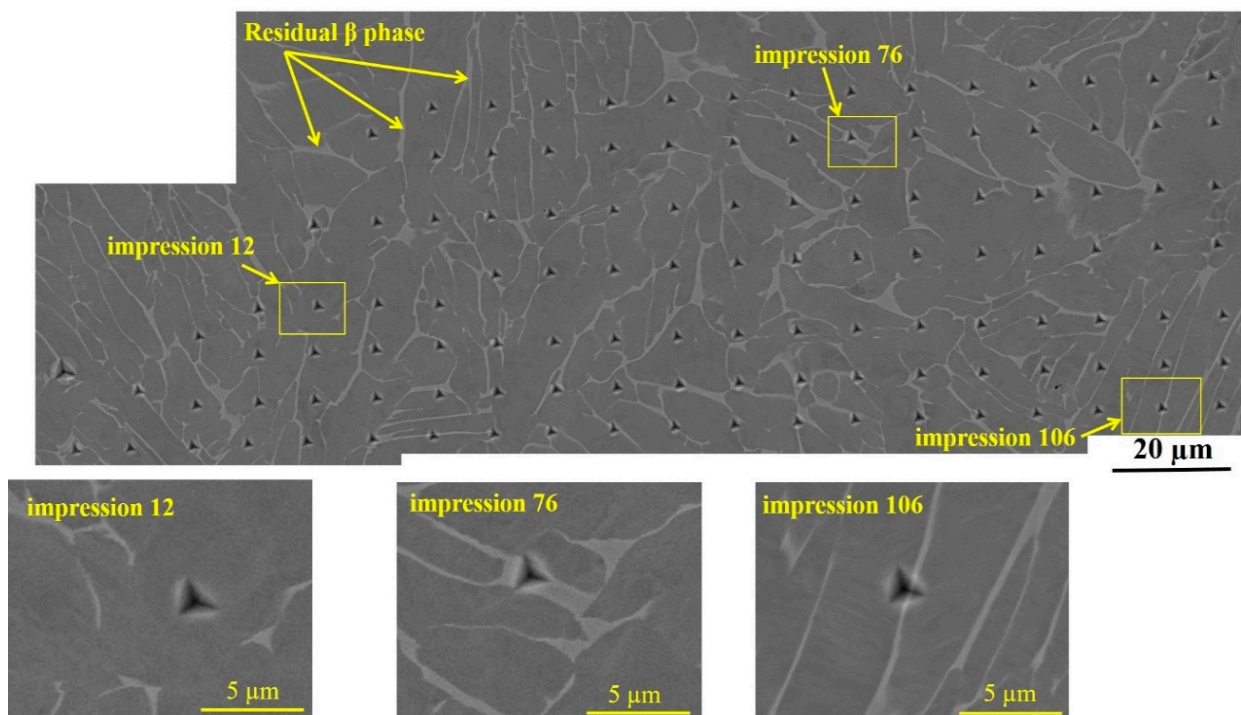


Figure 11. Backscatter electron images of 120 indents on the PM sample in unetched condition.

The EDS spectrum of the PM sample showed that the amount of vanadium in α (the dark grey regions in Figure 10) varies between nearly 0% and 4.9%, whereas in the β phase (light grey areas in Figure 10), it changes from 5% to 16.6%. This variation of vanadium in either the α or β phases is related to the segregation phenomenon [52], confirming that the microstructure of the PM sample, made with a furnace cooling rate of 3 °C/min, is a quasi-equilibrium, not a fully equilibrium transformation.

In contrast with the PM sample, the variation of the amount of vanadium in the microstructure of the L-PBF sample was much narrower, i.e., 3.5% to 4.2%. This observation reconfirms that the rapid cooling experienced by the β -phase transformation to martensitic phase α' prevented the vanadium atoms diffusion. For measuring the percentage of vanadium in L-PBF, more than ten spots were chosen according to the brightness and darkness of the regions, as observed in Figure 10b, but it was noticed the different contrast between acicular α' in the L-PBF samples was not associated with the percentage of vanadium. This suggests that the different contrast observed in the α' needles shape in Figure 10b is related to the crystallographic orientation differences between α' laths. The different orientations of the α' -laths can be observed in other studies where crystallographic texture is presented via EBSD analysis [53–55].

Based on the EDS analysis of the regions adjacent to individual indents and the nano-hardness value of each indent in the PM samples, the α phase has been categorized

into four groups, based on the amount of dissolved vanadium and aluminum in α . As seen from the graph and tabulated data in Figure 12, it seems there is a decreasing trend of nano-hardness of α when the vanadium content increases and aluminum decreases. Aluminum is a well-known substitutional strengthening element in titanium alloy [56–58] and its effect on the nano-hardness of titanium alloy has been reported in [59], but the changes in aluminum weight percentage in the α phase shown in Figure 12, compared with vanadium changes, is very little. So, the decreasing trend in nano-hardness of the α phase, observed in Figure 12, is believed to be more related to the higher vanadium concentration than trace reduction in aluminum. The hypothesis that may explain this observation is related to the radius of the vanadium atom ($R_V = 0.134$ nm), which is smaller compared to aluminum ($R_{Al} = 0.143$ nm) and titanium ($R_{Ti} = 0.145$ nm) atoms. When the vanadium atoms substitute the titanium atoms in the crystal lattice, the smaller size of the V atoms reduces lattice frictional forces (Peierls load) necessary for slip systems to activate. This makes it easier for the dislocations to move to initiate plastic deformation, i.e., lower hardness. In a way, it is hypothesized that the smaller size of substituting vanadium atoms relaxes the Ti crystal lattice and therefore the atomic displacement necessary for hardness measurement is easier, i.e., reduction in hardness.

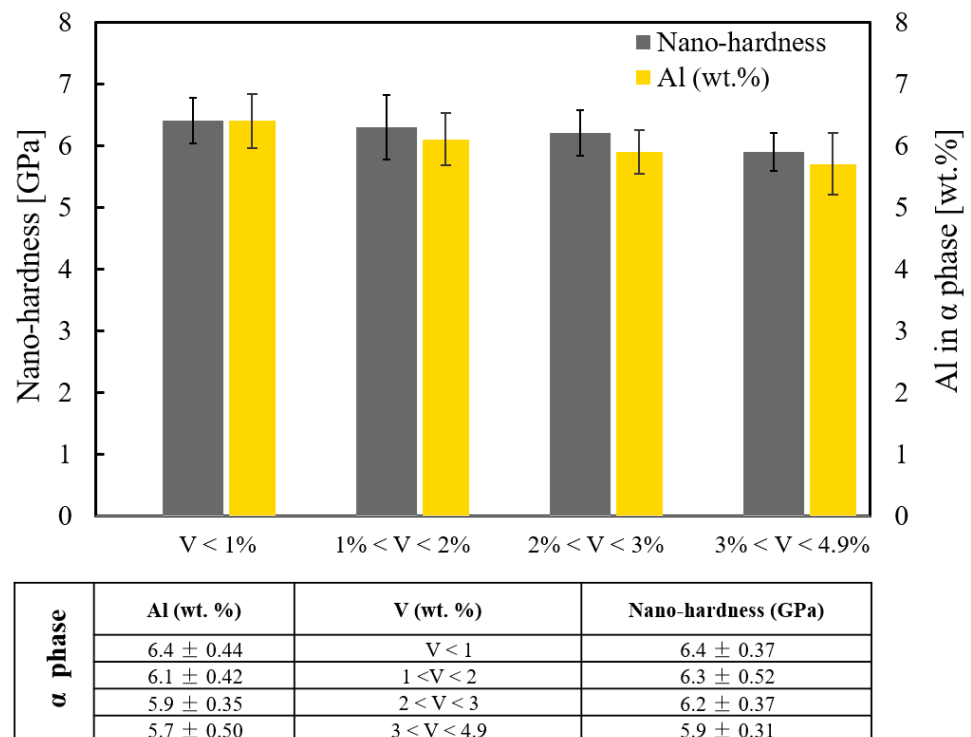


Figure 12. Nano-hardness values of the α phase with different contents of vanadium and aluminum.

Nano-hardness of Ti64 alloys with a bimodal microstructure of α and β phases has already been reported by other researchers [60,61] and the wide variation of nano-hardness of α , like 4.57 GPa to 6.84 GPa in [61], has been attributed to α grain orientation [61–63]. However, they have not investigated whether these changes in nano-hardness can be associated with variations in chemical composition and segregation. In addition to the effect of α -grain orientation on nano-hardness value, the mechanics of nano-indentation testing could introduce some variation in the reported results. The indentation size effect (known as ISE) [64–66] and tip radius of indenter [67–69] are some parameters that could be responsible for different values of the nano-hardness reported in the open literature.

The nano-hardness of α in this study, Figure 12, fits well in the range found in the open literature, see Table 4, and the slight difference may be due to phase chemistry and the mechanics of nano-hardness measurement mentioned above.

Figure 13 displays the graphs of load (P) vs. penetration depth (h) of nano-indentations of the L-PBF and the two phases of α and β in the PM samples. The graph shows the rate of loading and unloading, with the loading dwell time of 2 s as specified in the experimental procedure (Figure 13c). It is important to point out that the loading and unloading rates along with the dwell time and applied load plus the geometry of the indenter, all affect the value of nano-hardness. Table 4 summarizes the average of all the results of nano-hardness of all the phases observed in the microstructure of all the samples in this study. The graphs in Figure 13 reveal that the bcc structure of β phase is softer than the hcp phase of α and α' , confirming previous reports [46,58,70]. This is due to the fact that the bcc crystal structure has more slip systems than the hcp and consequently should exhibit better movement of dislocations and greater ductility. However, by comparison of the graphs for α and α' , Figure 13a,b as well as the values in Table 4, it seems α' does not really require greater loads for the same degree of plastic deformation, i.e., a penetration depth of 300 nm. The nano-hardness of the α phase is the average hardness of all the values of α discussed in Figure 12. Although in some articles [62,71] the effect of β phase and its grain boundaries (with the α phase) on nano-indentation results has been discussed, it is hard to find any reports in the open literature in which they have explicitly differentiated the nano-hardness of each phase of α and β of Ti64 alloy.

Table 4. Nano-hardness of α' , α , and β in L-PBF and PM samples.

Phase	Nano-Indentation Load (mN)	Indenter Penetration Depth (nm)	Nano-Hardness (GPa)	Reference
α' phase of L-PBF sample	10.3 ± 0.4	300	6.3 ± 0.27	This study
	500	2500	3.9	[72]
α phase	10.13 ± 0.72	300	6.2 ± 0.51	This study
	50	550–675	4.4–6.2	[60]
	2	110–150	4.09–4.71	[62]
	2	–	4.1–10.0	[73]
	8–10.6	300	4.57–6.84	[61]
β phase	9.6 ± 0.2	300	5.9 ± 0.37	This study

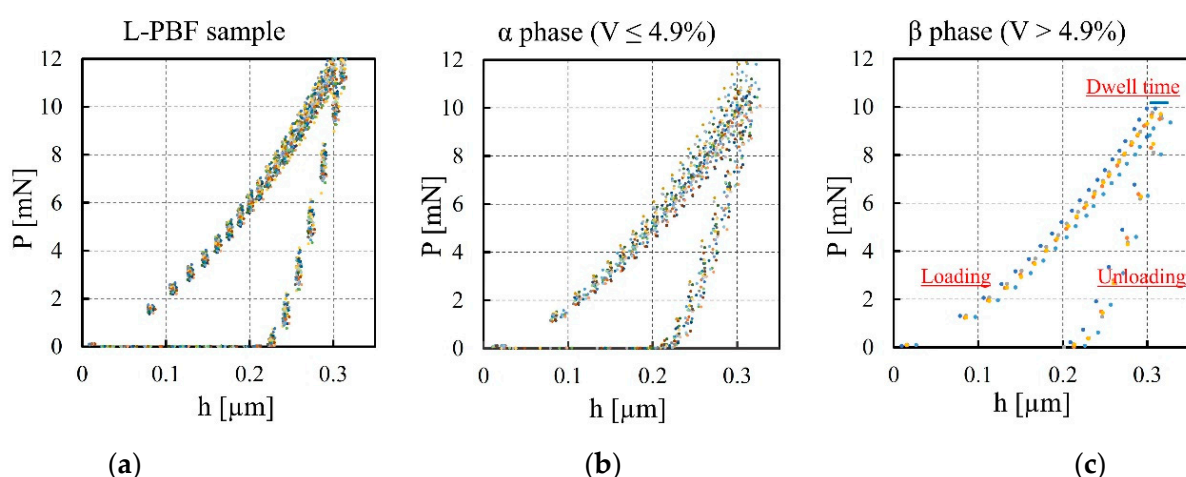


Figure 13. Loading and unloading indentations graphs of (a) L-PBF, (b) α phase-PM and (c) β phase-PM samples.

It is interesting to note that the standard deviation of nano-hardness value for α' , i.e., ± 0.27 as shown in Table 4, is lower than in α . It is related to the nearly uniform concentration of aluminum and vanadium in α' , which is not the case for the α phase as explained in Figure 12.

By comparing the nano-hardness values of α' and α (6.3 ± 0.27 GPa and 6.2 ± 0.51 GPa, respectively) it is clear that their nano-hardness values are nearly the same. Moreover, the refined laths structure of α' martensite, with a greater area of low angle boundaries as barriers for movement of dislocations, can increase the nano-hardness. This is illustrated in Figure 14, where a 300 nm deep indentation with a semi-equilateral triangle has encountered a few laths boundaries. Apart from α' laths' size and associated boundaries, the existence of the dislocations network, stacking faults, and twinning in α' martensite, as reported by Kurdi et al. [74], are expected to increase the nano-hardness of the L-PBF printed sample. In other words, the negligible increase in the nano-hardness value of α' (1.6%) is due to the opposing issues of defects in α' (hardening) and supersaturation of vanadium in α' (softening).

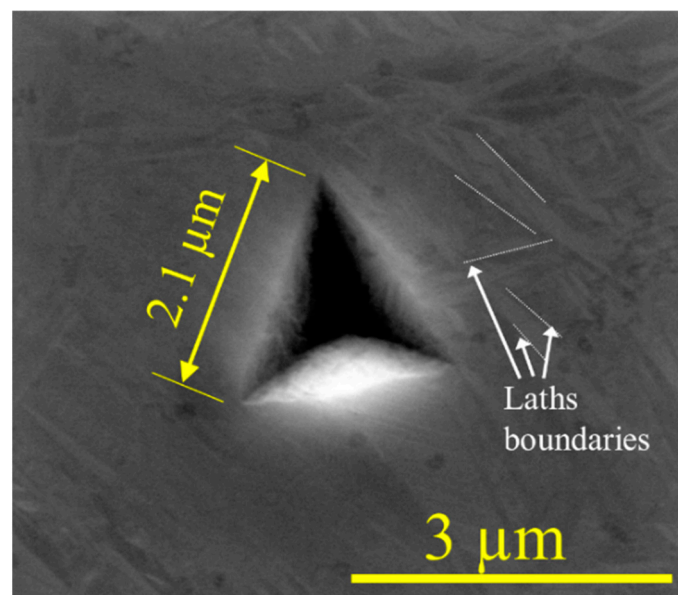


Figure 14. A 300 nm deep penetrated nano-indentation in L-PBF sample.

4. Conclusions

- The microstructural characterization of Ti64 parts fabricated by L-PBF reconfirms columnar growth of prior β grains upon solidification that transforms to acicular martensite hcp α' in contrast with Ti64 parts fabricated via the conventional powder metallurgy route, exhibiting diffusional transformation of β to a bimodal microstructure of α and β phases with nearly equiaxed α grains and $\alpha + \beta$ lamellae;
- The average micro-hardness of L-PBF fabricated parts is 391 HV compared with an estimated hardness of 310 HV of fully dense PM samples. The higher micro-hardness of L-PBF parts is associated with the laths' morphology and refinement of the microstructure of a single phase of α' in L-PBF parts, whereas in PM samples two phases of α and β are influencing the micro-hardness;
- The nano-hardness measurement enables isolation of the grains boundaries from interfering in the hardness measurement and thus rendering the true bulk hardness of individual phases of α' , α , and β ;
- Almost the same bulk nano-hardness values of α' and α , i.e., 6.3 GPa and 6.2 GPa, respectively, supports the hypothesis that only the morphology and refinement of α' are responsible for the greater microhardness values of L-PBF parts;
- The bulk nano-hardness of α in PM samples seems to be dependent on the concentration of vanadium solute atoms. A higher concentration of vanadium in the hcp crystal structure of α , lowers its hardness;

- It is hypothesized that the space created by smaller vanadium atoms substituting titanium atoms in α phase crystal lattice allows for the dislocations to move with lesser frictional stresses, leading to a softer α phase.

Author Contributions: Conceptualization, R.G. methodology, R.G.; formal analysis, A.D.B.; investigation, A.D.B.; writing—original draft preparation, A.D.B.; writing—review and editing, S.N., H.E.-H. and R.G.; supervision, R.G., S.N. and H.E.-H.; project administration, A.D.B. All authors have read and agreed to the published version of the manuscript.

Funding: This research received no external funding.

Institutional Review Board Statement: Not Applicable.

Informed Consent Statement: Not Applicable.

Data Availability Statement: The data stored at the University of Adelaide’s “Data storage facilities, BOX folder”.

Acknowledgments: This work has been supported by the Australian Government Research Training Program Scholarship (A.D.B) and The University of Adelaide. This work was performed in part at the Optofab node of the Australian National Fabrication Facility (ANFF) utilizing Commonwealth and South Australian State Government Funding.

Conflicts of Interest: The authors declare no conflict of interest.

References

- Banerjee, D.; Williams, J.C. Perspectives on Titanium Science and Technology. *Acta Mater.* **2013**, *61*, 844–879. [[CrossRef](#)]
- Geetha, M.; AKSingh RAsokamani Gogia, A.K. Ti based biomaterials, the ultimate choice for orthopaedic implants—A review. *Prog. Mater. Sci.* **2009**, *54*, 397–425. [[CrossRef](#)]
- Peters, M.; Leyens, C. Fabrication of Titanium Alloys. In *Titanium and Titanium Alloys*; Wiley-VCH Verlag GmbH & Co. KGaA: Weinheim, Germany, 2005; pp. 245–261.
- Kruth, J.-P.; Levy, G.; Klocke, F.; Childs, T. Consolidation phenomena in laser and powder-bed based layered manufacturing. *CIRP Ann.* **2007**, *56*, 730–759. [[CrossRef](#)]
- Brandt, M. *Laser Additive Manufacturing: Materials, Design, Technologies, and Applications*; Woodhead Publishing: Thorston, UK, 2016.
- Gu, D.; Shi, X.; Poprawe, R.; Bourell, D.L.; Setchi, R.; Zhu, J. Material-structure-performance integrated laser-metal additive manufacturing. *Science* **2021**, *372*, eabg1487. [[CrossRef](#)]
- Papazoglou, E.L.; Karkalos, N.E.; Karmiris-Obratański, P.; Markopoulos, A.P. On the Modeling and Simulation of SLM and SLS for Metal and Polymer Powders: A Review. *Arch. Comput. Methods Eng.* **2021**, *29*, 941–973. [[CrossRef](#)]
- Singh, D.D.; Mahender, T.; Reddy, A.R. Powder bed fusion process: A brief review. *Mater. Today Proc.* **2020**, *46*, 350–355. [[CrossRef](#)]
- Hu, Y.; Cong, W. A review on laser deposition-additive manufacturing of ceramics and ceramic reinforced metal matrix composites. *Ceram. Int.* **2018**, *44*, 20599–20612. [[CrossRef](#)]
- Hegab, H.A. Design for additive manufacturing of composite materials and potential alloys: A review. *Manuf. Rev.* **2016**, *3*, 11. [[CrossRef](#)]
- Yap, C.Y.; Chua, C.K.; Dong, Z.L.; Liu, Z.H.; Zhang, D.Q.; Loh, L.E.; Sing, S.L. Review of selective laser melting: Materials and applications. *Appl. Phys. Rev.* **2015**, *2*, 041101. [[CrossRef](#)]
- Yeong, W.; Yap, C.; Mapar, M.; Chua, C. State-of-the-art review on selective laser melting of ceramics in High Value Manufacturing: Advanced Research in Virtual and Rapid Prototyping. In Proceedings of the 6th International Conference on Advanced Research in Virtual and Rapid Prototyping, Leiria, Portugal, 1–5 October 2014.
- Randall, M.G. *Powder Metallurgy Science*, 2nd ed.; Metal Powder Industries Federation: Princeton, NJ, USA, 1994.
- Santos, L.V.; Trava-Airoldi, V.J.; Corat, E.J.; Nogueira, J.; Leite, N.F. DLC cold welding prevention films on a Ti6Al4V alloy for space applications. *Surf. Coat. Technol.* **2006**, *200*, 2587–2593. [[CrossRef](#)]
- Blakey-Milner, B.; Gradl, P.; Snedden, G.; Brooks, M.; Pitot, J.; Lopez, E.; Leary, M.; Berto, F.; du Plessis, A. Metal additive manufacturing in aerospace: A review. *Mater. Des.* **2021**, *209*, 110008. [[CrossRef](#)]
- Murr, L.; Quinones, S.; Gaytan, S.; Lopez, M.; Rodela, A.; Martinez, E.; Hernandez, D.; Martinez, E.; Medina, F.; Wicker, R. Microstructure and mechanical behavior of Ti-6Al-4V produced by rapid-layer manufacturing, for biomedical applications. *J. Mech. Behav. Biomed. Mater.* **2009**, *2*, 20–32. [[CrossRef](#)]
- Salmi, M. Additive Manufacturing Processes in Medical Applications. *Materials* **2021**, *14*, 191. [[CrossRef](#)]
- Ghomi, E.R.; Khosravi, F.; Neisiany, R.E.; Singh, S.; Ramakrishna, S. Future of additive manufacturing in healthcare. *Curr. Opin. Biomed. Eng.* **2021**, *17*, 100255. [[CrossRef](#)]
- Kumar, S. Selective Laser Sintering/Melting. In *Comprehensive Materials Processing*; Elsevier: Amsterdam, The Netherlands, 2014; pp. 93–134.

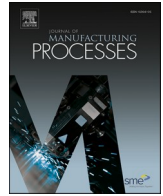
20. ASTM F2924-14; Standard Specification for Additive Manufacturing Titanium-6 Aluminum-4 Vanadium with Powder Bed Fusion. ASTM International: West Conshohocken, PA, USA, 2014.
21. Dareh Baghi, A.; Nafisi, S.; Hashemi, R.; Ebendorff-Heidepriem, H.; Ghomashchi, R. Experimental realisation of build orientation effects on the mechanical properties of truly as-built Ti-6Al-4V SLM parts. *J. Manuf. Processes* **2021**, *64*, 140–152. [[CrossRef](#)]
22. Dareh Baghi, A.; Ghomashchi, R.; Oskouei, R.H.; Ebendorff-Heidepriem, H. Nano-mechanical characterization of SLM-fabricated Ti6Al4V alloy: Etching and precision. *Metallogr. Microstruct. Anal.* **2019**, *8*, 749–756. [[CrossRef](#)]
23. Xie, B.; Fan, Y.; Zhao, S. Characterization of Ti6Al4V powders produced by different methods for selective laser melting. *Mater. Res. Express* **2021**, *8*, 076510. [[CrossRef](#)]
24. Thijs, L.; Verhaeghe, F.; Craeghs, T.; Humbeek, J.V.; Kruth, J.-P. A study of the microstructural evolution during selective laser melting of Ti-6Al-4V. *Acta Mater.* **2010**, *58*, 3303–3312. [[CrossRef](#)]
25. Rafi, H.K.; Karthik, N.V.; Gong, H.; Starr, T.L.; Stucker, B.E. Microstructures and Mechanical Properties of Ti6Al4V Parts Fabricated by Selective Laser Melting and Electron Beam Melting. *J. Mater. Eng. Perform.* **2013**, *22*, 3872–3883. [[CrossRef](#)]
26. Dareh Baghi, A.; Nafisi, S.; Hashemi, R.; Ebendorff-Heidepriem, H.; Ghomashchi, R. Effective post processing of SLM fabricated Ti-6Al-4 V alloy: Machining vs thermal treatment. *J. Manuf. Processes* **2021**, *68*, 1031–1046. [[CrossRef](#)]
27. Mukherjee, T.; Zuback, J.S.; De, A.; Debroy, T. Printability of alloys for additive manufacturing. *Sci. Rep.* **2016**, *6*, 19717. [[CrossRef](#)] [[PubMed](#)]
28. Martin, J.W.; Doherty, R.D.; Cantor, B. *Stability of Microstructure in Metallic Systems*; Cambridge University Press: Cambridge, UK, 2010.
29. Facchini, L.; Magalini, E.; Robotti, P.; Molinari, A.; Höges, S.; Wissenbach, K. Ductility of a Ti-6Al-4V alloy produced by selective laser melting of prealloyed powders. *Rapid Prototyp. J.* **2010**, *16*, 450–459. [[CrossRef](#)]
30. Kubiak, K.; Sieniawski, J. Development of the microstructure and fatigue strength of two phase titanium alloys in the processes of forging and heat treatment. *J. Mater. Process. Technol.* **1998**, *78*, 117–121. [[CrossRef](#)]
31. Jovanović, M.T.; Tadić, S.; Zec, S.; Mišković, Z.; Bobić, I. The effect of annealing temperatures and cooling rates on microstructure and mechanical properties of investment cast Ti-6Al-4V alloy. *Mater. Des.* **2006**, *27*, 192–199. [[CrossRef](#)]
32. Malinov, S.; Sha, W.; Guo, Z.; Tang, C.; Long, A. Synchrotron X-ray diffraction study of the phase transformations in titanium alloys. *Mater. Charact.* **2002**, *48*, 279–295. [[CrossRef](#)]
33. Thöne, M.; Leuders, S.; Riemer, A.; Tröster, T.; Richard, H.A. Influence of heat-treatment on Selective Laser Melting products-eg Ti6Al4V. In *2012 International Solid Freeform Fabrication Symposium*; University of Texas at Austin: Austin, TX, USA, 2012.
34. Sallica-Leva, E.; Caram, R.; Jardini, A.L.; Fogagnolo, J.B. Ductility improvement due to martensite α' decomposition in porous Ti-6Al-4V parts produced by selective laser melting for orthopedic implants. *J. Mech. Behav. Biomed. Mater.* **2016**, *54*, 149–158. [[CrossRef](#)]
35. Welsch, G.; Boyer, R.; Collings, E.W. *Materials Properties Handbook: Titanium Alloys*; ASM International: Almere, The Netherlands, 1994; p. 1169.
36. Ahmed, T.; Rack, H.J. Phase transformations during cooling in $\alpha + \beta$ titanium alloys. *Mater. Sci. Eng. A* **1998**, *243*, 206–211. [[CrossRef](#)]
37. Das, M.; Balla, V.K.; Basu, D.; Bose, S.; Bandyopadhyay, A. Laser processing of SiC-particle-reinforced coating on titanium. *Scr. Mater.* **2010**, *63*, 438–441. [[CrossRef](#)]
38. Prashanth, K.G.; Scudino, S.; Klauss, H.J.; Surreddi, K.B.; Löber, L.; Wang, Z.; Chaubey, A.K.; Kühn, U.; Eckert, J. Microstructure and mechanical properties of Al-12Si produced by selective laser melting: Effect of heat treatment. *Mater. Sci. Eng. A* **2014**, *590*, 153–160. [[CrossRef](#)]
39. Li, Y.; Gu, D. Parametric analysis of thermal behavior during selective laser melting additive manufacturing of aluminum alloy powder. *Mater. Des.* **2014**, *63*, 856–867. [[CrossRef](#)]
40. Hooper, P.A. Melt pool temperature and cooling rates in laser powder bed fusion. *Addit. Manuf.* **2018**, *22*, 548–559. [[CrossRef](#)]
41. Gianoglio, D.; Ciftci, N.; Armstrong, S.; Uhlenwinkel, V.; Battezzati, L. On the Cooling Rate-Microstructure Relationship in Molten Metal Gas Atomization. *Met. Mater. Trans. A* **2021**, *52*, 3750–3758. [[CrossRef](#)]
42. Bolzoni, L.; Ruiz-Navas, E.M.; Gordo, E. Feasibility study of the production of biomedical Ti-6Al-4V alloy by powder metallurgy. *Mater. Sci. Eng. C* **2015**, *49*, 400–407. [[CrossRef](#)] [[PubMed](#)]
43. Dunstan, M.K.; Paramore, J.D.; Fang, Z.Z. The effects of microstructure and porosity on the competing fatigue failure mechanisms in powder metallurgy Ti-6Al-4V. *Int. J. Fatigue* **2018**, *116*, 584–591. [[CrossRef](#)]
44. Fang, Z.Z.; Paramore, J.D.; Sun, P.; Chandran, K.R.; Zhang, Y.; Xia, Y.; Cao, F.; Koopman, M.; Free, M. Powder metallurgy of titanium—past, present, and future. *Int. Mater. Rev.* **2018**, *63*, 407–459. [[CrossRef](#)]
45. Molchanova, E.K. Phase Diagrams of Titanium Alloys Israel Program for Scientific Translations. *Jerusalem* **1965**, *90*, 93.
46. Peters, M.; Hemptnermacher, J.; Kumpfert, J.; Leyens, C. Structure and Properties of Titanium and Titanium Alloys. In *Titanium and Titanium Alloys*; Wiley-VCH Verlag GmbH & Co. KGaA: Weinheim, Germany, 2005; pp. 1–36.
47. Murr, L.E.; Gaytan, S.M.; Ramirez, D.A.; Martinez, E.; Hernandez, J.; Amato, K.N.; Shindo, P.W.; Medina, F.R.; Wicker, R.B. Metal Fabrication by Additive Manufacturing Using Laser and Electron Beam Melting Technologies. *J. Mater. Sci. Technol.* **2012**, *28*, 1–14. [[CrossRef](#)]
48. Zhang, L.-C.; Attar, H. Selective Laser Melting of Titanium Alloys and Titanium Matrix Composites for Biomedical Applications: A Review. *Adv. Eng. Mater.* **2016**, *18*, 463–475. [[CrossRef](#)]

49. Dareh Baghi, A.; Arputharaj, J.D.; Nafisi, S.; Ghomashchi, R. *L-PBF 3D Printing of Ti64 Alloy, Unpublished Results*; University of Adelaide: Adelaide, SA, Australia, 2022.
50. Gu, D.; Hagedorn, Y.-C.; Meiners, W.; Meng, G.; Batista, R.J.S.; Wissenbach, K.; Poprawe, R. Densification behavior, microstructure evolution, and wear performance of selective laser melting processed commercially pure titanium. *Acta Mater.* **2012**, *60*, 3849–3860. [[CrossRef](#)]
51. Attar, H.; Calin, M.; Zhang, L.C.; Scudino, S.; Eckert, J. Manufacture by selective laser melting and mechanical behavior of commercially pure titanium. *Mater. Sci. Eng. A* **2014**, *593*, 170–177. [[CrossRef](#)]
52. Callister, W.D.; Rethwisch, D.G. *Materials Science and Engineering: An Introduction*; Wiley: New York, NY, USA, 2007; Volume 7.
53. Medvedev, A.E.; Lui, E.W.; Edwards, D.; Leary, M.; Qian, M.; Brandt, M. Improved ballistic performance of additively manufactured Ti6Al4V with α - β lamellar microstructures. *Mater. Sci. Eng. A* **2021**, *825*, 141888. [[CrossRef](#)]
54. Liu, J.; Li, G.; Sun, Q.; Li, H.; Sun, J.; Wang, X. Understanding the effect of scanning strategies on the microstructure and crystallographic texture of Ti-6Al-4V alloy manufactured by laser powder bed fusion. *J. Mater. Process. Technol.* **2021**, *299*, 117366. [[CrossRef](#)]
55. Simonelli, M.; Tse, Y.Y.; Tuck, C. On the Texture Formation of Selective Laser Melted Ti-6Al-4V. *Met. Mater. Trans. A* **2014**, *45*, 2863–2872. [[CrossRef](#)]
56. Truax, D.; McMahon, C. Plastic behavior of titanium-aluminum alloys. *Mater. Sci. Eng.* **1974**, *13*, 125–139. [[CrossRef](#)]
57. Fitzner, A.; Prakash, D.; da Fonseca, J.Q.; Thomas, M.; Zhang, S.-Y.; Kelleher, J.; Manuel, P.; Preuss, M. The effect of aluminium on twinning in binary alpha-titanium. *Acta Mater.* **2016**, *103*, 341–351. [[CrossRef](#)]
58. Donachie, M.J. *Titanium: A Technical Guide*; ASM International: Novelt, OH, USA, 2000.
59. Fitzner, A.; Palmer, J.; Gardner, B.; Thomas, M.; Preuss, M.; da Fonseca, J.Q. On the work hardening of titanium: New insights from nanoindentation. *J. Mater. Sci.* **2019**, *54*, 7961–7974. [[CrossRef](#)]
60. Wen, Y.; Xie, L.; Wang, Z.; Wang, L.; Lu, W.; Zhang, L.-C. Nanoindentation characterization on local plastic response of Ti-6Al-4V under high-load spherical indentation. *J. Mater. Res. Technol.* **2019**, *8*, 3434–3442. [[CrossRef](#)]
61. Viswanathan, G.B.; Lee, E.; Maher, D.M.; Banerjee, S.; Fraser, H.L. Direct observations and analyses of dislocation substructures in the α phase of an α/β Ti-alloy formed by nanoindentation. *Acta Mater.* **2005**, *53*, 5101–5115. [[CrossRef](#)]
62. Han, F.; Tang, B.; Kou, H.; Li, J.; Feng, Y. Experiments and crystal plasticity finite element simulations of nanoindentation on Ti-6Al-4V alloy. *Mater. Sci. Eng. A* **2014**, *625*, 28–35. [[CrossRef](#)]
63. Zambaldi, C.; Yang, Y.; Bieler, T.R.; Raabe, D. Orientation informed nanoindentation of α -titanium: Indentation pileup in hexagonal metals deforming by prismatic slip. *J. Mater. Res.* **2011**, *27*, 356–367. [[CrossRef](#)]
64. Peng, Z.; Gong, J.; Miao, H. On the description of indentation size effect in hardness testing for ceramics: Analysis of the nanoindentation data. *J. Eur. Ceram. Soc.* **2004**, *24*, 2193–2201. [[CrossRef](#)]
65. Durst, K.; Backes, B.; Franke, O.; Göken, M. Indentation size effect in metallic materials: Modeling strength from pop-in to macroscopic hardness using geometrically necessary dislocations. *Acta Mater.* **2006**, *54*, 2547–2555. [[CrossRef](#)]
66. Rodriguez, R.; Gutierrez, I. Correlation between nanoindentation and tensile properties: Influence of the indentation size effect. *Mater. Sci. Eng. A* **2003**, *361*, 377–384. [[CrossRef](#)]
67. Lu, C.-J.; Bogy, D. The effect of tip radius on nano-indentation hardness tests. *Int. J. Solids Struct.* **1995**, *32*, 1759–1770. [[CrossRef](#)]
68. Shih, C.; Yang, M.; Li, J. Effect of tip radius on nanoindentation. *J. Mater. Res.* **1991**, *6*, 2623–2628. [[CrossRef](#)]
69. Sagadevan, S.; Murugasen, P. Novel Analysis on the Influence of Tip Radius and Shape of the Nanoindenter on the Hardness of Materials. *Procedia Mater. Sci.* **2014**, *6*, 1871–1878. [[CrossRef](#)]
70. Lei, X.; Dong, L.; Zhang, Z.; Hu, M.; Wang, Z.; Hao, Y.; Yang, R. Microtexture and nanoindentation of α and β Phases in Ti-6Al-1.5 Cr-2.5 Mo-0.5 Fe-0.3 Si titanium alloy. *Sci. Adv. Mater.* **2017**, *9*, 1476–1483. [[CrossRef](#)]
71. Weaver, J.; Kalidindi, S.R. Mechanical characterization of Ti-6Al-4V titanium alloy at multiple length scales using spherical indentation stress-strain measurements. *Mater. Des.* **2016**, *111*, 463–472. [[CrossRef](#)]
72. Hadadzadeh, A.; Asadi, E.; Shakil, S.I.; Amirkhiz, B.S.; Mohammadi, M.; Haghshenas, M. Indentation-derived mechanical properties of Ti-6Al-4V: Laser-powder bed fusion versus electron beam melting. *Mater. Lett.* **2021**, *301*, 130273. [[CrossRef](#)]
73. Li, R.; Riester, L.; Watkins, T.; Blau, P.J.; Shih, A.J. Metallurgical analysis and nanoindentation characterization of Ti-6Al-4V workpiece and chips in high-throughput drilling. *Mater. Sci. Eng. A* **2008**, *472*, 115–124. [[CrossRef](#)]
74. Kurdi, A.; Basak, A. Micro-mechanical behaviour of selective laser melted Ti6Al4V under compression. *Mater. Sci. Eng. A* **2021**, *826*, 141975. [[CrossRef](#)]



Contents lists available at ScienceDirect

Journal of Manufacturing Processes

journal homepage: www.elsevier.com/locate/manpro

Experimental realisation of build orientation effects on the mechanical properties of truly as-built Ti-6Al-4V SLM parts

Alireza Dareh Baghi^{a,*}, Shahrooz Nafisi^{a,b}, Reza Hashemi^c, Heike Ebendorff-Heidepriem^d,
Reza Ghomashchi^{a,d}

^a School of Mechanical Engineering, University of Adelaide, SA, 5005, Australia

^b Department of Chemical and Materials Engineering, University of Alberta, Edmonton, AB, T6G 1H9, Canada

^c College of Science and Engineering, Flinders University, SA, 5042, Australia

^d Institute of Photonics and Advanced Sensing, School of Physical Sciences, University of Adelaide, SA, 5005, Australia

ARTICLE INFO

Keywords:

Additive manufacturing
Selective laser melting
Ti-6Al-4V (Ti64)
Mechanical characterization

ABSTRACT

Studying the mechanical properties of Selective Laser Melting (SLM) fabricated titanium parts built in a horizontal direction, parallel to the substrate, in a truly as-built condition, has always been a challenge. The problem is mainly related to the stress relaxation of horizontal parts after removal from the substrate, which causes a noticeable level of distortion when compared with vertically printed parts with no observable distortion. In this study, a novel design has been developed that enables fabrication of straight undistorted horizontal parts via an SLM route with no post-processing steps, and thus the mechanical properties of horizontal Ti-6Al-4 V (Ti64) samples in their truly as-built condition have been reported and compared with their vertically built counterparts. The study reveals that the vertical samples suffer from premature fracture in their truly as-built condition, while the horizontal parts perform similarly to post-treated samples. The analysis of the tensile test results shows that the fracture stress (maximum stress) of the truly as-built vertical parts is below the yield stress (YS) of the horizontal parts in their truly as-built condition, i.e. nearly 38 % of the Ultimate Tensile Strength (UTS). In addition to the truly as-built condition, the effect of machining was also studied to further highlight the effect of as-built surface removal on the mechanical properties of both vertically and horizontally deposited Ti-6Al-4 V (Ti64) SLM parts.

1. Introduction

Ti-6Al-4 V (Ti64) has attracted significant interest for fabricating high integrity parts using additive manufacturing techniques, like SLM [1–3]. The alloy is widely used in diverse industrial fields, such as aerospace [4,5] and biomedical applications [6,7]. This has led to considerable study of the mechanical properties of Ti64 parts fabricated via SLM under different process parameters [3,8,9]. There is a large body of work in the open literature reporting on the mechanical properties of SLM fabricated parts, including Ti64, to highlight the anisotropic behaviour in mechanical properties with respect to the build directions, both vertical and horizontal [10–13]. SLM fabricated parts generally suffer from residual stresses originating from the very high temperature gradients and extreme cooling rates experienced during the process [14–16]. The residual stresses could be problematic in Ti64 parts [17,18]; compromising their mechanical performance. The horizontally

built long parts (such as tensile test samples) experience severe residual stresses, causing deflection to occur in the test pieces immediately upon support removal. For this reason, as-built horizontal parts must be stress relieved before being removed from the substrate [19,20] or they will need to be machined afterwards to eliminate distortion. The stress relieving process helps the horizontal parts stay straight and remain acceptable for tensile tests. Some researchers have made straight horizontal samples out of the deflected horizontal parts [13] or cut from horizontally-built blocks via machining [21,22]. In other words, there are no tensile properties available in the open literature for the as-built horizontal samples having no post fabrication treatment, i.e., being “truly as-built”, since the actual as-built horizontal samples are not straight and cannot be tested properly. Both processes of stress relieving and machining alter the condition of the SLM samples from their “truly as-built” conditions. ASTM F2924-14 states that “as-built refers to the state of components made by an additive process before any post

* Corresponding author.

E-mail address: Alireza.darehbaghi@adelaide.edu.au (A. Dareh Baghi).

<https://doi.org/10.1016/j.jmapro.2021.01.027>

Received 16 November 2020; Received in revised form 5 January 2021; Accepted 15 January 2021

1526-6125/© 2021 The Society of Manufacturing Engineers. Published by Elsevier Ltd. All rights reserved.

processing employed, except where the removal from a build platform is necessary or powder removal or support removal is required" [23]. Thus, according to this standard, neither the stress relieved parts nor the machined components could be considered as having a "truly as-built" condition.

Furthermore, it is obvious that any post fabrication treatment will increase the cost of production, while at the same time there is market pressure on cost reduction [24–27]. Therefore, by eliminating any post processes of machining, heat treatment or other treatments like hot-isostatic pressing (Hipping) [28] the final production cost should reduce significantly. However, since there is no reported mechanical characterization comparison between the *truly as-built* horizontal and vertical samples, it is required to evaluate whether as-built vertical or horizontal parts meet the expected mechanical characteristics of Ti64 manufactured by other processes than SLM, and to see if the as-built parts can exhibit reliable performance in their applications. In the current work, "truly as-built" SLM fabricated Ti-6Al-4 V undistorted horizontal tensile test pieces were realized by implementing an innovative design approach. The fabrication of the undistorted tensile test pieces made it possible to study the effect of the build direction on the tensile properties of the *truly as-built* Ti-6Al-4 V samples fabricated by SLM experimentally. Also, the as-built samples were machined to show how machining can improve the mechanical properties of both vertical and horizontal samples. It is important to specify the terminology used in this report. Hereafter, "as-built" signifies the "*truly as-built*" condition: test pieces fabricated with no post processes, including surface machining or heat treatment. The machined samples have their surface machined only, without any heat treatment.

2. Materials and experimental procedures

To fabricate the as-built straight horizontal samples, a 3D model of the samples was designed, such that the long axis of the samples is slightly arched (according to a pre-calculated radius). After removing this part from the substrate, the SLM-induced residual stresses relax and the curved sample obtains a straight-line profile, which is suitable for tensile tests. By fabricating both straight horizontal samples (via the above-mentioned innovative approach) and vertical samples, it becomes possible to study the effect of the build direction on the tensile properties of SLM-fabricated Ti-6Al-4 V experimentally in their as-built conditions. The machined tensile samples in this paper are made from vertical and horizontal SLM-fabricated cylindrical rods.

2.1. Materials

The gas atomized pre-alloyed powder Ti64 (grade 5) was supplied by TLS, Technik GmbH & CoTM, Germany [29]. The particle size distribution of the powder and its chemical analysis were provided through the powder manufacturer's certificate. Since the powder used in this investigation had already been used for parts' production, it was necessary to re-examine the powder for its chemical composition and particle morphology. Table 1 presents the results of the chemical analysis of the powder in its as-received, new condition and after being used. The ICP-AES technique was used for the elemental chemical analysis of Iron (Fe), Aluminium (Al), and Vanadium (V). The elemental percentages of Hydrogen (H), Nitrogen (N), and Oxygen (O) were measured using a LECO ONH836 analyser. Also, Carbon (C) elements were analysed by the LECO CS200 instrument.

Although there is an increase in the level of oxygen and a decrease in the level of aluminium in the used powder and bulk fabricated samples, these elements are still within the acceptable range provided in the standard, ASTM F2924-14 [23]. Fig. 1a shows the size distribution of the new and used powders, which were examined using a laser particle size analyser, Malvern Mastersizer 2000. The new powder shows a volume median size of $d(0.5) = 22.73 \mu\text{m}$, while the used powder exhibits an increase in median size, $30.00 \mu\text{m}$. This is probably due to a minor

agglomeration of loose, small particles in the SLM chamber during fabrication, leading to a slight increase in the median size of the whole batch. The oxygen pick-up and change of the particle size distribution (PSD) of the reused powder in this study is in agreement with other studies [30,31]. The morphology of the used powder was examined using an FEI Quanta 450 FEGSEM. Ti64 powder exhibits a spherical morphology, as shown in Fig. 1b, which makes the powders suitable for the SLM process because of their high flowability [32]. The cluster of small particles and partially sintered small particles in Fig. 1b explains the peak shift in the particles' size distribution graph of the used powder (Fig. 1a). Satellite phenomena can also be seen from the typical SEM image of the powder particles, Fig. 1b.

2.2. Experimental procedures

In this study, a 3D SYSTEMS ProX DMP 200 machine was used. This machine employs a 1070 nm wavelength (λ) laser source in continuous mode, with a maximum power capacity of 300 W. The SLM chamber is filled with argon at atmospheric pressure (101 K Pa) during deposition. The level of oxygen in the chamber was kept as low as 500 ppm and the substrate was not pre-heated. Table 2 summarises the optimised SLM process parameters [33] used in this investigation.

A bi-directional laser scanning strategy with a 90° interlayer rotation (criss-cross) was chosen for fabricating the tensile samples on a 12 mm thick substrate. Fig. 2 shows the schematic of the first batch of the horizontal samples used to measure the deflection after support removal, immediately after deposition. The coloured arrows in Fig. 2 show the laser path in alternating layers employed for the horizontal samples. The build direction is perpendicular to the plane of this page and the laser path has an alternating angle of $\pm 45^\circ$ with respect to the tensile axis of the test pieces.

The deflection of the first batch of the horizontal samples were measured, by a dial gauge, on the centre axis of both ends to the centre of test piece. That was approximately 1 mm as depicted in Fig. 3. The deflection distribution of the individual points along the tensile axis of two typical horizontal samples is shown in Fig. 4.

Once the deflection values of the fabricated samples (length = 126 mm) was determined (Fig. 4), a reversed design was considered to fabricate the samples with a maximum length of 80 mm. The selection of this length, 80 mm, was based on the maximum allowable height of the vertical parts to be built by the ProX-200 3D printing machine. As demonstrated in Fig. 4, a deflection of 0.5 mm was calculated for the samples with 80 mm length. In the next step, the samples were designed to be fabricated with a deflection of 0.5 mm, as shown in Fig. 5a. After removing the curved horizontal dumbbell samples from the substrate, they formed a straight profile shape. This confirmed the expected deflection analysed from Fig. 4. This design was used to fabricate both as-built parts (Fig. 5a) and rods for further machining (Fig. 5b). Moreover, three samples in each direction, vertical and horizontal, in the shape of dumbbells and cylindrical rods, were fabricated for the tensile tests. The machining process in this study for removing the as-built surface from rods was a turning process with an NC lathe machine. It is noteworthy that the final shape of the as-built and machined samples (Fig. 5c), complies with the small size specimens specified by ASTM E8 [34], for which the gauge length must be four times the gauge diameter. A universal tensile testing machine (Instron, model 5969 with a 50 kN load cell) was used in this study. All tensile tests were conducted at room temperature with a cross-head speed (displacement rate) of 0.2 mm/min.

For metallographic examinations, horizontal and vertical tensile test samples were sectioned transversally from their grip sections. All the metallographic samples were mounted in Bakelite and polished conventionally, with a final polish of $0.04 \mu\text{m}$ colloidal silica and

Table 1
Chemical composition (wt. %) of Ti64 (grade5) powder.

Element	Al	V	Fe	O	C	N	H	Ti
ASTM F2924–14	5.50–6.75	3.50–4.50	Max 0.3	Max 0.2	Max 0.08	Max 0.05	Max 0.015	Bal.
New powder according to the powder manufacturer’s certificate	6.39	3.88	0.2	0.077	0.011	0.005	<0.002	Bal.
Used powder according to the chemical analysis in this study	6.15	3.94	0.18	0.098	0.005	0.010	<0.002	Bal.
SLM-fabricated bulk sample	6.14	3.97	0.19	0.114	0.005	0.011	<0.002	Bal.

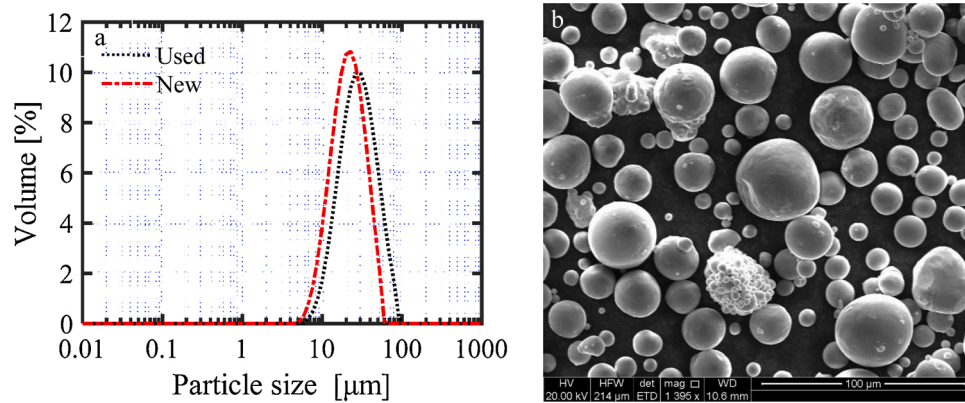


Fig. 1. a) Ti64 particle diameter distribution of new powder and used powder, b) Typical SEM image of used Ti64 powder particles after being sieved.

Table 2
SLM process parameters to fabricate Ti64 samples.

Laser Power, P (W)	Scanning velocity, v (mm/s)	Layer thickness, t (μm)	hatch spacing, h (μm)	Laser beam spot size, w ₀ (μm)
270	1800	30	85	70

applied load with 10 s dwell time on all samples. The final microhardness result for each sample was the average value of more than 6 indentations around the centre of the samples. The Rigaku MiniFlex 600 XRD machine used in this study, employed Cu radiation, operating at 40 kV and 15 mA, with a scan speed of 10°/min over a range of 2θ from 30° to 85°. All the metallographic samples were etched for microstructure and phase characterisation using Kroll’s reagent (3 % HF + 5 % HNO₃ +

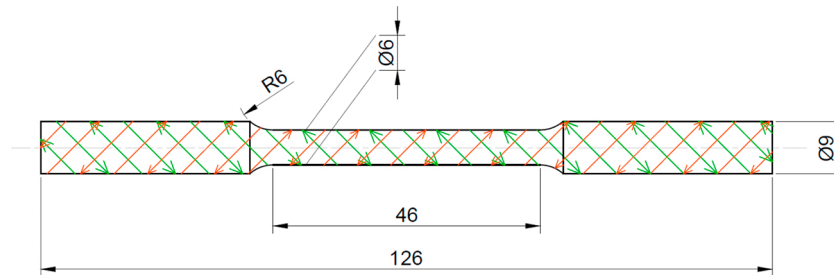


Fig. 2. Geometry of first batch of the horizontal samples.

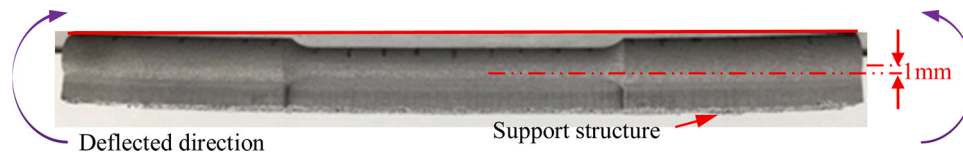


Fig. 3. Typical sample of the first batch of the horizontally-built parts after being removed from the substrate.

hydrogen peroxide (30 %) solution. Prior to etching, the metallographic samples were examined for both pore morphology and the level of porosity using optical microscopy and image analysis software, ImageJ.¹ More than 30 fields of view were examined for porosity measurements, to render a statistically viable result. Vickers’ microhardness tests (LECO LM700AT machine) were also performed on unetched samples at a 300 g

92 % distilled water) for 50 s. For microstructural analysis, a Zeiss Axio optical microscope Imager2 and a FEI Quanta 450 FEG-SEM were used.

3. Results and discussion

3.1. Microstructural characterisation

It is worth emphasizing again that the examined metallographic samples are both transverse sections to the tensile axis for both

¹ ImageJ is a trademark; (<https://imagej.net/Welcome>)

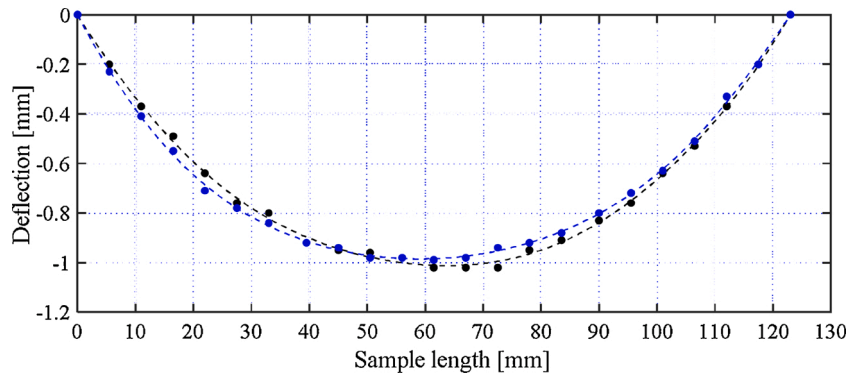


Fig. 4. Deflection curve of two typical horizontal samples from the first batch.

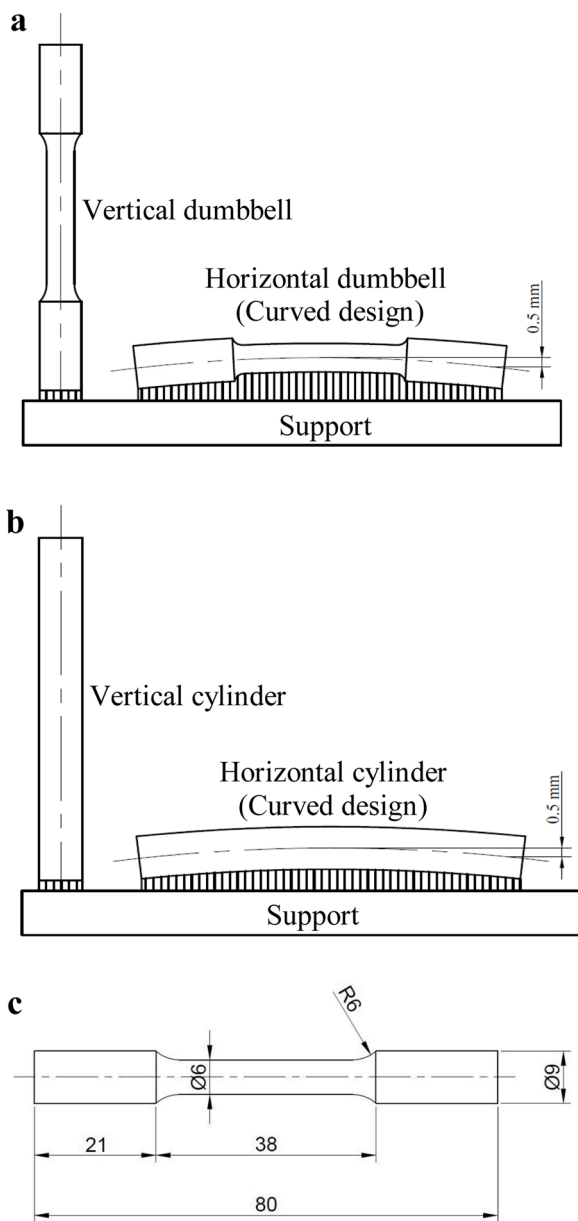


Fig. 5. a) Vertical sample and reversed deflected design of a horizontal dumbbell shape sample attached to the substrate, b) Vertical and horizontal cylinder to be machined, and c) Final test specimen dimensions, (all units in mm).

horizontal and vertical test pieces. However, the transverse cut of the grip section for the horizontal samples is actually a plane parallel to the build direction; whereas it is a plane perpendicular to the build direction in the vertical samples, Fig. 6a. Optical microscopy of polished samples reveals that the morphology of the pores appears to vary: semi-equiaxed in the horizontal samples and generally elongated in the vertical test pieces. The pores' morphologies are easily recognizable after the polished samples are etched (see Fig. 6b and c). The elongated pores shown in Fig. 6c have the same direction as the laser vector strategy, i.e., $\pm 45^\circ$ criss-cross, perhaps suggesting that there is a minor lack of fusion in the solidifying molten pool with its adjacent solidified track or with the previously-solidified layers, i.e., inter-track pores or inter-layer pores. Some of the semi-equiaxed pores observed in the horizontal samples could be the same elongated pores appearing in the vertical samples, given that sectioning the architecture and viewing the samples from a different angle could have altered their morphology. The porosity content of the transverse sections of the horizontal and vertical samples are summarised in Table 3. The very low content of porosity of 0.14 %, confirms the selection of appropriate process parameters to render SLM fabricated Ti64 parts with nearly full density (99.86 %). The magnitude of the standard deviation may also suggest the distribution of pores examined by 2D image analysis is nearly the same in two directions.

The microstructure of the etched transverse section of the horizontal sample, Fig. 6b, exhibits a columnar pattern; whereas the transverse section of the vertical sample, Fig. 6c, shows a chessboard pattern, which is the consequence of criss-cross alternating layering. The chessboard side length of $85 \mu\text{m}$ and diagonal length of $120 \mu\text{m}$ displayed in Fig. 6c or the $\sim 120 \mu\text{m}$ of columnar grain width in Fig. 6b, all correspond with the laser hatch spacing of $85 \mu\text{m}$, Table 2. The columnar architecture of the microstructure parallel to the build direction and the formation of a chessboard pattern perpendicular to the build direction are consistent with other studies [3,22,35]. Fig. 6.d illustrates a schematic representation of the 3D architecture of the SLM fabricated Ti64 parts according to the criss-cross alternating layering and with respect to the direction of applied tensile load for horizontal and vertical samples. It could be expected that this architecture, with respect to the applied loading direction, results in an anisotropy of the mechanical properties. The boundaries separating the individual columnar grains are believed to be the grain boundaries of the prior β phase upon solidification of the Ti64 [36]. The martensitic lath structure in the columnar or chessboard grains in Fig. 6b and c are due to the steep thermal gradient experienced during the SLM process, i.e., cooling rates of 10^4 - 10^6 [37–39], by which the β phase directly transforms to a martensitic α' phase.

The SEM micrographs in Fig. 7 show the lath morphology of the martensitic phase (α') is almost similar for both vertical and horizontal samples. The XRD spectrum in Fig. 8 confirms there is no trace of the bcc structure β -titanium phase in the SLM fabricated part, or, at least, it is below the detection limit of the XRD method. In the event that any β phase exists, the first peak of bcc should have appeared between planes

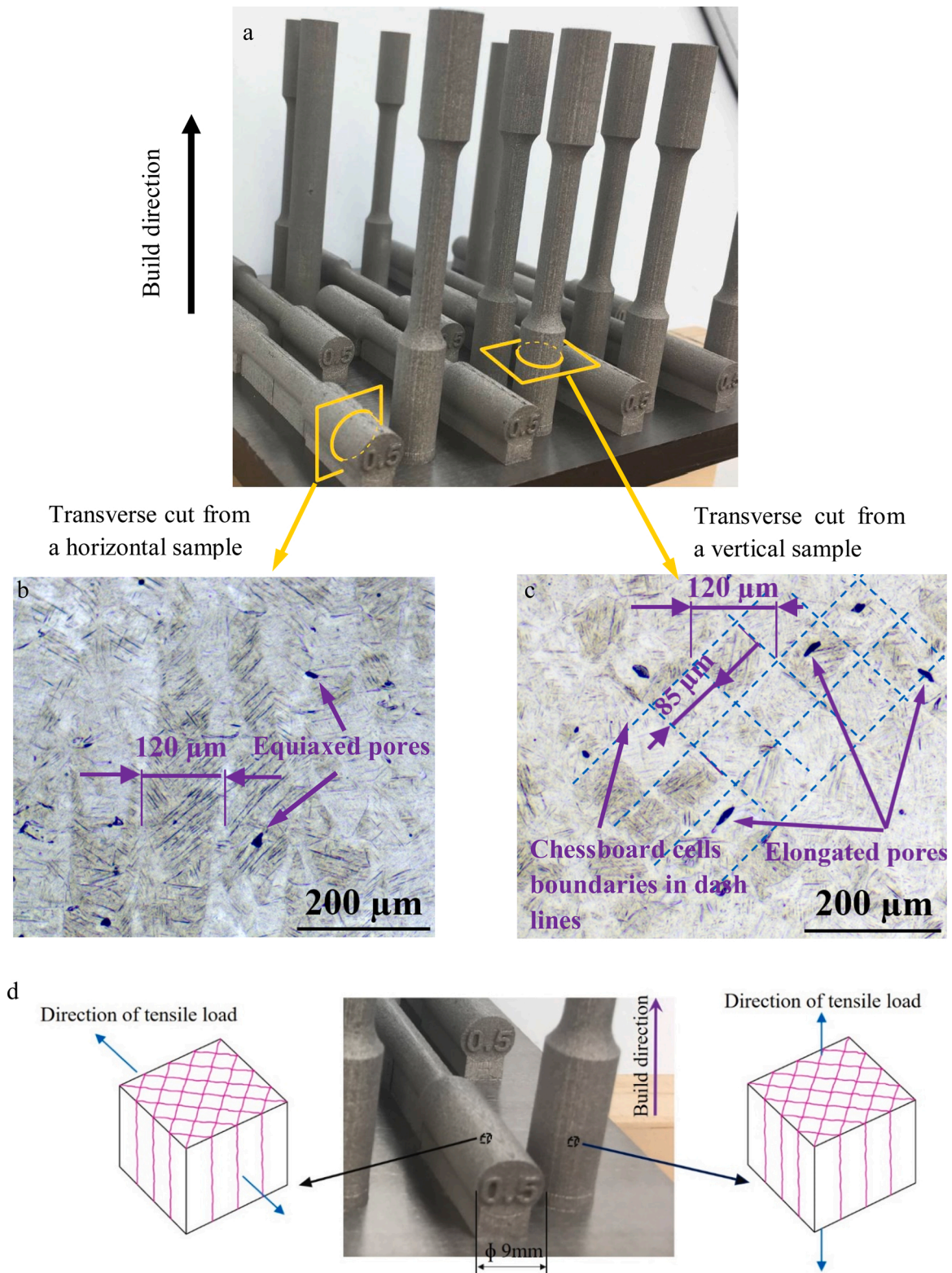


Fig. 6. a) Transverse cutting of horizontal and vertical tensile samples from the “grip section”. b and c) Optical micrographs of etched transverse sections of horizontal and vertical samples, respectively, and d) Schematic 3D model of microstructure architecture, according to the applied tensile load direction.

(002) and (101) of hcp α' ($2\theta=39^\circ$) and its second peak between planes (102) and (110) of hcp ($2\theta=57^\circ$), specified with the red dashed lines in Fig. 8 [40–42].

3.2. Mechanical properties

Fig. 9.a–d exhibits the engineering stress-strain graphs for all the SLM samples built in the horizontal and vertical directions, and in two separate conditions: as-built and machined. The tensile results extracted from the stress-strain graphs in Fig. 9a–d are summarised in Fig. 9e. The

Table 3

Results of 2D image analysis of two different sections of an SLM sample to measure the porosity distribution.

	Parallel to build direction (transverse cut from horizontal)	Perpendicular to build direction (transverse cut from vertical)	Average
Porosity, (%)	0.12 ± 0.08	0.16 ± 0.07	0.14 ± 0.07

effect of surface machining on the tensile properties varies greatly, depending on the build direction. By comparing the tensile properties of the machined horizontal samples with those of the as-built horizontals in Fig. 9a, it is obvious that the machining of the surface played a role in improving the tensile properties of the horizontally-built samples. This improvement is about 15 % for YS, almost 11 % for UTS and nearly 34 % for ductility (elongation), Fig. 9e. A similar trend is also true for the machined vertically-built tensile samples, Fig. 9b and e; however the surface machining of the verticals drastically improved the UTS and elongation at fracture by 180 % and 460 %, respectively. The build direction appears to have a significant effect on the tensile properties of as-built parts. The vertical samples in their as-built surface condition experienced premature fracture at an average stress of 482 MPa, still within the linear elastic region, as seen in Fig. 9b. Since the horizontal samples, in which the tensile loading is nearly parallel to the deposited layers, do not suffer from any early failures compared with the verticals, this makes the horizontal samples the better candidates to be used directly in service in the as-built condition. This is not the case for the verticals. From the graphs of stress-strain of the as-built vertical and horizontal samples shown in Fig. 9c, it is clear that the tensile properties of as-built verticals are far less than their horizontal counterparts. However, Fig. 9d shows that the machined verticals and horizontal are very similar in their strengths but the strain at fracture of the machined verticals is still nearly half that of the horizontal samples, which will be discussed later in this section. The variation of Young's modulus for all samples, according to Fig. 9e, is approximately 4 %. This means the build direction and associated surface condition of the samples does not have any significant effect on the elasticity (stiffness), which is not the case for YS and UTS. As explained in the section on microstructural characterisation, the direction of tensile loading with respect to the columnar architecture (Fig. 6d) can result in anisotropy of the mechanical properties but there are other factors affecting the mechanical properties, especially in the as-built vertical. The different behaviour of vertical samples under two conditions of as-built and machined, Fig. 9b, may suggest that the interrelationship between the surface topography of the test pieces and the loading axis needs to be examined closely to verify if the build direction has any effect on the directionality of the valleys and hills of the roughness profile with respect to the loading axis.

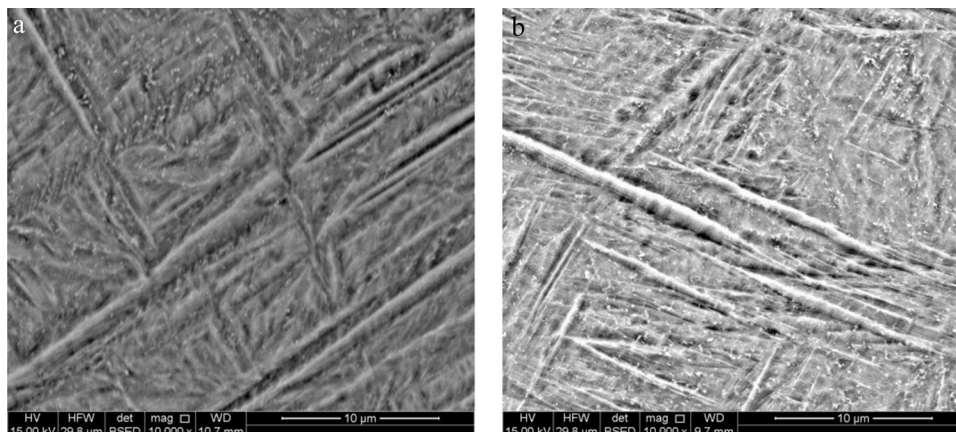


Fig. 7. Backscattered Electron micrographs of the etched samples sectioned transversely from; a) a horizontal sample, and b) a vertical sample.

Fig. 10 shows the surface topography of the as-built horizontal and vertical samples prepared longitudinally with respect to the applied tensile load. The peaks to valleys patterns on the outer surface of the horizontal sample in Fig. 10b is completely different from those observed in the vertical samples, Fig. 10c. The wavelength (peak to peak distance) on the outer surface of horizontal samples is greater compared with that of the as-built vertical. The short wavelength of the asperities on the outer surface of an as-built vertical sample is mainly correlated to the 30 µm layer thickness. This short wavelength, beside the unfused layers near the outer surface of the as-built vertical sample, leads to sharp, deep valleys (notches), as can be seen from Fig. 10c. The sharp valleys on the surface of the as-built vertical sample could act as stress concentration points, magnifying the applied stress at the surface and thus encouraging crack initiation. The high level of stress may then guide the crack towards the centre at a faster rate, causing premature fracture. It is also possible that the induced residual stress along the build direction, which is the tension on the edge of sample [15,43], may contribute to the stress concentration at the sharp notches. It should also be mentioned that the outer side surface of vertical samples is actually the edge of the sample where the laser track finishes. The higher stress level is then responsible for faster crack growth, resulting in a flat fracture surface for the as-built vertical samples. As has already been discussed for tensile properties, Fig. 9e shows that, by removing the surface layer of the vertical samples via machining, a considerable improvement in the mechanical properties could be achieved. Further investigation is required to show whether the surface characteristics (the sharp notches on the surface) of the as-built vertical samples alone are

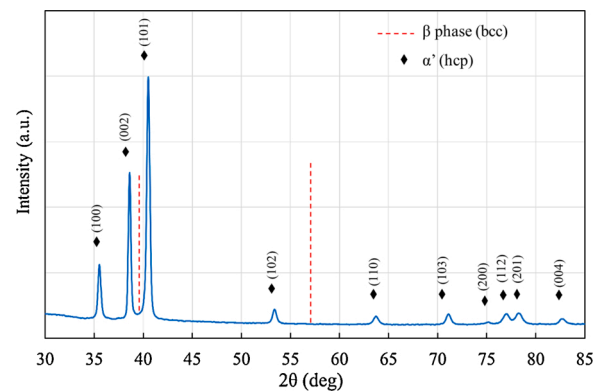


Fig. 8. The XRD spectrum of the SLM sample shows no trace of β phase, (the red dashed lines show the position of the expected peaks of the β phase) (For interpretation of the references to colour in this figure legend, the reader is referred to the web version of this article).

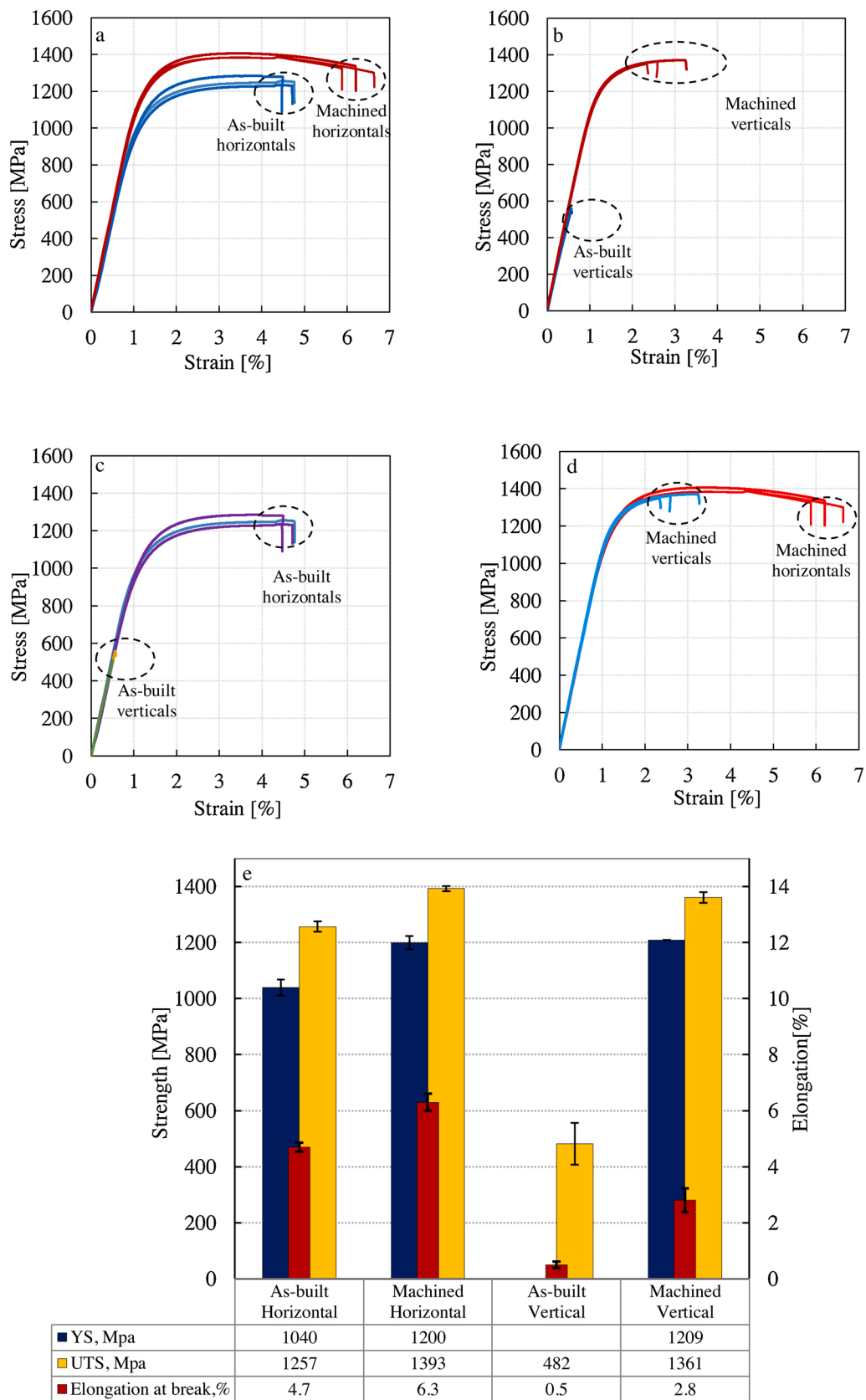


Fig. 9. The stress-strain plots, a) machined and as-built horizontals, b) machined and as-built verticals, c) as-built horizontals and verticals, d) machined horizontals and verticals, e) tensile properties of horizontal and vertical samples in two conditions of as-built and machined.

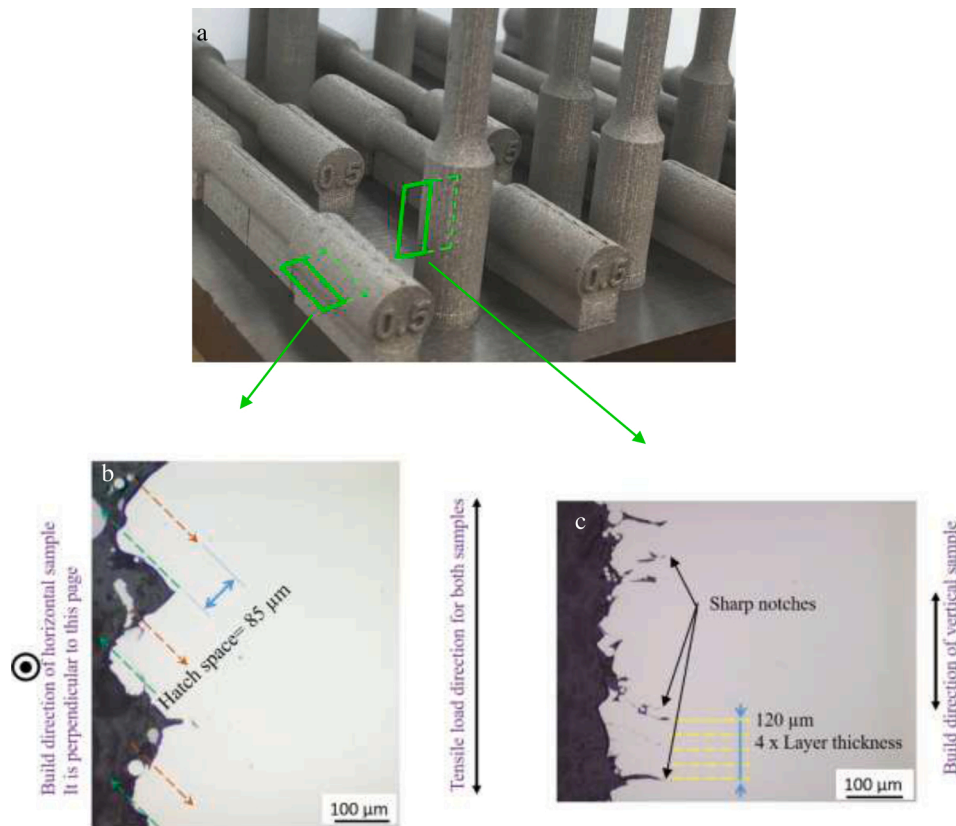


Fig. 10. a) Longitudinal cutting direction for outer surface morphology, b) Optical microscopy of an as-built horizontal sample, and c) an as-built vertical sample.

responsible for the premature failure or the residual stresses, or both. The observed lower ductility of machined vertical samples with respect to their horizontal counterparts could partially be attributed to the sharp angles of inter-layered pores, appearing perpendicular to the applied tensile load, Fig. 6c. In other words, anisotropy of pores with respect to the direction of applied load could be a potential cause of anisotropy of the mechanical properties. Porosities, which are inevitable SLM-induced defects [11,44], often limit the ductility of Ti64 parts [45]. In some studies [12,20], it is shown that these thin flattened pores, which are due to the lack of fusion between layers, may act as local stress risers, with some role played in the early fracture of the vertical samples. Moletsane et al. [46] reported that the elongated (inter-layer) pores contribute to the residual stress and can lower the ductility of as-built samples. This may explain the lower elongation of the machined vertical samples with elongated pores, compared with the machined horizontal samples. The average Vickers' microhardness of the transverse cut of the tensile samples from their grip sections were measured at 407 ± 12 (HV) and 423 ± 17 (HV) for the horizontal and vertical specimens, respectively. The microhardness values reveal that the hardness in both directions is nearly the same; however, the tensile load results show that there is a considerable anisotropy between the vertical and horizontal samples. Thus, Vickers' hardness is an indication of the hardness of the microstructure fabricated by the SLM process, but serious attention must be paid not to be misled by the hardness, as it does not reveal any effects of induced defects and the architecture of the microstructure on the mechanical properties and the anisotropy. A possible parameter which may influence the anisotropy of mechanical properties of SLM fabricated parts is the crystallographic texture. Some researchers [39,47] found that although the columnar prior grains show a strong $\langle 001 \rangle$ β texture parallel to the build direction, the α' martensitic phase formed from β during cooling exhibits just a random texture. This means that the crystallographic texture in SLM-fabricated Ti64 parts is weak. Beladi et al. [40] reported that the overall texture strength of α' martensitic

structure is considerably weaker compared with the $(\alpha + \beta)$ microstructure produced in a diffusional transformation. This is further confirmed by the measured microhardness values for the two orientations of vertical and horizontal with only 4 % difference. Therefore, texture appears not to be the main contributor of the anisotropy in mechanical properties, such as the observed difference in elongation of vertical and horizontal samples in current study. Although differences in ductility have been reported between the two deposition directions of machined samples, in some studies, the ductility was the opposite, i.e. the vertical samples showed higher ductility [13,48]. Therefore, it may be concluded that the anisotropic mechanical properties are an intrinsic feature of the SLM 3D printing process, affected by a range of parameters including component size and geometry, microstructure architecture and phases, solidification mechanism affecting crystallographic planes, porosity content and morphology and, of course, the process parameters. They pose a considerable challenge to the design and fabrication process for SLM components.

Fig. 11 shows the graphs of the UTS versus elongation of the machined horizontal (Fig. 11a) and vertical (Fig. 11b) samples in this study, compared with the results reported in the literature for the non-heat treated but machined samples [2,3,12,13,22,35,49–52]. Also, the SLM machines used by the researchers are specified in Fig. 11. The elongation of the machined horizontal samples in Fig. 11a shows a variation between 2%–11.8%, while the UTS varies between 1143 MPa and 1393 MPa, which is not as wide as for the elongation. It can be noted that the highest elongation is related to the part with the lowest UTS. Also, Fig. 11a reveals that the tensile strength, UTS, and ductility of Ti64 parts fabricated with different SLM machines and different process parameters approximate to a trend that shows an interrelationship between the ductility and strength of the samples, i.e., the ductility and strength vary inversely with respect to each other. This relationship between strength and ductility is very common in most materials fabricated with other manufacturing routes. However, the mechanical

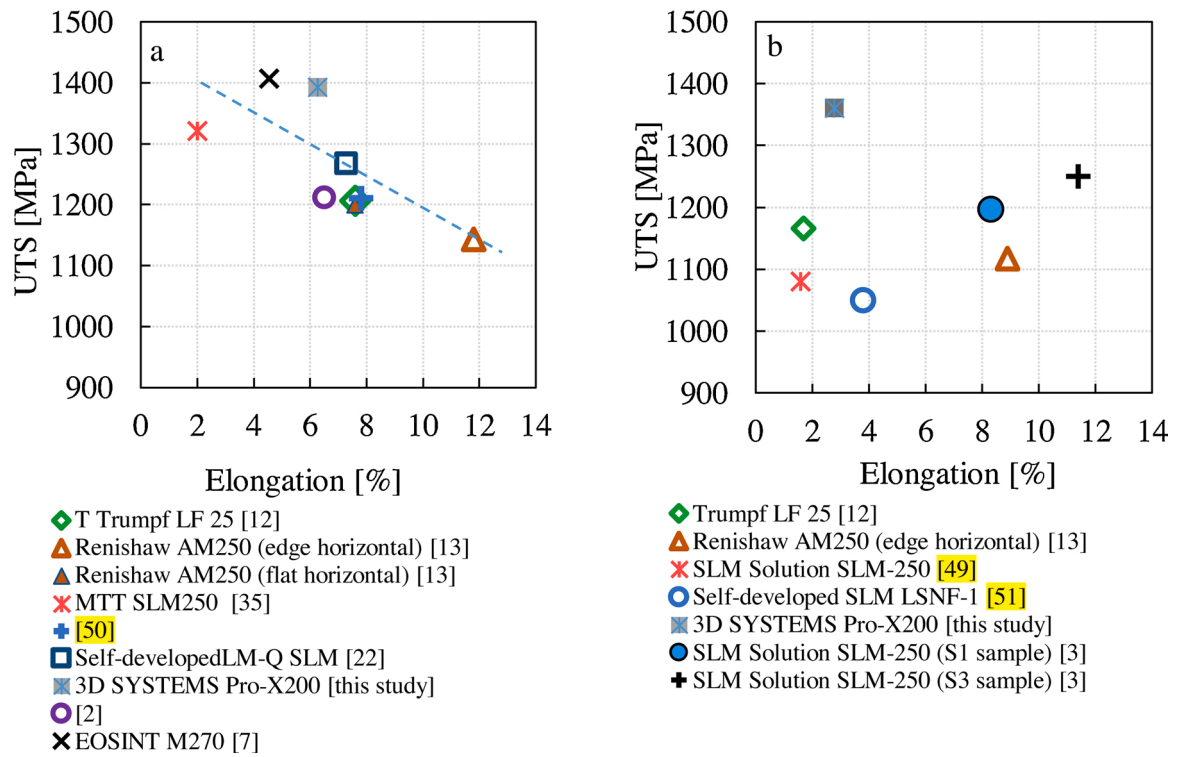


Fig. 11. UTS versus Elongation of SLM fabricated Ti64 parts, a) machined horizontals, and b) machined verticals.

strength versus the elongation of the vertical samples in Fig. 11b shows the widely-dispersed results in the open literature, making it hard to conclude confidently that UTS and ductility vary inversely, regardless of the machine and process parameters. The scattered mechanical

properties of vertical samples noticed in the literature, may be due to the direction of applied load with respect to orientation of defects which results in magnification of applied stress more acutely for vertical samples. In another words, regardless of the SLM machine and the

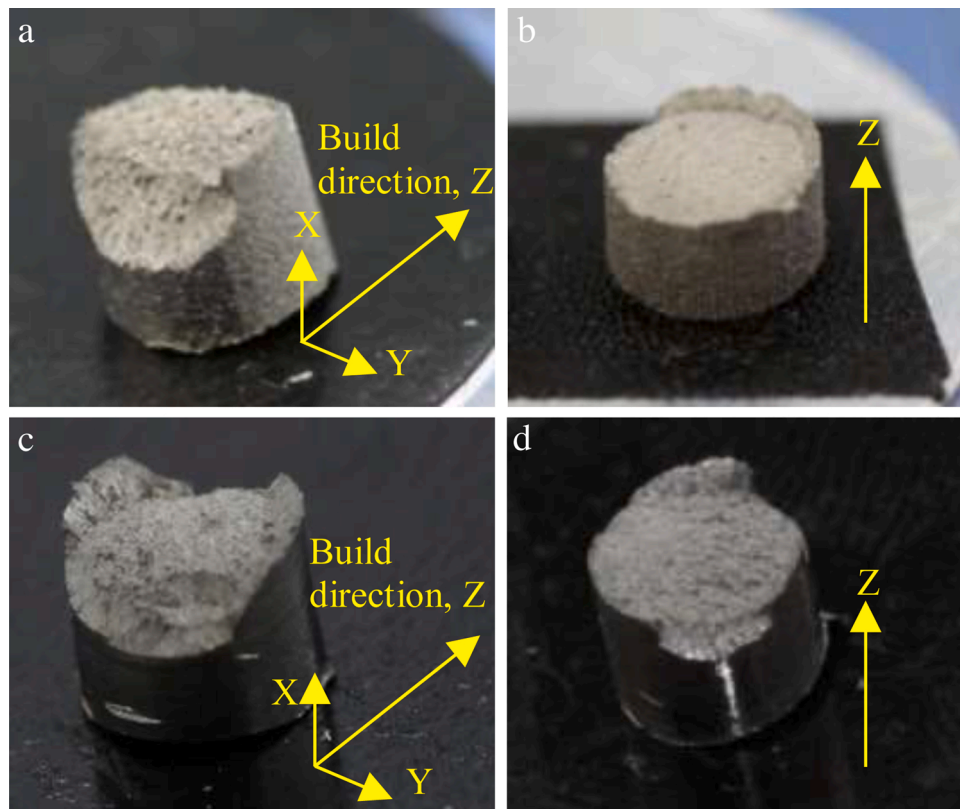


Fig. 12. Typical fracture surfaces of (a) as-built horizontal sample, (b) as-built vertical sample, (c) machined horizontal sample and (d) machined vertical sample.

process parameters, the mechanical properties of SLM fabricated Ti64 parts in the machined condition can be predictable to some extent when the parts are supposed to carry the load parallel to the deposited layer (horizontal samples), but it is not true for vertical samples.

3.3. Fracture analysis

A visual inspection of the fracture surface is summarised in Fig. 12. As mentioned earlier, for statistical significance, three tensile samples of each group were fabricated and tested. Fig. 12 only displays the cut sections of one typical sample from each group. The fracture surface of the as-built horizontal sample (Fig. 12a), machined horizontal (Fig. 12c) and machined vertical (Fig. 12d) with the shear lips around the edge periphery, indicate the ductile fracture mode for these samples, whereas the flat fracture surface of the as-built vertical, Fig. 12b, without a well-developed shear lip on a portion of the edge periphery of the fracture surface, resembles the brittle fracture mode. Having two different modes of fracture (brittle and ductile) is inconceivable for the SLM parts fabricated and tested at the same conditions. The flatness of the fracture surface for the as-built vertical sample may be attributed to the crack initiation site, propagation, and speed of crack growth; otherwise, the mode of fracture is the same for both the horizontal and vertical samples. It means that the flat fracture surface of an as-built vertical sample does not represent the brittle fracture mode, but instead displays a catastrophic failure caused by overload, i.e., fast ductile fracture. The fact that the vertical as-built sample does not show well-developed shear lips may be an indication that the crack initiates at the surface for vertical samples. This observation supports the hypothesis in the previous section, where the sharp valleys on the surface of the as-built vertical were suggested as acting as stress raiser and crack initiation sites.

Optical microscopy of the etched longitudinal section of the fracture surface is shown in Fig. 13. The flat fracture surface of the as-built vertical sample has been further highlighted in Fig. 13a. In addition, Fig. 13b, confirms the effectiveness of the sharp rooted surface profile of the as-built vertical sample in crack initiation from the surface of the as-

built verticals. In contrast with the vertical samples, Fig. 14 displays the uneven fracture surface of the as-built horizontal samples. The shear lips on each side of the as-built horizontal sample confirm the last stage of fracture takes place near the surface of the horizontal samples, i.e., gives an indication of crack initiation at the centre of the test pieces, propagating towards the surface. This is the classic mechanism of ductile fracture through void coalescence that takes place in a horizontal sample.

The fracture surfaces of the machined horizontal and vertical samples are presented in Fig. 15, showing bulk fractures in the middle of the samples and shear lips around the periphery. The fracture surface of the vertical sample, Fig. 15a, exhibits a layered topography, meaning that the fracture surface seems to alternate between layers whilst propagating. The quasi-cleavage features with dimples in both the horizontal and vertical samples may indicate a mixed mode of ductile and brittle fracture. A typical microcrack, which connects an inter-layer unfused site to the fracture surface, is clearly seen from the magnified inset in Fig. 15a; while in the magnified inset of Fig. 15b, showing a horizontal sample, typical inter-track voids and microcracks are visible. The fracture surface of the machined vertical sample is completely different from the as-built vertical shown in Fig. 13a. For the machined samples, regardless of the deposition direction (horizontal or vertical), the cracks seem to be initiated within the specimens by void coalescence which then propagates towards the surface. The fracture regions in shear lips are bordered with broken lines in both the vertical and horizontal samples.

In order to confirm the hypothesis of fast fracture in the as-built vertical due to the lack of micro-void coalescence in contrast with the other samples, the porosity contents of the fractured test pieces at the vicinity of the fracture surface within the gauge length were measured and plotted in Fig. 16. As shown in Fig. 16, the levels of porosity developed in the gauge section of both horizontal samples (machined and as-built), are almost the same, meaning that void coalescence is taking place in both the machined and as-built horizontal samples. This confirms the fracture mechanism is the same for both conditions. There

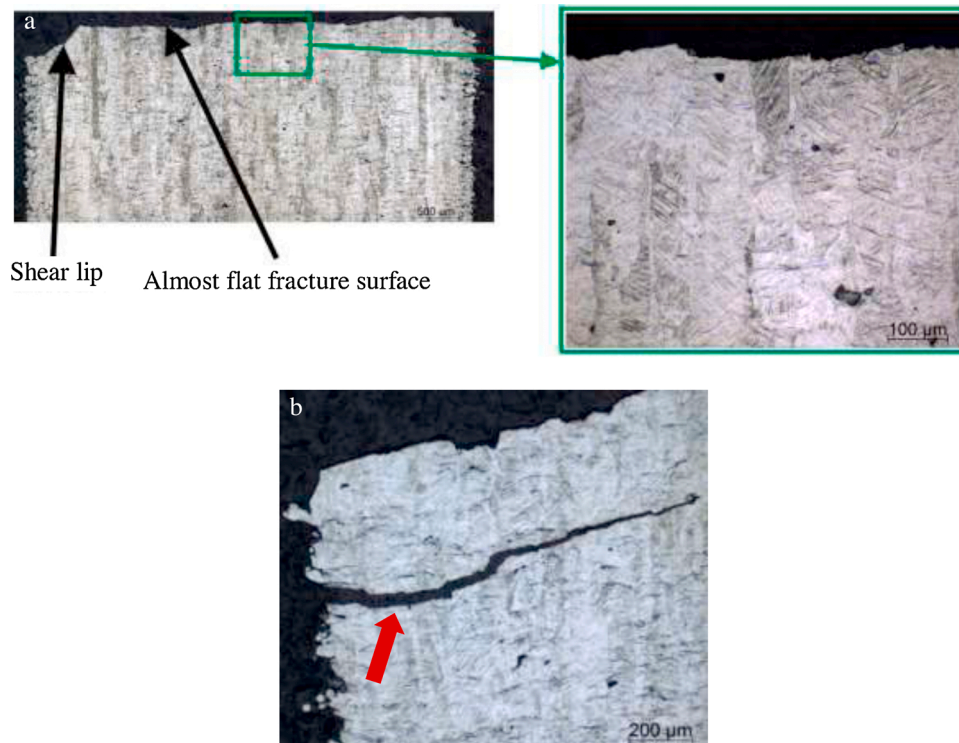


Fig. 13. Optical micrographs of the longitudinal section of the as-built vertical samples to show a) its flat fracture surface and b) the formation of surface initiated crack as a result of the sharp-rooted surface profile.

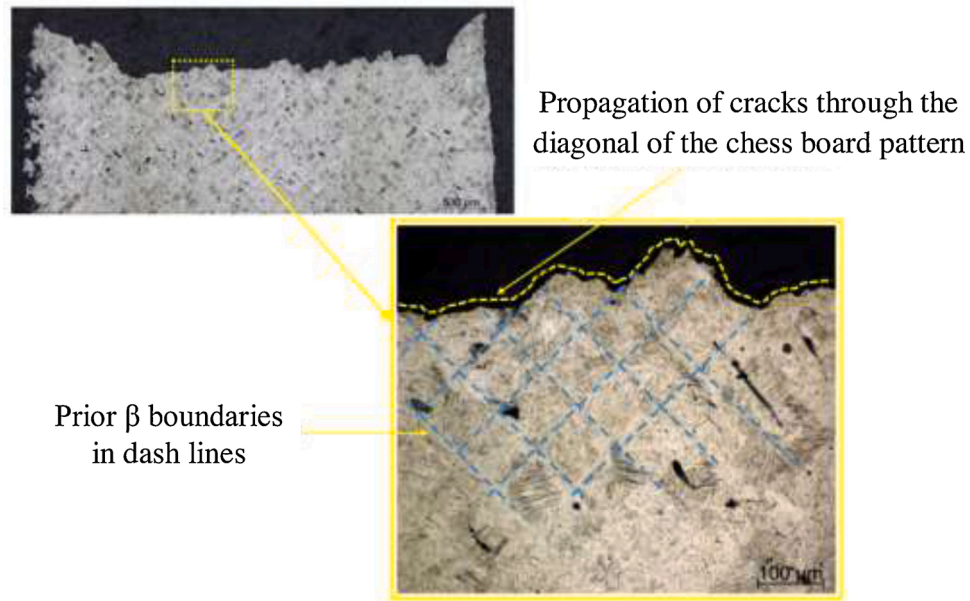


Fig. 14. Optical micrograph of a crack path for the fracture surface of the as-built horizontal sample with well-developed shear lips.

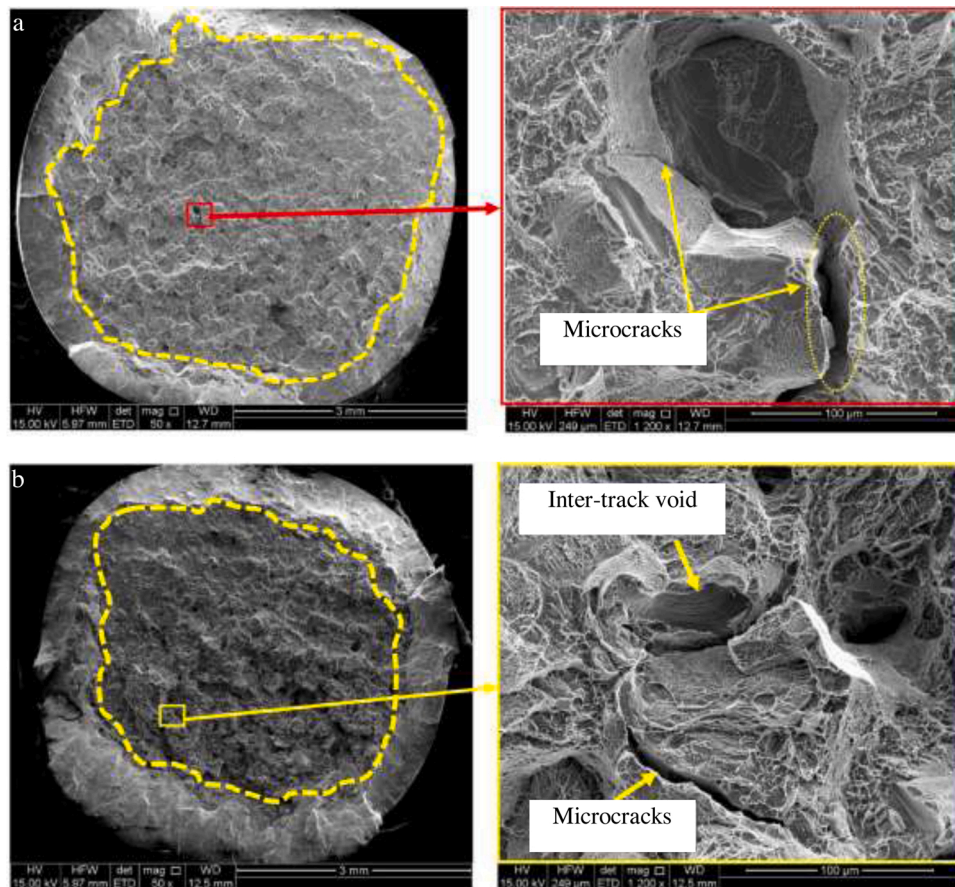


Fig. 15. SEM micrographs of the fracture surfaces of a) machined vertical with microcracks inter-connecting between layers. The broken lines show the borderline of the shear lips regions and bulk fracture surfaces on the machined tensile samples, and b) machined horizontal with a typical inter-track void and microcrack.

is an increase of around five fold to the average porosity in their grip sections. Although the porosity in the gauge section of the machined vertical exhibits nearly a three times increase to its grip section (which confirms the void coalescence mechanism), the as-built vertical behaved

completely differently. In fact, the as-built vertical sample did not show any changes in the porosity level near the fracture surface when compared with its grip section. These results reconfirm that the fracture of the as-built vertical sample did not initiate from the centre of the part

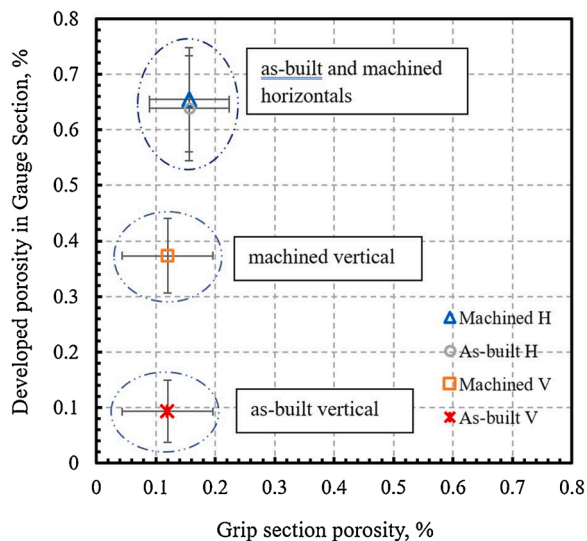


Fig. 16. Developed porosity in the gauge section of all samples near the fracture surface (gauge section) vs the porosity in the grip section.

by coalescence of the voids and development of pores, but from its periphery surface. In addition, Fig. 16 reveals that the porosity increase in the gauge section of the machined vertical sample is far less than both the machined and as-built horizontal samples. This result means that the pores' coalescence in machined vertical samples is not as prevalent as for the horizontal samples and, if related to the anisotropy of pores, it may justify a lower elongation value for the machined vertical samples when compared with both the machined and as-built horizontal samples.

4. Conclusions

This work reports a novel design approach to fabricate undistorted “truly as-built” Ti-6Al-4 V horizontal samples via an SLM technique where the samples are not treated under any post-fabrication processes, such as machining and/or heat treatment. These horizontal samples are now valid for tensile tests and can be compared with their vertical counterparts. This study highlights that alignment of the SLM layering direction with respect to the tensile loading direction in as-built samples is critical. This research paper shows that “truly as-built” samples, in which the applied load is aligned with deposited layers like in the horizontal samples, can be acceptable for some applications, without any post process treatments. But vertical samples, in which the applied load is perpendicular to the deposited layers, suffer from premature failure under just 38 % of the nominal load that their horizontal counterparts can carry before failure. This means that the vertical samples are not suitable to be used directly in any applications prior to post processing, which was the machining process in this paper. It is believed that this shortcoming in vertical samples is related to the deficiencies in the vertical as-built surfaces, which in turn, can be correlated to the quality of the surface and/or induced residual stress on the surface. Furthermore, it is shown that a relationship between the strength along the deposited layer (as for horizontal samples) and ductility of SLM fabricated Ti64 can be established, regardless of the SLM machine and process parameters: i.e., they vary inversely with respect to each other. However, such interrelationships between the strength perpendicular to the deposited layers and ductility remain rather uncertain.

Declaration of Competing Interest

We wish to confirm that there are no known conflicts of interest associated with this publication.

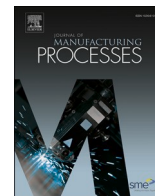
Acknowledgements

This work was performed in part at the OptoFab node of the Australian National Fabrication Facility (ANFF) utilizing Commonwealth and South Australian State Government funding. Adelaide Microscopy is gratefully acknowledged for providing access to electron microscopy facilities. A. Dare Baghi is grateful to the Australian Government and Adelaide University for the PhD scholarship.

References

- [1] Shipley H, McDonnell D, Culleton M, Lupoi R, O'Donnell G, Trimble D. Optimisation of process parameters to address fundamental challenges during selective laser melting of Ti-6Al-4V: A review. *Int J Mach Tools Manuf* 2018;128: 1–20. <https://doi.org/10.1016/j.ijmactools.2018.01.003>.
- [2] Hollander DA, von Walter M, Wirtz T, Sellei R, Schmidt-Rohlfing B, Paar O, Erli H-J. Structural, mechanical and in vitro characterization of individually structured Ti-6Al-4V produced by direct laser forming. *Biomaterials* 2006;27(7):955–63. <https://doi.org/10.1016/j.biomaterials.2005.07.041>. 2006/03/01/.
- [3] Xu W, Brandt M, Sun S, Elambasseril J, Liu Q, Latham K, et al. Additive manufacturing of strong and ductile Ti-6Al-4V by selective laser melting via in situ martensite decomposition. *Acta Mater* 2015;85:74–84.
- [4] Banerjee D, Williams JC. Perspectives on titanium science and technology. *Acta Mater* 2013;61(3):844–79. <https://doi.org/10.1016/j.actamat.2012.10.043>. 2013/02/01/.
- [5] Santos LV, Trava-Airoldi VJ, Corat EJ, Nogueira J, Leite NF. DLC cold welding prevention films on a Ti6Al4V alloy for space applications. *Surf Coat Technol* 2006; 200(8):2587–93. <https://doi.org/10.1016/j.surfcoat.2005.08.151>. 2006/01/24/.
- [6] Geetha M, Singh AK, Asokamani R, Gogia AK. Ti based biomaterials, the ultimate choice for orthopaedic implants – A review. *Prog Mater Sci* 2009;54(3):397–425. <https://doi.org/10.1016/j.pmatsci.2008.06.004>. 2009/05/01/.
- [7] Murr L, Quinones S, Gaytan S, Lopez M, Rodela A, Martinez E, et al. Microstructure and mechanical behavior of Ti-6Al-4V produced by rapid-layer manufacturing, for biomedical applications. *J Mech Behav Biomed Mater* 2009;2(1):20–32.
- [8] Song B, Dong S, Zhang B, Liao H, Coddet C. Effects of processing parameters on microstructure and mechanical property of selective laser melted Ti6Al4V. *Mater Des* 2012;35:120–5.
- [9] Gong H, Rafi K, Gu H, Janaki Ram GD, Starr T, Stucker B. Influence of defects on mechanical properties of Ti-6Al-4V components produced by selective laser melting and electron beam melting. *Mater Des* 2015;86:545–54. <https://doi.org/10.1016/j.matdes.2015.07.147>.
- [10] Hartunian P, Eshraghi M. Effect of build orientation on the microstructure and mechanical properties of selective laser-melted Ti-6Al-4V alloy. *J Manuf Mater Process* 2018;2(4):69.
- [11] Rafi HK, Karthik NV, Gong H, Starr TL, Stucker BE. Microstructures and mechanical properties of Ti6Al4V parts fabricated by selective laser melting and Electron beam melting. *J Mater Eng Perform* 2013;22(12):3872–83. <https://doi.org/10.1007/s11665-013-0658-0>.
- [12] Vilaro T, Colin C, Bartout JD. As-fabricated and heat-treated microstructures of the Ti-6Al-4V alloy processed by selective laser melting. *Metall Mater Trans A* 2011;42(10):3190–9. <https://doi.org/10.1007/s11661-011-0731-y>.
- [13] Simonelli M, Tse YY, Tuck C. Effect of the build orientation on the mechanical properties and fracture modes of SLM Ti-6Al-4V. *Mater Sci Eng A* 2014;616:1–11.
- [14] Zaeh MF, Branner G. Investigations on residual stresses and deformations in selective laser melting. *Prod Eng* 2010;4(1):35–45.
- [15] Merclis P, Kruth JP. Residual stresses in selective laser sintering and selective laser melting. *Rapid Prototyp J* 2006;12(5):254–65. <https://doi.org/10.1108/13552540610707013>.
- [16] Kruth J-P, Deckers J, Yasa E, Wautlhé R. Assessing and comparing influencing factors of residual stresses in selective laser melting using a novel analysis method. *Proc Inst Mech Eng Part B J Eng Manuf* 2012;226(6):980–91.
- [17] Yadroitsava I, Yadroitsava I. Evaluation of residual stress in stainless steel 316L and Ti6Al4V samples produced by selective laser melting. *Virtual Phys Prototyp* 2015; 10(2):67–76. <https://doi.org/10.1080/17452759.2015.1026045>.
- [18] Yadroitsava I, Grewar S, Hattings D, Yadroitsava I. Residual stress in SLM Ti6Al4V alloy specimens. 7th International Light Metals Technology Conference, LMT 2015, July 27, 2015 - July 29, 2015, Port Elizabeth, South Africa, 2015, Vol. 828-829: Trans Tech Publications Ltd, in Materials Science Forum 2015:305–10. <https://doi.org/10.4028/www.scientific.net/MSF.828-829.305> [Online]. Available: <https://doi.org/10.4028/www.scientific.net/MSF.828-829.305>.
- [19] Greitemeier D, Dalle Donne C, Syassen F, Eufinger J, Melz T. Effect of surface roughness on fatigue performance of additive manufactured Ti-6Al-4V. *Mater Sci Technol* 2016;32(7):629–34.
- [20] Rafi HK, Starr TL, Stucker BE. A comparison of the tensile, fatigue, and fracture behavior of Ti-6Al-4V and 15-5 PH stainless steel parts made by selective laser melting. *Int J Adv Manuf Technol* 2013;69(5–8):1299–309. <https://doi.org/10.1007/s00170-013-5106-7>.
- [21] Facchini L, Magalini E, Robotti P, Molinari A, Höges S, Wissenbach K. Ductility of a Ti-6Al-4V alloy produced by selective laser melting of prealloyed powders. *Rapid Prototyp J* 2010;16(6):450–9.
- [22] Vrancken B, Thijs L, Kruth J-P, Van Humbeeck J. Heat treatment of Ti6Al4V produced by Selective Laser Melting: microstructure and mechanical properties.

- J Alloys Compd 2012;541:177–85. <https://doi.org/10.1016/j.jallcom.2012.07.022>.
- [23] ASTM F2924-14, Standard Specification for Additive Manufacturing Titanium-6 Aluminum-4 vanadium with Powder Bed Fusion. 2014.
- [24] Li Qiang, Ibrahim Kucukkok, Zhang David Z. Production planning in additive manufacturing and 3D printing. *Comput Oper Res* 2017;83(July):157–72.
- [25] Kadir AiniZuhraAbdul, Yusof Yusri, Md SaidinWahab. Additive manufacturing cost estimation models—a classification review. *Int J Adv Manuf Technol* 2020;107: 4033–53.
- [26] Cunningham CR, Wikshåland S, Xu F, Kemakolam N, Shokrani A, Dhokia V, et al. Cost modelling and sensitivity analysis of wire and arc additive manufacturing. *Procedia Manuf* 2017;11:650–7.
- [27] Huang Runze, Ulu Erva, Kara Levent Burak, Whitefoot Kate S. Cost minimization in metal additive manufacturing using concurrent structure and process optimization. In: *Proceedings of the ASME 2017 International Design Engineering Technical Conferences and Computers and Information in Engineering Conference*. Volume 2A: 43rd Design Automation Conference; 2017. https://doi.org/10.1115/DETC2017-67836_V02AT03A030. ASME.
- [28] Jamshidi P, Aristizabal M, Kong W, Villapun V, Cox SC, Grover LM, Attallah MM. Selective laser melting of Ti-6Al-4V: the impact of post-processing on the tensile, fatigue and biological properties for medical implant applications. *Materials* 2020; 13(12):2813.
- [29] Antonysamy AA, Meyer J, Prangnell PB. Effect of build geometry on the β -grain structure and texture in additive manufacture of Ti6Al4V by selective electron beam melting. *Mater Charact* 2013;84:153–68. <https://doi.org/10.1016/j.matchar.2013.07.012>. 2013/10/01/.
- [30] Tang H, Qian M, Liu N, Zhang X, Yang G, Wang J. Effect of powder reuse times on additive manufacturing of Ti-6Al-4V by selective electron beam melting. *Jom* 2015;67(3):555–63.
- [31] Quintana OA, Tong W. Effects of oxygen content on tensile and fatigue performance of Ti-6Al-4 V manufactured by selective laser melting. *JOM* 2017;69 (12):2693–7.
- [32] Kumar S. *Selective laser Sintering/Melting*. Comprehensive materials processing, vol. 10. Elsevier; 2014. p. 93–134.
- [33] Baghi AD. *Additive Manufacturing of Titanium-Based Biomedical Alloys*. PhD Project School of Mechanical Engineering, The University of Adelaide; 2020.
- [34] ASTM E8/E8M -16a standard test methods for tension testing of metallic materials. 2016.
- [35] Mertens A, Reginster S, Paydas H, Contrefois Q, Dormal T, Lemaire O, et al. Mechanical properties of alloy Ti-6Al-4V and of stainless steel 316L processed by selective laser melting: Influence of out-of-equilibrium microstructures. *Powder Metall* 2014;57(3):184–9.
- [36] Yang J, Han J, Yu H, Yin J, Gao M, Wang Z, et al. Role of molten pool mode on formability, microstructure and mechanical properties of selective laser melted Ti-6Al-4V alloy. *Mater Des* 2016;110:558–70.
- [37] Yasa E, Deckers J, Kruth J-P, Rombouts M, Luyten J. Experimental investigation of charpy impact tests on metallic SLM parts. *Innovative Developments in Design and Manufacturing Advanced Research in Virtual and Rapid Prototyping*. 2009. p. 207–14.
- [38] Thijs L, Verhaeghe F, Craeghs T, Humbeeck JV, Kruth J-P. A study of the microstructural evolution during selective laser melting of Ti-6Al-4V. *Acta Mater* 2010;58(9):3303–12. <https://doi.org/10.1016/j.actamat.2010.02.004>.
- [39] Simonelli M, Tse YY, Tuck C. On the texture formation of selective laser melted Ti-6Al-4V. *Metall Mater Trans A* 2014;45(June (6)):2863–72. <https://doi.org/10.1007/s11661-014-2218-0>. journal article.
- [40] Beladi H, Chao Q, Rohrer GS. Variant selection and intervariant crystallographic planes distribution in martensite in a Ti-6Al-4V alloy. *Acta Mater* 2014;80: 478–89.
- [41] Galarraga H, Warren RJ, Lados DA, Dehoff RR, Kirka MM, Nandwana P. Effects of heat treatments on microstructure and properties of Ti-6Al-4V ELI alloy fabricated by electron beam melting (EBM). *Mater Sci Eng A* 2017;685:417–28.
- [42] Li B, Shen Y, Hu W, Luo L. Surface modification of Ti-6Al-4V alloy via friction-stir processing: microstructure evolution and dry sliding wear performance. *Surf Coat Technol* 2014;239:160–70.
- [43] Rangaswamy P, Holden T, Rogge R, Griffith M. Residual stresses in components formed by the laserengineered net shaping (LENS®) process. *J Strain Anal Eng Des* 2003;38(6):519–27.
- [44] Hrabě N, Quinn T. Effects of processing on microstructure and mechanical properties of a titanium alloy (Ti-6Al-4V) fabricated using electron beam melting (EBM), Part 2: energy input, orientation, and location. *Mater Sci Eng A* 2013;573: 271–7. <https://doi.org/10.1016/j.msea.2013.02.065>. 2013/06/20/.
- [45] Carroll BE, Palmer TA, Beese AM. Anisotropic tensile behavior of Ti-6Al-4V components fabricated with directed energy deposition additive manufacturing. *Acta Mater* 2015;87:309–20. <https://doi.org/10.1016/j.actamat.2014.12.054>. 2015/04/01/.
- [46] Moletsane M, Krakhmalev P, Kazantseva N, Du Plessis A, Yadroitsava I, Yadroitsev I. Tensile properties and microstructure of direct metal laser-sintered Ti6Al4V (ELI) Alloy. *South Afr J Ind Eng* 2016;27(3):110–21.
- [47] Sridharan N, Chaudhary A, Nandwana P, Babu SS. Texture evolution during laser direct metal deposition of Ti-6Al-4V. *Jom* 2016;68(3):772–7.
- [48] Frey M, Shellabear M, Thorsson L. *Mechanical testing of DMLS parts*. Munich: EOS whitepaper, EOS GmbH; 2009.
- [49] Leuders S, Thöne M, Riemer A, Niendorf T, Tröster T, Richard HA, et al. On the mechanical behaviour of titanium alloy TiAl6V4 manufactured by selective laser melting: Fatigue resistance and crack growth performance. *Int J Fatigue* 2013;48: 300–7. <https://doi.org/10.1016/j.ijfatigue.2012.11.011>.
- [50] Zhao J-R, Hung F-Y, Lui T-S, Wu Y-L. The relationship of fracture mechanism between high temperature tensile mechanical properties and particle Erosion resistance of selective laser melting Ti-6Al-4V alloy. *Metals* 2019;9(5):501.
- [51] Yang J, Yu H, Wang Z, Zeng X. Effect of crystallographic orientation on mechanical anisotropy of selective laser melted Ti-6Al-4V alloy. *Mater Charact* 2017;127: 137–45.
- [52] Murr LE, Quinones SA, Gaytan SM, Lopez MI, Rodela A, Martinez EY, Hernandez DH, Martinez E, Medina F, Wicker RB. Microstructure and mechanical behavior of Ti-6Al-4V produced by rapid-layer manufacturing, for biomedical applications. *J Mech Behav Biomed Mater* 2009;2(January (1)):20–32. <https://doi.org/10.1016/j.jmbbm.2008.05.004>. Research Support, Non-U.S. Gov't Review.



Effective post processing of SLM fabricated Ti-6Al-4 V alloy: Machining vs thermal treatment

Alireza Dareh Baghi^{a,*}, Shahrooz Nafisi^a, Reza Hashemi^b, Heike Ebendorff-Heidepriem^c,
Reza Ghomashchi^{a,c}

^a School of Mechanical Engineering, University of Adelaide, SA 5005, Australia

^b College of Science and Engineering, Flinders University, SA 5042, Australia

^c Institute of Photonics and Advanced Sensing, School of Physical Sciences, University of Adelaide, SA 5005, Australia

ARTICLE INFO

Keywords:

Additive manufacturing
Selective laser melting (SLM)
Ti-6Al-4V (Ti64)
Mechanical characterisation

ABSTRACT

Anisotropy in the mechanical properties with respect to the build direction of Selective Laser Melting (SLM) fabricated titanium parts is a known, challenging problem, which can be mitigated using a post processing method such as heat treatment. This paper investigates the potential sources of anisotropy associated with SLM fabricated Ti64 parts and studies the influence of heat treatment on the anisotropy in mechanical properties' behaviour in two directions: vertical and horizontal. SLM fabricated samples were machined and stress-relieved at 670 °C. In addition, annealing at 850 °C was performed on the machined samples to investigate the effect of heat treatment at a higher temperature on the anisotropy behaviour of the machined parts. The tensile test results showed that the difference in elongation at fracture between the vertical and horizontal samples (elongation anisotropy) will reduce from 125% in non-heat treated samples to 36% when the samples are annealed.

Microstructural analyses revealed an anomaly, which is named the fish scale feature in this work. This newly-found type of defect was significantly identifiable in non-heat treated samples; however, after annealing it completely disappeared from the microstructure. It is believed that the fish scale defect plays a role in the failure of vertical samples.

The same stress-relieving and annealing processes were then investigated on as-built vertical samples. The outcome revealed that the annealing process provides a greater improvement than machining. The results demonstrate that each post process, either machining or annealing, can eliminate the premature failure problem of as-built vertical samples, which occurs at a fracture strain of 0.5% under 482 MPa stress. Machining improves the fracture strength of the non-machined vertical samples to 1361 MPa at a strain of 2.8%; whereas annealing can enhance the fracture stress (premature) from 482 MPa to 1069 MPa, with a significant increase in fracture strain from 0.5% to 4%. The observations were found to be correlated to the phase change in the microstructure, mitigating the influence of defects such as the fish scale feature and full removal of the residual stress during annealing.

1. Introduction

The selective laser melting (SLM) fabrication method, as one of the additive manufacturing (AM) techniques, has drawn extensive attention because of its ability to produce intricate parts in one single manufacturing process. One of the advantages of the SLM route is its ability to process high melting temperature materials, such as Ti-based light alloys [1,2], where conventional methods, such as casting and machining, may be neither viable for the required mechanical and

physical properties nor cost effective. Ti-6Al-4V (Ti64), with its wide applications in the aerospace [3,4] and biomedical [5,6] fields, is among the titanium alloys shaped by SLM with some interesting outcomes. Despite the high strength offered by SLM-fabricated Ti64 parts, the ductility is inferior when compared with conventionally manufactured components. This is due to the non-equilibrium martensitic phase α' appearing in the microstructure, which is associated with the rapid solidification rates encountered during the SLM process [7–11].

In addition, there may be a certain degree of undesirable anisotropy

* Corresponding author.

E-mail address: Alireza.darehbaghi@adelaide.edu.au (A. Dareh Baghi).

<https://doi.org/10.1016/j.jmpro.2021.06.035>

Received 17 April 2021; Received in revised form 17 May 2021; Accepted 17 June 2021

Available online 26 June 2021

1526-6125/© 2021 The Society of Manufacturing Engineers. Published by Elsevier Ltd. All rights reserved.

Table 1
Chemical composition (wt%) of Ti64 (grade5) powder.

Item	Al	V	Fe	O	C	N	H	Ti
ASTM F2924-14	5.50–6.75	3.50–4.50	Max 0.3	Max 0.2	Max 0.08	Max 0.05	Max 0.015	Bal.
Powder	6.15	3.94	0.18	0.098	0.005	0.010	<0.002	Bal.
SLM fabricated bulk samples	6.14	3.97	0.19	0.114	0.005	0.011	<0.002	Bal.

in the mechanical properties, depending on the build direction, for vertically- or horizontally-built parts [11–15]. In a previous study by the authors [16], the effect of build orientation on the tensile properties of as-built vertical and horizontal Ti64 samples was studied for which the unwanted distortion that normally occurs in as-built horizontal parts was eliminated through a novel design. It was reported that the post machining process can improve the mechanical properties of truly as-built vertical and horizontal parts in terms of ductility and strength, but they still suffer from anisotropy in ductility (elongation % at fracture), i.e., 6.3% for machined horizontal as against 2.8% for machined vertical parts.

This raises an important question as to whether or not a post heat treatment would be able to effectively resolve the problem of anisotropy in mechanical properties observed in the SLM fabricated Ti64 alloy (both horizontal and vertical parts). Despite a reasonable number of reports in the literature studying the mechanical strength and elongation (with and without heat treatment) [17–19], there is still limited information available in terms of how and why an applied thermal treatment might mitigate the influence of build orientation and the resultant anisotropy on the mechanical properties of SLM fabricated Ti64 parts [11].

Also, it has already been reported that the as-built (non-machined surface) vertical parts suffer from premature failure; and importantly, the mechanical strength vs the elongation of vertical sample reviewed in open literature, showed widely-dispersed results compared with horizontally built parts [16]. Chlebus et al. [20] discuss how the drastic decrease in the ultimate tensile strength (UTS) of their vertical samples, compared with two series of horizontal samples, is mainly related to the high level of residual stresses and the orientation of flat-shape pores (with their small tip radii) with respect to the applied tensile load. Thus, the vertical samples are susceptible to fail under lower stresses and strains, resulting in premature failure in the as-built (non-machined surface) condition.

In the absence of generally optimised process parameters to fabricate the parts with the most consistent mechanical properties, especially in as-built vertical parts, finding an effective post process, to save the vertical parts from premature failure, is vital. It has been reported that the premature failure of as-built vertical samples may be resolved by machining the outer surface [16]. However, a post machining process may not be preferable as additive manufacturing aims to produce parts in one step without the need for another fabrication process such as

machining. Also, machining may not be feasible for complex parts that are conveniently fabricated using additive manufacturing. This highlights the need to explore if a post heat treatment can be an effective substitute for machining, with the aim of preventing the occurrence of premature failure in as-built vertical parts.

This paper therefore aims to study how and why a post heat treatment can first reduce anisotropy and then make significant improvements in the mechanical properties of SLM fabricated Ti64 alloy with an emphasis on as-built vertical parts. This will be accomplished through a careful investigation of the microstructure (including phase analysis and defects).

The findings of this study will be useful in manufacturing applications where machining of the as-built SLM titanium parts is very costly or may not be feasible, especially for parts carrying the service load along the layer deposition (as happens in vertically built parts).

2. Materials and experimental procedures

2.1. Materials

The gas atomized pre-alloyed powder Ti64 (grade 5) was supplied by TLS, Technik GmbH & Co, Germany [21]. The ICP-AES technique was used for the elemental chemical analysis of iron (Fe), aluminium (Al), and vanadium (V). The elemental percentages of hydrogen (H), nitrogen (N), and oxygen (O) were measured using a LECO ONH836 analyser. In addition, the carbon (C) content was analysed by the LECO CS200 instrument. Table 1 presents the results of the chemical analysis of the powder and SLM fabricated sample. All elements, especially the impurities and oxygen in both the Ti64 powder and bulk sample, are within the acceptable range recommended by ASTM F2924-14 [22].

The morphology of the powder was examined using an FEI Quanta 450 FEGSEM. The powder exhibits a spherical morphology, Fig. 1a, which confirms the suitability of the powder for SLM processing. Fig. 1b shows the powder size distribution measured by a laser particle size analyser, Malvern Mastersizer 2000.

2.2. SLM fabrication equipment and method

A 3D SYSTEMS ProX DMP 200 machine was used to fabricate the tensile samples. This machine has a build platform of 140 mm × 140 mm and is equipped with a laser as the heat source, with a maximum power

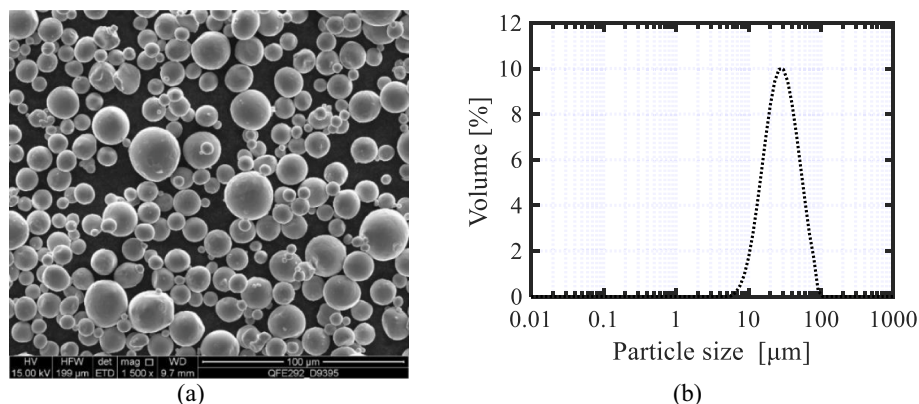


Fig. 1. a) Typical SEM image of Ti64 powder particles, b) Ti64 particle diameter distribution of powder.

Table 2
SLM process parameters to fabricate Ti64 samples.

Laser power, P (W)	Layer thickness, t (μm)	Scanning velocity, v (mm/s)	hatch spacing, h (μm)
270	30	1800	85

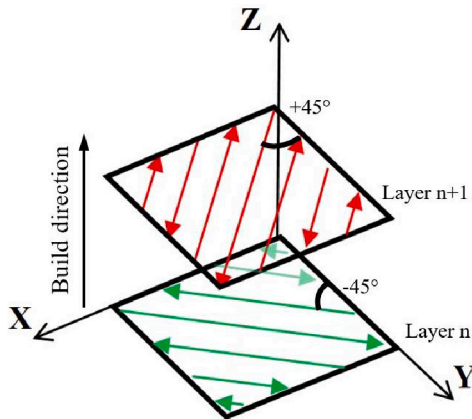


Fig. 2. Laser scan strategy and build direction.

of 300 W in continuous mode and 1070 nm wavelength. Argon at atmospheric pressure (101 KPa) filled the build chamber of the machine, while the oxygen level was kept below 500 ppm. Table 2 presents the SLM process parameters, optimised to fabricate almost fully dense Ti64 parts. Also, a bi-directional laser strategy with an interlayer 90° rotation ($\pm 45^\circ$ with respect to the X and Y axes) was chosen, Fig. 2.

2.3. Tensile samples preparation and heat treatment cycles

In the previous report [16] it was shown that surface machining can significantly improve the mechanical properties of as-built parts, especially in vertical samples. As a result, machined samples are a suitable candidate for investigation of heat treatment on the anisotropy in mechanical properties for both horizontal and vertical samples. By machining the outer surface of the as-built samples, the surface imperfections are removed, and the heat treatment results will not be influenced by surface defects.

In addition to the heat treatment of the machined samples, the effect of heat treatment on the mechanical properties of non-machined (as-built) vertical samples is also investigated. This extra investigation on

as-built vertical samples alone aims to compare the effect of surface machining and heat treatment separately and identify the most influential post process in eliminating premature failure in the as-built vertical samples.

Therefore, the tensile test samples studied in this research are summarised as below in three groups:

- **MH: Machined Horizontal** samples made from cylindrical rods deposited horizontally, (Fig. 3a).
- **MV: Machined Vertical** samples made from SLM fabricated vertical rods, (Fig. 3b).
- **NMV: Non-Machined Vertical** samples, which are as-built tensile test samples, deposited vertically, (Fig. 3c).

For the MH and MV tensile samples, horizontal and vertical cylindrical rods were initially heat treated, followed by a turning process to make machined tensile test samples, Fig. 4. It is noteworthy that the shape of the final tensile test samples (MH, MV and NMV), shown in Fig. 4, complies with the ASTM E8 [23] standard, where the gauge length is 4D (four times the gauge diameter “D”).

Two heat treatments cycles; i.e., stress-relieving and annealing, were conducted in a horizontal resistance heating tube furnace model AY-TF-

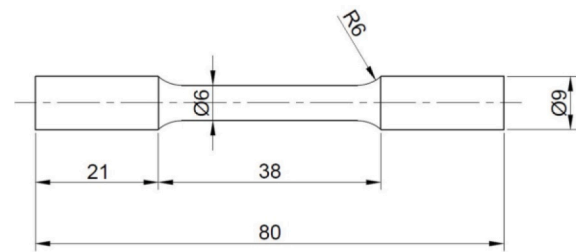


Fig. 4. Dimensions of the tensile test samples (in mm) according to ASTM E8 [27].

Table 3
Heat treatments performed on the cylindrical samples prior to machining.

Heat treatment	Temperature, °C	Soaking time, hr	Cooling type
Stress-relieving	670 °C (± 10)	5	Controlled furnace cooling from 670 °C to 250 °C in 12 h
Annealing	850 °C (± 10)	2	Controlled furnace cooling from 850 °C to 250 °C in 12 h

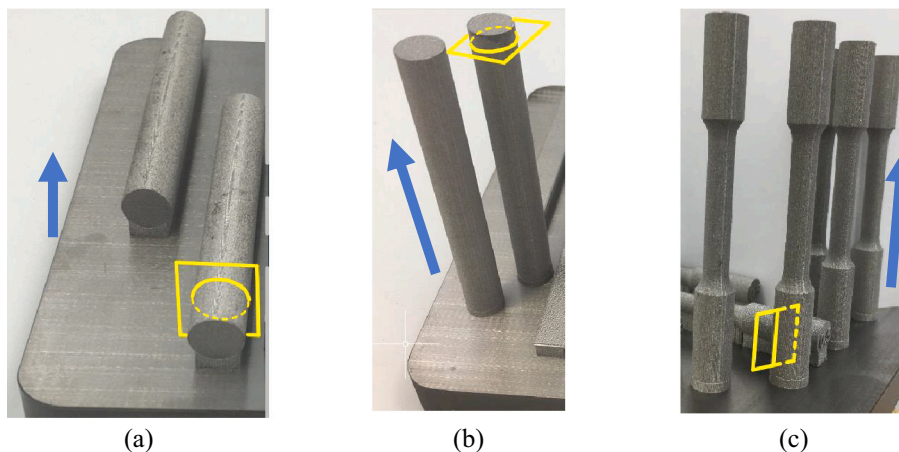


Fig. 3. a) horizontal deposited rods, b) vertical deposited rods and c) non-machined vertical samples (NMV). (Arrows show the SLM build direction; and the sketched planes demonstrate sectioning for preparation of the metallographic samples).

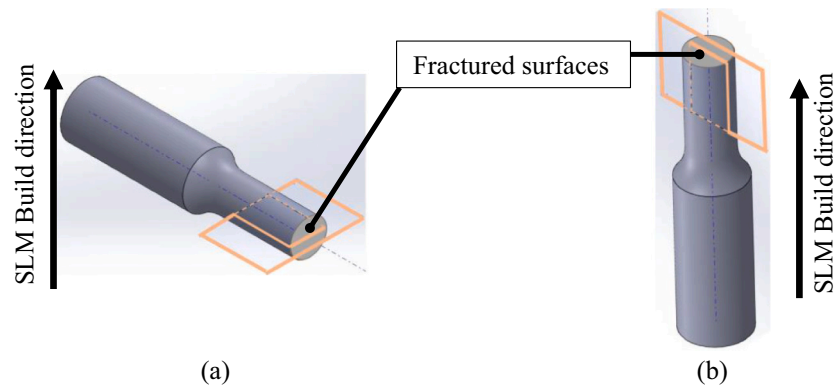


Fig. 5. Longitudinal sectioning through the fractured surfaces of a) MH and b) MV samples.

80–175, with a heating rate of 5 °C/min under an inert gas (argon) atmosphere. Temperature control was performed according to SAE AMS 2801B [24] (Table 3).

Due to the statistical significance of tensile test results, three samples of each group of MH, MV and NMV were allocated for each heat treatment cycle, i.e., stress relieving and annealing. Apart from the samples dedicated to two cycles of heat treatments, three tensile samples of each group were also assigned to the non-heat treated condition as reference samples. Therefore, nine samples of each group of MH, MV and NMV and ultimately twenty seven samples in total, have been fabricated for this study.

To prepare metallographic samples, transverse cuts (planes shown in Fig. 3a and b) were collected from the grip section of the MH and MV tensile samples. To investigate the effect of the as-built surface of the NMV on the tensile properties, the metallographic samples were prepared by longitudinally sectioning the NMV sample, Fig. 3c. Alongside the metallographic samples collected from transverse sections of the MV and MH samples, the fractured surfaces of the MH and MV samples were sectioned longitudinally (along the tensile axis) as demonstrated in Fig. 5, for crack path characterisation.

2.4. Analysis methods

All metallographic samples were etched using Kroll's reagent (3% HF + 5% HNO₃ + 92% distilled water) for 50 s. Prior to etching, all samples in the polished condition were examined for porosity content via the 2D area fraction method, employing optical microscopy and image analysis software, ImageJ.¹ Phase identifications of the sectioned samples were conducted with X-ray diffraction in a Rigaku MiniFlex 600 XRD machine with Cu radiation, operating at 40 kV and 15 mA, with a scan speed of 10°/min over a range of 2θ from 30° to 80°. For the microstructural analysis, a Zeiss optical microscope Imager2, an FEI Quanta 450 FEG-SEM, and FIB SEM Helios Nanolab FEI Dual Beam were used. Hardness of all sectioned samples from the grip sections (Fig. 3a and b) were measured by a Vickers microhardness device (LECO, LM-700AT) with a 300 g load and dwell time of 10s. Six indentations were performed near the centre of each sample and the average microhardness is reported. An Instron testing machine model 5969 with a load capacity of 50kN was used for conducting the tensile tests with a displacement of 0.20 mm/min at room temperature.

3. Results and discussion

3.1. Microstructural characterisation

The optical micrographs in Fig. 6 reveal the formation of a columnar

structure in non-heat treated, stress-relieved and annealed MH samples. The chessboard patterns observed for the MV samples, Fig. 6, are further confirmation of columnar grains formation in Ti64 SLM printed samples. The columnar grains in non-heat treated SLM fabricated Ti64 parts, has already been reported by other researchers [1,25–27]. The boundaries separating the columnar grains are the prior β grains boundaries. Since the temperatures of both stress-relieving and annealing treatments are below the β transus temperature, i.e., 1000 ± 20 °C [28], it is expected to find the columnar grain architecture with the prior β boundaries preserved [11,17].

The 3D sketch of the columnar architecture of the microstructure (macrostructure) in all samples of MH and MV, shown in Fig. 7, confirms that the microstructure in vertical and horizontal samples is the same but the direction of applied load on their microstructure is different. In vertical samples, the tensile load is aligned with the columnar grains; while in horizontal samples the load is along the diagonal of the cubic columnar grains.

Fig. 8, which is the stacked XRD spectra of three metallographic samples, reveals the existence of (HCP) α and/or α' phase in all samples, while the phase of β (BCC) is observed only in stress-relieved and annealed samples. It is hard to differentiate the HCP α from the α' martensitic phase via the XRD technique, as both α and α' have the same crystal structure with very similar lattice parameters [7,29–31]. The main difference between α and α' is related to crystal distortion, which is due to the supersaturation of vanadium in the diffusionless transformation of β to the α' martensitic phase [32,33].

In addition, the XRD spectrum in Fig. 8 for non-heat treated samples are somewhat broadened, compared with other samples. Broadening of XRD peaks is related to the small crystal size (or particles) and strain [34]. Although non-heat treated SLM fabricated Ti64 samples usually suffer from residual stresses, it cannot be positively confirmed that the broadening of non-heat treated samples can be related to strain, but may be due to the small acicular shape of the α' martensitic phase, which will be discussed later.

The full width at half maximum (FWHM) of the main peak of the HCP phase α/α' of all samples, which is associated with plane (101), shown in

Table 4, presents a maximum broadening value of 0.40° for the non-heat treated sample. Jovanovic et al. [30] reported that an FWHM above 0.20° is evidence of a martensitic phase.

The lowest value of FWHM in Table 4 for annealed samples, 0.09°, may represent the value of FWHM for the HCP α phase without any α' phases in the structure. It has already been reported [11,35,36] that any heat treatment above 800 °C fully decomposes the α' phase to α. So, it is confirmed that the value of FWHM, 0.09°, for annealed samples is associated with a fully HCP α phase. The FWHM value of 0.12° in the stress-relieved samples may indicate that the microstructure contains both α' and α phases.

For further microstructure characterisation, optical and SEM

¹ ImageJ is a trade mark; (<https://imagej.net>).

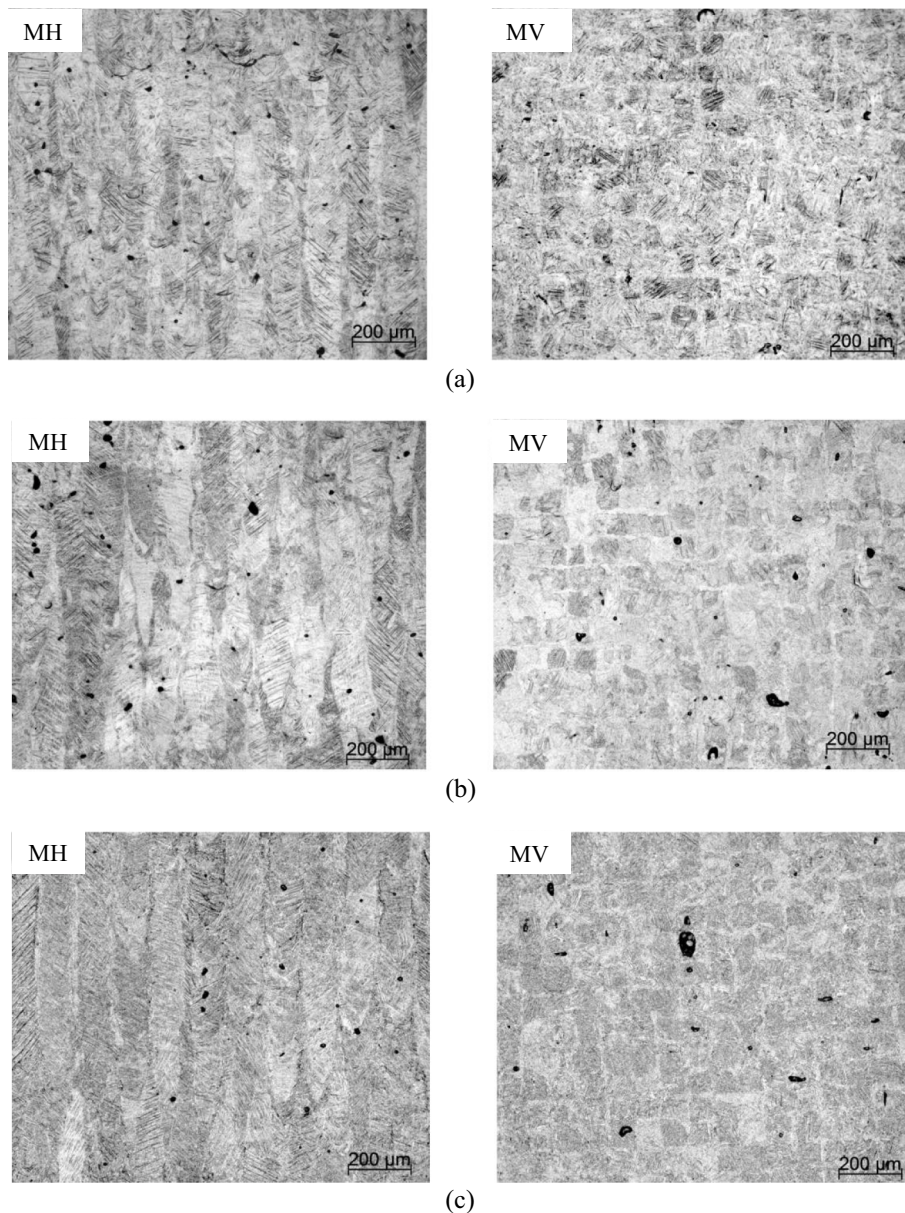


Fig. 6. Optical micrographs of the grains architecture in MH and MV samples: a) non-heat treated, b) stress-relieved and c) annealed.

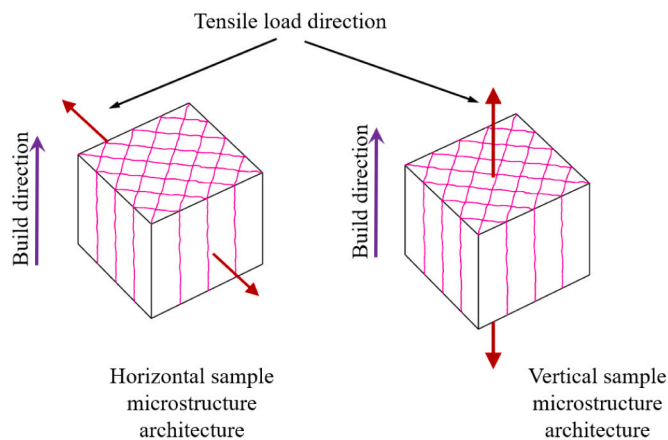


Fig. 7. 3D Schematic of a columnar microstructure in SLM fabricated samples.

micrographs of the samples with higher magnification is required. As the microstructure of the columnar architecture for both MH and MV samples are very similar, only MH metallographic samples are examined under higher magnification, Fig. 9.

Optical and SEM micrographs of non-heat treated samples, Fig. 9a, exhibit the acicular (tiny needle shape) martensitic phase of α' (HCP), which is the result of rapid cooling and diffusionless transforming of the β phase to α' . There is some degree of coarsening of needle shape HCP phase due to the stress-relieving and annealing processes. The width of acicular α' in stress-relieved and annealed samples appears to have increased, as shown in the optical micrographs, the left images of Fig. 9b and c. Also, some new fine particles, (bright spots in the SEM micrographs of Fig. 9b and c), precipitated within the α' matrix, particularly at the lath boundaries.

The EDS examinations of the precipitated bright spots in stress-relieved and annealed samples confirmed them as rich in vanadium. The EDS of a few bright spots in stress-relieved and annealed samples, displayed in Fig. 10, shows that the percentage of vanadium varies from 5.0% to 10.2%, which is above the nominal 4% V in the Ti64 powder. As

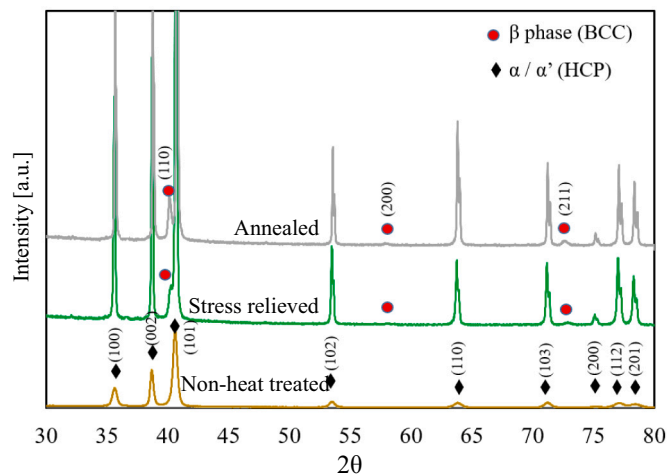


Fig. 8. XRD spectra of three sample sections from differently-treated MH samples.

Table 4

FWHM of the peak of the HCP phase of the samples at 2θ diffraction nearly 40.6° , plane (101).

Sample	non-heat treated	Stress relieved	Annealed
FWHM, ($^\circ$)	0.40	0.12	0.09

the vanadium rich phase in Ti64 alloy is the β phase [37,38], the bright spots in stress-relieved and annealed samples are also β phase, which was earlier confirmed in the XRD spectra, Fig. 8. It should be noted that the scale of the SEM image in Fig. 10a is different from Fig. 10b. Apart from the β phase observed in the stress-relieved and annealed samples, very few white particles are also detectable in the SEM of non-heat treated samples, Fig. 9a. These white particles in the non-heat treated sample could be β phase, which are precipitated from α' when a deposited layer with α' microstructure is reheated by the following deposited layers [20,39], but neither the XRD spectrum nor the EDS analysis confirm the existence of any β phase. However, it does not necessarily mean that there is no β phase in the non-heat treated samples, since the β phase fraction might be below the detection limit of the XRD technique. Thus, it is assumed that the non-heat treated sample is fully composed of the α' martensitic phase.

As seen from the SEM micrographs in Fig. 9b and c, the bright spots' sizes, β phase, are larger but fewer in the annealed sample compared with that of those that are stress-relieved, as has already been reported by other researchers [33]. The β phase in the stress-relieved samples looks like short needle-shaped particles; however, in the annealed samples, they appear to have coarsened, with wider and elongated needles along (α/α') phase boundaries with some globular β particles. The optical micrograph of the annealed sample, Fig. 9c, reveals the lamellar microstructure of α (white laths) with β (in black), alongside some globular α phases (shown with arrows). The prior β boundary, which appears as a coarsened α -lath (displayed with a dash line), confirms the prior β boundaries as the preferred sites for diffusion and phase nucleation during annealing.

The image analysis of SEM micrographs in Fig. 9b and c, exhibits about 4% and 13% of β constituent in stress-relieved and annealed samples respectively. It should be mentioned that, although image analysis is not an accurate method for measurement of the percentages of existing phases with different crystal structures (HCP and BCC) in the microstructure, it can be a good indication for comparing the volume fraction of the β phase existing in stress-relieved and annealed samples. From the equilibrium phase diagram of Ti64 [38], it is expected to observe a 13.7% β phase, which is similar to the image analysis of 13%.

The estimated β content of 4% in stress-relieved samples, which is far less than the expected 13.7% β in equilibrium conditions, confirms that the microstructure of stress-relieved samples still contains the α' phase. This is in good agreement with the FWHM of XRD spectrum in the stress-relieved samples discussed earlier.

Table 5 shows the porosity content of the non-heat treated MH and MV samples measured via optical microscopy using ImageJ software. The average porosity of 0.14% shows that the SLM fabricated samples in this study were nearly fully dense, around 99.85%. There is a small difference between the porosity contents in the two samples that is believed to be due to the build direction.

The arrows in Fig. 11 show the equiaxed and elongated pores observed in non-heat treated MH and MV samples, respectively. The axes of elongated pores in Fig. 11 are aligned with the criss-cross laser vector, i.e., $\pm 45^\circ$, Fig. 2. These elongated pores are associated with a minor lack of fusion either between the adjacent solidified tracks or between the previously-solidified layers.

In addition to porosity defects, there are some anomalies detected within the non-heat treated and stress-relieved test piece. In Fig. 12a, some fish scale features are shown (arrows) in the transverse section of the non-heat treated MH sample. Interestingly, these features cannot be found in the annealed samples.

The fish scale features depict the melt pool boundaries and for that reason, their orientations can identify the build direction. After performing the stress-relieving process, the number of detectable fish scale features decreases, while in annealed samples these features completely disappear. It is important to note that the fish scale phenomenon, which has not been clearly reported or characterised previously, has different morphology to melt pool boundaries reported in some studies [40–43]. Fig. 12b shows a SEM image of the inset in Fig. 12a where this feature appears as an uneven surface topography, possibly caused by different reactions of the material composition of this feature to Kroll's reagent. Fig. 13a displays a portion of the area shown in Fig. 12b but from a different angle viewed in FIB. The arrows in Fig. 13a and b show the platinum deposited path, which has already been represented by a dash line in Fig. 12b, where the cross section is created by Ga ion beam sputtering. Fig. 13b reveals the results of an EDS line scan in different areas: two horizontal lines close to the surface, where platinum has been deposited, and two vertical lines perpendicular to the etched surface. All results have been normalised to remove the element of platinum from the weight percentage analysis of the main elements: titanium, aluminium, and vanadium.

The EDS results of all four lines reveal the fact that the fish scale feature is a result of negative segregation of the melt pool tip, where the aluminium percentage has dropped from its nominal 6% to an average of 3.5%. Thus, the fish scale phenomenon can be described as an HCP α'/α phase with a lack of aluminium. It has already been reported that Ti64 is a material susceptible to composition change during SLM fabrication and that the aluminium in Ti64 is the most volatile element [44].

Fig. 14a reveals some bright areas (shown with arrows) in the optical microscopy of an annealed sample that has similar shapes of melt pool boundaries to the fish scale feature. The inset in Fig. 14a has been displayed with higher magnification in Fig. 14b. The globular and coarse α phase, enclosed in the crescent in Fig. 14b, confirms that the fish scale features in non-heat treated samples act in the same way as the prior β boundaries for any phase nucleation during phase transformation. In other words, fish scale features, because of the negative segregation in their aluminium compositions, are preferred diffusion sites for receiving aluminium atoms and releasing the super-saturated vanadium.

As mentioned in Section 2, apart from the investigation into the anisotropy of mechanical properties for MH and MV samples, the influence of heat treatment on the tensile properties of NMV has also been studied. As the microstructure of an NMV sample is the same as the other samples, the polished metallographic sample of the NMV sample does not require etching, but the outer surface of the NMV sample should be examined.

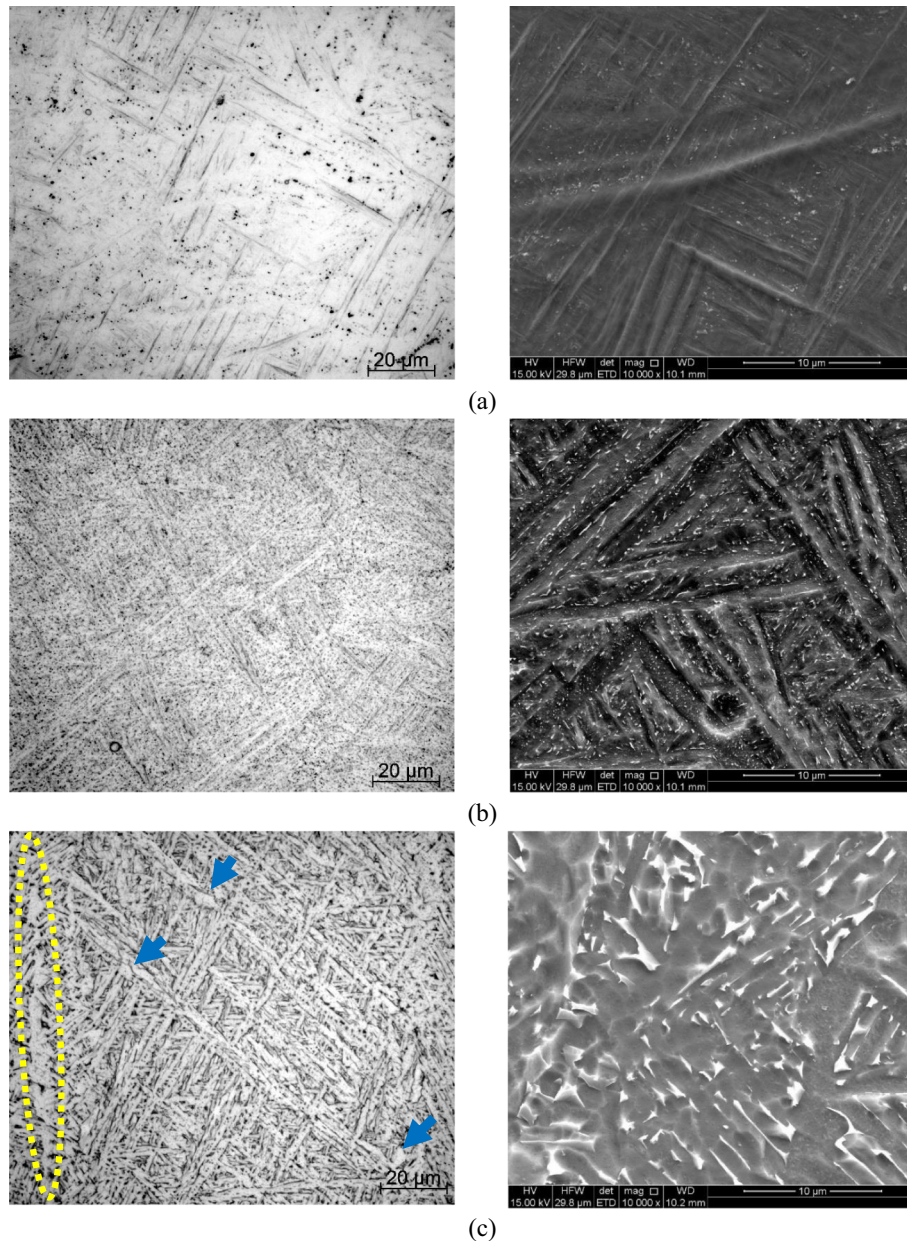


Fig. 9. Optical micrographs (left) and SEM (right images) of MH samples; a) non-heat treated, b) stress-relieved and c) annealed. (Arrows show the globular α phase).

Fig. 15 displays a micrograph of the longitudinal section of the outer surface of an NMV sample in a polished condition. Alongside some sharp valleys, shown with arrows in Fig. 15, two micro-grooves displayed with dash lines are noticeable. These micro-grooves, with their planes perpendicular to the tensile load and 150 μm deep, could influence the mechanical properties of NMV, as discussed in the next section.

3.2. Mechanical properties

Fig. 16 displays the stress-strain graphs for MH and MV samples in three conditions: non-heat treated, stress-relieved, and annealed while the tabulated tensile results are shown in Fig. 17. As seen from Figs. 16 and 17, the two heat treatment procedures of stress-relieving and annealing lower the UTS and YS of both MH and MV samples, compared with non-heat treated samples, while the % elongation of most samples increases after being heat treated. In addition, the Young's modulus shows an increase from non-heat treated samples to annealed ones. The change in the modulus is related to phase changes in the samples during

heat treatment since, in multi-phase Ti64 alloy, the Young's modulus is affected by the moduli of existing phases and their volume fraction in the microstructure [28]. The average UTS of non-heat treated MH and MV samples, which is 1377 MPa, lowers to an average of 1228 MPa after stress-relieving (which is a 11% drop); however, for annealed samples, the average UTS lowers to 1137 MPa, showing a drop of 17%.

Improvement of ductility (which is the increase of elongation and strain at fracture) in an annealed condition for both build orientations is much higher than for stress-relieving treatment. The improvement of ductility in MH is 41% after stress-relieving and 64% after the annealing process. But for MV samples, stress-relieving does not increase the ductility; however, a drastic increase of 170% in the elongation is observed after the annealing process.

The difference in elongation between MH and MV samples in non-heat treated conditions is 125%, while by annealing this difference lowered to 36%. In other words, annealing the properties leads to greater uniformity in the sample, irrespective of build direction. It should also be noted that the elongation of MH samples is always higher

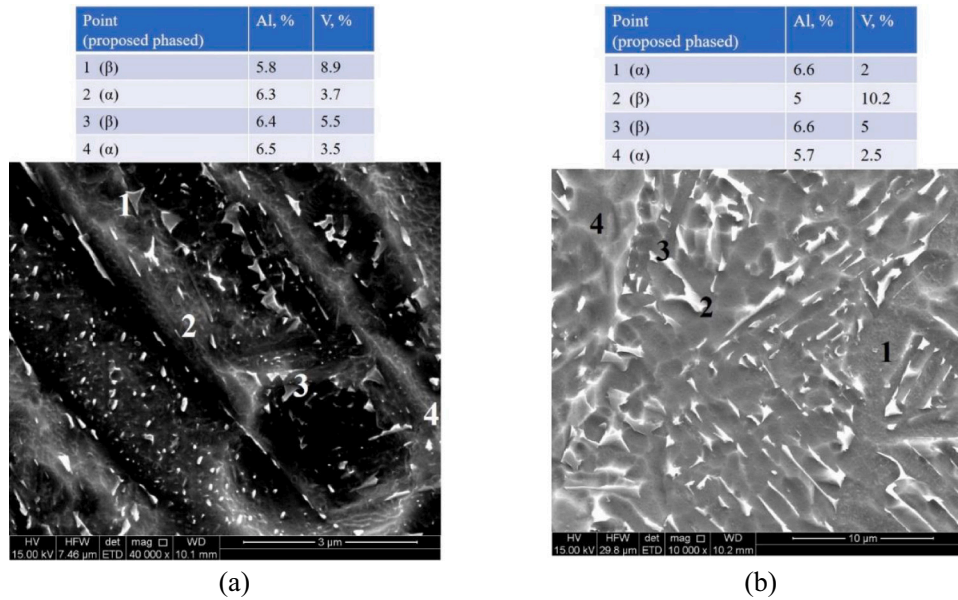


Fig. 10. EDS point analysis of: a) a stress-relieved sample, b) an annealed sample.

Table 5
Porosity content in vertical and horizontal samples.

	Transverse section from MH sample	Transverse section from MV sample	Average
Porosity content, (%)	0.12 ± 0.08	0.16 ± 0.07	0.14 ± 0.07

than that of MV. The difference in YS between MH and MV is 0.19% in an annealed condition and 1.8% in stress-relieved samples, which is negligible compared with the elongation anisotropy revealed from the tensile tests. Thus, this investigation mainly focuses on the effect of heat treatment on the elongation anisotropy observed in MH and MV samples.

Fig. 18 displays the microhardness of the microstructure of each treatment for both verticals and horizontal, showing that the hardness of MH and MV samples in each condition of treatment is nearly the same, with around 3% difference. Fig. 18 shows that the non-heat treated sample with a fully martensitic microstructure has the highest average hardness compared with the lowest hardness, which is related to the annealed sample with fully decomposed α' to α and β phases. The average hardness of stress-relieved samples is in between the hardness of non-heat treated and annealed samples. The average results of microhardness in the samples in Fig. 18 correspond with the UTS of the same samples extracted from tensile tests, Fig. 17. The decrease in mechanical

strength, UTS and YS, after heat treatment processes (which are comparable with their microhardness) are mainly related to the phase transformation from non-heat treated single phase martensite α' with acicular morphology, to β and lamellar α with increased laths size - compared with α' - as observed in stress-relieved and annealed samples.

Since the mechanical properties of titanium alloys are strongly affected by the microstructure which in turn, are influenced by morphology and the sizes of the two phases of β and α , [45,46], any phase transformation of SLM fabricated Ti64 parts during heat treatment explains any changes in the mechanical properties.

While the UTS and YS decrease through these heat treatment processes, the ductility of most samples increases, which is believed to be associated with the plasticity of the $\alpha + \beta$ microstructure [3]. Although the trends of decrease in the hardness of three different samples, Fig. 18, are in good agreement with the decrease of UTS in those samples, the hardness cannot explain the anisotropy of elongation between MV and MH samples. This is due to the nature of the microhardness test, which is static and localized; unable to reveal the effects of defects and their orientations' contribution to elongation.

As discussed in Section 3.1, by performing the heat treating processes, either stress-relieving or annealing, the columnar architecture is preserved but at the same time the prior β boundaries, as the preferred nucleation site for the new α and β phases, may reduce the degree of directionality in annealed samples due to the formation of coarse and semi-equiaxed morphology for the α phase.

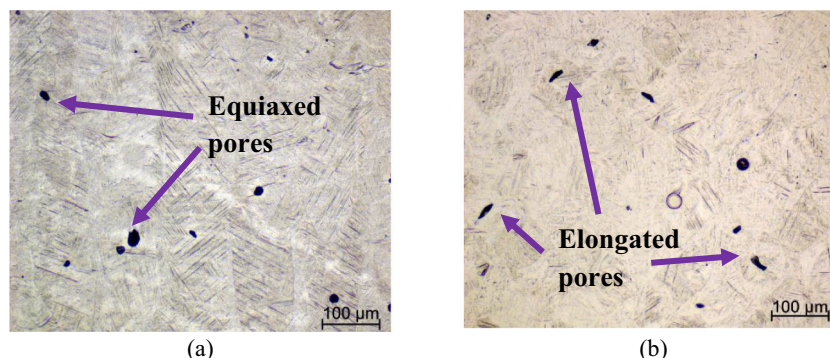


Fig. 11. Optical micrographs of the transverse section of a) MH and b) MV samples.

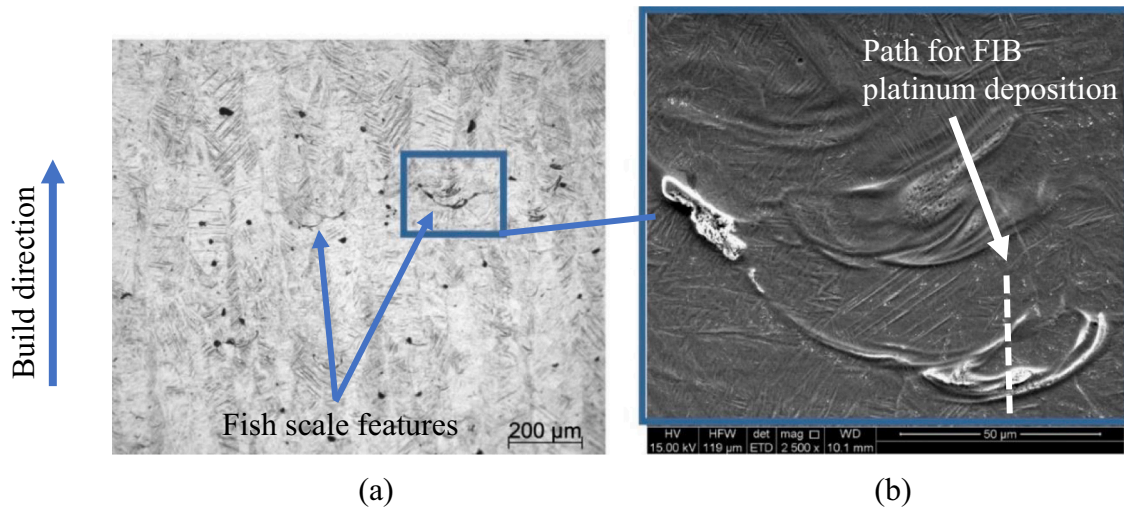


Fig. 12. a) Optical microscopy of a non-heat treated sample, b) the SEM image of inset in the optical microscopy image.

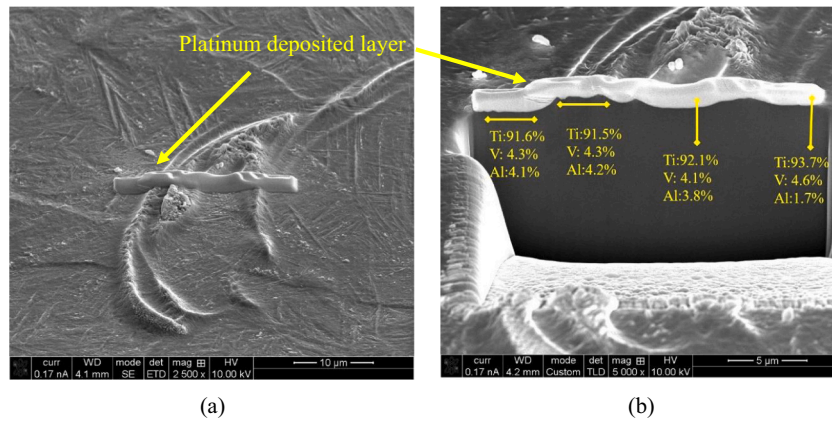


Fig. 13. a) Platinum deposited layer according to the dash line in Fig. 12, as a preparation for sectioning with FIB, b) location of the EDS lines and the average results of each line.

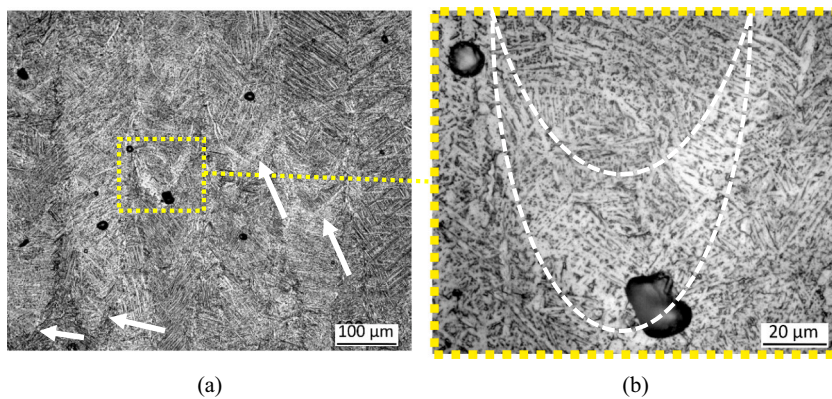


Fig. 14. a) Optical micrograph of columnar grains in an annealed sample and b) the magnified inset with coarse and globular α phase. (Arrows show the melt pool boundaries).

The other factor affecting the elongation anisotropy can be related to the pores' morphologies and their orientations with respect to the loading direction. As discussed in a previous publication [16], the sharp edges of flattened pores in MV samples with tensile load perpendicular to the pores' edges and planes could increase cracking susceptibility in MV samples. The increased cracking susceptibility, along with the

contribution of residual stress, as reported by [47], could be a potential reason for lowering elongation of non-heat treated MV samples, leading to anisotropy in elongation of non-heat treated parts.

In annealed samples, residual stresses are fully released, as the annealing temperature is 850 °C, which is above the temperature recommended for complete stress-relieving, i.e., 730 °C [11,32]. Thus, the

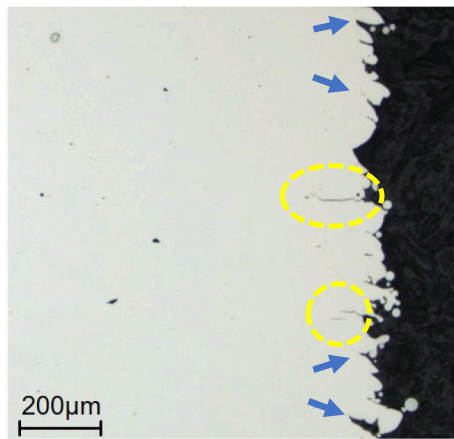


Fig. 15. Optical microscopy of the outer surface of an NMV sample.

improvement in anisotropy of elongation observed in annealed samples is believed to show that the residual stresses on the pores' edges in MV samples are completely removed. In stress-relieved MV samples, the elongation is very similar to the non-heat treated MV, suggesting that the anisotropy in stress-relieved samples does not show any improvement. It is believed that the residual stresses in the stress-relieved samples are not completely released, considering the treatment temperature (670 °C) is below 730 °C. Thus, the remaining residual stress in stress-relieved samples with the contribution of the sharp edges of (elongated) flattened pores is still dominant in keeping the low elongation of verticals. The partial phase transformation in stress-relieved MV appears to be less effective in improving the ductility. Apart from the elongated pores and their flat sharp edges, fish scale features might also be responsible for lower elongation of the MV samples in non-heat treated and stress-relieved samples. It is suggested that the negative segregation and inhomogeneity observed in the fish scale feature could alter the wetting angle of the melt-pool for the already deposited layer, rendering a lack of coherency between the stacked layers. These features can be potential sites for void formation in the fracture of non-heat treated and stress-relieved MV samples, which will be discussed in the

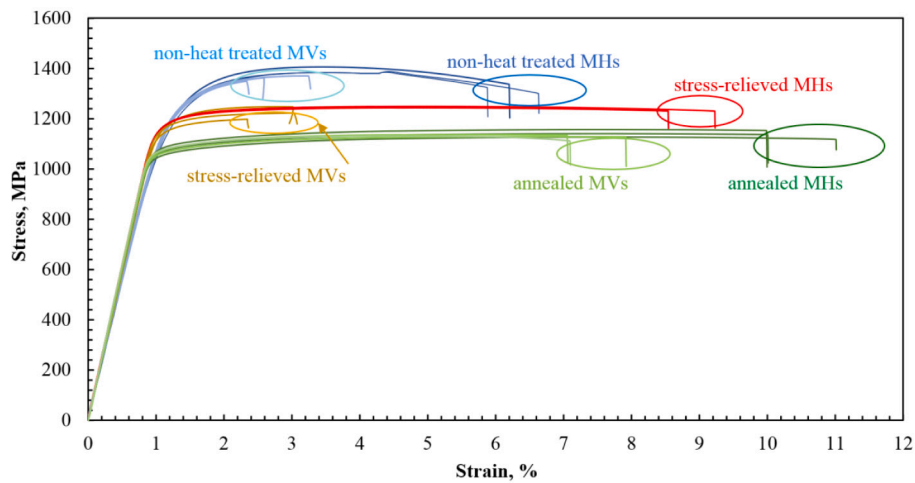


Fig. 16. The stress-strain graphs of MH and MV samples.

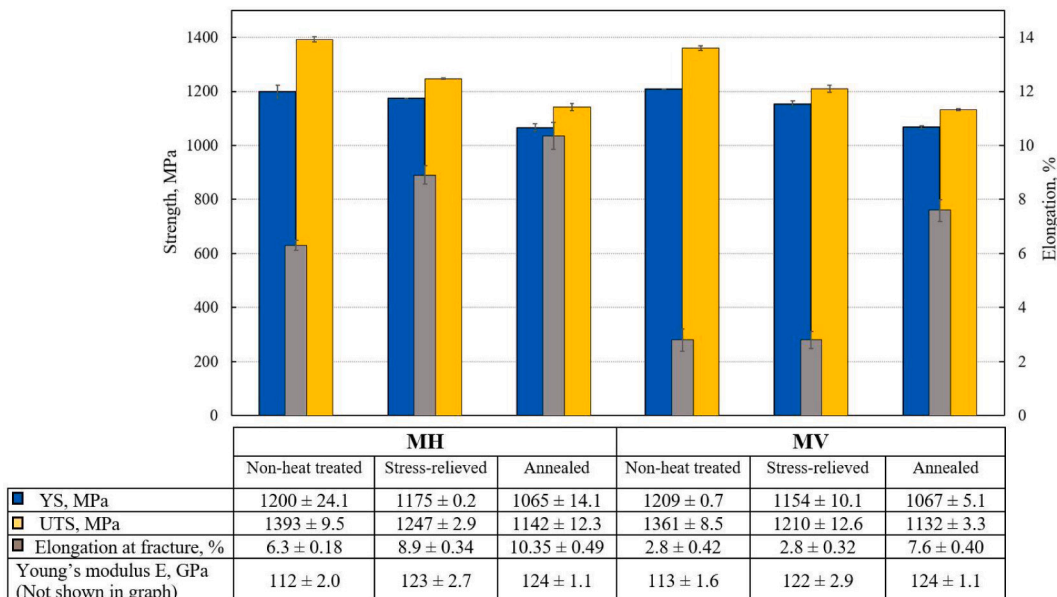


Fig. 17. Tensile properties histogram of all the machined samples. (MH and MV).

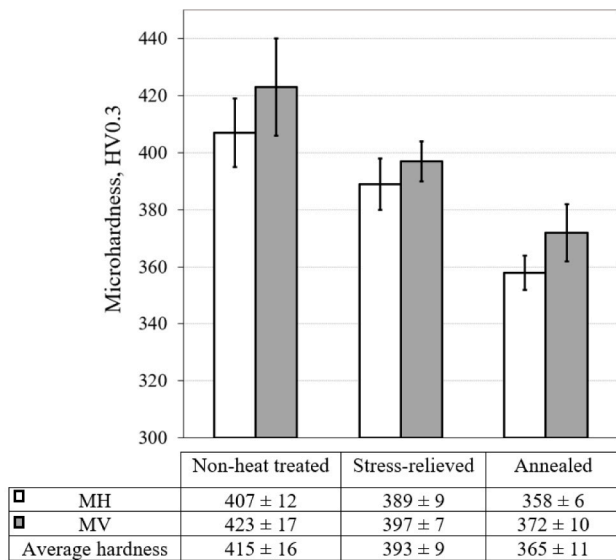


Fig. 18. Measured microhardness of the transverse sections of all samples.

next section.

Fig. 19 shows the stress-strain diagrams of MV and NMV (non-machined vertical) samples under different heat treatments. Generally, NMV, when compared with MV, show lower mechanical properties in terms of their strengths (YS and UTS) and also elongation, as shown in the histogram in Fig. 20a and b. The non-heat treated NMV samples (known as, as-built), suffer from premature failure and they fracture at an average stress of 482 MPa, which is around 35% of the UTS of their machined counterparts, i.e., non-heat treated MV samples. By conducting stress-relieving on NMV samples, all the tensile properties of NMV significantly improve. This confirms that the main reasons for premature failure of non-heat treated NMV is the contribution of sharp valleys and micro grooves on the outer surface and residual tensile stresses (which might be very high on the surface). By removing either the rough surface of NMV (via machining and making MV) or releasing the residual stresses (even partially by stress-relieving), the vertical samples will not suffer from premature failure: see Figs. 19 and 20.

Although the elongation of stress-relieved NMV, which is around 1.7% compared with the non-heat treated NMV (0.5%), shows a good improvement, it is not acceptable in comparison with non-heat treated MV. Annealing the NMV can improve the elongation to 4.0%, compared

with 1.7% in stress-relieved NMV samples. This can be attributed to the fully decomposed α' to α and β in the microstructure and consequently fully releasing the residual stresses in the annealed samples. However, it can be noticed that the outer surfaces of NMV samples play a major role in elongation. The effect of sharp valleys (or micro grooves) in annealed NMV samples, even in the absence of residual stress, is so high that it reduces the elongation to nearly 53% of their annealed MV counterparts. Nevertheless, in some applications, where the shape of components is intricate and machining is not viable, the annealing process can improve the as-built mechanical properties even when the loads are applied along the deposition layers, as for NMV samples.

3.3. Fracture surface analysis

Fig. 21 displays the SEM of the fracture surfaces of all MH samples in this study. As seen from Fig. 21a to c, apart from the shear lip around the periphery of all the samples, the fracture surfaces of non-heat treated and stress-relieved samples are uneven; however, in annealed samples the surface is rather even. Fig. 21d and e, reveal quasi-cleavage features (as reasons for uneven surfaces) and microcracks in non-heat treated and stress-relieved MH samples, suggesting a mixed mode of ductile and brittle fracture. In the annealed sample, Fig. 21f, the quasi-cleavage features cannot be observed, meaning that the annealed MH sample behaves like a ductile material. Also, a qualitative comparison of the dimples in all fracture surfaces, Fig. 21d to f, indicates that in the annealed sample the dimples are larger and more uniform compared with those in the other two samples, which confirms the ductility of the annealed sample is relatively better.

Fig. 22 displays the fracture surfaces of all MH samples sectioned longitudinally along the axis of tensile samples and etched for metallographic examination and analysis of crack paths. Fig. 22a to c display the images of the entire fracture surfaces. As can be seen in the close-up images, Fig. 22d to f, the fracture has generally propagated through the chess board pattern in the MH samples, regardless of the heat treatment conditions, meaning that all MH samples had transgranular fractures. Apart from the very few elongated pores in the microstructure near the fracture surfaces of all samples, Fig. 22d to f, there are no microcracks near the fracture surface, suggesting that the voids' coalescence in MH samples occurred uniformly on the final fracture surface. Also, the chess board pattern has distorted to a diamond shape (with different lengths of diagonals) confirming lateral plastic deformation of the columnar grains.

The SEM micrographs of the fracture surfaces of all MV samples are displayed in Fig. 23. All machined verticals (MV) exhibit a bulk fracture

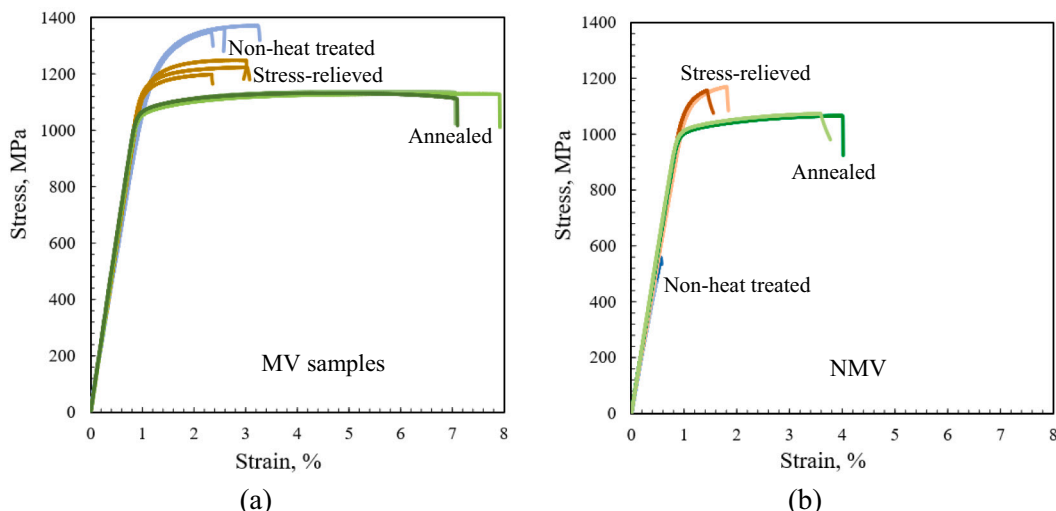


Fig. 19. The stress-strain graphs of non-heat treated, stress-relieved and annealed: a) MV and b) NMV samples.

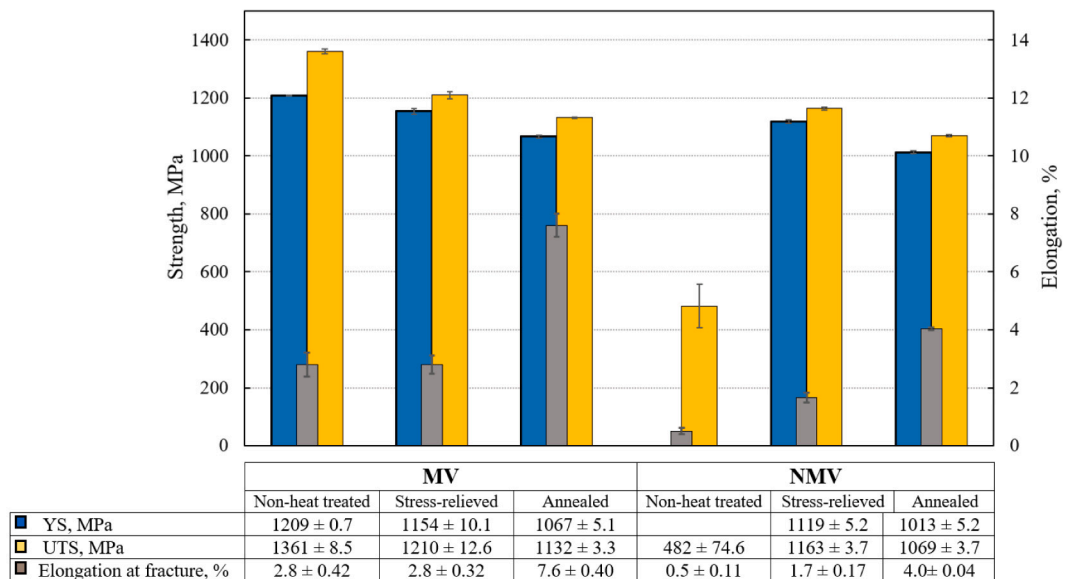


Fig. 20. Tensile properties histogram of all vertical samples.

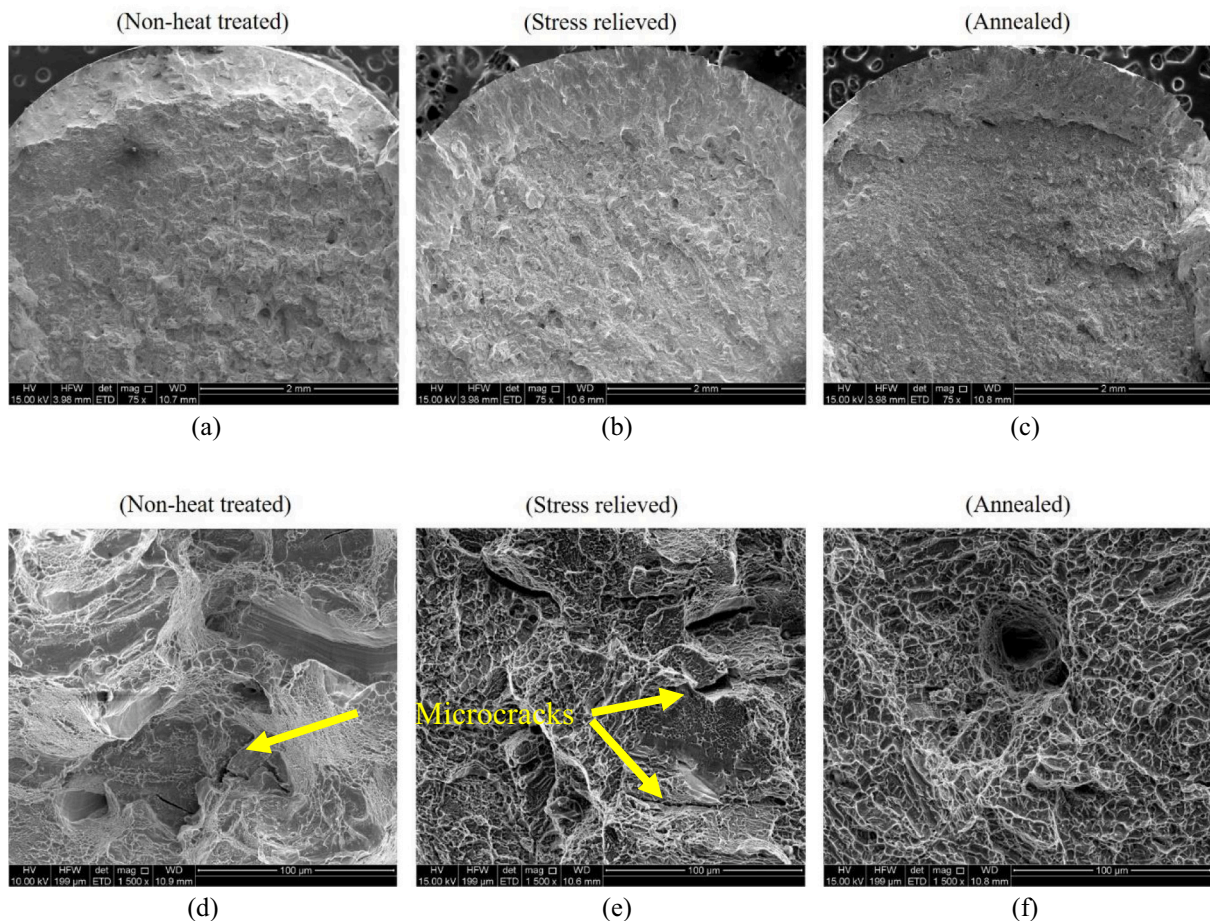


Fig. 21. SEM micrographs of fractured surfaces of MH samples, to show the formation shear lips and fracture topography a) to c) and the formation of dimples at higher magnification as a measure of ductility d) to f).

in the middle due to the coalescence of the voids, which propagate towards the outer surfaces of the samples where the shear lips occur. It should be noticed that the entirety of the shear lips surrounding the fracture surfaces of all MV are not shown in Fig. 23a to c. The fracture

surfaces of non-heat treated and stress-relieved verticals unveil a layered topography in Fig. 23a and b, meaning the cracks initiate on different deposited layers; while propagating they then alternate and connect with each other from one layer to another. The layered topography is not

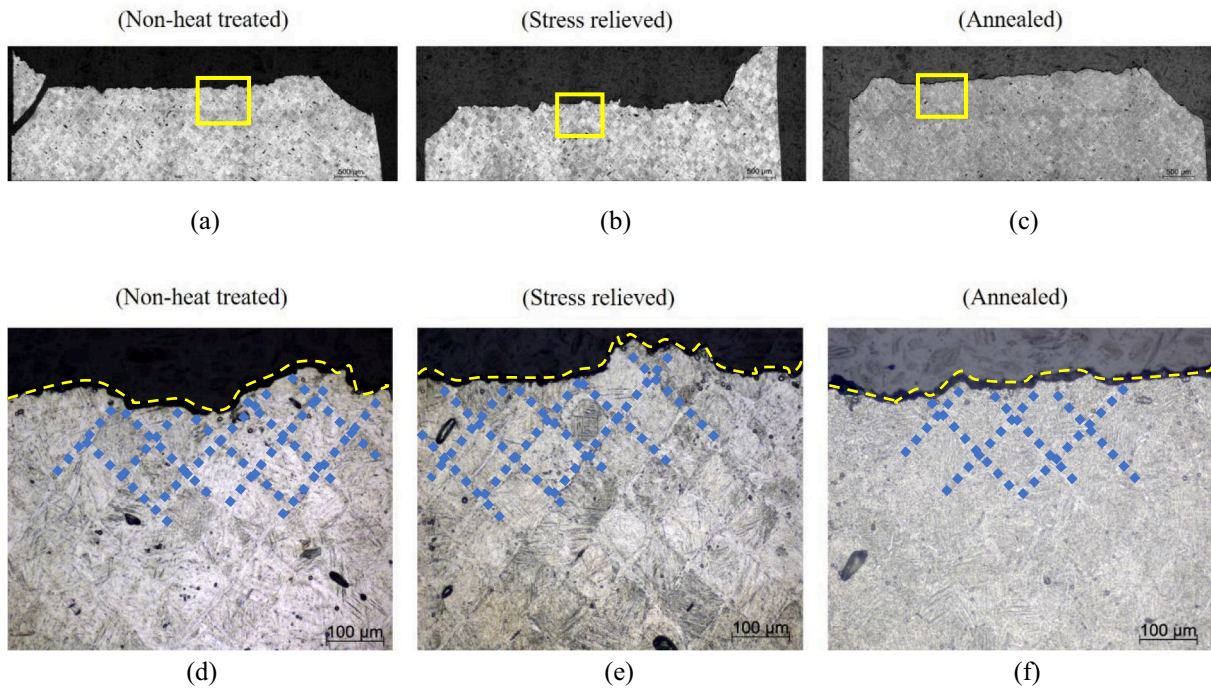


Fig. 22. Optical micrographs of etched fractured surfaces (longitudinally sectioned) of MH samples; a) to c) whole fracture surface with shear lips, d) to f) magnification of corresponding insets in a) to c).

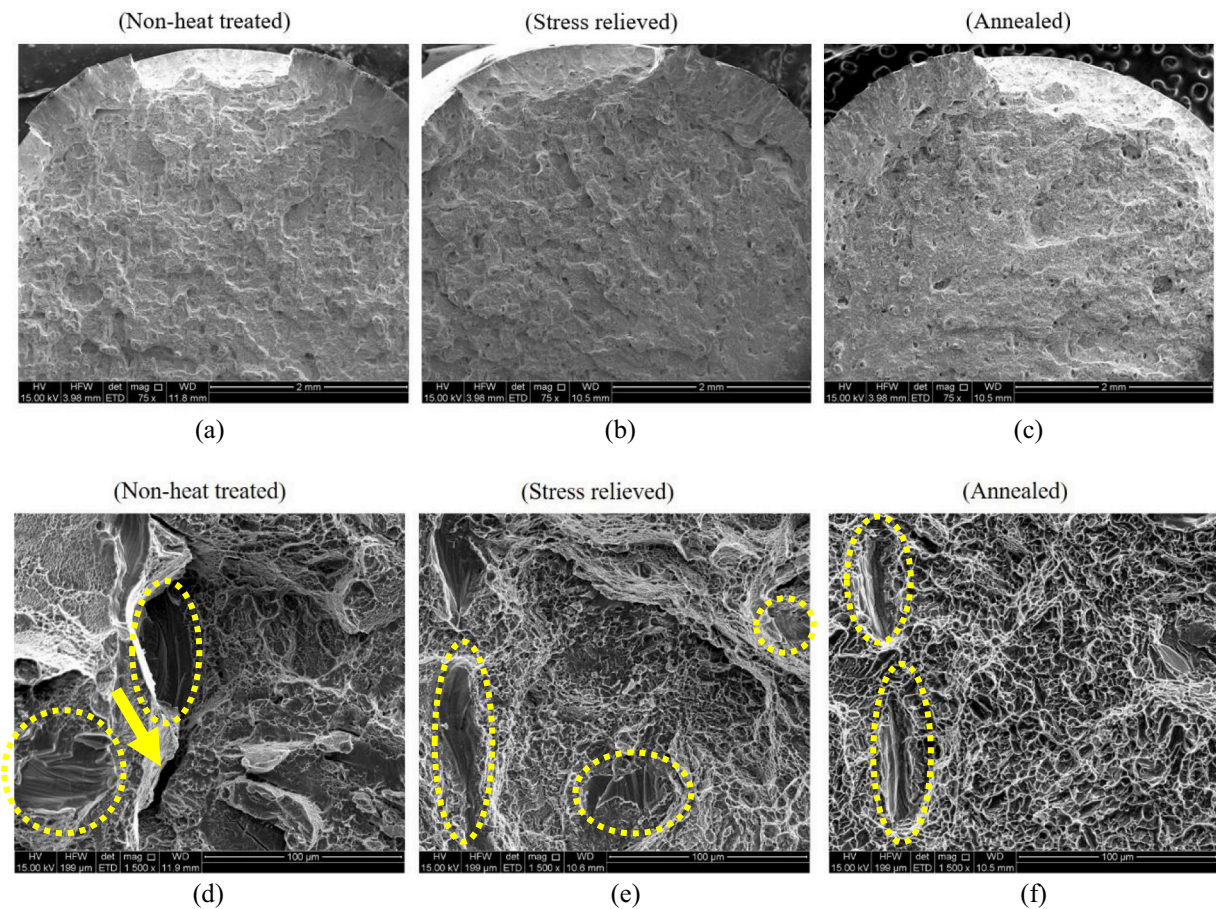


Fig. 23. SEM micrographs of all MV fractured surfaces; a) to c) fracture topography and partial views of shear lips, d) to f) lack of fusions and dimples formation in all samples. (Arrow shows a microcrack in the non-heat treated MV).

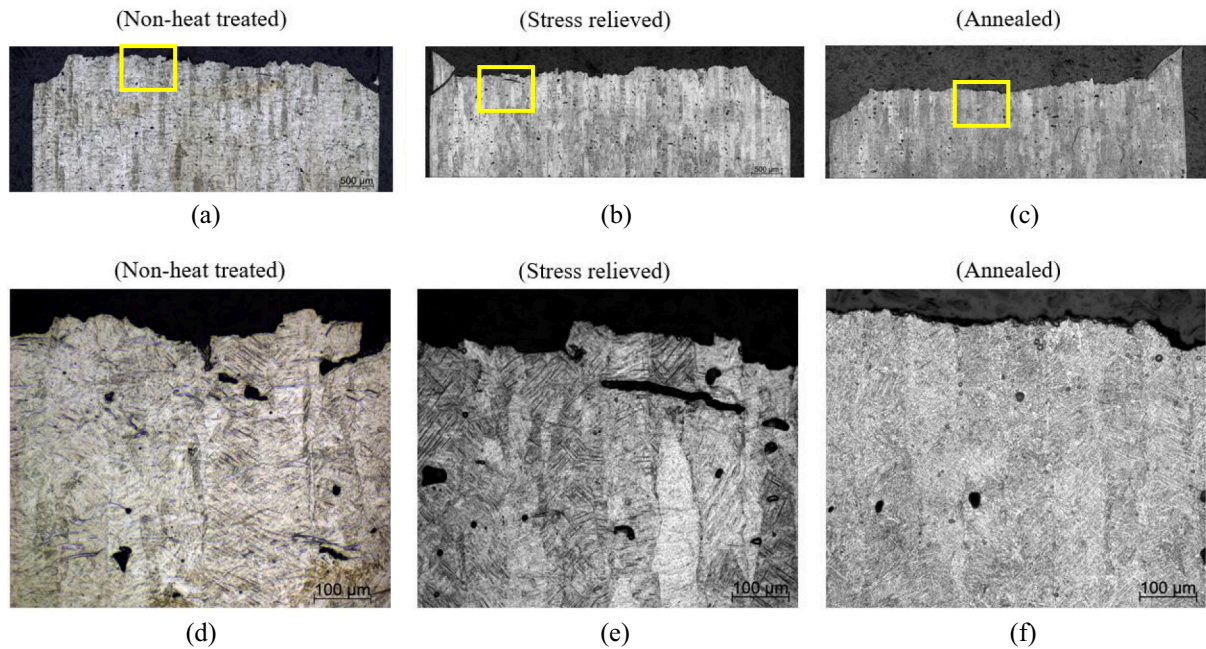


Fig. 24. Optical micrographs of etched fracture surfaces (longitudinally sectioned) of MV samples; a) to c) shear lips seen under magnification 50, d) to f) magnification of corresponding insets in a) to c).

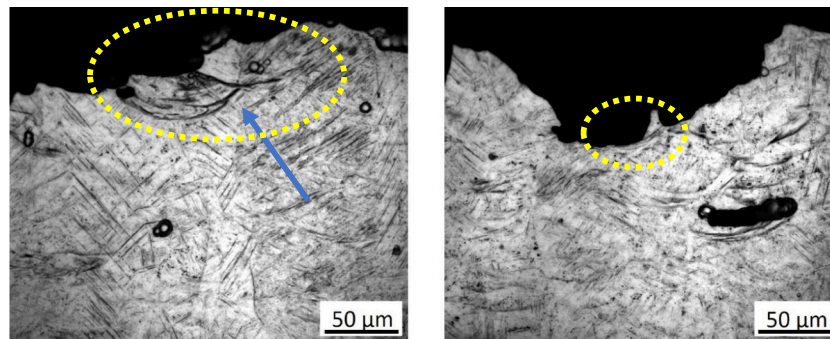


Fig. 25. Two sites of a fractured surface of a non-heat treated MV sample.

dominant in the annealed verticals, compared with the other verticals, explaining the smooth fracture surface in annealed MV samples. The dash lines in Fig. 23d to f show the inter layer voids as a consequence of the lack of fusion observed in all verticals; however, in Fig. 23d an inter-layer void is shown as a crack initiation site, which has connected through a microcrack to the upper fracture surface. Also, the dimples in the annealed MV samples, Fig. 23f, are more regular than for the other MV samples, Fig. 23d and e: indeed they are similar to what was observed in the annealed MH samples.

Fig. 24 displays the optical microscopy of the etched samples longitudinally cut from the fracture surfaces of all MV samples. Fig. 24a to c shows images of the entire fracture surfaces, confirming the uneven surfaces of non-heat treated and stress-relieved MV samples compared with the relatively even fracture surface of the annealed MV. Fig. 24d to f, which contain the corresponding insets to Fig. 24a to c, shows some microcracks developed underneath the fracture surface in non-heat treated and stress-relieved MV samples. The formation of microcracks may explain the lower ductility (% elongation) in non-heat treated and stress-relieved MV samples compared with MH.

Fig. 25 unveils two observed sections of a fractured surface of an MV sample (non-heat treated) in which the crack has propagated through the fish scale features, suggesting that the fish scale features may be the

preferred sites for initial voids' or microcracks' formation.

Thus, the microcracks observed in non-heat treated and stress-relieved MV samples are believed to have originated from flattened pores (as inter-layer voids) between the layers or from a lack of coherency between the stacked layers, which is associated with fish scale features. The effect of flattened pores as a stress riser in vertical samples has already been noticed by others [11,48]; however, the effect of fish scale features as microcrack initiating sites is not yet clear. The drastic improvement in the elongation of verticals during annealing may be attributed to removal of fish scales and complete transformation of α' to $\alpha + \beta$ along with coarsening of lamellar α and β , which are in favour of the higher ductility of annealed verticals. In addition, the release of residual stress could also be instrumental in improving the ductility of annealed verticals.

4. Conclusions

This study reveals that the annealing process presents a uniform elongation and lowers anisotropy on Machined Horizontal and Machined Vertical (MH and MV) samples. Furthermore, annealing results in better properties in Non-Machined Vertical (NMV) samples compared with the machining post process on the non-heat treated

verticals. The detailed conclusions are listed below:

- The annealing increases the elongation of both MH and MV samples; however, the stress-relieving increases the elongation of MH samples alone and does not change the elongation of the MV samples.
- After annealing, the elongation of non-heat treated MV (2.8%) and MH (6.3%) increases to 7.6% and 10.35%, respectively. Therefore, the annealing not only increases the ductility of both MV and MH samples, but also helps to mitigate the anisotropy in ductility. All improvements in mechanical properties, with emphasis on the elongation, are attributed to the phase changes (α' to $\alpha + \beta$) and releasing the SLM process-induced residual stresses.
- The fish scale features, as the sites with low coherency between the stacked layers, can potentially contribute to lowering the elongation of non-heat treated and stress-relieved vertical samples.
- The elongation of 4.0% in annealed NMV compared with the elongation of 2.8% of non-heat treated MV proves that the annealing process is more effective than the machining for improving the elongation of verticals where only one post process can be chosen.
- The results of this study can be applied to improve the mechanical properties of as-built verticals, especially where machining is not feasible, such as intricate parts.

Declaration of competing interest

We wish to confirm that there are no known conflicts of interest associated with this publication

Acknowledgements

This work was undertaken in part at the OptoFab node of the Australian National Fabrication Facility (ANFF), utilizing Commonwealth and South Australian State Government funding. Adelaide Microscopy is gratefully acknowledged for the access provided to their electron microscopy facilities. A. Dareh Baghi is grateful to the Australian Government and Adelaide University for his PhD scholarship.

References

- [1] Xu W, et al. Additive manufacturing of strong and ductile Ti-6Al-4V by selective laser melting via in situ martensite decomposition. *Acta Mater* 2015;85:74–84.
- [2] Attar H, Calin M, Zhang LC, Scudino S, Eckert J. Manufacture by selective laser melting and mechanical behavior of commercially pure titanium. *Mater Sci Eng A* 2014;593:170–7. <https://doi.org/10.1016/j.msea.2013.11.038>.
- [3] D. Banerjee and J. C. Williams, "Perspectives on Titanium Science and Technology," *Acta Materialia*, vol. 61, no. 3, pp. 844–879, 2013/02/01/ 2013, doi: <https://doi.org/10.1016/j.actamat.2012.10.043>.
- [4] L. V. Santos, V. J. Trava-Airoldi, E. J. Corat, J. Nogueira, and N. F. Leite, "DLC cold welding prevention films on a Ti6Al4V alloy for space applications," *Surf Coat Technol*, vol. 200, no. 8, pp. 2587–2593, 2006/01/24/ 2006, doi: <https://doi.org/10.1016/j.surfcoat.2005.08.151>.
- [5] M. Geetha, A. K. Singh, R. Asokamani, and A. K. Gogia, "Ti based biomaterials, the ultimate choice for orthopaedic implants – A review," *Prog Mater Sci*, vol. 54, no. 3, pp. 397–425, 2009/05/01/ 2009, doi: <https://doi.org/10.1016/j.pmatsci.2008.06.004>.
- [6] Murr L, et al. Microstructure and mechanical behavior of Ti-6Al-4V produced by rapid-layer manufacturing, for biomedical applications. *J Mech Behav Biomed Mater* 2009;2(1):20–32.
- [7] Facchini L, Magalini E, Robotti P, Molinari A, Höges S, Wissenbach K. Ductility of a Ti-6Al-4V alloy produced by selective laser melting of prealloyed powders. *Rapid Prototyp J* 2010;16(6):450–9.
- [8] Koike M, et al. Evaluation of titanium alloys fabricated using rapid prototyping technologies—electron beam melting and laser beam melting. *Materials* 2011;4(12):1776–92. <https://doi.org/10.3390/ma4101776>.
- [9] E. Sallica-Leva, A. L. Jardini, and J. B. Fogagnolo, "Microstructure and mechanical behavior of porous Ti-6Al-4V parts obtained by selective laser melting," *J Mech Behav Biomed Mater*, Research Support, Non-U.S. Gov't vol. 26, pp. 98–108, Oct 2013, doi: <https://doi.org/10.1016/j.jmbbm.2013.05.011>.
- [10] Zhang L-C, Attar H. Selective laser melting of titanium alloys and titanium matrix composites for biomedical applications: a review. *Adv Eng Mater* 2016;18(4): 463–75. <https://doi.org/10.1002/adem.201500419>.
- [11] Vilaro T, Colin C, Bartout JD. As-fabricated and heat-treated microstructures of the Ti-6Al-4V alloy processed by selective laser melting. *Metall Micro Trans A* 2011;42(10):3190–9. <https://doi.org/10.1007/s11661-011-0731-y>.
- [12] Rafi HK, Karthik NV, Gong H, Starr TL, Stucker BE. Microstructures and mechanical properties of Ti6Al4V parts fabricated by selective laser melting and electron beam melting. *J Mater Eng Perform* 2013;22(12):3872–83. <https://doi.org/10.1007/s11665-013-0658-0>.
- [13] Sercombe T, Jones N, Day R, Kop A. Heat treatment of Ti-6Al-7Nb components produced by selective laser melting. *Rapid Prototyp J* 2008;14(5):300–4.
- [14] Simonelli M, Tse YY, Tuck C. Effect of the build orientation on the mechanical properties and fracture modes of SLM Ti-6Al-4V. *Mater Sci Eng A* 2014;616:1–11.
- [15] P. Hartunian and M. Eshraghi, "Effect of Build Orientation on the Microstructure and Mechanical Properties of Selective Laser-Melted Ti-6Al-4V Alloy," *J. Manuf. Mater. Proc.*, vol. 2, no. 4, p. 69, 2018.
- [16] A. Dareh Baghi, S. Nafisi, R. Hashemi, H. Eberdorff-Heidepriem, and R. Ghomashchi, "Experimental realisation of build orientation effects on the mechanical properties of truly as-built Ti-6Al-4V SLM parts," *J Manuf Process*, vol. 64, pp. 140–152, 2021/04/01/ 2021, doi: <https://doi.org/10.1016/j.jmapro.2021.01.027>.
- [17] Vrancken B, Thijs L, Kruth J-P, Van Humbeeck J. Heat treatment of Ti6Al4V produced by selective laser melting: microstructure and mechanical properties. *J Alloys Compd* 2012;541:177–85. <https://doi.org/10.1016/j.jallcom.2012.07.022>.
- [18] Khorasani A, Gibson I, Goldberg M, Littlefair G. On the role of different annealing heat treatments on mechanical properties and microstructure of selective laser melted and conventional wrought Ti-6Al-4V. *Rapid Prototyp J* 2017;23:295–304.
- [19] A. M. Khorasani, I. Gibson, A. Ghaderi, and M. I. Mohammed, "Investigation on the effect of heat treatment and process parameters on the tensile behaviour of SLM Ti-6Al-4V parts," *Int J Adv Manuf Technol*, vol. 101, no. 9, pp. 3183–3197, 2019/04/01 2019, doi: <https://doi.org/10.1007/s00170-018-3162-8>.
- [20] E. Chlebus, B. Kuznicka, T. Kurzynowski, and B. Dybala, "Microstructure and mechanical behaviour of Ti-6Al-7Nb alloy produced by selective laser melting," *Mater Charact*, vol. 62, no. 5, pp. 488–495, 2011/05/01/ 2011, doi: <https://doi.org/10.1016/j.matchar.2011.03.006>.
- [21] "https://www.tls-technik.de." (accessed).
- [22] "ASTM F2924-14, Standard Specification for Additive Manufacturing Titanium-6 Aluminium-4 Vanadium with Powder Bed Fusion," 2014.
- [23] "ASTM E8/E8M -16a Standard Test Methods for Tension Testing of Metallic Materials," 2016.
- [24] "SAE AMS 2801B, Heat Treatment of Titanium Alloy Parts (R2014)," 2014.
- [25] B. Wysocki, P. Maj, R. Sitek, J. Buhagiar, K. J. Kurzydowski, and W. Świążkowski, "Laser and electron beam additive manufacturing methods of fabricating titanium bone implants," *Appl Sci*, vol. 7, no. 7, p. 657, 2017.
- [26] Yang J, Yu H, Wang Z, Zeng X. Effect of crystallographic orientation on mechanical anisotropy of selective laser melted Ti-6Al-4V alloy. *Mater Charact* 2017;127: 137–45.
- [27] X. Zhao et al., "Comparison of the microstructures and mechanical properties of Ti-6Al-4V fabricated by selective laser melting and electron beam melting," *Mater Des*, vol. 95, pp. 21–31, 2016/04/05/ 2016, doi: <https://doi.org/10.1016/j.matdes.2015.12.135>.
- [28] A. S. M. International and C. Handbook, "ASM handbook. Vol. 4, Vol. 4," (in English), 1991. [Online]. Available: <http://products.asminternational.org/hbk/do/navigate?navOn=true&src=/content/V04/D00/A01/index.html>.
- [29] Kubiak K, Sieniawski J. Development of the microstructure and fatigue strength of two phase titanium alloys in the processes of forging and heat treatment. *J Mater Process Technol* 1998;78(1–3):117–21.
- [30] M. T. Jovanović, S. Tadić, S. Zec, Z. Mišković, and I. Bobić, "The effect of annealing temperatures and cooling rates on microstructure and mechanical properties of investment cast Ti-6Al-4V alloy," *Mater Des*, vol. 27, no. 3, pp. 192–199, 2006/01/01/ 2006, doi: <https://doi.org/10.1016/j.matdes.2004.10.017>.
- [31] S. Malinov, W. Sha, Z. Guo, C. C. Tang, and A. E. Long, "Synchrotron X-ray diffraction study of the phase transformations in titanium alloys," *Mater Charact*, vol. 48, no. 4, pp. 279–295, 2002/06/01/ 2002, doi: [https://doi.org/10.1016/S1044-5803\(02\)00286-3](https://doi.org/10.1016/S1044-5803(02)00286-3).
- [32] Thöne M, Leuders S, Riemer A, Tröster T, Richard HA. Influence of heat-treatment on selective laser Melting products-e.g. Ti6Al4V. 2012.
- [33] E. Sallica-Leva, R. Caram, A. L. Jardini, and J. B. Fogagnolo, "Ductility improvement due to martensite α' decomposition in porous Ti-6Al-4V parts produced by selective laser melting for orthopedic implants," *J Mech Behav Biomed Mater*, vol. 54, pp. 149–158, 2016/02/01/ 2016, doi: <https://doi.org/10.1016/j.jmbbm.2015.09.020>.
- [34] Cullity B. Element of X-ray diffraction, Addison-Wesley Reading, MA Google Scholar. 1978.
- [35] F. J. Gil, M. P. Ginebra, J. M. Manero, and J. A. Planell, "Formation of α' -Widmanstätten structure: effects of grain size and cooling rate on the Widmanstätten morphologies and on the mechanical properties in Ti6Al4V alloy," *J Alloys Compd*, vol. 329, no. 1, pp. 142–152, 2001/11/14/ 2001, doi: [https://doi.org/10.1016/S0925-8388\(01\)01571-7](https://doi.org/10.1016/S0925-8388(01)01571-7).
- [36] Mur FG, Rodriguez D, Planell J. Influence of tempering temperature and time on the α' -Ti-6Al-4V martensite. *J Alloys Compd* 1996;234(2):287–9.
- [37] Molchanova EK. Phase diagrams of titanium alloys. Israel Program for Scientific Translations. 1965.
- [38] M. Peters, J. Hemptenmacher, J. Kumpfert, and C. Leyens, "Structure and Properties of Titanium and Titanium Alloys," in *Titanium and Titanium Alloys*: Wiley-VCH Verlag GmbH & Co. KGaA, 2005, pp. 1–36.
- [39] Agius D, Kourousis KI, Wallbrink C, Song T. Cyclic plasticity and microstructure of as-built SLM Ti-6Al-4V: the effect of build orientation. *Mater Sci Eng A* 2017;701: 85–100.

- [40] I. Yadroitsev, P. Krakhmalev, and I. Yadroitsava, "Selective laser melting of Ti6Al4V alloy for biomedical applications: Temperature monitoring and microstructural evolution," *J Alloys Compd*, vol. 583, pp. 404–409, 2014/01/15/2014, doi: <https://doi.org/10.1016/j.jallcom.2013.08.183>.
- [41] Gong H, Rafi K, Gu H, Starr T, Stucker B. Analysis of defect generation in Ti-6Al-4V parts made using powder bed fusion additive manufacturing processes. *Addit Manuf* 2014;1-4:87–98. <https://doi.org/10.1016/j.addma.2014.08.002>.
- [42] Yang J, et al. Role of molten pool mode on formability, microstructure and mechanical properties of selective laser melted Ti-6Al-4V alloy. *Mater Des* 2016; 110:558–70.
- [43] Yasa E, Kruth JP. Microstructural investigation of selective laser melting 316L stainless steel parts exposed to laser re-melting. *Procedia Eng* 2011;19:389–95. <https://doi.org/10.1016/j.proeng.2011.11.130>.
- [44] Mukherjee T, Zuback JS, De A, DebRoy T. Printability of alloys for additive manufacturing. *Sci Rep* 2016;6:19717. <https://doi.org/10.1038/srep19717>.
- [45] "Titanium Alloys," in *Handbook of Advanced Materials*, 2004, ch. 8, pp. 271–319.
- [46] F. Froes, "Titanium alloys," *Handbook of advanced materials*, p. 271, 2004.
- [47] Moletsane M, Krakhmalev P, Kazantseva N, Du Plessis A, Yadroitsava I, Yadroitsev I. Tensile properties and microstructure of direct metal laser-sintered Ti6AL4V (ELI) alloy. *S Afr J Ind Eng* 2016;27(3):110–21.
- [48] Rafi HK, Starr TL, Stucker BE. A comparison of the tensile, fatigue, and fracture behavior of Ti-6Al-4V and 15-5 PH stainless steel parts made by selective laser melting. *Int J Adv Manuf Technol* 2013;69(5-8):1299–309. <https://doi.org/10.1007/s00170-013-5106-7>.

**Appendix B: Papers not presented in this
thesis**



Nano-mechanical Characterization of SLM-Fabricated Ti6Al4V Alloy: Etching and Precision

Alireza Dareh Baghi¹ · Reza Ghomashchi¹ · Reza H. Oskouei² · Heike Ebendorff-Heidepriem³

Received: 17 April 2019 / Revised: 13 September 2019 / Accepted: 15 September 2019
© ASM International 2019

Abstract

In this research, we are reporting that the nanoindentation results vary between etched and unetched SLM-fabricated titanium alloy (Ti6Al4V) in spite of the same microhardness values. The dimensionless roughness parameter α , as a metric for the sensitivity of nano-hardness values on the surface roughness, is used to highlight whether etching plays any role. Although the value of α for both samples is below the recommended maximum value, the effect of etching is still significant. The hypothesis for a 19% increase in nano-hardness of etched samples is also discussed in this paper. Furthermore, the maximum proposed value of α ($\alpha < 0.05$) appeared to be invalid for SLM-fabricated titanium and a lower value of α may need to be proposed as a critical value.

Keywords Nanoindentation · Microindentation · Titanium alloys · Selective laser melting (SLM)

Introduction

Indentation techniques, as a non-destructive testing procedure, have been used for decades to characterize the mechanical properties of metals within both industry and academia alike. By introducing new technologies, the concept of indentation instrumentation has been refined to enable more in-depth analysis of the materials' mechanical properties through nanoindentation. They have facilitated researchers' capacity to quantify the hardness and modulus of elasticity through an analysis of the load (F) versus the penetration depth (h_p) of the indenter tip [1]. In nanoindentation techniques, the materials usually experience an elastic–plastic deformation during the loading of the indenter, followed by elastic deformation during unloading. The nanoindentation application can now be expanded to measure fracture

toughness [2, 3], Poisson's ratio [4], and residual stresses [5–7]. Nanoindentation is used in conjunction with microscopy to identify the phases of interest for localized characterization of mechanical properties [8]. However, for the selection of a specific micro-constituent, the clarity of the phase boundary upon which the indenter is impressed is a challenge for unetched samples.

To reveal the actual microstructure and differentiate between the phases and grains, it is common practice to etch the polished metallographic samples. However, since the etching process may cause some changes to the surface topography, especially near the grain and phase boundaries, it has become critical to understand the effect of etching on the accuracy of phase characterization via nanoindentation. The influence of sample preparation and the importance of the surface finish in terms of the nanoindentation results have been reported by a number of researchers [9–11].

It is clear that if the nanoindentation is performed after polishing and before etching (which is common and recommended), the validity of the results is higher and more reliable. Problems arise when the indentation marks disappear after etching. Thus, the nanoindentation might be conducted after etching, which is a challenge because of possible changes to the accuracy of the results. It should be mentioned that light etching is inevitable during chemical–mechanical polishing processes in some cases. For the above reasons, the effect of etching on the accuracy

✉ Alireza Dareh Baghi
alireza.darehbaghi@adelaide.edu.au;
a.darehbaghi@yahoo.com.au

¹ School of Mechanical Engineering, University of Adelaide, Adelaide, Australia

² College of Science and Engineering, Flinders University, Adelaide, Australia

³ Institute for Photonics and Advanced Sensing, School of Physical Sciences, University of Adelaide, Adelaide, Australia

Table 1 SLM process parameters used for fabrication of Ti64 specimens

Laser power, P , W	Laser spot size, w_0 , μm	Scanning velocity, v , mm/s	Layer thickness, t , μm	Hatch spacing, h , μm
270	70	1800	30	85

of nanoindentation results has become an important issue that warrants investigation. A review of the open literature confirms that the influence of etching on nanoindentation results, the focus of this work, has not been studied previously.

This is the theme of the current research, where we endeavor to highlight the effect of etching on the mechanical characterization of selective laser melting (SLM) of a powder bed, 3D printed, Ti6Al4V (Ti64) using nanoindentation. SLM-fabricated Ti64 parts are composed of single-phase grains, and therefore, any variation in the nanoindentation results cannot be attributed to changes in the constituent grains. In other words, SLM-fabricated Ti64 samples are suitable for this investigation. In this report, it will be discussed why the hardness of etched samples of SLM-fabricated titanium is higher than the unetched ones and that the increase of hardness is associated to the geometry of the surface asperities.

Experimental Procedures

Sample Preparation

A cylindrical sample, 10 mm diameter and 15 mm long, was fabricated horizontally using a ProX DMP 200 selective laser melting (SLM) machine. The SLM process parameters are summarized in Table 1. The cylinder was sectioned transversally by means of a diamond cutting saw to prepare two equal disks, 7.4 mm thick. This ensures that the two samples have a similar microstructure. Both samples were prepared for metallographic analysis employing a conventional method, with a fine final polishing of 0.04 μm colloidal silica for 25 min on a Tegramin-25 polishing machine (Struers). A microstructural analysis was carried out on a Zeiss optical microscope and an FEI Quanta 450 FEG-SEM in secondary electron mode, with an accelerating voltage of 20 kV.

Etching the metallographic samples reveals that the microstructure of SLM-fabricated Ti6Al4V samples is composed of columnar grains containing fine needle-shaped martensitic α' phase, Fig. 1, as also reported by others [12–14]. The basic principles of additive manufacturing techniques and the mechanics of the SLM process are widely available in the open literature [15, 16].

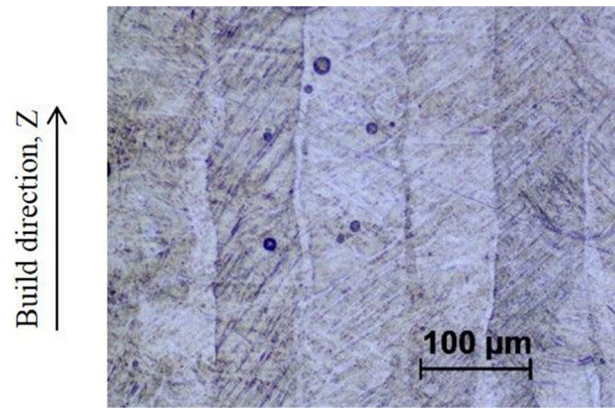


Fig. 1 Optical micrograph of the etched (4% HF, 5% HNO₃, 91% H₂O) SLM-fabricated Ti6Al4V to show the formation of the columnar structure containing fine needle-shaped martensitic (α') phase

One set of samples was left in the as-polished (unetched) condition and the other was etched with Kroll's reagent for 25 s. The light etching was designed to minimize the effect of the etchant on the surface topography and nano-scale asperities, while revealing the microstructure. Kroll's reagent contains 4% HF (48% concentration), 5% HNO₃ (70% concentration), and 91% distilled water.

Microhardness and Nanoindentation Tests

Prior to nanoindentation tests, Vickers' microhardness measurements were performed on both the etched and unetched samples using an automatic microhardness tester, LECO LM700AT. A load of 500gr with a dwelling time of 10 s was chosen for all the measurements. Six indents were taken for each sample and the average values are presented as the microhardness.

The nanoindentation testing was performed using a Fischer-Cripps IBIS nanoindentation system, with a three-sided Berkovich indenter and IBIS software. The indentation straight line map, consisting of 23 indents with a 10 μm space between the center of the indents, was impressed in both the etched and unetched samples, perpendicular to the SLM build direction Z, so as to cover at least two columnar grains (Fig. 1) with a total path length of 220 μm . The tests were conducted at a constant penetration depth of 600 nm for all the points. To analyze the surface roughness of the etched and unetched samples, the surface profiles of both samples were captured using a Veeco Contour GT-K1 optical surface-profiling system and Vision64 analysis software. The etched sample surface with three selected nanoindentations was also examined with a laser confocal microscope, Olympus LEXT OLS5000. Figures 2 and 3 shows the SEM micrographs of the areas in which the nanoindentation tests were conducted for the unetched and etched samples, respectively.

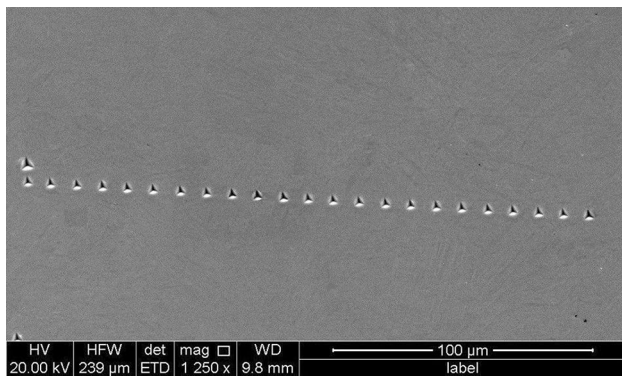


Fig. 2 SEM micrograph of nano-indents on an unetched SLM-fabricated Ti6Al4V sample

Results and Discussion

The Vickers’ microhardness and nano-hardness results are summarized in Table 2. It is clear that the microhardness measurements are almost the same, confirming that etching

does not have any effect on the hardness value if tested in microscale. In contrast with the microhardness values, Table 2, there is a significant change between the nano-hardness values of the etched and unetched samples.

During the etching process of a Ti64 alloy, the chemical reaction expected to take place between the reagent and titanium is given as Eq 1, and the chemical products are NO₂ gas and hydrofluotitanic acid [17]; neither product deposits nor bonds with the surface of the sample. In addition, the etched sample was thoroughly washed, cleaned, and dried with hot air. In other words, the deviation in the nano-hardness of the etched sample is not related to the formation of any new phases or products on the surface. Figure 4 shows the graphs of load, (*P*), versus penetration depth, (*h_i*), of the nanoindenter during the loading and unloading stages for all the 23 indentations conducted for the etched and unetched samples. When the load vs penetration depth distributions, Fig. 4, are compared for all the samples, it becomes obvious that the etched sample has a much wider distribution than the unetched samples. The etched samples also show higher

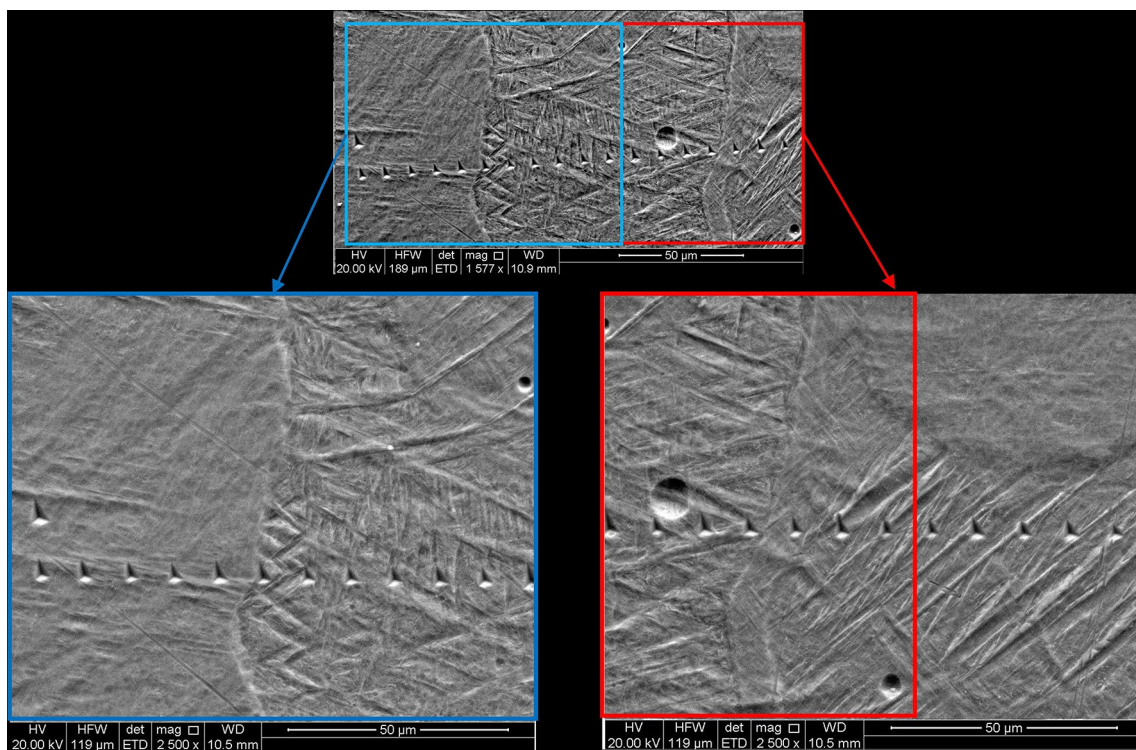


Fig. 3 SEM micrograph of the etched sample after indentation

Table 2 Vickers microhardness and nano-hardness of etched and non-etched samples

Samples	Vickers microhardness, HV	Coefficient of variation for microhardness, %	Nano-hardness, HV	Coefficient of variation for nano-hardness, %
Unetched sample	389 ± 9.0	2.3	532 ± 15.0	2.74
Etched sample	390 ± 7.0	1.8	633 ± 95.0	14.96

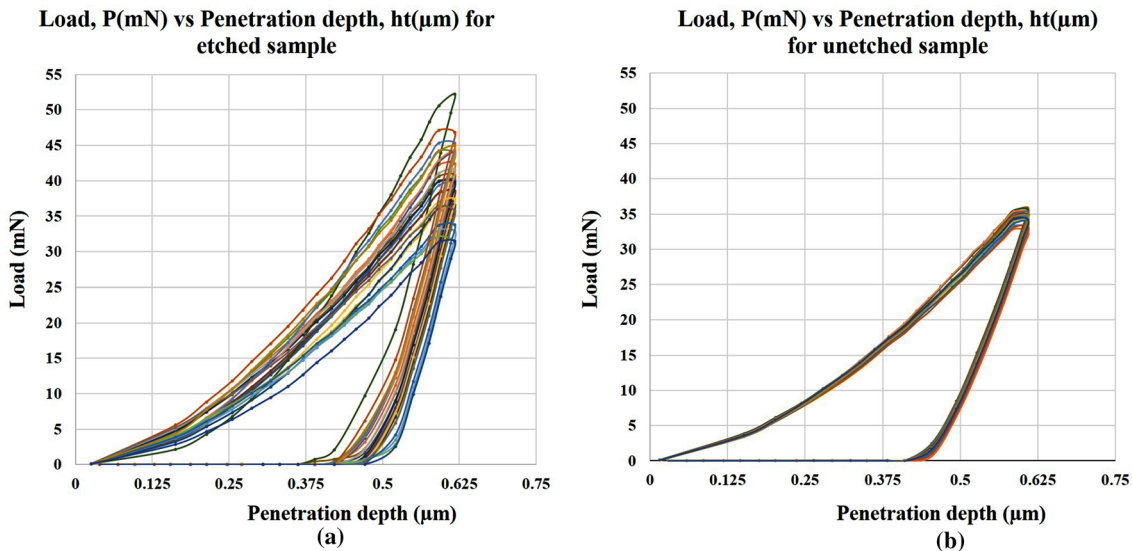


Fig. 4 Loading and unloading indentation curves of: (a) an etched sample, and (b) an unetched sample

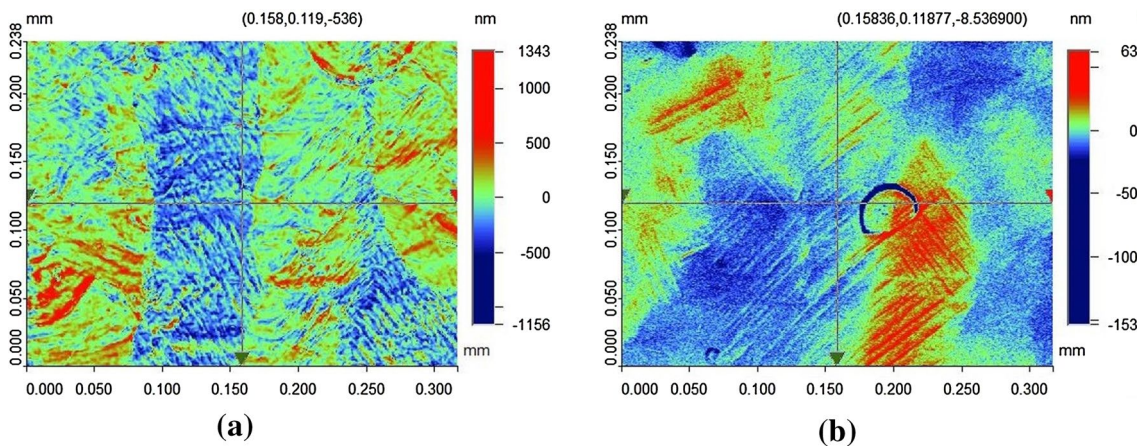


Fig. 5 Typical 2D surface profile of: (a) an etched sample, and (b) an unetched sample

values of hardness than the unetched samples, which will be discussed later.

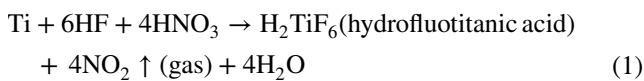


Figure 5 displays the surface profile of one of the randomly selected areas of each sample, while Table 3 shows the quantitative roughness values and the comparison between the etched and unetched samples.

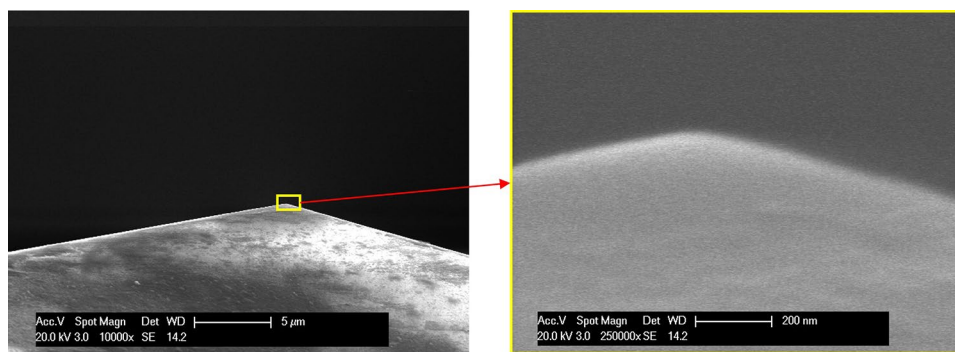
The mean roughness (S_a) of the etched sample is approximately twenty times greater than that of the unetched sample, showing that the unetched surface is much smoother than the etched surface. The surface mean roughness of the unetched sample is only 1.25% of the 600 nm indentation

Table 3 Roughness of etched and unetched samples measured by optical surface-profiling system

Samples	S_a , nm	Coefficient of variation, %
Unetched sample	7.5 ± 0.8	11.5
Etched sample	145.8 ± 8.9	6.1

depth, while, for the etched sample, it is 24%. This means that the absolute value of mean roughness by itself cannot be a criterion for the validity of the hardness measured by nanoindentation and the depth of penetration needs to be accounted for. For this reason, another system of

Fig. 6 SEM image of a three-sided Berkovich indenter tip



measurement is required, in which the penetration of the indentation can be considered.

Johnson [18] quantifies the surface roughness by a dimensionless parameter α defined as Eq 2:

$$\alpha = \frac{\sigma_s R}{a_0^2} \quad (2)$$

where σ_s is the standard deviation (or root-mean-square) of the asperity heights, R is the indenter radius, and a_0 is the contact radius that would be obtained for a smooth surface (i.e., an unetched sample surface) under the same load P . By introducing a_0 in Eq 2, the depth of penetration is included indirectly in the measurement. The value of α actually represents the significance of the effect of the surface roughness on the hardness measurement. A low value of α means that the effect of roughness is insignificant which leads to a valid outcome. As the depth of penetration increases beyond the surface roughness, the indenter is in direct contact with the actual bulk material and not just the asperities. Therefore, a deeper indentation provides a true indication of the hardness of the bulk material. It has been found by Johnson [18] that the effect of surface roughness on the validity of elastic contact equations becomes significant when $\alpha > 0.05$. Their findings are based on the theory of contact mechanics, Hertz theory, which has been developed for the cases where the contact surfaces are not smooth.

The calculated values of α for both etched and unetched samples in the nanoindentation tests are 0.016 and 0.0008, respectively. Although α for an etched sample is higher than the value for an unetched sample, it is still lower than the proposed critical value of 0.05. Despite having a value of $\alpha < 0.05$, the hardness and the coefficient variation of an etched sample are significantly different from those of unetched sample. This means that the proposed magnitude of α , below 0.05 for the evaluation of nanoindentation results, is not valid for SLM-fabricated titanium parts.

In order to calculate the value of α , σ_s for a Gaussian random profile needs to be derived from Eq 3.

$$\sigma_s = \left(\frac{\pi}{2}\right)^{\frac{1}{2}} S_a \quad (3)$$

By substituting the values of S_a (which can be taken from Table 3) into Eq 3, the corresponding σ_s values for the etched and unetched samples are 182.7 nm and 9.4 nm, respectively.

The tip radius of the Berkovich indenter was determined from three different SEM images of the indenter tip at various magnifications. The radius R was estimated by measuring the radius of a fitted arc on the SEM image of the indenter tip using standard geometric modeling software (i.e., AutoCAD). The SEM micrographs in Fig. 6 show the tip geometry of the Berkovich indenter. The value of 150 nm measured for the nanoindenter tip radius, R , is substituted in Eq 2. The contact radius of the penetrated Berkovich nanoindenter, a_0 , on the smooth surface, is assumed to be the radius of a fitted circle inside the impressed triangle mark. The value of a_0 for the nanoindentation in this study is therefore the radius of a circle fitted inside the equilateral triangle impressed mark, Fig. 8, which is calculated to be 1300 nm.

The microhardness Vickers tester, by contrast, has a square-based pyramid indenter and forms a diamond shape indentation on the surface. Figure 7 shows the optical image of the Vickers indentations under the microscope of the Vickers microhardness tester. Using the same Eq 2 for the microhardness indentation, the value of α is calculated as 0.002 and 0.0001 for the etched and unetched samples, respectively. The value of a_0 for the Vickers pyramid indentation is assumed to be the radius of a fitted circle inside the diamond shape impressed indentation (Fig. 7) which is calculated to be 17,000 nm.

The tip radius of indenter R , 3000 nm, is calculated geometrically by measuring the diagonal of a small indentation under a 5 gr applied load. Both values of α for the etched and unetched for microhardness indentations are far lower than the proposed α ; i.e., 0.05. The proposed criterion ($\alpha < 0.05$) appears to be applicable for microhardness results where the surface roughness changes due to the etching process, which has been shown not to induce microhardness changes. This is not the case for the nanoindentation results, where there is a significant change in the etched sample hardness, which has a wider distribution in spite of having α values below 0.05.

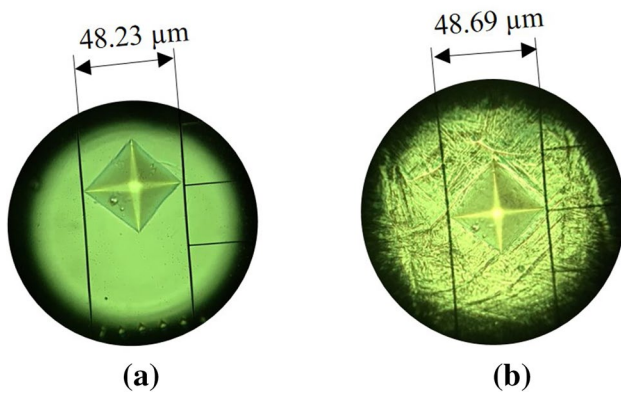


Fig. 7 Optical images of the diamond shape indentations made by Vickers pyramid indenter on the surface of (a) unetched sample, and (b) etched sample

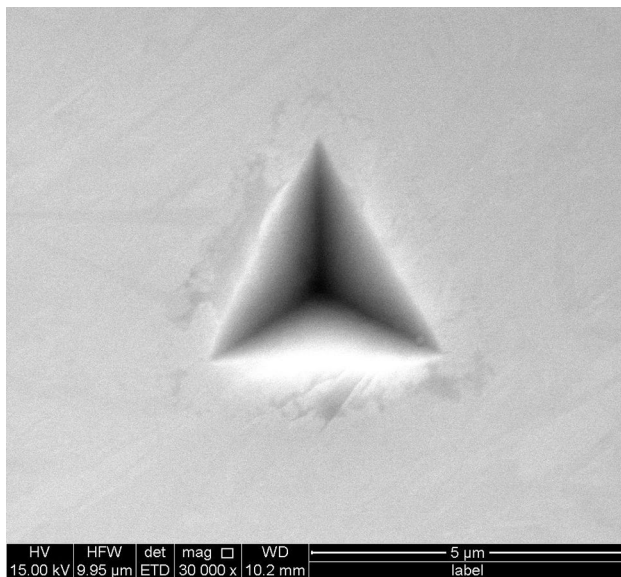
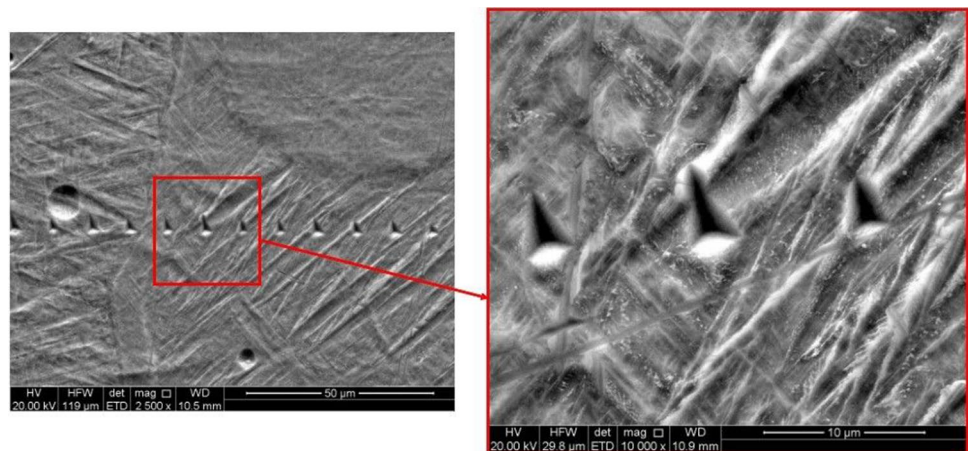


Fig. 8 SEM image of the equilateral triangle indentation formed by the Berkovich indenter on the surface of the unetched sample

Fig. 9 Three selected indents created on the surface of the etched sample



For better understanding and thorough investigation, apart from the surface profile analysis, SEM images of the indentations were taken under high magnification to observe whether there are any changes in the geometry of the indents. The indent, created by a three-sided Berkovich indenter, should show an equilateral triangle from the top view, assuming the sample surface is perfectly flat and smooth (i.e., with a low roughness value) and the indented material is also homogenous. The high resolution SEM image of the unetched sample (Fig. 8) displays an impressed equilateral triangle mark created with a 600 nm indentation depth, with sides of $4 \pm 0.14 \mu\text{m}$. According to the geometrical calculation, a three-sided Berkovich indenter can theoretically create an equilateral triangle with $4.52 \mu\text{m}$ sides when the indenter has penetrated 600 nm in a homogenous substance. The difference between the sides of the triangle's impression in the sample and the theoretical calculation could be related to the elastic deformation during and after unloading of the indenter, compressive residual stresses and the actual penetration depth of 600 nm, which may not be a full 600 nm due to the variable distance between the indenter and the unetched surface at the start of the test.

However, the SEM image of the etched sample (Fig. 9), magnified section, exhibits non-uniform triangles, which are similar to isosceles triangles, formed by the indenter on the surface of the etched sample. The triangles are also individually different in their sizes. The changes in the size and geometry of the indentations may have originated from the peaks and valleys of the rough surface of the etched sample. Figure 10 shows the 3D image of the surface of the etched sample in the same region of the three indentations in the magnified section of Fig. 9. The 3D image confirms that the top vertex of the middle triangle indentation has pressed a high peak, red area, of the asperity. This high peak causes the impressed mark forms an isosceles triangle which is also confirmed in the drafted model in Fig. 11b. SEM image of the middle indentation with a high magnification can also be seen in Fig. 10.

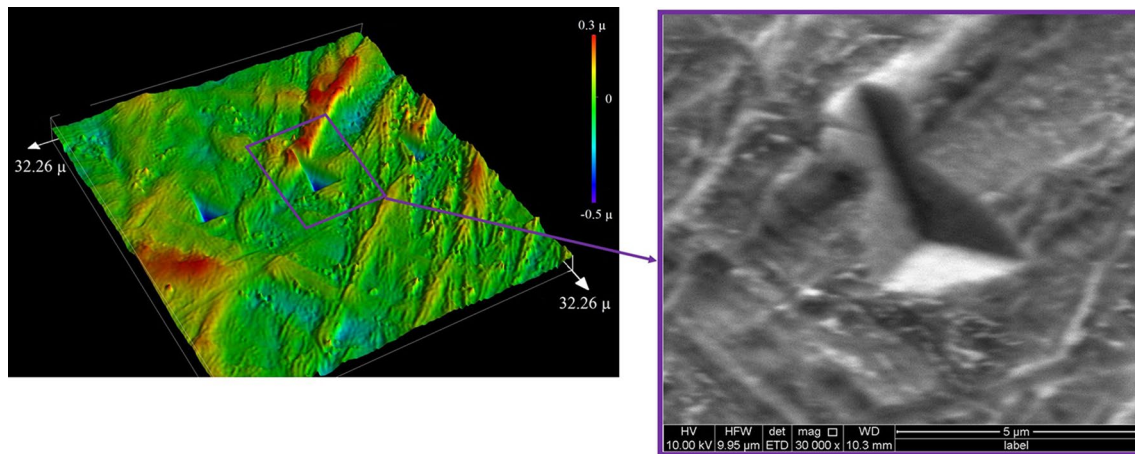


Fig. 10 A 3D image of the etched sample surface with three indentations and the SEM image of an indent with an isosceles triangle shape

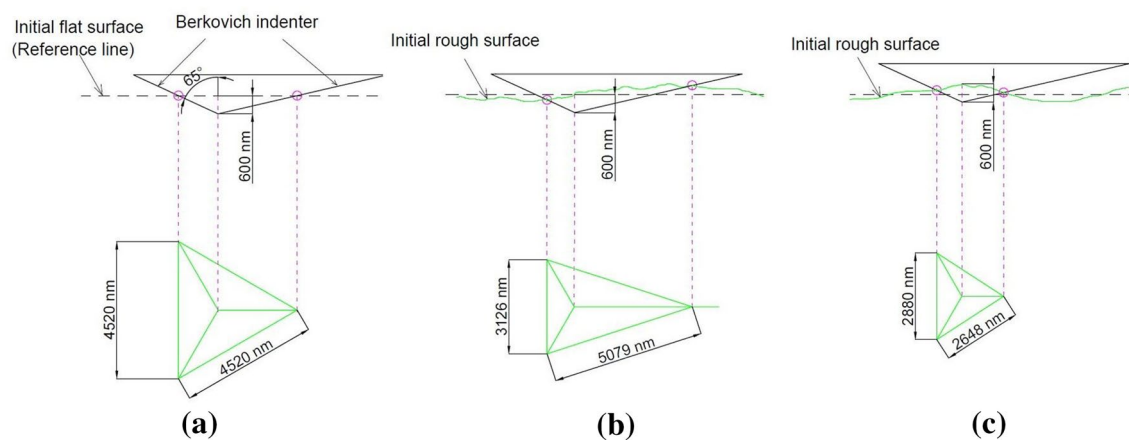


Fig. 11 Impressed mark created by a 600 nm indenter penetration on surfaces with different roughness conditions (a) a fully flat surface, (b) a rough surface with a peak to valley ratio of around 300 nm,

and (c) the same rough surface condition but with an indent created on top of a peak

Figure 11 demonstrates schematically how a rough surface could have an impact on the geometry and size of the impressed indents, in comparison with the indentations on the flat and smooth surface of a homogenous material, with the assumption that the material does not experience an elastic deformation during and after unloading of the indenter. In order to deform the peaks and valleys of the rough surface through the nanoindentation process, higher force and more energy are required, as the higher volume of material resists against the plastic deformation. In an unlikely case, if the indenter contacts and penetrates perfectly at the top of a peak, as shown in Fig. 11c, lower force and less energy is required for plastic deformation and the indentation will be smaller.

For this reason, the indents created on the etched samples need more energy for plastic deformation and consequently show higher hardness in comparison with the unetched sample, as presented in Table 4. The plastic deformation energy consumed for each indentation which was calculated using IBIS software (Table 4), is the area enclosed under the curve [load (P) vs penetration depth (h_t) graphs, Fig. 4] obtained during the loading and unloading stages for individual indentation. Considering the above discussion, the changes in the size and the geometry of individual impressed indents on the etched sample can explain the deviation of the $P-h_t$ curves shown in Fig. 4a.

Table 4 Energy consumed for plastic deformation in nano-Joule (nJ), for creation of indentations on the surface of etched and unetched samples

Samples	Average consumed energy, nJ	Coefficient of variation, %
Unetched sample	5.88 ± 0.09	1.5
Etched sample	6.99 ± 0.71	10.2

Conclusions

The analysis of both the etched and unetched samples during nanoindentation and microindentation testing reveals etching may result in errors in the nanoindentation analysis for SLM-fabricated titanium samples. A dimensionless roughness parameter α has been calculated for both the microindentation and the nanoindentation of both samples to evaluate the sensitivity of the indentation hardness results to changes in surface roughness due to etching. The largest value of α , 0.016, which belongs to the nanoindentation of the etched sample, is still lower than the maximum recommended α value of 0.05, yet the etched sample showed a 19% increase in its apparent nano-hardness when compared with the unetched sample. This means that the proposed magnitude of α , at below 0.05, for hardness numbers to be independent of the surface roughness is not valid for nanoindentations of SLM-fabricated titanium parts. It seems a lower value of α may need to be proposed as a critical value, which requires further investigation. The increase in the nano-hardness of the etched sample appears to be related to the peaks and valleys of the etched surface. It is therefore suggested that for characterization of mechanical properties via nanoindentation and collection of valid data for either etched or unetched samples, the area to be subjected to nanoindentation tests should first be examined by a surface profilometer to obtain the surface roughness and its condition before any indentation is made. If there is no access to an accurate surface-profiling system, the area subjected to the nanoindentation test should be examined using SEM after indentation. The actual geometry of the individual indentations observed by SEM (under the same load P) could be a qualitative indication of nanoindentation accuracy, where the formation of equilateral triangle indents would be evidence of more accurate measurements. Any changes in the geometry of individual indentations increase the uncertainty of the results.

Acknowledgements This work has been supported by the Australian Government Research Training Scholarship Program and The University of Adelaide. Alson Kwun Leung Ng is acknowledged for his work on hydrofluoric acid etching and Adelaide Microscopy for providing access to nanoindenter and SEM facilities. This work was performed, in part, at the Optofab node of the Australian National Fabrication Facility (ANFF), utilizing Commonwealth and South Australian State Government Funding.

References

1. W.C. Oliver, G.M. Pharr, Measurement of hardness and elastic modulus by instrumented indentation: advances in understanding and refinements to methodology. *J. Mater. Res.* **19**, 3–20 (2011)
2. M. Sebastiani, K. Johanns, E.G. Herbert, G.M. Pharr, Measurement of fracture toughness by nanoindentation methods: recent advances and future challenges. *Curr. Opin. Solid State Mater. Sci.* **19**, 324–333 (2015)
3. D.S. Harding, W.C. Oliver, G.M. Pharr, Cracking during nanoindentation and its use in the measurement of fracture toughness. *MRS Proc.* **356**, 663–668 (2011)
4. J.-H. Kim, S.-C. Yeon, Y.-K. Jeon, J.-G. Kim, Y.-H. Kim, Nanoindentation method for the measurement of the Poisson's ratio of MEMS thin films. *Sens. Actuators A* **108**, 20–27 (2003)
5. L.-N. Zhu, B.-S. Xu, H.-D. Wang, C.-B. Wang, Measurement of residual stresses using nanoindentation Method. *Crit. Rev. Solid State Mater. Sci.* **40**, 77–89 (2015)
6. J.-I. Jang, Estimation of residual stress by instrumented indentation: a review. *J. Ceram. Proc. Res.* **10**, 391–400 (2009)
7. J. Dean, G. Aldrich-Smith, T. Clyne, Use of nanoindentation to measure residual stresses in surface layers. *Acta Mater.* **59**, 2749–2761 (2011)
8. M. Karam-Abian, A. Zarei-Hanzaki, H.R. Abedi, The local characterization of individual phase mechanical properties using nano-indentation and in situ scanning probe microscopy in an advanced high strength steel. *Steel Res. Int.* **88** (2017). <https://doi.org/10.1002/srin.201600274>
9. Y. Liu, A. Ngan, Depth dependence of hardness in copper single crystals measured by nanoindentation. *Scr. Mater.* **44**, 237–241 (2001)
10. S. Pathak, D. Stojakovic, R. Doherty, S.R. Kalidindi, Importance of surface preparation on the nano-indentation stress-strain curves measured in metals. *J. Mater. Res.* **24**, 1142–1155 (2009)
11. Z. Wang, *Influences of sample preparation on the indentation size effect and nanoindentation pop-in on nickel*. Doctor of Philosophy, The University of Tennessee Knoxville, 2012
12. L. Thijs, F. Verhaeghe, T. Craeghs, J.V. Humbeeck, J.-P. Kruth, A study of the microstructural evolution during selective laser melting of Ti–6Al–4V. *Acta Mater.* **58**, 3303–3312 (2010)
13. H.K. Rafi, N.V. Karthik, H. Gong, T.L. Starr, B.E. Stucker, Microstructures and mechanical properties of Ti6Al4V parts fabricated by selective laser melting and electron beam melting. *J. Mater. Eng. Perform.* **22**, 3872–3883 (2013)
14. M. Koike, P. Greer, K. Owen, G. Lilly, L.E. Murr, S.M. Gaytan et al., Evaluation of titanium alloys fabricated using rapid prototyping technologies—electron beam melting and laser beam melting. *Materials* **4**, 1776–1792 (2011)
15. M. Brandt, *Laser Additive Manufacturing: Materials, Design, Technologies, and Applications* (Woodhead Publishing, Cambridge, 2016)
16. S. Kumar, Selective laser sintering/melting, in *Comprehensive Materials Processing*, vol 10 (Elsevier, 2014), pp. 93–134
17. D.M. Allen, *The Principles and Practice of Photochemical Machining and Photoetching* (Adam Hilger, Techno House, Bristol, 1986), p. 97
18. K.L. Johnson, *Contact Mechanics* (Cambridge University Press, Cambridge, 1987)

Publisher's Note Springer Nature remains neutral with regard to jurisdictional claims in published maps and institutional affiliations.

Machining Versus Heat Treatment in Additive Manufacturing of Ti6Al4V Alloy



Alireza Dareh Baghi, Shahrooz Nafisi, Reza Hashemi, Heike Ebendorff-Heidepriem, and Reza Ghomashchi

Abstract Anisotropy in the mechanical properties of Laser Powder Bed Fusion (L-PBF)-fabricated titanium parts, which could be problematic in service, is dependent on the build directions and may be mitigated by post-fabrication treatments such as surface machining or heat treatment. However, investigation of the anisotropy in truly as-printed conditions, i.e., prior to any post-process, is always a challenge as the horizontally built parts are noticeably distorted compared to vertically built ones. In this study, by deploying a novel design, straight horizontal samples in the as-printed condition were fabricated. This allowed a comparison to be made possible in the mechanical properties of two built orientations of vertical and horizontal in the as-printed condition. This paper discusses how the surface machining or post-thermal treatment influences the anisotropy in the mechanical properties compared to as-printed conditions. It further highlights how annealing process at a temperature of 850 °C is more effective than stress relieving at a temperature of 670 °C to nearly diminish the anisotropy in mechanical properties even without any need for machining. Therefore, when machining becomes less feasible due to the geometrical complexity of L-PBF parts, a thermal treatment may be the solution for better service performance.

A. Dareh Baghi (✉) · S. Nafisi · R. Ghomashchi
School of Mechanical Engineering, University of Adelaide, Adelaide, SA 5005, Australia
e-mail: alireza.darehbaghi@adelaide.edu.au

S. Nafisi
e-mail: shahrooznafisi@gmail.com

R. Ghomashchi
e-mail: reza.ghomashchi@adelaide.edu.au

R. Hashemi
College of Science and Engineering, Flinders University, Tonsley, SA 5042, Australia
e-mail: reza.hashemi@flinders.edu.au

H. Ebendorff-Heidepriem · R. Ghomashchi
Institute of Photonics and Advanced Sensing, School of Physical Sciences, University of Adelaide, Adelaide, SA 5005, Australia
e-mail: heike.ebendorff@adelaide.edu.au

Keywords Laser powder bed fusion · Ti6Al4V · Build direction · Machining · Stress relieving · Annealing

Introduction

The manufacture of engineering components out of Ti-6Al-4V (Ti64) by additive manufacturing (AM) techniques, particularly selective laser melting (SLM) or as currently recommended nomenclature of Laser Powder Bed Fusion (L-PBF), has attracted a wide range of attention due to its capability in making complex geometries in one single fabrication step. L-PBF made Ti64 parts have been used in various fields, such as aerospace [1, 2] and biomedical [3, 4] fields. Although the L-PBF-fabrication process for Ti64 parts provides high strength, it shows lower ductility in comparison with the conventionally manufactured counter parts [5–7]. Furthermore, undesirable anisotropy is another reported drawback in the mechanical properties of both vertical- and horizontal-built samples [7–11]. In the current report, the effect of build orientation (i.e., vertical and horizontal) on the tensile properties of Ti64 parts fabricated under two conditions of machined and non-machined (as-printed) is analyzed. Importantly, a novel method to address the challenge of distortion in the as-printed horizontal samples is developed. With this new method, non-distorted horizontal samples were fabricated under the as-printed conditions (with no heat treatment) [12]. In addition, the influence of two heat treatment cycles, including stress relieving and annealing, is compared with or without the effects of the machining process on the mechanical properties to highlight if thermal treatment alone could be used when machining becomes impractical due to the geometrical complexity of the as-printed unit [13].

Experimental Procedures

Materials and SLM Equipment

The pre-alloyed Ti64 (grade 5) powder was sourced from a commercial German supplier, TLS, Technik GmbH & Co. Table 1 summarizes the powder and bulk samples' chemical analyses. The alloy composition and the impurities and oxygen content in both the Ti64 powder and the printed samples are within the acceptable range specified by ASTM F2924-14 [14]. The powder characteristics verified using a laser particle size analyzer, Malvern Mastersizer 2000 having a volume median size of $d(0.5) = 22.73 \mu\text{m}$. The L-PBF machine of 3D SYSTEMS ProX DMP 200 machine which employs a 1070 nm wavelength (λ) laser source in a continuous mode, and having a maximum power capacity of 300 W, was used. The optimized L-PBF process parameters implemented in this investigation are given in Table 2. Also, a bi-directional laser strategy with an interlayer 90° rotation was selected.

Table 1 Elemental analysis by ASTM, commercial Ti64 (grade5) powder, and as-printed, (wt.%) [13]

Item	V	Al	Fe	O	C	N	H	Ti
Powder	3.94	6.15	0.18	0.098	0.005	0.010	<0.002	Bal.
SLM fabricated bulk samples	3.97	6.14	0.19	0.114	0.005	0.011	<0.002	Bal.
ASTM F2924-14	3.50–4.50	5.50–6.75	Max 0.3	Max 0.2	Max 0.08	Max 0.05	Max 0.015	Bal.

Table 2 Printing parameters employed [12]

Laser power, P (W)	Hatch space, h (μm)	Scanning velocity, v (mm/s)	Layer thickness, t (μm)	Laser beam diameter, w ₀ (μm)
270	85	1800	30	70

Tensile Samples Preparation

Before fabricating any samples for investigation in this work, two horizontal dumbbell shape samples were firstly made for measuring the deflection of as-printed horizontal samples after being removed from substrate. Then, a reverse deflected (convex) design was considered to fabricate all horizontal samples [12]. As shown in Fig. 1a and b, a reverse deflection of 0.5 mm was considered for fabrication of all horizontal samples, either the as-printed dumbbell shape or horizontal rods. The curved horizontal samples, when removed from the substrate, presented a straight profile shape. Apart from reverse deflected horizontal samples, as-printed vertical tensile samples, as shown in Fig. 1a, and vertical rods (Fig. 1b) were fabricated on substrate. The cylindrical rods, either vertical or horizontals, were used to be

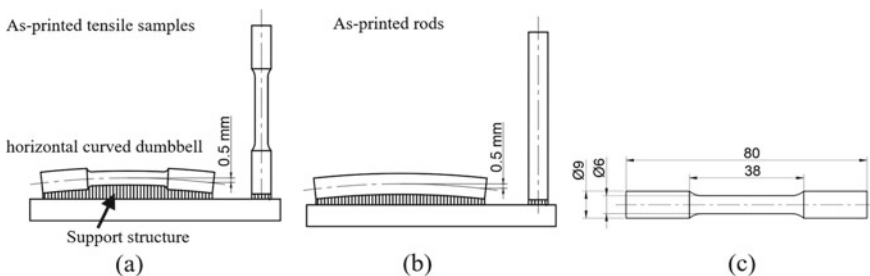


Fig. 1 a As-printed vertical and convex horizontal samples, b vertical and horizontal rods for fabrication of MV and MH samples, and c final size of all machined and non-machined tensile samples (in mm) [12]

Table 3 Thermal treatment procedures performed on the cylindrical samples prior to machining [13]

Heat treatment	Temperature, °C	Soaking time, h	Cooling type
Stress relieving	670 °C (± 10)	5	Controlled furnace cooling from soaking temperature to 250 °C in 12 h
Annealing	850 °C (± 10)	2	

surface machined (via turning process) to make machined tensile samples. In this way, the effect of built orientations in the as-printed and surface machined conditions is systematically examined. It has to be emphasized that the final shape of tensile samples, either as-printed or machined samples, Fig. 1c, conforms with the small size specimens defined by ASTM E8 [15]. In this work apart from studying the effect of L-PBF built direction on tensile mechanical properties in two conditions of as-printed (non-machined) and machined, the effect of two cycles of heat treatments of stress relieving and annealing on the mechanical properties of the machined vertical (MV) and horizontal (MH) samples was investigated.

The nomenclature of tensile test samples examined in this study is summarized as:

- **NMH**: Non-Machined Horizontal samples, as-printed (non-heat treated) tensile test samples, deposited horizontally (Fig. 1a),
- **NMV**: Non-Machined Vertical samples also known as as-printed (non-heat treated) vertical samples, deposited vertically (Fig. 1a),
- **MH**: Machined Horizontal samples made from cylindrical rods deposited horizontally (Fig. 1b),
- **MV**: Machined Vertical samples made from SLM fabricated vertical rods (Fig. 1b).

Table 3 presents the two heat treatment processes used in the present study.

Results and Discussion

Microstructural Characterisation

The microstructures of the as-printed (non-heat treated), stress-relieved, and annealed of both the horizontal build and vertical build test coupons are shown in Fig. 2, depicting the formation of a columnar architecture. The chessboard pattern formed for the vertical build samples is a further evidence to confirm the formation of columnar grains in L-PBF (SLM) printed Ti64 samples. The solidification of columnar grain architecture for L-PBF specimens has already been reported widely in the open literature, e.g. [16–19]. The columnar grains containing laths substructure are separated by the prior β grain boundaries. The columnar grain architecture with the prior β boundaries appeared unchanged at the temperatures for both stress relieving and

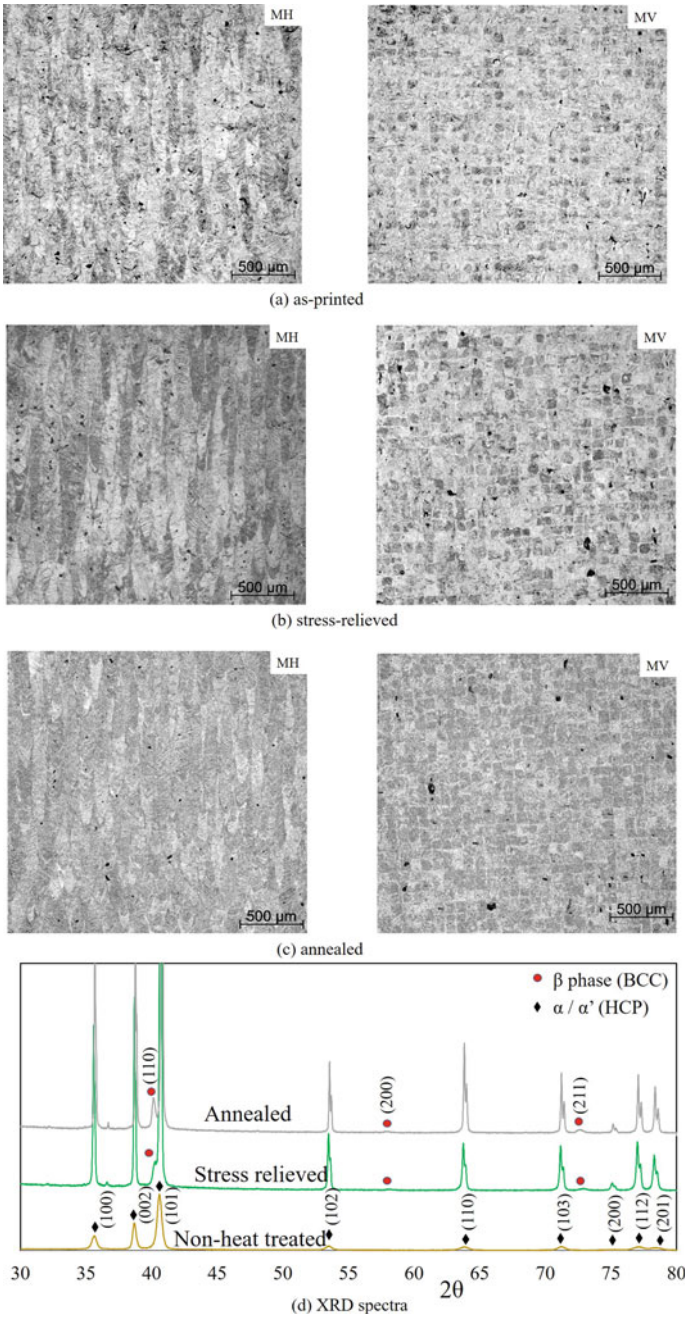


Fig. 2 Optical micrographs of the grains architecture in MH and MV samples along with phase identification (Color figure online)

annealing treatments [6, 7]. This is due to the fact that these temperatures are below the β transus temperature, i.e., 1000 ± 20 °C [20]. The XRD analysis confirmed the formation of α' (α) and β phases and their crystal structures for all test pieces, Fig. 2d.

When the microstructure in Fig. 2 is examined closer, in addition to the resolving of the lath morphology of the martensite α' , it becomes clear that there is some small amount of a 2nd phase segregated within the columnar structure as shown in Fig. 3. The formation of white phase is barely detectable in the as-printed specimens (see the area circled in Fig. 3a), but it is quite distinctive within the stress-relieved and annealed samples, Fig. 3b, c. The chemical analysis of the white phase reveals higher vanadium concentration; see the EDS spectra in Fig. 3, which may be an indication of β phase formation. The formation of α' (α) phase was confirmed through XRD analysis, Fig. 2d, where the formation of β phase in the as-printed, non-heat treated, specimens is not confirmed by the XRD analysis. This is most likely due to its concentration being below the detection limit of XRD technique. The white spots' sizes of the V-rich phase are larger but fewer in the annealed sample compared with that of the stress-relieved. This confirms the diffusion controlled process for the formation of white phase increasing with temperature as has already been reported by other researchers [21]. Image analysis (quantitative metallography) of micrographs in Fig. 3b and c showed that the V-rich phase content increased from ~4% to just above 13% with increasing the temperature from 670 to 850 °C. This is an interesting point of having $\alpha'(\alpha) \rightarrow \beta$ transformation well below the transus temperature. This

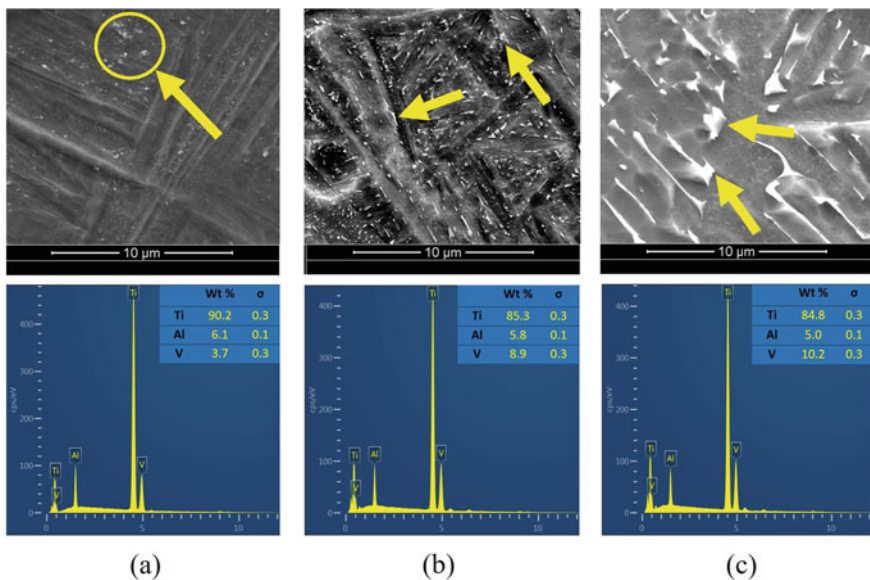


Fig. 3 SEM micrographs and EDS spectra of the MH samples; **a** as-printed, **b** stress-relieved, and **c** annealed. (Arrows show the V-rich β phase). The V content increases for stress-relieved and annealed samples (Color figure online)

might be an indication of HCP martensite phase inhomogeneity during printing considering the small melt pool size to create some localized super saturation of α' with vanadium.

Mechanical Properties

In order to highlight the effect of surface machining and/or heat treatment, the vertical built samples were tested in tension for as-printed, machined, and post-heat treated (stress-relieved and annealed) as shown in Fig. 4. It is interesting to mention that the as-printed, non-machined, and non-heat treated, vertical test coupons prematurely fail at a stress level well below the yield strength for Ti64 alloy. However, when it is machined (MV in non-heat treated condition) or heat treated (either stress-relieved or annealed) but in non-machined condition (NMV), the properties vary immensely and there are strength values in excess of 1000–1200 MPa. In addition to achievable high yield and tensile strengths, the ductility of specimens varies depending on the surface quality, i.e. machined/non-machined and stress-relieved or annealed. As expected, the ductility of the annealed specimens is always higher than the ductility of either the as-printed or stress-relieved. Machining the surface layer, however, improves the magnitude of ductility whether for as-printed, stress-relieved, or annealed.

In another trial, we tried to highlight the effect of built direction, and therefore, both the vertical built and horizontal built were tested as shown in Fig. 5. It is evident that machining and thus reducing surface roughness improve the tensile properties regardless of the build direction, as-printed or heat treated. The striking point, however, in this Fig. 5 is the superiority of horizontal built on the ductility of

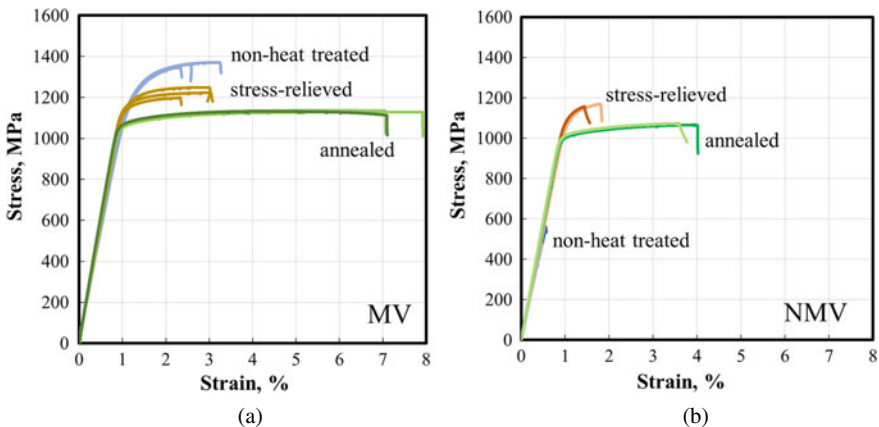


Fig. 4 Engineering stress–strain distribution for the non-heat treated, stress-relieved, and annealed specimens, **a** MV and **b** NMV [13] (Color figure online)

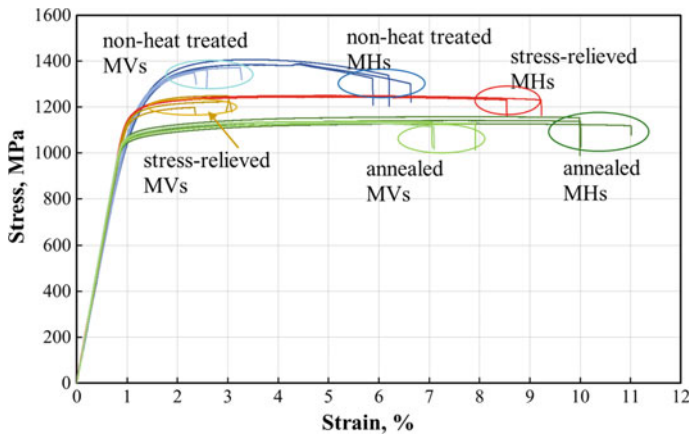


Fig. 5 Engineering stress–strain distribution for machined samples (MH and MV) [13] (Color figure online)

all specimens. As a clear outcome, it can be claimed the horizontal built generate some improvement in the tensile properties of the alloy.

In order to explain the changes in tensile properties with respect to build direction, machining, and thermal treatment, it is important to analyse the relationship between the axis of tensile loading with respect to the build direction. Furthermore, it is required to show the geometry of valleys and peaks (surface asperities) when it comes with the roughness of the surface. This will provide some clues of loading experienced at the surface of the specimens with respect to the geometry and directionality of the valleys and peaks with respect to tensile loading. It also resolves the issue as why machining generally improves mechanical properties or why thermal treatment is effective even with non-machined specimens. This will then help us to come up with conclusion of whether it is the machining which is more helpful or it is the thermal treatment which should be a “must do” treatment. Such conclusion has great bearings in industry since machining may not be as straight forward as it may look if we have a complex geometry part while we may get away with a simple thermal treatment of the most complex geometry. In order to answer this question, references should be made to Fig. 6 where the surface topography is shown for both build directions, Fig. 6b and c, along with the interrelationship of the tensile loading and specimens’ grain architecture, Fig. 6a.

The pattern for peaks and valleys for the outer surface of the horizontal sample in Fig. 6b is entirely different from those viewed in the vertical samples, Fig. 6c. The distance between successive peaks, i.e. wavelength, on the outer surface of horizontal samples is greater than that of the as-printed vertical. The short wavelength of the asperities on the outer surface of the as-printed vertical sample is mainly correlated with the 30 μm layer thickness used during printing. The short wavelength, coupled with the unused layers near the outer surface of the as-printed vertical samples, leads to the formation of sharp deep notches (micro-grooves), as evident

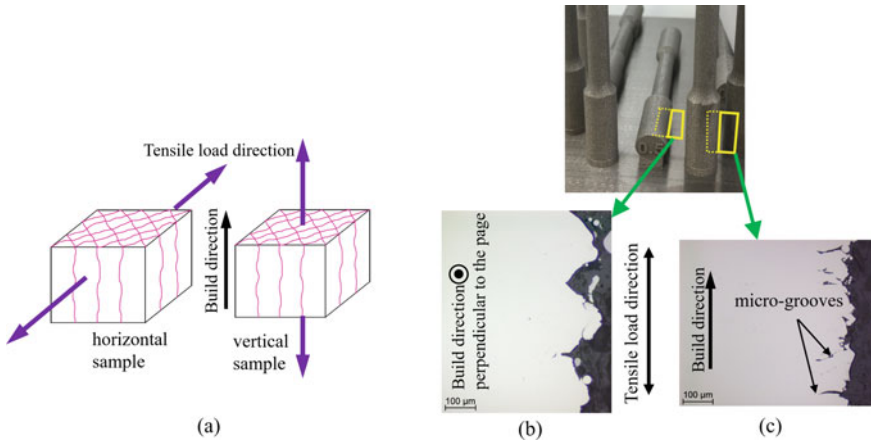


Fig. 6 a Schematic representation of tensile loading-build direction interrelationship, b, c longitudinal representation of the outer surface topography; optical microscopy of b NMH and c a NMV samples [12, 13] (Color figure online)

from Fig. 6c. These micro-grooves, which have their planes perpendicular to the tensile load, could impact the mechanical properties of NMV. They are used as intense stress raisers magnifying the stress at those grooves tips and thus leading to overall premature failure well below the yield as shown in Fig. 4b. It has to be mentioned that the residual stresses generated due to the characteristics of L-PBF process are another important issue which exacerbates the premature failure of the vertical built specimens. Machining of the surface layer completely removes the peaks and valleys and therefore the issue of stress intensification. It is also believed thermal treatment like stress relieving and particularly annealing removes the residual stresses and also expected to slightly change the sharpness of the valleys (due to changes in the radii of curvature at the surface of the peaks/valleys with the curvature at the tip of the valleys and peaks, a diffusion flux will be established towards the tip to increase the radius of curvature at the tip) to make them less sensitive with respect to the direction of tensile loading and thus reducing the likelihood of premature failure as witnessed for non-machined, non-heat treated vertical built specimens.

Conclusions

The effect of build direction, surface machining, and post-thermal treatment is studied for L-PBF of Ti6Al4V alloy to highlight if a simple thermal treatment could be sufficient to optimize the mechanical properties L-PBF parts.

1. The build direction plays an important role on the integrity of printed specimens and as-printed horizontal specimens are of higher tensile strength and ductility in comparison with vertical built ones.

2. As-printed vertical samples fail prematurely which was attributed to the geometry of the surface peaks and valley with respect to the direction of tensile loading.
3. Both machining and post-thermal treatment (stress relieving and annealing) improve the ductility of as-printed specimens.
4. Specimens built horizontally have superior ductility to their vertical built counterparts for all three conditions of as-printed, machined, and post-thermal treated.
5. Thermal treatment is capable of improving the ductility of as-fabricated parts in roughly similar magnitude as machining.
6. Since machining may not be a straight forward operation for most complex geometry parts, it is believed a simple thermal treatment, e.g. heating and slow cooling, may be sufficient for industrial parts.

Acknowledgements This work was performed in part at the OptoFab node of the Australian National Fabrication Facility (ANFF) utilizing Commonwealth and South Australian State Government funding. Adelaide Microscopy is gratefully acknowledged for providing access to electron microscopy facilities. A. Dare Baghi is grateful to the Australian Government and Adelaide University for the PhD scholarship.

References

1. Banerjee D, Williams JC (2013) Perspectives on titanium science and technology. *Acta Mater* 61:844–879
2. Santos LV, Trava-Airoldi VJ, Corat EJ, Nogueira J, Leite NF (2006) DLC cold welding prevention films on a Ti6Al4V alloy for space applications. *Surf Coat Technol* 200:2587–2593
3. Geetha M, Singh AK, Asokamani R, Gogia AK (2009) Ti based biomaterials, the ultimate choice for orthopaedic implants—a review. *Prog Mater Sci* 54:397–425
4. Murr L, Quinones S, Gaytan S, Lopez M, Rodela A, Martinez E et al (2009) Microstructure and mechanical behavior of Ti–6Al–4V produced by rapid-layer manufacturing, for biomedical applications. *J Mech Behav Biomed Mater* 2:20–32
5. Thijs L, Verhaeghe F, Craeghs T, Humbeeck JV, Kruth J-P (2010) A study of the microstructural evolution during selective laser melting of Ti–6Al–4V. *Acta Mater* 58:3303–3312
6. Vrancken B, Thijs L, Kruth J-P, Van Humbeeck J (2012) Heat treatment of Ti6Al4V produced by selective laser melting: microstructure and mechanical properties. *J Alloy Compd* 541:177–185
7. Vilaro T, Colin C, Bartout JD (2011) As-fabricated and heat-treated microstructures of the Ti-6Al-4V Alloy processed by selective laser melting. *Metall Mater Trans A* 42:3190–3199
8. Rafi HK, Karthik NV, Gong H, Starr TL, Stucker BE (2013) Microstructures and mechanical properties of Ti6Al4V parts fabricated by selective laser melting and electron beam melting. *J Mater Eng Perform* 22:3872–3883
9. Sercombe T, Jones N, Day R, Kop A (2008) Heat treatment of Ti-6Al-7Nb components produced by selective laser melting. *Rapid Prototyp J* 14:300–304
10. Simonelli M, Tse YY, Tuck C (2014) Effect of the build orientation on the mechanical properties and fracture modes of SLM Ti–6Al–4V. *Mater Sci Eng A* 616:1–11
11. Hartunian P, Eshraghi M (2018) Effect of build orientation on the microstructure and mechanical properties of selective laser-melted Ti-6Al-4V alloy. *J Manuf Mater Process* 2:69

12. Dareh Baghi A, Nafisi S, Hashemi R, Ebendorff-Heidepriem H, Ghomashchi R (2021) Experimental realisation of build orientation effects on the mechanical properties of truly as-built Ti-6Al-4V SLM parts. *J Manuf Process* 64:140–152
13. Dareh Baghi A, Nafisi S, Hashemi R, Ebendorff-Heidepriem H, Ghomashchi R (2021) Effective post processing of SLM fabricated Ti-6Al-4V alloy: Machining vs thermal treatment. *J Manuf Process* 68:1031–1046
14. ASTM F2924-14 (2014) Standard specification for additive manufacturing titanium-6 aluminum-4 vanadium with powder bed fusion
15. ASTM E8/E8M-16a (2016) Standard test methods for tension testing of metallic materials
16. Xu W, Brandt M, Sun S, Elambasseril J, Liu Q, Latham K et al (2015) Additive manufacturing of strong and ductile Ti-6Al-4V by selective laser melting via in situ martensite decomposition. *Acta Mater* 85:74–84
17. Wysocki B, Maj P, Sitek R, Buhagiar J, Kurzydłowski KJ, Świąszkowski W (2017) Laser and electron beam additive manufacturing methods of fabricating titanium bone implants. *Appl Sci* 7:657
18. Yang J, Yu H, Wang Z, Zeng X (2017) Effect of crystallographic orientation on mechanical anisotropy of selective laser melted Ti-6Al-4V alloy. *Mater Charact* 127:137–145
19. Zhao X, Li S, Zhang M, Liu Y, Sercombe TB, Wang S et al (2016) Comparison of the microstructures and mechanical properties of Ti-6Al-4V fabricated by selective laser melting and electron beam melting. *Mater Des* 95:21–31
20. Roger G, IMI T, Shannon RC (1991) Heat treating of titanium and titanium alloys. In: Teledyne Allvac in ASM handbook, vol 4, ASM International, pp 913–923
21. Sallica-Leva E, Caram R, Jardini AL, Fogagnolo JB (2016) Ductility improvement due to martensite α' decomposition in porous Ti-6Al-4V parts produced by selective laser melting for orthopedic implants. *J Mech Behav Biomed Mater* 54:149–158